Hydrophobic 2,7-Octadienyl Ether Cellulose Nanofibrils Using Butadiene Sulfone as Dual Reagent and Medium: Synthesis, Characterization, and Applications

By

JURI FUKUDA

DISSERTATION

Submitted in partial satisfaction of the requirements for the degree of

DOCTOR OF PHILOSOPHY

in

Agricultural and Environmental Chemistry

in the

OFFICE OF GRADUATE STUDIES

of the

UNIVERSITY OF CALIFORNIA DAVIS

Approved:

_____

Professor You-Lo Hsieh, Chair

_____

Professor Tina Jeoh

_____

Professor Mark Mascal

Committee in Charge

2022

DEDICATION

My Best Friend: Ms. Jo Madrid

Juri Fukuda
March 2022
Agricultural and Environmental Chemistry graduate group

ABSTRACT

Cellulose nanofibers from bioresources have garnered intensive research interest in the past decades due to their unique properties including high tensile strength and modulus, low density, biocompatibility/biodegradability, and abundant hydroxyls for surface chemistry. The nanofibers with surface negative charges, such as cellulose nanocrystals (CNCs) and cellulose nanofibrils (CNFs) obtained from sulfuric acid hydrolysis and 2,2,6,6-tetramethyl-piperidin-1-yl-oxyl (TEMPO) mediated oxidation, respectively, have been widely studied as reinforcements in hydrophilic polymer nanocomposites, hydrogels/aerogels, and nanopapers, however, they are not compatible with hydrophobic polymers or organic solvents. Currently, the most common way to produce hydrophobic nanocelluloses is functionalization of CNCs and TEMPO-CNFs that were previously prepared from cellulose, which is not the most efficient way to obtain nanocellulose. This Ph.D. dissertation describes our streamlined approach to produce hydrophobic nanocelluloses that are compatible with hydrophobic polymers and organic solvents in an environmentally-sustainable method, and their applications.

The novel method of generating hydrophobic nanocellulose was demonstrated by one pot telomerization combined with mechanical shearing directly from native cellulose derived from rice straw. Butadiene sulfone (BDS) served both as 1,3-butadiene (1,3-BD) reagent and as a reaction medium to carry out the telomerization reaction. Optimized telomerization of 1,3-BD with cellulose at 110 °C, followed by disintegration of 2,7-octadienyl-ether (ODE) functionalized

cellulose by mechanical blending yielded ca. 27-41 wt % ODE-nanocelluloses (NCs). The thickness of these NCs, as measured by atomic force microscope (AFM), varied with the choice of solvent: 3.7 nm in dimethyl sulfoxide (DMSO), 6.3 nm in tetrahydrofuran (THF), and 4.4 nm in $CHCl_3$. The surface ODE groups were confirmed by fourier transform infrared spectroscopy (FTIR) peaks at 2800-2980 cm^{-1} for the methylene stretching vibration and at 1640-1704 cm^{-1} for the C=C stretching vibration. Solution state ^{1}H, ^{13}C, Heteronuclear Single Quantum Coherence (HSQC), and homonuclear correlation spectroscopy (COSY) nuclear magnetic resonance (NMR) elucidated the structure of ODE groups and cellulose backbones in ODE-CNFs. The Tmax of ODE-CNFs (332 °C) was revealed to be far superior to that of TEMPO-CNFs.

The direct disintegration of ODE-cellulose into ODE-NCs in organic media was demonstrated using ultra-sonication. This is a benefit because it avoids an extra solvent exchange step in producing a fabricated nanocomposite. Scale-up (0.5 g cellulose) telomerization at the optimal condition generated ODE-NCs with a degree of substitution (DS) of 0.67 mmol ODE/g-cell. This agrees relatively well with the DS 0.74 mmol ODE/g-cell of ODE-NCs produced from the original scale (0.1 g cellulose), validating the scale-up reaction. To optimize the DS for ODE-cellulose, diffusion of liquid BDS into cellulose was improved by pre-sonicating cellulose (50 % amplitude (*A*), 3 min) in dimethylformamide (DMF) prior to telomerization at the average temperature range between 103 °C and 110 °C. This produced ODE-cellulose with the optimal DS 1.2 mmol ODE/g cellulose ("g-cell") and 1.8 mmol ODE/g-cell in the temperature range of 100-110 °C. The 1.2 DS ODE-cellulose was further sonicated (50 % *A*, 20 min) to yield 45.5 % ODE-NCs in toluene. The 1.8 DS ODE-cellulose was further sonicated (50 % *A*, 20 min) to yield 73.3 % ODE-NCs in linseed oil (LO). Both were directly brought into processing of nanocomposites. The reinforcing effect of 2 % 1.2ODE-NCs and the ability of alkene groups in 1.2ODE-NCs to

associate/cross-link with polybutadiene (PBD) and styrene-blk-isoprene-blk-styrene block copolymer (PSIS) were demonstrated in nanocomposite films formed under varied conditions. The optimal condition for reinforcing cellulose paper with 0.07 % 1.8ODE-NCs in LO was heating at 70 °C for 16 h, because it successfully transformed cellulose paper into the most reinforced hydrophobic paper.

Cellulose has been optimally isolated from almond shells (AS) in 35.2 % yield by a two-step $NaClO_2$/KOH process. Subsequent TEMPO (2,2,6,6-tetramethyl-piperidin-1-yl)oxyl mediated oxidization generated ribbon shaped cellulose nanofibrils (CNF) with 1.2 ± 0.44 nm height, 5.2 ± 1.2 nm width, and 1.6 ± 0.8 μm length in 90 % yield. Anisotropic 4.3 cross-sectional width-to-height aspect ratio with dominant hydrophilic planes and high length-to-height aspect ratio (1167) are distinctively unique to AS-CNFs. This study elucidated how this characteristic served in construction of material forms by analyzing different assembling and disassembling behaviors by three CNF material forms created under vaired solidification conditions. Fibers that were rapidly frozen (-196 °C) and freeze-dried were readily 100 % redispersible in water into CNFs with the original size indicating that they were assembled by predominantly polar-polar CNF associations. Aerogels fabricated from a slow freezing (-20 °C) and freeze-drying process, exhibited an amphiphilic characteristic by absorbing both water and chloroform. They redispersed only 10 wt % in water into CNFs with the original size indicating that nonpolar-nonpolar interfacial CNF associations are their dominant force for assembling along with some polar-polar CNF interactions. Films, from the slowest solidification via casting under the ambient condition, exhibited polar surfaces with water contact angles of 34-42° while they were partially redispersible in water (71.7 wt %), ethanol (11.4 wt %) and dimethylacetamide (7.4 wt %), indicating that they were formed by using dominant polar-polar and minor nonpolar-nonpolar interfacial associations.

The higher char residues of the films in TGA may indicate that slow solidification process in air induced a calcitrant characteristic. All data combined suggest that solidification speed and environments largely influence strength and surface hydrophobicity/hydrophilicity/amphiphilicity of TOCNF materials, and their fundamental basis of material construction seems to be supported by polar-polar TOCNF associations between wider hydrophilic-to-hydrophobic planes which are characteristic to AS-TOCNFs.

ACKNOWLEDGEMENTS

I would like to express my sincere gratitude to my research advisor Professor You-Lo Hsieh for providing me her continuous support, patience, deep insights, and broad knowledge in analytical and material science throughout the long journey of my Ph.D. study. Besides my advisor, I would like to thank the rest of my dissertation committee: Professor Tina Jeoh, and Professor Mark Mascal for their time, willingness to serve on my thesis committee, and kind support. I would like to thank my QE committee: Professor Gang Sun, Professor Neil Schore, Professor David Britt, Professor Nitin Nitin, and Professor Matt J. Hengel for their heartwarming encouragement. I appreciate the Facilities Engineer, Mr. Scott Berg in the Chemistry Department, for kindly taking care of technical problems critical to keep my research going from time to time.

I am very grateful for the financial support of the California Rice Board, USDA Western Sun Grant Program, and the Jastro Shield Research Award.

I am so grateful for my friends, Dr. Steven Sciamanna (UC Berkeley) and Sandy Roadcap, who provided me warm friendship, support, and encouragement. Steve not only helped me to modify my autoclave vessel and the heating system for the scale-up reaction but also enlightened me by his deep insights every time we discussed about science. Sandy provided me a tremendous help by proofreading my dissertation, and graciously and meticulously guided me to refine it. I thank my husband John Frances Mahoney for his immense patience and support throughout my long journey. Last, but not least, tremendous gratitude for Ms. Jo Madrid who provided me consistent emotional and mental support throughout this endeavor.

CONTENTS

LIST OF FIGURES

Figure 1-12. (a) Schematic illustration of nanocomposite preparation: modification of CNF network with allyl glycidyl ether (mCNFs), covalent grafting of PMMA on mCNFs via free radical polymerization (mCNF-g-PMMA), physical blend of modified CNF/PMMA (mCNF-b-PMMA), and "blend" of CNF/PMMA prepared by diffusion of high molar mass PMMA into the porous CNF network gel (CNF-b-PMMA). Schematic representations of the relative CNF/PMMA distribution and SEM images of cryo-fractured surface of (b, b', b'') CNFs blended with PMMA (CNF-b-PMMA); (c, c', c'') modified CNFs blended with PMMA (mCNF-b-PMMA); (d, d', d'') modified CNFs grafted with PMMA (mCNF-g-PMMA); (e) stress-strain curves.[94]

Figure 1-13. Illustration of the cross-linking network in nanocomposites: (a) mercaptoundecanoyl-CNCs and natural rubber (NR)[45] (b) H-bond network in epoxidized (E) NR/un-modified CNCs; (c) dual cross-linking networks: H-bonds and covalent bonds in ENR/modified CNCs; (d) Stress-strain curve of the composite with 3, 5, 10 % m-CNCs.

Figure 1-14. (a) Photographs of electrolyte wettability of PP separator, CNF separator. (b) Photograph of electrolyte immersion height of PP separator, CNF separator.[117] (c) SEM images of electrospun SP prepared at various solution flow rates (25.5 and 65.5 mL min^{-1}).[119]

Figure 2-1. A side product formed by Diels-Alder reaction on ODE-cellulose: (a) reaction scheme during telomerization at 120 °C and (b) ^{1}H NMR of Diels-Alder side-product.

Figure 2-2. Telomerization reaction and process flow chart and products.

Figure 2-3. AFM (a, c, e, g) and TEM (b, d, f, h) of CNFs in the aqueous supernatant (aq. sn.) from telomerization (4, 6, and 8 ODE/AGU, 90 or 110 °C) and blending (30 k rpm, 30 min). Wt % CNFs and their thicknesses (T, nm), widths (W, nm), and lengths (L, μm) were determined from 3, 100, 30 and 13 measurements, respectively.

Figure 2-4. ODE-cellulose and ODE-NCs from 6ODE110: (a) XRD of ODE-cellulose; (b) organic dispersions (0.1 wt %) of the aqueous precipitate (aq. ppt), immediately after vortexing (top) and after 1 h (bottom); (c) ODE-NC in organic supernatant and consumption of BDS. Optical microscope images of representative microfibrils in DMSO (6ODE110) precipitate (1.5 k rpm,15 min); (d) transmission; (e) under crossed polars. Width (W, μm) and length (L, μm) were determined from 50-100 measurements. The organic supernatant and gelled precipitate from 6ODE110 in m-cresol and toluene after centrifugation (1.5 k rpm, 15 min): AFM of supernatant (0.0005 w/v % on HOPG) in (f) m-cresol and (g) toluene. Photos of gelled precipitate in (h) m-cresol and (i) toluene. The insets are respective dispersion before centrifugation and resting for one hour after vortexing for 3 sec. (j) UV-vis transmittance of 0.01 w/v % organic supernatants; FTIR ODE-NC in (k) $CHCl_3$, (l) DMSO, (m) DMF, (n) THF.

Figure 2-5. AFM (a and b on mica. c-d, f-g, i-k, and n on HOPG) and TEM (e, h, l-m on carbon) images of ODE-CNFs from: (a-e) 6ODE110; (f) unmodified CNF control; (g and h) 8ODE110; (i, l) 4ODE90; (j, m) 4ODE110 in THF or $CHCl_3$ supernatants; (k) 6ODE110 dispersed in DMSO, and the inset shows CNF bundles; (n) 6ODE110 dispersed in DMF. All at 0.0005 w/v %. The specimen for TEM was negatively stained with (e) 2 % uranyl acetate or (h, l, m) phosphotungstic acid. Measurements for thicknesses, widths and lengths were based on n=100 for thickness (T, nm), and n=30 for width (W, nm) and length (L, μm). Area percent nanofibrils and nanoparticles (CNF/NP) were indicated.

LIST OF SCHEMES

LIST OF TABLES

CHAPTER 1: Literature Review

1.1 Introduction

A vast knowledge base of cellulose nanofibers has been established after a few decades of intensive research conducted worldwide, leading to considerable progress in understanding their characteristics and potential applications. This chapter reviews current literature on: 1) the fundamentals of cellulose, such as sources, structures, and intrinsic properties, 2) chemical derivation methods of nanocellulose from a plant source, 3) nanocellulose surface modifications, and applications suited for their surface properties. The chapter concludes with current issues and needs in nanocellulose studies, leading to my research covered by Chapter 2-5.

1.2 Fundamentals of Plant Cellulose and Cellulose Nanofibers

1.2.1 Cellulose source and structure

Cellulose is the most abundant polymer on earth, originating in wood, plants, algae, tunicates, and bacteria. Due to its availability, cellulose-based materials have been ubiquitous in our society in the form of paper, textiles, and consumables[1]. Cellulose is found in plant cell walls as structural reinforcing material along with lignin and hemicellulose (**Figure 1-1**). Lignin is composed of cross-linked phenolic precursors such as paracoumaryl alcohol, coniferyl alcohol, and sinapyl alcohol, while hemicellulose is a mixed polysaccharide consisting of xyloglucans, xylans, glucomannans, and mixed linkage β-glucans. While lignin-precursors and -oligomers adsorb on the surface of cellulose microfibrils[2], hemicellulose interacts with cellulose via H-bonding and covalent bonding[3,4]. Wood, one of the most industrially important cellulose sources, is composed of ca. 45 % cellulose, *ca*. 25 % hemicellulose and *ca*. 20 % lignin. Cellulose is typically isolated from lignin and hemicellulose by three steps, 1) organic extraction (2:1

toluene/ethanol) to remove waxes and other extractives, 2) delignification by $NaClO_2$, and (3) hemicellulose removal by alkaline (5 % KOH) treatment[5].

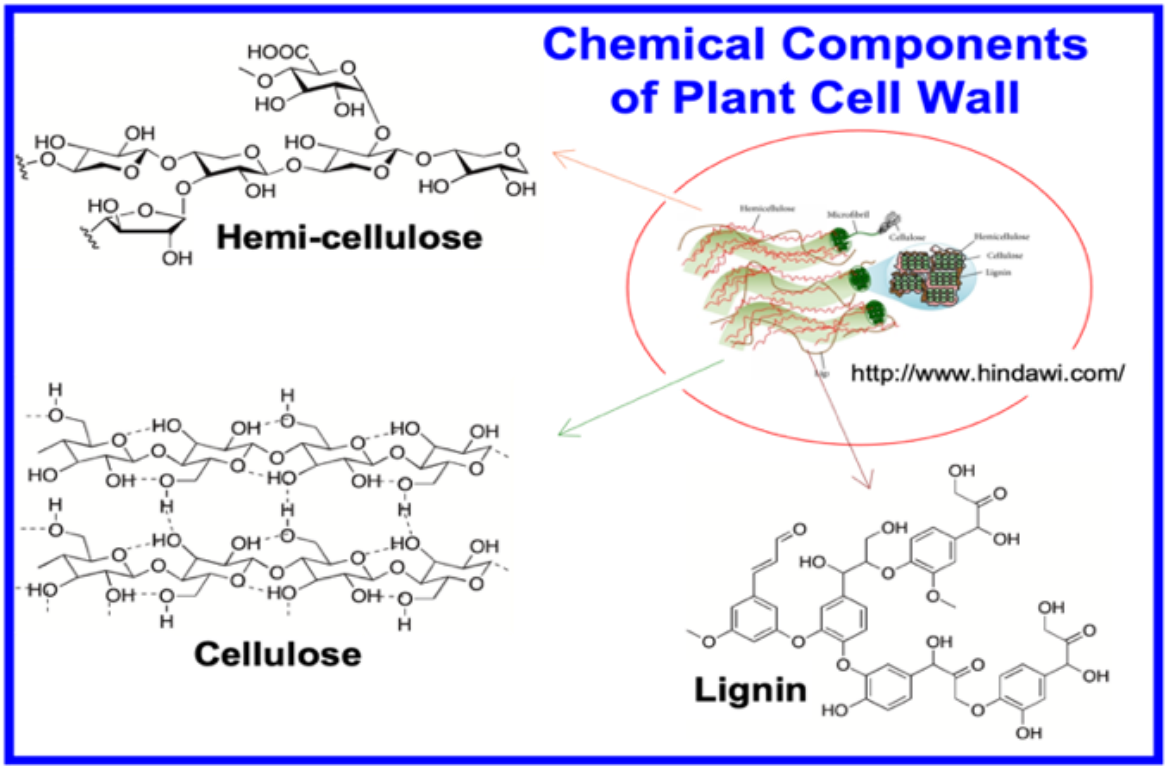

Figure 1-1. Chemical components of plant cell walls.

Cellulose is a linear β-1,4-linked glucan homopolymer. Each single cellulose chain possesses a directional chemical asymmetry with respect to the termini of its molecular axis, with one end being a reducing end with a hemiacetal group and the other having a nonreducing end[6]. The parallel chains of cellulose are hierarchically constructed into elementary fibrils, then to microfibrils (**Figure 1-2**) by extensive hydrogen bonds between cellulose chains. Microfibrils are thought to be composed of *ca.* 36 glucan chains[7,8], and the degree of polymerization (DP) could be as high as ca. 14,000–15,000 in the secondary cell wall of cotton[9].

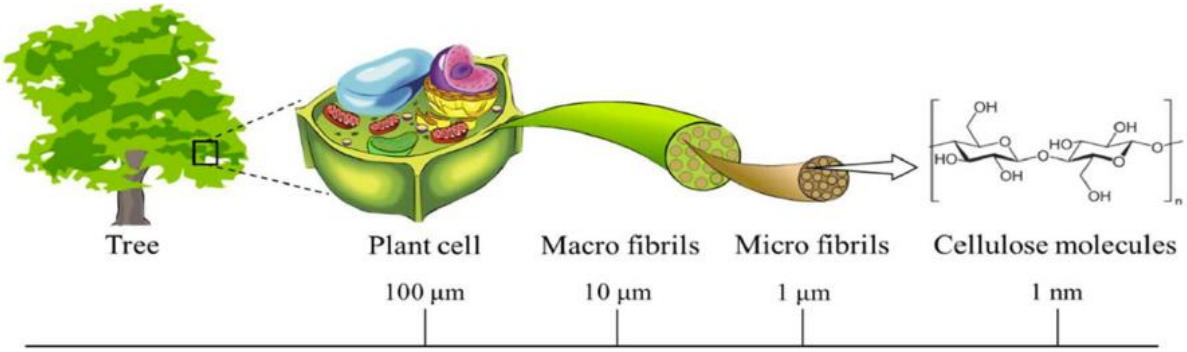

Figure 1-2. Hierarchical structure of cellulose microfibrils from higher plants.[10]

1.2.2 Crystal structure of cellulose

Native cellulose is composed of crystalline and amorphous domains. The crystalline domain has one crystal structure, cellulose I, which include two allomorphs, Iα and Iβ. In cellulose chains, both Iα and Iβ adopt parallel configurations, but cellulose Iα adopts single-chain triclinic unit cell while cellulose Iβ exists as a two-chain monoclinic unit cell.[11] Iα belongs to a triclinic unit cell (a = 6.717 Å, b = 5.962 Å, c = 10.400 Å, α = 118.08°, β = 114.80°, and γ = 80.37°) (**Figure 1-3b**) containing one cellulose chain per unit cell[12]. On the other hand, Iβ exists in a monoclinic unit cell (a = 7.784 Å, b = 8.201 Å, c = 10.38 Å, α = β = 90°, and γ = 96.5°) (**Figure 1-3b**) that encloses two cellulose chains[12].

The main difference between Iα and Iβ is the relative displacement of the sheets in the chain direction. For both Iα and Iβ, the second sheet (II) is shifted down along the cellulose chain axis that is parallel to the plane by ~c/4 with respect to the first sheet (I) (green arrow, **Figure 1-3c**). In Iα the third sheet (III) continues shifting downward relative to II by ~c/4. However, in Iβ it is shifted upward by ~c/4, creating a relative difference of ~c/2 in the third sheet (III) with respect to II in Iα and Iβ. Another minor difference identified by synchrotron and neutron diffraction study is the H-bond geometry between Iα and Iβ, in which the interchain O6H•••O3 bond distances are

shorter in Iβ (1.779 Å, 2.040 Å) compared to Iα (1.853 Å, 2.176 Å), and the average bond angle is larger in Iβ (∠OHO = 156.2°) compared to that of Iα (∠OHO = 134.3°)[9], which is thought to be one of the factors that makes the Iβ structure more stable than the Iα structure.[12-14]

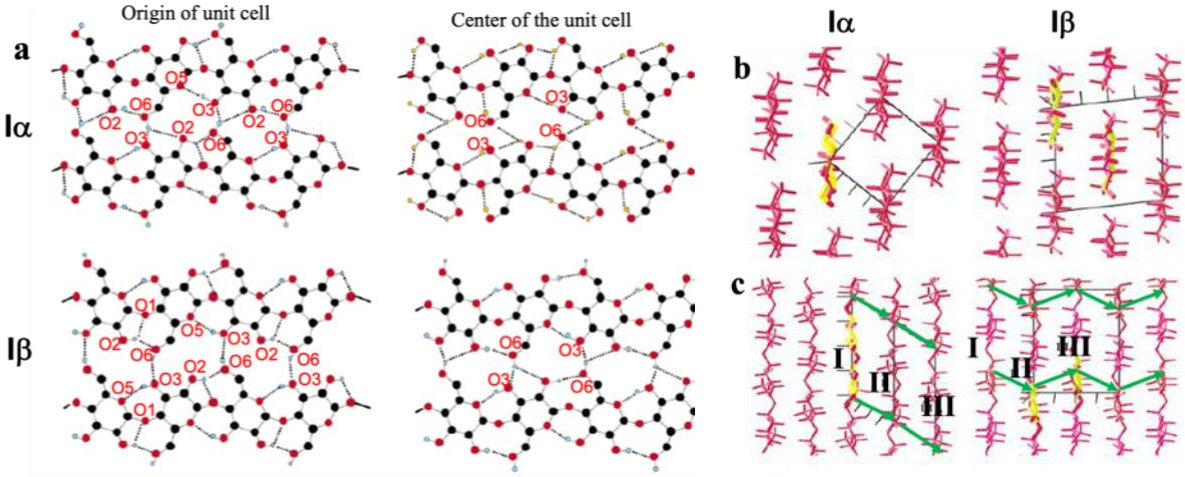

Figure 1-3 (a) Hydrogen-bonding patterns in cellulose Iα and Iβ: crystalline network at the origin and center of the unit cell for Iα and Iβ.[12–14] Projections of the crystal structures of cellulose Iα and Iβ: (b) down the chain axes, with triclinic unit cell for Iα and monoclinic for Iβ shown by black lined boxes; (c) perpendicular to the chain axis. The cellulose chains are represented by pink skeletal models. The asymmetric unit of each structure is also represented in thicker lines with carbons in yellow.[12,13]

1.3 Nanocellulose

1.3.1 Nanocellulose isolation

Nanocelluloses are nano-dimensioned crystal domains isolated from micro-sized cellulosic materials, such as wood pulp, microcrystalline cellulose, cotton, and others. The two general types of nanocellulose are shorter, rod-shaped cellulose nanocrystals (CNC), and thinner, longer, and more flexible cellulose nanofibrils (CNF)[5,15]. They are obtained by top-down separation of crystalline domains from coexisting amorphous domains through chemical, enzymatic, or mechanical means (shear force, ball-milling, high-pressure homogenizers, grinders, refiners, cryo-

crushing, ultrasonic treatment, micro-fluidization), or a combination of chemical and mechanical means[15].

Of the chemical separation methods to obtain nanocelluloses, the most common are acid hydrolysis with sulfuric acid (H_2SO_4, ~64 wt %) and 2,2,6,6-tetramethylpiperidin-1-yl-oxyl (TEMPO) mediated oxidation. H_2SO_4 hydrolysis produces negatively charged CNCs with diameters and lengths of ca. 10-100 nm and ca. 100-350 nm (**Figure 1-4a, d**), respectively, depending on the cellulose sources, with high crystallinity (Crystallinity Index (CrI) up to 90 %) but low yields, typically < 30 %[16-18]. TEMPO-mediated oxidation, on the other hand, originally reported for soluble polysaccharides[19] and developed for cellulose by Isogai and coworkers[22], generates cellulose with C6 oxidized to the carboxylic acid oxidation state (**Figure 1-4b, e)**. That material is then mechanically sheared to produce CNFs with a diameter of 2-10 nm and length varying between tens of nanometers to micrometers (**Figure 1-4c, f**).[20] CNFs exhibit lower crystallinity (CrI 60-70 %), but the process to make them generally has much higher yields (>90 %) than those of CNCs[18, 21, 22]. The longer CNFs have the ability to entangle, offering additional mechanical strength, and the large surface area provides more hydroxyls for surface modification.

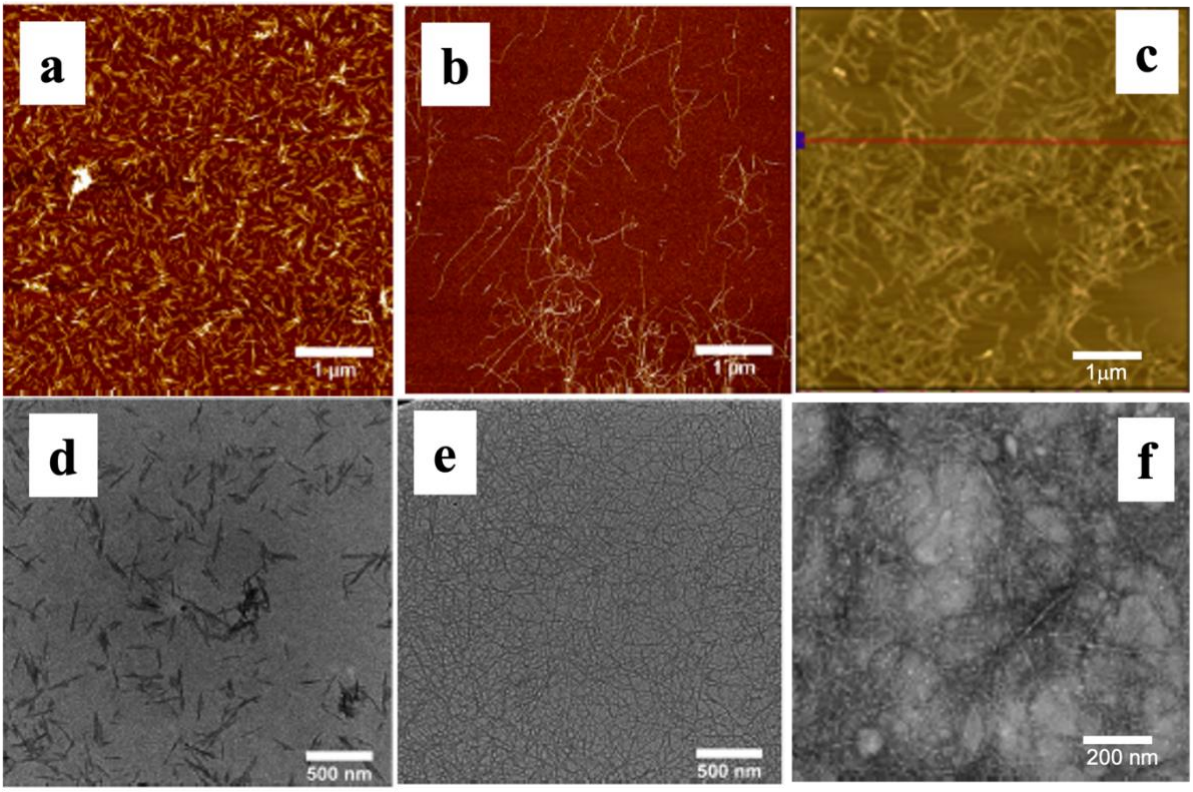

Figure 1-4. AFM images of CNCs and CNFs from wood cellulose by different derivation methods: (a) H_2SO_4; (b) TEMPO; (c) TEMPO and mechanical blending; TEM images of same for (d) H_2SO_4; (e) TEMPO; (f) TEMPO and mechanical blending.[18,20]

Additionally, recent studies have reported two newly developed chemical separation methods to produce nanocelluloses by using hydrogen chloride (HCl) vapor[23] and deep eutectic solvent (DES)[24,25], which give high yields of CNCs and CNFs.

Cotton cellulose fibers (Whatman 1 filter papers) were hydrolyzed by application of HCl vapor in equilibrium with an aqueous HCl solution in a desiccator for longer than 1 hour under pressure (4.8 kPa ~ 8.2 kPa)[23]. The resulting CNCs with a yield of 80 - 97.5 wt % did not have charges, therefore, they were dispersed in formic acid[26] to be analyzed by atomic force microscopy (AFM), which revealed dimensions of 7.5 nm diameter and 150-200 nm length. Scanning electron microscopy indicated that the morphological changes due to hydrolysis are minor. The CNC CrI by wide angle X-Ray scattering increased with increasing HCl vapor pressure (CrI = 64.7 % at 8.2

kPa, 4 h), which was also confirmed by solid phase ^{13}C nuclear magnetic resonance spectroscopy (NMR) (**Figure 1-5a, b**).

Deep eutectic solvents are newly emerging green solvents, readily biodegradable, and typically consist of a hydrogen bond donor (e.g., alcohol, amine, carboxylic acid) and acceptor (halogen salt) pair[27,28]. They have been used to pretreat biomass[29–31] and to produce microcellulose[32] and nanocellulose[24,25,28,33]. A combination of choline chloride (Ch-Cl) and oxalic acid was reported to be the most effective DES for production of CNCs with highest length-to-width aspect ratio (W/L: 1:36), highest CrI (71 %), and highest yield (88%) compared to other acid pairs, such as oxalic acid, *p*-toluenesulfonic acid or levulinic acid [28], or the combination of Ch-Cl and urea[33].

Ma et al. effectively combined the DES treatment of poplar wood kraft pulp (46.1 % cellulose, 34.7 % hemicellulose, 19.1 % lignin) with ultrasonic disintegration of cellulose to generate CNCs and CNFs (**Figure 1-5c, d**). A 1:1 ratio of Ch-Cl and oxalic acid, diluted to 10, 20, or 30 % in water, was used to isolate cellulose (80 °C, 1 h) in 90-91 % purity. The pretreated cellulose was dissociated into CNFs in 10 % hydrated DES, and CNCs in 20 or 30 % hydrated DES by ultrasonic treatment (800 W, 20 kHz, 600 rpm stirring speed) for 20 min, with a CrI of 70 % and charge densities of 0.05-0.12 mmol COO^-/g cellulose (g-cell). This demonstrated that DES pretreatment, in combination with ultrasonic energy, increased the accessibility of cellulose pulp functional groups and facilitated the disintegration of pulp into nanocelluloses.

Jiang et al. demonstrated isolation of lignin-containing CNCs (LCNCs) from thermomechanical pulp (TMP) by comparing treatments of a binary (Ch-Cl/oxalic acid in 1:1 molar ratio) and a ternary (Ch-Cl/oxalic acid/*p*-toluenesulfonic acid in 2:1:1 molar ratio) DES both combined with 30 min mechanical blending (**Figure 1-5e**).[25] LCNCs, obtained at the optimal

condition of using a ternary DES at 80 °C for 3 h pretreatment, had a width of around 6 nm, thickness of 3.3 nm, cellulose I CrI of 57.4%, high lignin content of 47.8%, and higher yield of 66% compared with LCNCs obtained from the binary DES (39 % Y). Also, LCNCs from this process exhibited a high thermal stability (Tmax = 358 °C), indicating promising application potential.

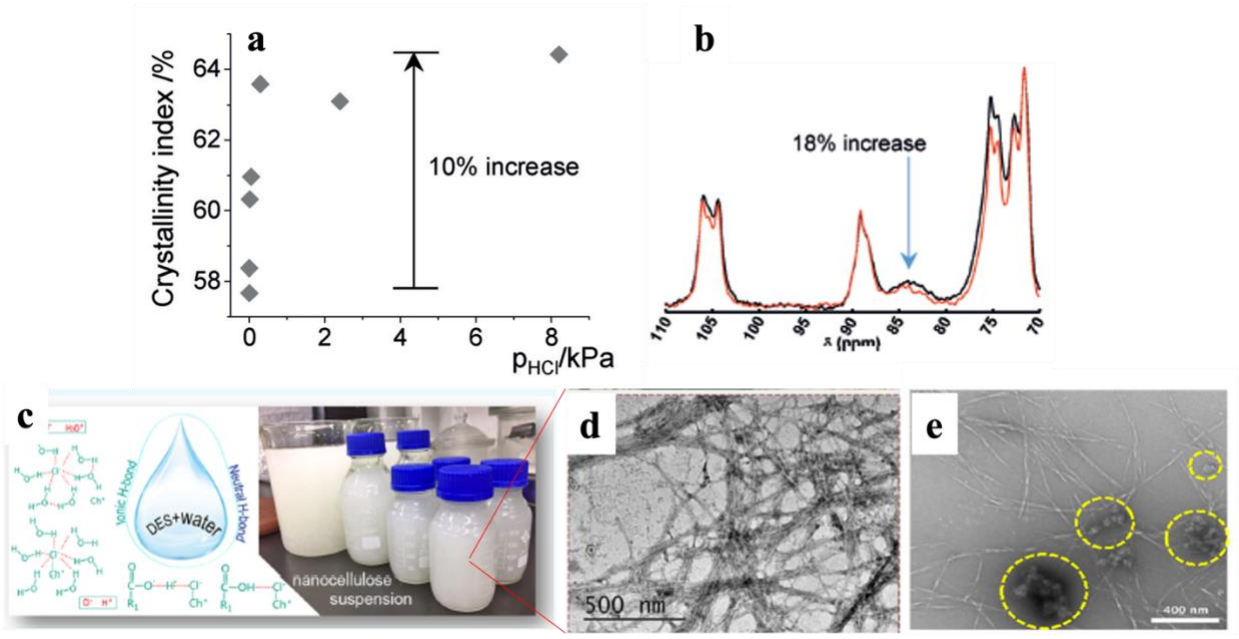

Figure 1-5. The degree of crystallinity: (a) as determined by WAXS diffractograms after four hours of exposure to HCl vapor (measurement error: 0.1 %); b) NMR spectra of an untreated control reference and a sample exposed to 8.19 kPa HCl vapor for four hours.[23] DES treatment of kraft pulp: (c) the hydrated DES; (d) TEM of CNFs (10 % aqueous DES).[24] (e) TEM images of lignin containing LCNCs after ternary DES treatment (lignin aggregates are highlighted with yellow dashed circles).[25]

1.3.2 Properties of nanocelluloses

The intrinsic tensile strength and Young's Modulus of CNCs have been reported to be 7.5 GPa[34] and 150 GPa[35], respectively, and those of CNFs are 233 MPa[36] and 145 GPa[35]. These values are very high for organic materials and the moduli of CNCs are approaching that of multiwalled carbon nanotubes (MWCT). For example, the tensile strength of MWCT is 29 GPa[37] and Young's

modulus is 270–950 GPa[38]. CNCs also exhibit a low coefficient of thermal expansion and thermal conductivity (i.e., ∼0.72−5.7 W m^{-1} K^{-1} for single CNCs and ∼0.22−0.53 W m^{-1} K^{-1} for their organized nanostructured films)[39]. These exceptional mechanical and thermal properties, in combination with their large aspect ratio and low density, make CNCs and CNFs promising bio-based nanomaterials for reinforcing nanocomposites.

1.4 Surface Modification of Nanocellulose

1.4.1 Hydrophilic modification

CNCs from H_2SO_4 hydrolysis and CNFs from TEMPO-mediated oxidation both carry negative charges in their respective sulfate esters and carboxylate functionalities. Charge densities of CNCs and CNFs, which are measured by zeta potential and/or conductometric titration, vary depending on the reaction conditions e.g., the concentration of reagents, temperature, reaction length, and the source of cellulose. By conductometric titration, charge densities normally range between 0.29-0.38 mmol SO_4^-/g-cell for CNCs[16], and 0.59-1.68 mmol COO^-/g-cell for CNFs after mechanical blending[15].

Ultra-sonication has also been shown to disintegrate TEMPO-oxidized cellulose. For example, TEMPO-oxidized wood and tunicate cellulose, both 0.01 w/v % in water, were fully disintegrated into nanofibrils with 1.8 μm length and 2.6-3.6 nm width[40] by 80 min sonication (300 W, 19.5 kHz). In another report, sonication of TEMPO-oxidized cellulose derived from Douglas fir kraft pulp for 10 min produced CNFs (1.1 mmol/g) with 2.5-4.0 nm width in ca. 90 % yield[41]. Also, sulfuric acid hydrolysis of bleached softwood kraft pulp conducted under sonication (1000-1200 W) generated shorter (96 nm) but more uniform lengths of CNCs than those without sonication (150 nm) with similar widths of 10-20 nm[42]. Even unmodified cellulose isolated from poplar wood powder has been disintegrated into nanofibrils by sonication (1000W, 20-25 kHz, 30

min) in water with average width and length of 13.0 nm and 2~3 μm, respectively, in 30 min[43].

Both H_2SO_4-hydrolyzed CNCs and TEMPO-oxidized CNFs are negatively charged and exhibit superior aqueous dispersibility over chemically unmodified nanocelluloses. They are suitable only for aqueous applications, such as reinforcing hydrophilic polymers[44], hydrogels, and aerogels[45,46], but are not compatible with hydrophobic matrices.

1.4.2 Hydrophobic modification

To date, efforts to improve dispersibility/compatibility of nanocellulose in organic solvents and hydrophobic polymers have been directed toward modifying surface hydroxyls of previously-isolated CNCs and CNFs. This section reviews surface modification reactions of CNCs and CNFs with various non-charged functional groups, such as esters[47–50], silyls[51,52], amides[53–56], and others (**Figure 1-6**), with a focus on the dispersibility of the products in organic solvents. Also, the issues of those processes will be discussed at the end of Chapter 1.

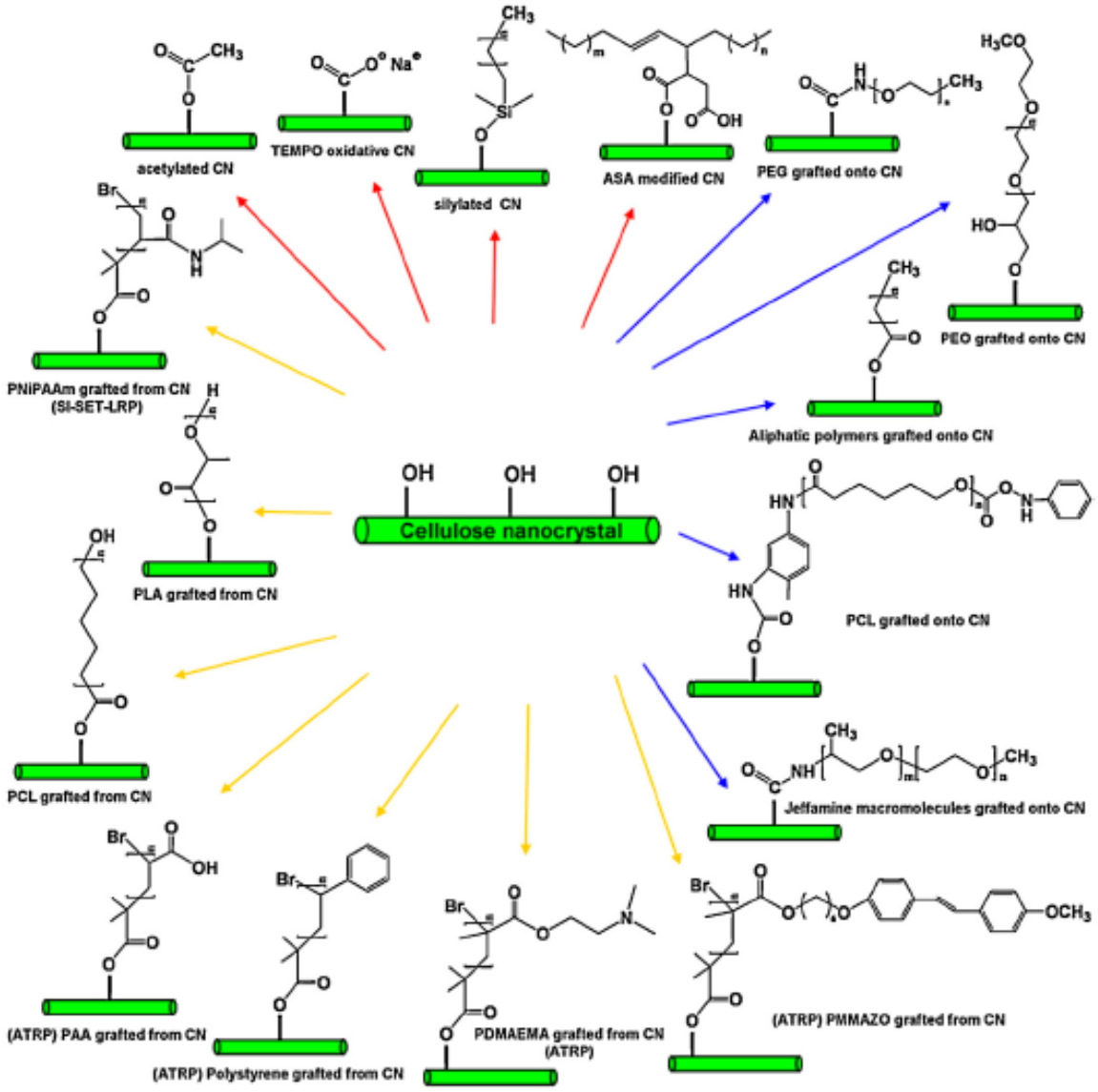

Figure 1-6. Various surface functional groups on nanocellulose.[57]

1.4.2.a Esterification

Among esterification reactions, acetylation of CNCs is the most widely studied in addition to acetylation of cellulose fibers[58–60]. The reaction proceeds by mixing CNCs with acetic anhydride and acetic acid in the presence of a catalyst (i.e., sulfuric or perchloric acid) in either a heterogenous or homogenous process. The heterogenous process uses a diluent solvent such as pyridine or toluene (80 ºC for 5 h) to produce only surface-acetylated CNCs, preserving their

morphology and crystal structure[58]. In the homogenous process, a continuous reduction in the diameter of cellulose crystals during the reaction is observed by transmission electron microscopy (TEM) and X-ray diffraction (XRD), while the longitudinal dimension was less affected (**Figure 1-7a, b**).[59]

CNCs from cotton were esterified using 11-mercaptoundecanoic acid with acetic anhydride and glacial acetic acid, in the presence of a catalytic amount of concentrated sulfuric acid, and stirred at 40 ºC for 3 days to add thiol functionality[50]. The thiol product with the optimal degree of substitution (DS) of 0.85 mmol/g was dispersible in toluene. It was subsequently used for the cross-linking reaction with rubber through free-radical thiolene cross-linking. This treatment provided reinforcement of the natural rubber (cis-1,4-polyisoprene) nanocomposite.

CNCs derived from the tunicate *Halocynthia roretzi* were esterified by an unconventional method of mixing them with an aqueous emulsion of *iso*-octadecenyl succinic anhydride, freeze-drying, and heating to 105 °C[47] to produce esterified CNCs. These CNCs had bulk DS of 0.0158-0.024 (functional group substitutions per 3 OH groups), and were dispersible in N, N-dimethylacetamide (DMAc), ethanol, chloroform ($CHCl_3$), toluene, and 1,4-dioxane.

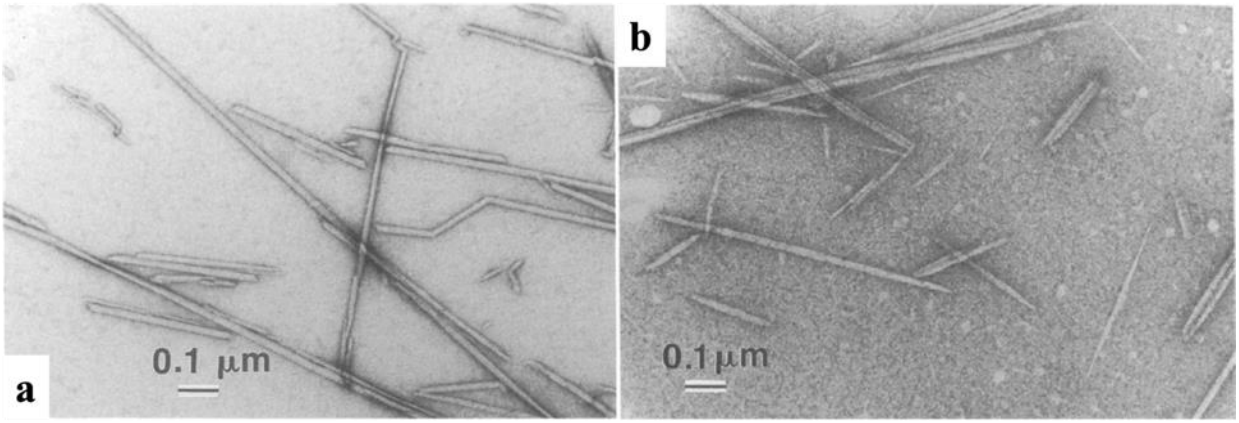

Figure 1-7. (a) Dispersion of microcrystals of tunicin before acetylation. (b) As in (a) but after partial acetylation to DS 0.17 (per 3 OH groups).[59]

1.4.2.b Silylation

The silylation of CNCs derived from hydrolysis of tunicate was conducted in toluene at room temperature using a series of alkyldimethylchlorosilanes with the carbon backbone of the alkyl moieties ranging from the short carbon length of isopropyl to the longer lengths represented by n-butyl, n-octyl and n-dodecyl. This reaction used an equimolar amount of imidazole to neutralize the hydrochloric acid by-product[51]. The morphological integrity of silylated CNCs was preserved when DS was between 0.6 and 1. At DS = 0.6 (per 3 OH groups), CNCs are readily suspendable in tetrahydrofuran (THF) (**Figure 1-8c-e**) and exhibited birefringence under a polarized light microscope. However, at DS greater than 1, the CNCs were disintegrated into cellulose chains, losing the original CNC morphology and characteristics (**Figure 1-8f-h**). To optimize the control of the highly reactive nature of this reaction, cellulose microfibrils extracted from the homogenization of parenchymal cell walls were silylated with the more hindered isopropyl dimethylchlorosilane[52] to obtain silylated CNFs with DS = 0.36 (per 3 OH groups) that were suspendable in THF. The same reaction condition was applied to silylation of sugar beet pulp to generate microfibrils.

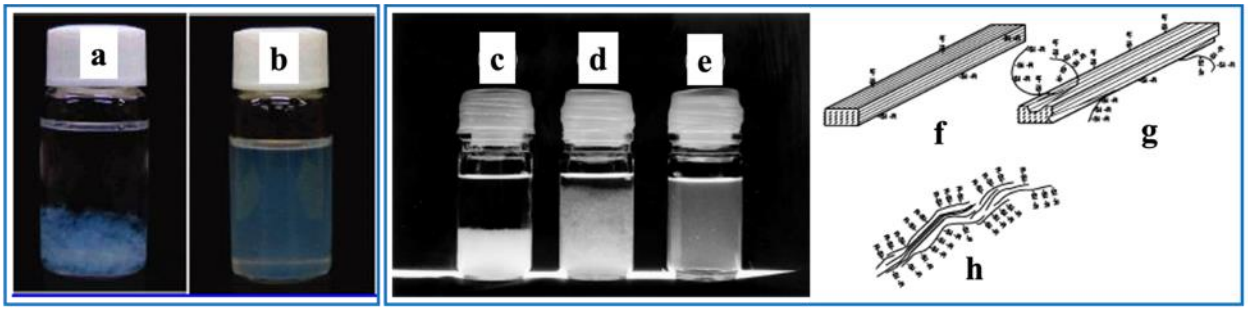

Figure 1-8. Dispersibility of CNCs in 1,4-dioxane: (a) unmodified CNCs; (b) esterified CNCs.[47] Silylated tunicin CNCs in THF: (c) phase-separated unmodified CNCs; (d) flocculated suspension of silylated CNCs with DS=0.4; (e) non-flocculated suspension of silylated CNCs with DS=0.6. (f-h) Models of surface silylated CNCs: (f) onset of surface silylation; (g) silylated CNCs with DS under 1; (h) DS=1, too many cellulose chains have been derivatized, and CNCs have become highly swollen and partly dissolved.[51]

1.4.2.c Grafting

The graft polymerization of styrene on CNC, hydrolyzed from cotton[61] or microcrystalline cellulose (MCC)[62], through surface-initiated atom transfer radical polymerization (SI-ATRP), was conducted to increase surface hydrophobicity of CNCs. For both examples (cotton, MCC) of SI-ATRP, the macromolecular initiator was prepared by an esterification of CNCs with 2-bromoisobutyryl bromide (Br-iBuBr) with triethylamine as a catalyst followed by Soxhlet purification (dichloromethane/ethanol). The modified CNCs were then grafted with styrene in the presence of 2-bromoisobutyrate as the sacrificial initiator, a catalytic amount of copper(I) bromide, and the ligand to generate CNCs grafted with polymerized styrene. When sourced from cotton they are called CNC-g-PS1[62], and when sourced from MCC they are called CNC-g-PS2[61]. Both types are 120-180 nm length (**Figure 1-9a-d**). According to scanning electron microscopy (SEM) images, CNC-g-PS1 was dispersed evenly in a polymethylmethacrylate (PMMA) composite film up to 1 wt % content, whereas homogeneity was lost in the 2 wt % CNC-g-PS1 composite film. The film with 1 wt % CNC-g-PS1 exhibited the highest breaking strength improvement (25%) and elongation of the nanocomposite (34%) compared with its non-grafted counterpart. This is due to a favorable interfacial association between PMMA and modified CNCs[62]. Moradi et al. used the dried CNC-g-PS2 as an absorbent demonstrating the capacity of CNC-g-PS2 to absorb the organic compound 1,2,4-trichlorobenzene (TCB) from water. CNC-g-PS2 absorbed 50 % of its weight in TCB as compared to 30 wt % absorption by its non-grafted counterpart.[61]

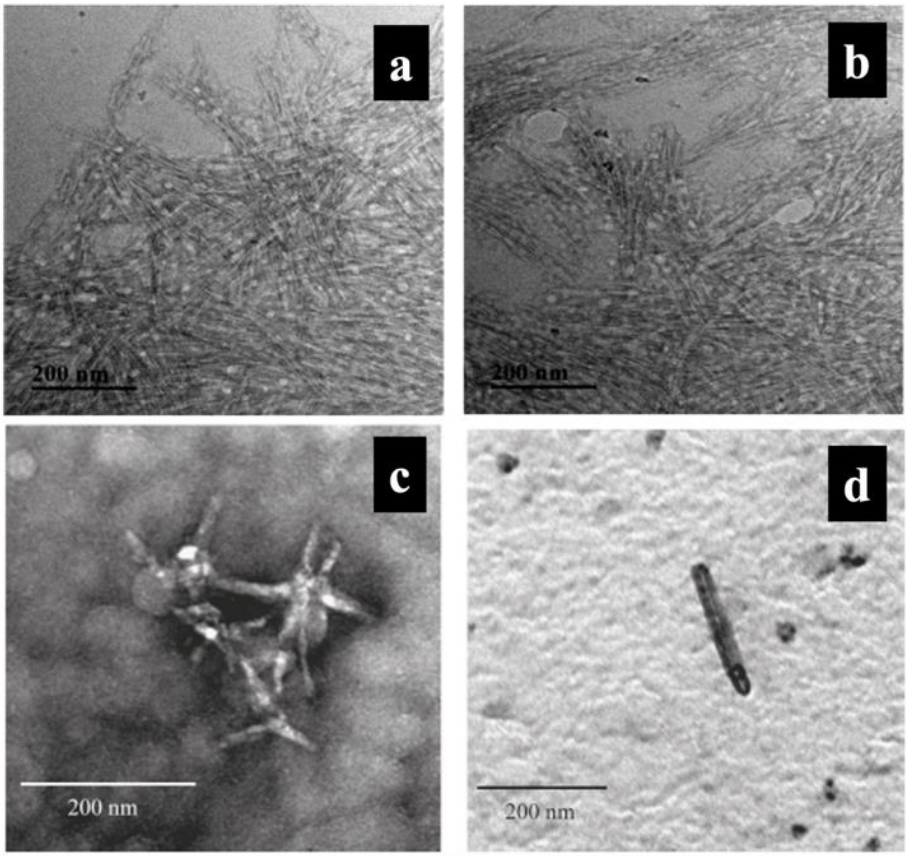

Figure 1-9. TEM images: (a) unmodified CNCs; (b) CNCs grafted with styrene; (c) CNCs grafted with styrene stained with uranyl acetate; (d) stained with OsO_4.[62]

1.4.2.d Amidation

Hydrolyzed (2.5 N HCl) Whatman cellulose powder (CF11) was TEMPO-oxidized (0.95 mmol/g), then grafted with poly (ethylene glycol) with an amino terminal group (PEG-NH_2, MW1000 *Da*) via a two-step reaction using water soluble 1-ethyl-3-(3-dimethylaminopropyl) carbodiimide hydrochloride (EDC) and N-hydroxysuccinimide (NHS) as coupling agents[53] (**Scheme 1-1)**. PEG-grafted CNCs showed a grafting degree of 0.2-0.3 g PEG/g-cell and the same dimensions as those of the un-grafted CNCs, 5-10 nm widths, and 100-200 nm lengths. The freeze-dried PEG-grafted CNFs were rendered suspendable in both water and $CHCl_3$.

TEMPO-oxidized CNFs derived from *Pinus pinaster*[54] (0.42-1.84 mmol/g), or from Douglas fir pulp[55] (0.26 mmol/g) were amidated with octadodecylamine[55], benzylamine[54] (0.02

mmol/g), hexylamine[54] (0.03 mmol/g), dodecylamine[54] (0.01 mmol/g), PEG 2070[54] (0.04 mmol/g) and PEG 2005[54] (0.02 mmol/g) (**Scheme 1-1**), or octadecyl-amine[55] (0.27 mmol/g) using carbodiimine and NHS as an activating system and stirring for 24 h. All CNFs amidated with benzylamine, hexylamine, dodecylamine, PEG 2070, and PEG 2005 formed stable dispersions in toluene[54], and CNFs amidated with octadecyl-amine[55] were lyophilized to render them dispersible in isopropyl alcohol, THF, and toluene, exhibiting birefringence under crossed polars confirming anisotropic fibrils. The advantage of amide linkage is a greater stability than that of an ester linkage against severe conditions, such as acidic, basic, or high heat environments.

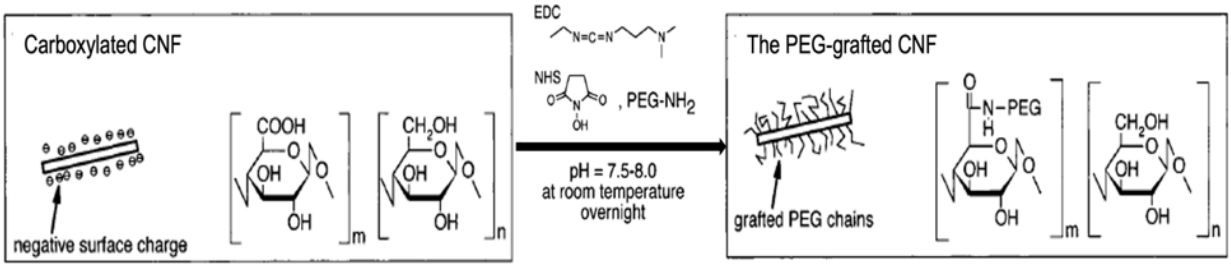

Scheme 1-1. Schematic illustration of amidation reaction between CNFs and PEG-NH_2.[53]

1.4.2.e Click chemistry

Click chemistry, first introduced to nanocellulose by Argyropoulos' group[63], was also used as a means to graft polymers onto nanocelluloses, starting by amidation of TEMPO-oxidized CNFs with propargyl amine[64]. Through amidation of carboxyl groups of CNFs with amino groups of propargylamine using EDC/NHS as the activating system, CNFs bearing alkynyl groups were prepared as an alkynyl-CNF precursor. In parallel, polycaprolactone diol (PCL) was converted into azido-PCL as the counterpart of the CNF precursor in two steps: first, tosylation of PCL to produce PCL-OTs, and second, nucleophilic displacement to convert PCL-OTs into azido-PCL by using sodium azide. Finally, azido-PCL was grafted onto alkynyl-CNF precursor in THF in the presence of $CuSO_4 \cdot 5H_2O$ and ascorbic acid as catalysts at room temperature in the dark for 2 days.

(**Scheme 1-2**) In summary, the click chemistry reaction brought CNCs with alkyne functionality, and polymers with the azide functionality, together by the Cu(I)-catalyzed Huisgen 1,3-dipolar cycloaddition, demonstrating an elegant process of CNC grafting. However, the process requires multiple steps which are time-consuming.

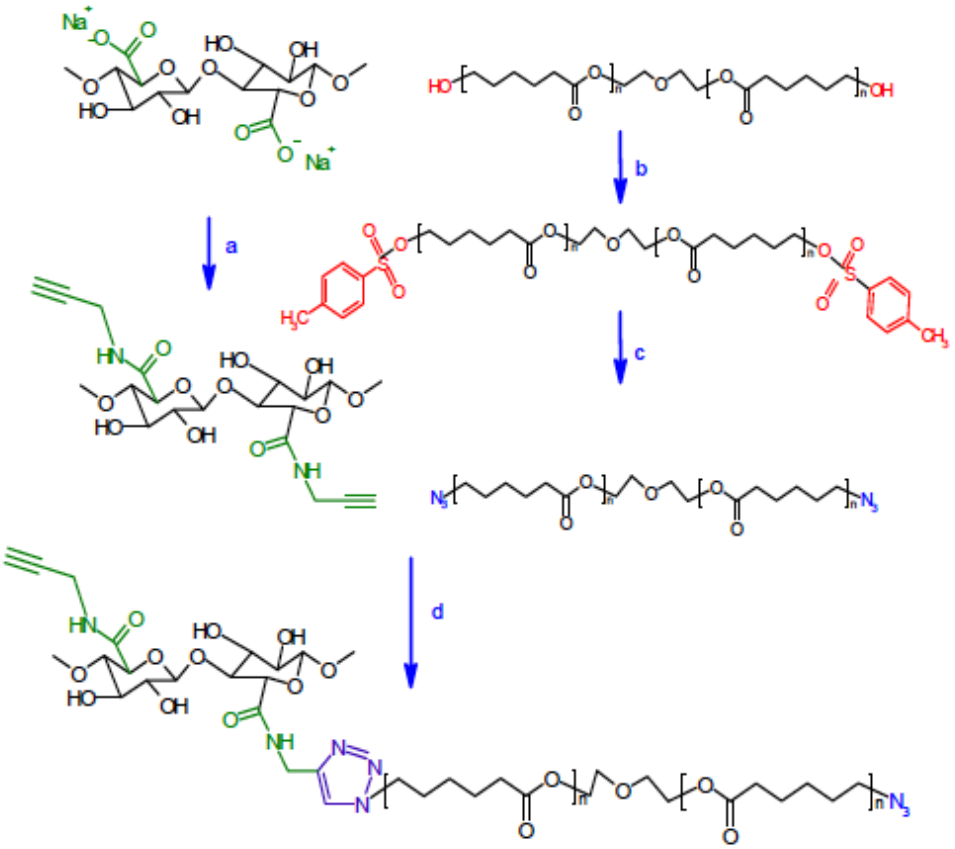

Scheme 1-2. Strategy of oxidized nanocellulose modification: (a) propargylamine, MES buffer pH 4, EDC/NHS, R.T., 24 h; (b) TsCl, THF, triethylamine, triethylamine hydrochloride, R.T., 24h; (c) DMF, NaN_3, R.T., 24 h; (d) THF, sodium ascorbate, $CuSO_4$, $5H_2O$, R.T., 48 h.[64]

All the above methods reviewed were effective ways of converting hydrophilic CNCs and CNFs that were previously isolated, into more hydrophobic and organic solvent-compatible nanocelluloses. However, the multiple reaction steps are time-consuming processes for those nanocelluloses that are already hydrolyzed or oxidized. Therefore, the next section reviews more efficient processes of functionalization of cellulose followed by defibrillation.

1.5 Esterification of Cellulose Followed by Defibrillation

In pursuit of efficiency, hydrophobization of cellulose is typically combined with mechanical disintegration such as grinding, cryo-crushing, ultrasonication, high-pressure homogenization, or ball-milling.

For example, acetylation of cotton linter cellulose was conducted[65,66] in an acid mixture (4 wt % cellulose) composed of hydrochloric acid and acetic acid or butyric acid for up to 25 h, followed by mechanical agitation in a Waring laboratory blender for 20 or 40 min, which generated acetylated CNCs in 25-50 nm diameters, 170-280 nm lengths, and the degree of substitution (DS) of 0.02-0.12 mmol/g depending on the reaction time. The product from 20 h reaction formed a stable suspension in ethyl acetate for at least 1 h.

Acetylation of kenaf cellulose with acetic anhydride in 5 wt % pyridine was followed by intensive mechanical treatment: high speed blending in aqueous media, cryo-crushing, and high-pressure homogenizing (500 bar, 40 times), to produce 10-20 nm wide CNFs with DS = 1.16 (per 3 OH groups) which formed milky acetone and ethanol dispersions that were stable for two months[49].

Cellulose from wood pulp filter paper was first pre-treated by a fiber standard dissociation device for 20 min, then refined by a vertical refiner for 20 min, freeze-dried, and soaked in acetic acid for 15 h, then acetylated with acetic anhydride.[48] Finally, acetylated nanocellulose was isolated by ultrasonication (40 kHz) at 68–75 ºC for 6 h into 10-100 nm wide acetylated CNCs, with DS = 0.47 (per 3 OH groups) and 85.4 % yield, forming a milky gel in water at 5 wt %.

Simultaneous acetylation and defibrillation were carried out by ball-milling of cellulose (Whatman CF11) with hexanoyl chloride (2.5 mL/g cell) in dimethylformamide (DMF) for 16 h followed by centrifuge washing and sonication in DMF to collect a non-sedimenting suspension

containing 15-20 nm wide surface-esterified CNFs with DS = 0.54 mmol/g[67] (**Figure 1-10a**). The crystallinity was practically unchanged from the original cellulose, indicating that ball-milling in DMF was fundamentally different from ball-milling under dry condition, which destroys crystallinity. Notably, the DMF could be substituted for THF, $CHCl_3$, aniline, or tert-butyl alcohol, but not acetone, ethanol, toluene, or water (**Figure 1-10b**).

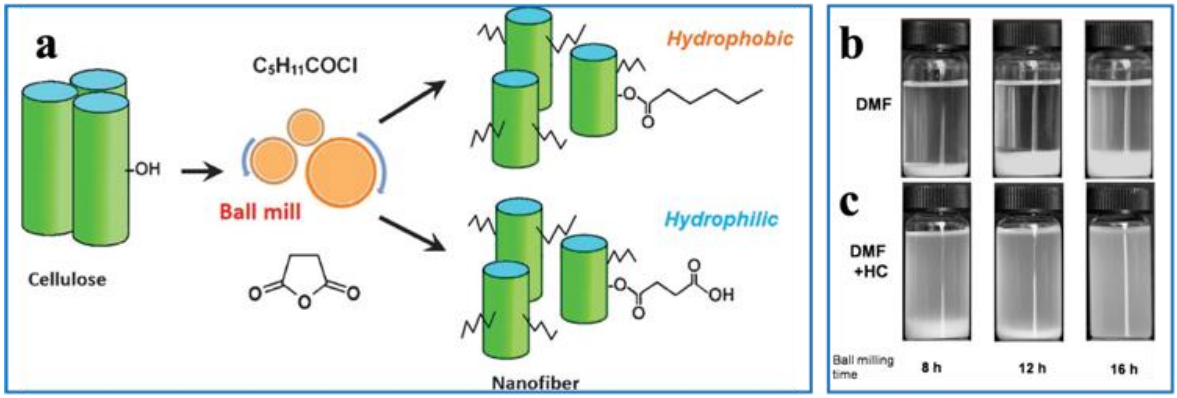

Figure 1-10. Esterification and ball-milling: (a) surface esterification of cellulose nanofibers by ball-milling; change in dispersion by esterification and ball-milling (after 24 h standing) (b) in DMF; (c) dispersion by hexanoyl chloride at 16 h. The apparent increase in sediment volume in the control sample is due to bulking.[67]

The above examples demonstrated functionalization of cellulose and disintegration by mechanical forces into nanocellulose, either in two steps[48,49,65] or simultaneously[67]. Thus, these approaches are more efficient than producing the CNCs/CNFs, then modifying their surface. However, all these approaches involve multiple steps, additional chemicals, and the limitation of linkage choices to esters.

1.6 Polymer Reinforcement by Hydrophobic Nanocelluloses

Nanocelluloses have been effectively used to produce reinforced polymer nanocomposites with a "greener footprint"[68]. The high strength and length/width aspect ratio (ca. 10 - 1000) of nanocelluloses are the essential characteristics for modulating stress-transfer and load-bearing in

hydrophobic polymer matrixes, such as polylactic acid (PLA)[69–71], polyurethane (PU)[72], and PMMA[73]. In order to improve interfacial adhesion between nanocelluloses and hydrophobic polymers to obtain the maximum reinforcing effect, hydrophobization of nanocellulose to carry a variety of functional groups is critical, as previously discussed. This section (1.6) reviews polymers reinforced with surface-modified nanocelluloses.

1.6.1 PLA

Recent studies have been focused on the transformation of biodegradable materials toward various applications such as the packaging, automotive, textile, medicine, tissue engineering, biomedical, and agricultural industries[74–82]. Biodegradable polymers are PLA, polybutylene adipate terephthalate (PBAT), polybutylene succinate (PBS), polyhydroxyalkanoates (PHA), and starch, etc. Among those, PLA is a linear aliphatic thermoplastic bio-polyester, most commonly obtained by fermentation of corn and potato starch. PLA has highly promising properties such as transparency, stiffness, low toxicity, biocompatibility, biodegradability, and competitive cost[74,83], while its limitations are brittleness and low crystallization rate[84]. To address these limitations, environmentally-friendly and biocompatible reinforcing and nucleating agents such as nanocelluloses[71,85–87], wood flour, and starch particles[88] have been examined as well as inorganic materials[89–93]. Particularly, extensive studies of the reinforcing effect of nanocellulose in PLA have demonstrated the superior effect obtained when a nanocellulose surface is modified with hydrophobic functional groups for improved interfacial association with the PLA matrix[86,87].

CNCs (15 nm width, 200-300 μm length) obtained from hydrolysis of cotton cellulose were silylated with n-dodecyldimethylchlorosiliane to generate silylated CNCs (SCNCs) dispersible in $CHCl_3$ and THF[85]. A film cast from 1 wt % SCNCs in a PLA-$CHCl_3$ mixture showed improved

tensile modulus, strength, and degree of crystallinity by 27 %, 21 % and 110 %, respectively, compared to that with 1 wt % unmodified CNCs.

CNCs derived from ramie fibers were grafted by ring-opening polymerization (ROP) of L-lactide with a catalytic amount of tin (II) ethylhexanoate ($Sn(Oct)_2$) in toluene to yield PLA-grafted CNC (CNC-g-PLA) nanohybrids[71]. The resulting CNC-g-PLA nanohybrids formed a stable suspension in $CHCl_3$ (**Figure 1-11a, b**), which was then incorporated in PLA by melt blending (155~170 ºC) to form PLA/CNC-g-PLA films. PLA films with un-grafted CNCs turned dark after melt blending, suggesting thermal degradation of the CNC, while PLA films with grafted CNCs (PLA/CNC-g-PLA) did not. There was no distinct melting temperature in the pristine PLA (Mn:130,000g/mol) due to its quasi-amorphous nature, whereas PLA/CNC-g-PLA exhibited two melting peaks at 150 and 159 ºC, regardless of the grafted CNC content, (**Figure 1-11d**) corresponding to polymorphism from more structured crystals. This observation indicated that the grafted CNC-g-PLA impacts the crystallization of the PLA matrix as a nucleating agent. Above the Tg (70 ºC), the storage modulus (E') of PLA/CNC-g-PLA increased with the CNC-g-PLA content (2%-8%), attributed to the enhanced growth of PLA crystal, which restricts the polymer chains' mobility.

These studies demonstrated the important role of chemical grafts on CNCs in enhancing their compatibility with the polymeric matrix, and improving the final properties of the PLA nanocomposites.

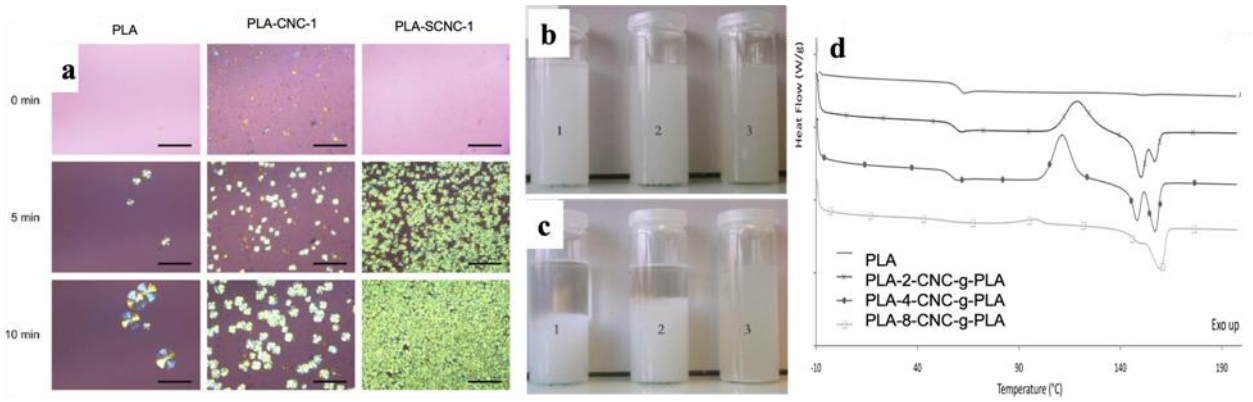

Figure 1-11. (a) Polarized optical microscope images of PLA, PLA–CNC1, and PLA–SCNC1 acquired at 0, 5 and 10 min at 125 ºC after quenching from melt[84] at 210 ºC, scale bar, 200 μm. Characteristics of PLA grafted and ungrafted CNC: (b-c) suspensions in $CHCl_3$ of (1) unmodified CNCs, (2) a physical mixture of PLA/CNC, and (3) a CNC-g-PLA nanohybrid; pictures recorded (b) immediately after the stirring was stopped; and (c) 72 h later. (d) DSC traces during heating cycle of unfilled PLA and PLA-g-CNC based nanocomposites.[72]

1.6.2 Polymethylmethacrylate (PMMA)

PMMA is an optically clear thermoplastic, widely used as a substitute for silica glass, due to its high impact strength, light weight, shatter-resistance, and other outstanding properties including weather and scratch resistance[94]. It is an amorphous and atactic polymer due to the presence of the methyl group in the polymer backbone preventing it from packing closely in a crystalline fashion.[95] Also, methyl ester side chains of PMMA that hinder the rotation of the backbone dihedrals prevent them from moving apart from each other when an external stress is added, leading to brittleness at room temperature, especially under an impact force[96]. The applications of PMMA include optical fibers, optical sensors, LEDs[95,97], biomedical equipments[94], and photocatalysis[98]. Additives such as nanocelluloses are needed to improve brittleness and impact strength.

CNFs (~6.6 nm diameter, 0.7-1.5 μm length) extracted from Nordic paper pulp via enzymatic hydrolysis were surface modified by allyl glycidyl ether (AGE) with the addition of triethylamine in acetone stirring at room temperature for 24 h, then polymerized with MMA

monomer *in situ* with 2:1 mole ratio of 2,2′-azobis(2-methylpropionitrile) (AIBN) / MMA to produce covalently grafted nanocomposite, mCNF-g-PMMA (**Figure 1-12a**)[99]. mCNF-g-PMMA (38 % CNF, 10 % AGE content) exhibited much higher optical transparency, thermal-stability and hygro-mechanical properties than (a) the physical blend of AGE modified CNFs (38% content), (b) unmodified CNFs (30 % content) with PMMA, or (c) pure PMMA in a water-soaked state (**Figure 1-12e**) did. Morphological differences among three nanocomposites analyzed by SEM showed that the layered structure is more ordered and defined for mCNF-g-PMMA due to covalent linking of mCNFs and the PMMA polymer network (**Figure 1-12b-j**). These results demonstrated the conjugated network of hydrophobized CNFs and the polymer matrix provides superior mechanical strength even under moist conditions. However, this procedure involves many steps and the amount of AIBN (2:1 AIBN/MMA monomer) used for polymerization of mCNFs and MMA may be more than necessary for free-radical polymerization.

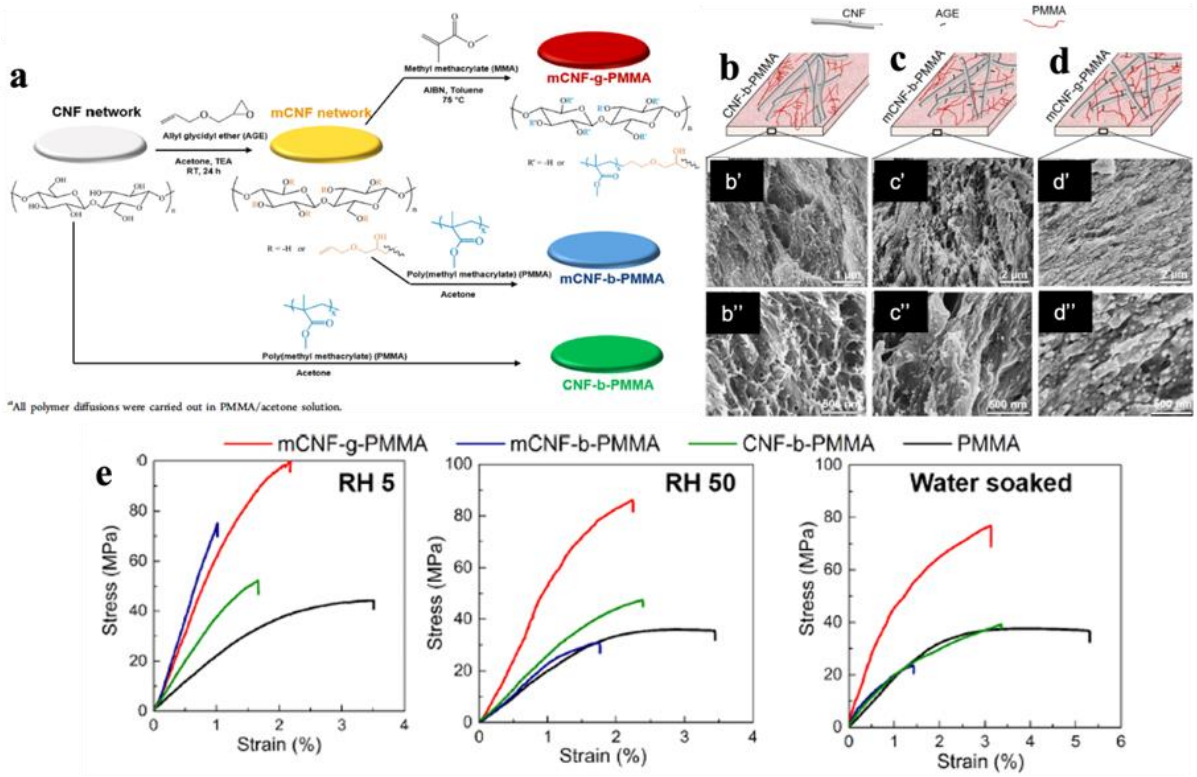

Figure 1-12. (a) Schematic illustration of nanocomposite preparation: modification of CNF network with allyl glycidyl ether (mCNFs), covalent grafting of PMMA on mCNFs via free radical polymerization (mCNF-g-PMMA), physical blend of modified CNF/PMMA (mCNF-b-PMMA), and "blend" of CNF/PMMA prepared by diffusion of high molar mass PMMA into the porous CNF network gel (CNF-b-PMMA). Schematic representations of the relative CNF/PMMA distribution and SEM images of cryo-fractured surface of (b, b', b'') CNFs blended with PMMA (CNF-b-PMMA); (c, c', c'') modified CNFs blended with PMMA (mCNF-b-PMMA); (d, d', d'') modified CNFs grafted with PMMA (mCNF-g-PMMA); (e) stress-strain curves.[99]

1.6.3 Natural rubber elastomers

Natural rubber (NR) and synthetic rubbers are the two general types of elastomers. Natural rubber is cis-1,4-polyisoprene (2-methyl 1,3-butadiene) while synthetic rubbers include poly(styrene-butadiene) rubber (SBR), polybutadiene, poly(acrylonitrile-butadiene) rubber (NBR), isoprene-isobutylene copolymer (butyl rubber), polychloroprene rubber, silicone rubber, and polyurethane, etc.[100,101] Among these, natural rubber is characterized by its superior physical properties, such as elasticity, flexibility, and abrasion resistance that cannot be fully mimicked by synthetic rubber[102], except for NBR which has notable swelling resistance towards oils

(hydrocarbon, gasoline, etc.) with maximum volume swell of 30 %[103]. Both natural and synthetic rubbers are used in diverse applications for surgical gloves, automobile tires, footwear, latex, aerospace, healthcare equipment and devices, footwear, toys, sealants, adhesives, and belts for mechanical parts.[101,104] However, there are some drawbacks, primarily for natural rubber, such as low modulus and strength[50,104]. Therefore, crosslinking and adding reinforcing fillers from various sources, such as carbon black[105], silica[106,107], or nanocelluloses[50], to improve mechanical characteristics is necessary.

Natural rubber covalently cross-linked with surface modified CNCs has been reported to show significantly improved thermomechanical properties and reduced stress-softening characteristics[50]. Esterification of CNCs (obtained from sulfuric acid hydrolysis of cotton cellulose) with mercaptoundecanoic acid produced surface-modified m-CNCs (0.85 mmol/g-cell) with thiol functionality and good dispersibility in toluene. Subsequently, the terminal thiol groups on CNCs and alkene groups of isoprene were cross-linked via photo-initiated free radical thiol-ene coupling to form a NR/m-CNC film (**Figure 1-12a**). The cross-linking density of the NR/m-CNC film increased significantly (0.053-0.078 mmol/g) as CNC content increased (2-10 %), whereas the cross-linking density of NR/un-modified CNC film did not. This provided evidence that the m-CNCs are well-dispersed in NR. The NR/m-CNC nanocomposite with 10 wt % of m-CNCs showed much higher tensile strength (10.2 ± 1.3 MPa), % strain to failure (1210 ± 110 %), and toughness (4.60 ± 0.57 MJ m^{-3}) than NR reinforced with unmodified CNCs. The NR/m-CNCs nanocomposites also showed much reduced stress-softening effects (Mullins effect), meaning that in NR/m-CNC films the covalent bonds formed at the interface between m-CNCs and the NR matrix prevented loss of stress transfer at the interface. The NR/m-CNC film retained stiffness even after several repeated loading cycles, while the NR/un-modified CNC film did not.

CNCs with 10-20 nm width and 500 nm-2μm length were derived from tunicate and grafted with maleic anhydride by ring-opening esterification to introduce carboxylic acids as pendant groups (m-CNCs). A nanocomposite of m-CNC/epoxidized natural rubber (ENR) was compression molded at 180 ºC and 10 MPa for 1 h, which induced a chemical reaction between carboxyl groups on m-CNCs and epoxy groups on ENR to produce covalent β-hydroxyl ester linkages. Fourier transform infrared spectroscopy (FTIR) revealed that the interfacial interaction between m-CNCs and ENR involved both covalent cross-linking and an H-bonding network between hydroxyl groups on m-CNCs and epoxy oxygens on ENR (Figure 1-12b). The composite with 5 % m-CNCs exhibited almost 3-fold improvement in strength, while the composite with 5 % un-modified CNCs improved only 2-fold, both with respect to that of pure ENR. This indicated that H-bonding and covalent linkage between m-CNCs and ENR enhanced the reinforcing effect of m-CNCs on the composite. Doubling m-CNC content to 10 % did not double the strength compared to that of 5% m-CNC composite[108].

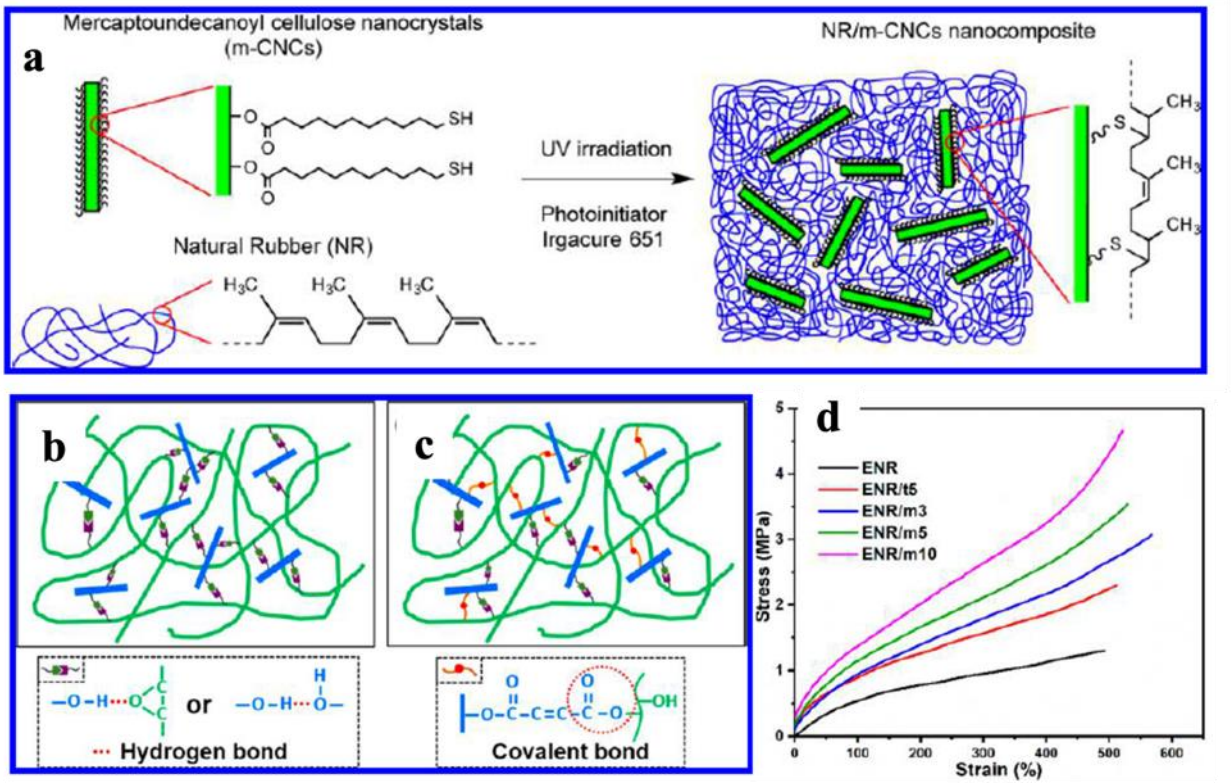

Figure 1-13. Illustration of the cross-linking network in nanocomposites: (a) mercaptoundecanoyl-CNCs and natural rubber (NR)[50] (b) H-bond network in epoxidized (E) NR/un-modified CNCs; (c) dual cross-linking networks: H-bonds and covalent bonds in ENR/modified CNCs; (d) Stress-strain curve of the composite with 3, 5, 10 % m-CNCs.

1.6.4 Polyethylene terephthalate (PET)

Polyethylene terephthalate (PET) is the most used thermosetting polymer belonging to the poly(alkylene terephthalate (PAT)) family, and is also one of the major polymers recycled[109]. Due to its light weight and transparent characteristics it is used in numerous products such as water and beverage bottles and other packaging materials [110]. It is also recycled for use as fibers in textiles[110,111]. As a textile material, PET has excellent properties of wash-and-wear, chemical resistance, heat stability, high tenacity, and resistance to wrinkling[112]. However, the poor water and moisture absorption of PET makes it less desirable in many applications, i.e., sportswear, undergarments, furniture, and bedding, due to the lack of polar groups (-OH, -COOH, $-NH_2$) on its polymer backbone[113]. To cope with this drawback, denier reduction by aminolysis and

hydrolysis[114,115], co-polymerization and graft co-polymerization of hydrophilic monomers with PET in the presence of an initiator[116], and plasma surface modification of textile fabrics[117] are the available approaches to improving hydrophilicity of polyester. However, each method leads to undesirable consequences, such as the loss of mechanical strength of fabric due to the polymer chain scission[114,115], high cost and lengthy processing time[116], or requiring complex and expensive operating devices[117].

Nanocellulose has also been employed as a sustainable surface modifier. Zaman et al. applied cationically modified CNCs formulated with acrylic binders to modify the surface properties of PET fabric, such as coating durability, moisture retention, and wettability[113]. After the treatment, the surface properties of the fabric were changed from hydrophobic to hydrophilic, and the cationic CNC-containing textile surface finish showed superior adhesion to the cationic dyeable (i.e., anionic) PET surface over the same surface treated with unmodified CNCs. Zhang et al. applied CNFs generated from electrospinning of TENCEL fibers with N-methylmorpholine-N-oxide monohydrate (NMMO) toward a CNF/PET nonwoven composite lithium-ion battery separator, through a wet-laid nonwoven (papermaking) process.[118] The CNF/PET composite lithium-ion battery separator exhibited optimal properties in wettability (**Figure 1-14a**), mechanical strength, thermal resistance, and electrochemical performance compared to conventional polypropylene (PP) separators. Furthermore, the porosity of the CNF/PET composite lithium-ion battery separator (70%) was higher than that of a PP lithium-ion battery separator (40%), which is favorable for electrolyte uptake (**Figure 1-14b**). Following the discovery by Hasegawa et al. in 1995 that cellulose dissolved in TFA becomes acetylated at C6-hydroxyls, and is then hydrolyzed partly back to the original hydroxyls during evaporation of the solvent[119], Rodrigues et al. developed reconstruction of the dissolved sisal pulp (83 % α-cellulose) in TFA

into sub-micron and nanoscale fibrils via electrospinning[120] (**Figure 1-14c**). By using this technology, Santos et al. evaluated the effect of cellulose on composite mats with recycled PET prepared by dissolution in trifluoroacetic acid (for 48 h or 72 h) and electrospinning[121]. The presence of cellulose nanofibrils in the electrospun PET mats changed the surface from hydrophobic to highly hydrophilic, and the tensile strength of the mats increased by 4.7-fold for 48 h and 5.3-fold for 72 h of dissolution time. The resulting mats can be applied as filters and membranes.

Clearly, the addition of nanocellulose effectively modified the surface polarity and reinforced the PET composite, however, to gain compatibility with PET, the surface modification of nanocellulose required the use of corrosive TFA and NMMO which are not commonly used for polymer processing. In addition, while electrospinning is a unique and versatile technology to transform nano-scale fibers into different morphologies by an unparalleled operational simplicity, there is still a strong need to implement scale-up production in the most efficient way. The following issues in industrial applications need to be addressed: (i) large volume processing, (ii) accuracy and reproducibility in all fabrication stages, and (iii) safety and environmental attributes of electrospinning.[122]

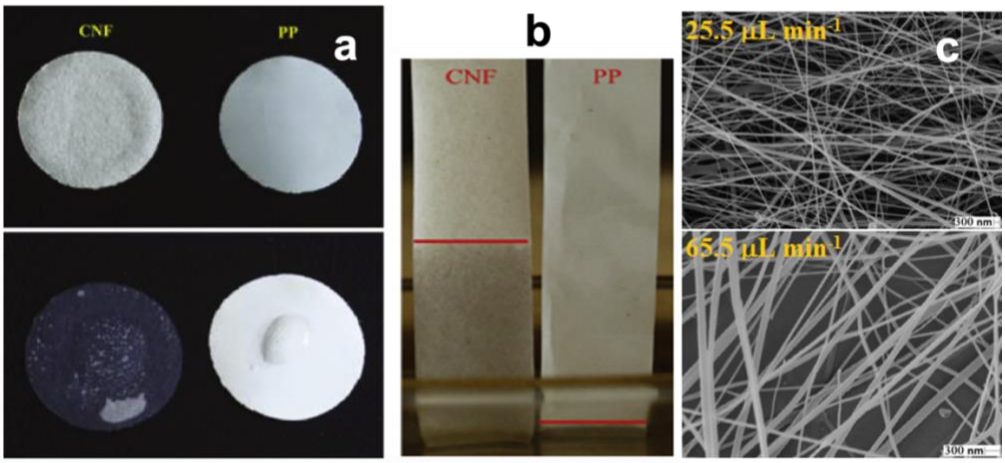

Figure 1-14. (a) Photographs of electrolyte wettability of PP lithium-ion battery separator, CNF separator. (b) Photograph of electrolyte immersion height of PP lithium-ion battery separator, CNF separator.[118] (c) SEM images of electrospun PP prepared at various solution flow rates (25.5 and 65.5 mL min^{-1}).[120]

1.6.5 Vegetable oils

Vegetable oils (VOs) are renewable, biodegradable building blocks that can form a variety of VO-based polymers through free radical, cationic, olefin metathesis, and condensation polymerization[123]. However, VO-based material structures such as films lack strength and requires reinforcement by other polymers[124-126], cross-linkers[127], or nanocelluloses[128,129]. These VO-derived polymers have been reported to exhibit a broad range of thermophysical and mechanical properties, extending from soft and flexible rubbers to hard and rigid plastics, depending on the ratio of VO/monomers, i.e., furfural methacrylate[124], divinyl benzene[124,126] nanocelluloses[128-130], or cross-linkers[127,131].

Thiol-Michael addition of pentaerythritol tetrakis(3-mercaptopropionate) (EP3MP) to a derivative of high oleic sunflower oil (HOSO) containing enone groups, was used to prepare HOSO derived renewable thermosets. This process took place in the presence of CNCs modified with a surfactant (s-CNCs) to form a nanocomposite thermoset film[128]. The film with 5% s-CNCs showed a 2-fold improvement in modulus (78 MPa) and strength (1.6 MPa) compared to the

modulus and strength of HOSO film cross-linked with EP3MP but without s-CNCs (32 MPa, 0.7 MPa, respectively).

Polyurethane (PU) film derived from castor oil derivatized with hydroxyl groups and polymerized with methylene diphenyl diisocyanate (MDI) was reinforced with 10-15 nm wide CNCs (hydrolyzed from Avicel MCC)[129]. The nanocomposite film with 0.5 % CNCs exhibited a 33% increase in modulus (643 MPa) with respect to pristine PU. These examples demonstrate the promise of VOs as future alternatives to petroleum-based thermosets. However, fabrication of VO-based materials is still nascent and requires more research to create viable products.

Among VOs, linseed oil (LO) contains the highest amount of unsaturation (**Table 1-1**). There is monounsaturation at C9 in oleic acid, double unsaturation at C9 and C12 in linoleic acid, and triple unsaturation at C9, C12 and C15 in α-linoleic acid. LO is known to undergo complex oxidative degradation (Scheme 1-2) promoted by three bis-allylic hydrogen atoms leading to the cross-linked structure of LO films as they dry under air without additional chemicals[133,134]. Thus, such films are commonly used as a natural surface coating of wood products[115]. Chapter 3 discusses the application of LO nanocomposites with modified CNFs as a surface coating on cellulose paper.

Table 1-1. Vegetable oils.

Vegetable Oil	**Viscosity (mPa·m) @T (°C)**	**Total unsaturated** (%)	**Saturated (%)**		**[137]Mono-unsaturated (%)**			**[137]Polyunsaturated (%)**	
			Palmitic (16:0)	Stearic (18:0)	Oleic (18.:1)	Gondoic (20:1)	Erucic (22:1)	Linoleic (12:2n6)	α-Linoleic (18:3n3)
Flaxseed (linseed)	*33.1 @ 25 6.0 @ 100	90	3	7	21	_	_	16	53
Sunflower	[135]48.8 ± 0.2 @ 26 [135]23.4 ± 0.1 @ 50	88	7	5	19	< 0.5	_	68	1
Corn	[136]59.2 ± 0.8 @ 22 [136]9.0 ± 0.8 @ 100	87	11	2	28	_	_	58	1
Soybean	[136]57.1 ± 1.1 @ 22 [136]8.3 ± 0.6 @ 100	85	11	4	24	< 0.4	_	54	7

*https://www.engineeringtoolbox.com

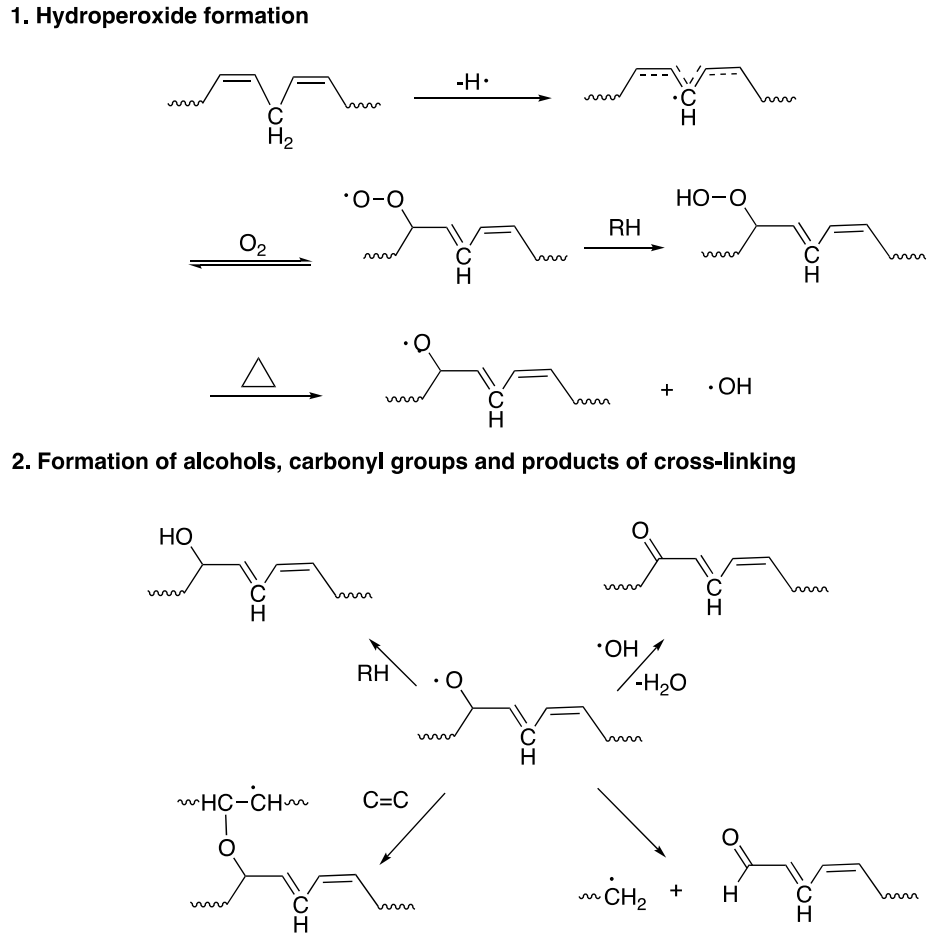

Scheme 1-3. Oxidative degradation process of fatty acid chains in linseed oil.[132]

1.7 Summary and Research Needs

This review focused on the fundamentals of two types of negatively charged nanocelluloses, CNCs and CNFs, and their surface functionalization reactions to gain compatibility with organic solvents and hydrophobic polymers. There are multiple challenges in the surface modification of CNCs and CNFs, i.e., the control of nanocellulose properties (such as size, aspect ratio and morphology) and the preservation of crystal integrity.

While much has been reported in the area of surface modification, most of the methods are still heavily dependent on toxic chemicals as well as time- and energy-intensive processes that are

difficult to scale-up towards industrial applications, due largely to the compartmentalized steps of nanocellulose extraction, functionalization, and material processing.

Therefore, this Ph.D. research was designed for developing more streamlined strategies that lead to producing 2D functional materials from 1D nanocellulose. CNFs were the focus of the projects, due to their larger surface areas which are more suitable for reactions than CNCs. The objectives are: 1) to simplify the process by hydrophobization of cellulose followed by disintegration of the modified cellulose into CNFs, which bypasses a TEMPO-oxidation step; 2) to obtain improved surface synergism with common polymer solvents represented in clear CNF dispersions (0.1 w/v %) by optimizing degree of substitution; 3) to lean toward the concept of green chemistry by reducing chemical use and energy consumption.

For hydrophobization, the unique recyclable reagent butadiene sulfone was used as a pre-cursor for telomerization of 1,3-butadiene with cellulose, creating a distinctive ether linkage that is less acid-labile and less polar than the frequently-produced ester linkage. Next, the efficient disintegration method of the modified cellulose was investigated by comparing mechanical blending and ultra-sonication. Finally, these processes were developed into a facile sequence of "synthesis / disintegration / nanocomposite formation" by incorporating synthetic hydrophobic polymers or a bio-degradable vegetable oil. All studies presented in this dissertation utilized cellulose from a biomass source such as rice straws and almond shells.

1.8 References

(1) Lavoine, N.; Desloges, I.; Dufresne, A.; Bras, J. Microfibrillated Cellulose – Its Barrier Properties and Applications in Cellulosic Materials: A Review. *Carbohydrate Polymers* **2012**, *90* (2), 735–764. https://doi.org/10.1016/j.carbpol.2012.05.026.

(2) Houtman, C.J; and Atalla, R.H. Cellulose-lignin interactions (a computational study). *Plant physiology* **1995**, *107*(3), pp.977-984. https://doi.org/10.1104/pp.107.3.977.

(3) Zhang, N.; Li, S.; Xiong, L.; Hong, Y.; Chen, Y. Cellulose-hemicellulose interaction in wood secondary cell-wall. *Modelling and Simulation in Materials Science and Engineering* **2015**, *23*(8), p.085010. https://doi.org/10.1088/0965-0393/23/8/085010.

(4) Khodayari, A.; Thielemans, W.; Hirn, U.; Van Vuure, A.W.; Seveno, D. Cellulose-hemicellulose interactions-a nanoscale view. *Carbohydrate Polymers* **2021**, *270*, p.118364. https://doi.org/10.1016/j.carbpol.2021.118364.

(5) Lu, P.; Hsieh, Y.-L. Preparation and Characterization of Cellulose Nanocrystals from Rice Straw. *Carbohydrate Polymers* **2012**, *87* (1), 564–573. https://doi.org/10.1016/j.carbpol.2011.08.022.

(6) Tao, H., Lavoine, N.; Jiang, F.; Tang, J.; Lin, N. Reducing end modification on cellulose nanocrystals: strategy, characterization, applications and challenges. *Nanoscale horizons* 2020, *5*(4), pp.607-627. https://doi.org/10.1039/D0NH00016G.

(7) Taylor, N. G. Cellulose Biosynthesis and Deposition in Higher Plants. *New Phytologist* **2008**, *178* (2), 239–252. https://doi.org/10.1111/j.1469-8137.2008.02385.x.

(8) Qian, X.; Ding, S.-Y.; Nimlos, M. R.; Johnson, D. K.; Himmel, M. E. Atomic and Electronic Structures of Molecular Crystalline Cellulose Iβ: A First-Principles Investigation. *Macromolecules* **2005**, *38* (25), 10580–10589. https://doi.org/10.1021/ma051683b.

(9) Brett, C. T. Cellulose Microfibrils in Plants: Biosynthesis, Deposition, and Integration into the Cell Wall. In *International Review of Cytology*. Elsevier 2000, Vol. 199, 161–199. https://doi.org/10.1016/S0074-7696(00)99004-1.

(10) Trache, D.; Tarchoun, A. F.; Derradji, M.; Hamidon, T. S.; Masruchin, N.; Brosse, N.; Hussin, M. H. Nanocellulose: From Fundamentals to Advanced Applications. *Frontiers in Chemistry* **2020**, *8*, 392-424. https://doi.org/10.3389/fchem.2020.00392.

(11) Somerville, C. Cellulose synthesis in higher plants. *Annu. Rev. Cell Dev. Biol.* **2006**, *22*, pp.53-78. https://doi.org/10.1146/annurev.cellbio.22.022206.160206.

(12) Nishiyama, Y.; Langan, P.; Chanzy, H. Crystal Structure and Hydrogen-Bonding System in Cellulose Iβ from Synchrotron X-Ray and Neutron Fiber Diffraction. *J. Am. Chem. Soc.* **2002**, *124* (31), 9074–9082. https://doi.org/10.1021/ja0257319.

(13) Nishiyama, Y.; Sugiyama, J.; Chanzy, H.; Langan, P. Crystal Structure and Hydrogen Bonding System in Cellulose I $_{\alpha}$ from Synchrotron X-Ray and Neutron Fiber Diffraction. *J. Am. Chem. Soc.* **2003**, *125* (47), 14300–14306. https://doi.org/10.1021/ja037055w.

(14) Šturcová, A.; His, I.; Apperley, D. C.; Sugiyama, J.; Jarvis, M. C. Structural Details of Crystalline Cellulose from Higher Plants. *Biomacromolecules* **2004**, *5* (4), 1333–1339. https://doi.org/10.1021/bm034517p.

(15) Jiang, F.; Han, S.; Hsieh, Y.-L. Controlled Defibrillation of Rice Straw Cellulose and Self-Assembly of Cellulose Nanofibrils into Highly Crystalline Fibrous Materials. *RSC Adv.* **2013**, *3* (30), 12366-12375. https://doi.org/10.1039/c3ra41646a.

(16) Beck-Candanedo, S.; Roman, M.; Gray, D. G. Effect of Reaction Conditions on the Properties and Behavior of Wood Cellulose Nanocrystal Suspensions. *Biomacromolecules* **2005**, *6* (2), 1048–1054. https://doi.org/10.1021/bm049300p.

(17) Lu, P.; Hsieh, Y.-L. Preparation and Properties of Cellulose Nanocrystals: Rods, Spheres, and Network. *Carbohydrate Polymers* **2010**, *82* (2), 329–336. https://doi:10.1016/j.carbpol.2010.04.073.

(18) Jiang, F.; Hsieh, Y.-L. Chemically and Mechanically Isolated Nanocellulose and Their Self-Assembled Structures. *Carbohydrate Polymers* **2013**, *95* (1), 32–40. https://doi.org/10.1016/j.carbpol.2013.02.022.

(19) de Nooy, A. E. J.; Besemer, A. C.; van Bekkum, H. Highly Selective Nitroxyl Radical-Mediated Oxidation of Primary Alcohol Groups in Water-Soluble Glucans. *Carbohydrate Research* **1995**, *269* (1), 89–98. https://doi.org/10.1016/0008-6215(94)00343-E.

(20) Sacui, I. A.; Nieuwendaal, R. C.; Stranick, S. J.; Jorfi, M.; Weder, C.; Foster, E. J.; Olsson, R. T.; Gilman, J. W. Comparison of the Properties of Cellulose Nanocrystals and Cellulose Nanofibrils Isolated from Bacteria, Tunicate, and Wood Processed Using Acid, Enzymatic, Mechanical, and Oxidative Methods. *ACS Appl. Mater. Interfaces* **2014**, *6* (9), 6127–6138. https://doi.org/10.1021/am500359f.

(21) Saito, T.; Kimura, S.; Nishiyama, Y.; Isogai, A. Cellulose Nanofibers Prepared by TEMPO-Mediated Oxidation of Native Cellulose. *Biomacromolecules* **2007**, *8* (8), 2485–2491. https://doi.org/10.1021/bm0703970.

(22) Isogai, A.; Saito, T.; Fukuzumi, H. TEMPO-Oxidized Cellulose Nanofibers. *Nanoscale* **2011**, *3* (1), 71–85. https://doi.org/10.1039/C0NR00583E.

(23) Kontturi, E.; Meriluoto, A.; Penttilä, P. A.; Baccile, N.; Malho, J.-M.; Potthast, A.; Rosenau, T.; Ruokolainen, J.; Serimaa, R.; Laine, J.; Sixta, H. Degradation and Crystallization of Cellulose in Hydrogen Chloride Vapor for High-Yield Isolation of Cellulose Nanocrystals. *Angew. Chem. Int. Ed.* **2016**, *55* (46), 14455–14458. https://doi.org/10.1002/anie.201606626.

(24) Ma, Y.; Xia, Q.; Liu, Y.; Chen, W.; Liu, S.; Wang, Q.; Liu, Y.; Li, J.; Yu, H. Production of Nanocellulose Using Hydrated Deep Eutectic Solvent Combined with Ultrasonic Treatment. *ACS Omega* **2019**, *4* (5), 8539–8547. https://doi.org/10.1021/acsomega.9b00519.

(25) Jiang, J.; Carrillo-Enríquez, N. C.; Oguzlu, H.; Han, X.; Bi, R.; Song, M.; Saddler, J. N.; Sun, R.-C.; Jiang, F. High Production Yield and More Thermally Stable Lignin-Containing Cellulose Nanocrystals Isolated Using a Ternary Acidic Deep Eutectic Solvent. *ACS Sustainable Chem. Eng.* **2020**, *8* (18), 7182–7191. https://doi.org/10.1021/acssuschemeng.0c01724.

(26) van den Berg, O.; Capadona, J. R.; Weder, C. Preparation of Homogeneous Dispersions of Tunicate Cellulose Whiskers in Organic Solvents. *Biomacromolecules* **2007**, *8* (4), 1353–1357. https://doi.org/10.1021/bm061104q.

(27) Abbott, A. P.; Boothby, D.; Capper, G.; Davies, D. L.; Rasheed, R. K. Deep Eutectic Solvents Formed between Choline Chloride and Carboxylic Acids: Versatile Alternatives to Ionic Liquids. *J. Am. Chem. Soc.* **2004**, *126* (29), 9142–9147. https://doi.org/10.1021/ja048266j.

(28) Sirviö, J. A.; Visanko, M.; Liimatainen, H. Acidic Deep Eutectic Solvents As Hydrolytic Media for Cellulose Nanocrystal Production. *Biomacromolecules* **2016**, *17* (9), 3025–3032. https://doi.org/10.1021/acs.biomac.6b00910.

(29) Satlewal, A.; Agrawal, R.; Bhagia, S.; Sangoro, J.; Ragauskas, A. J. Natural Deep Eutectic Solvents for Lignocellulosic Biomass Pretreatment: Recent Developments, Challenges and Novel Opportunities. *Biotechnology Advances* **2018**, *36* (8), 2032–2050. https://doi.org/10.1016/j.biotechadv.2018.08.009.

(30) Vigier, K. D. O.; Chatel, G.; Jérôme, F. Contribution of Deep Eutectic Solvents for Biomass Processing: Opportunities, Challenges, and Limitations. *ChemCatChem* **2015**, *7* (8), 1250–1260. https://doi.org/10.1002/cctc.201500134.

(31) Tang, X.; Zuo, M.; Li, Z.; Liu, H.; Xiong, C.; Zeng, X.; Sun, Y.; Hu, L.; Liu, S.; Lei, T.; Lin, L. Green Processing of Lignocellulosic Biomass and Its Derivatives in Deep Eutectic Solvents. *ChemSusChem* **2017**, *10* (13), 2696–2706. https://doi.org/10.1002/cssc.201700457.

(32) Li, P.; Sirviö, J. A.; Haapala, A.; Liimatainen, H. Cellulose Nanofibrils from Nonderivatizing Urea-Based Deep Eutectic Solvent Pretreatments. *ACS Appl. Mater. Interfaces* **2017**, *9* (3), 2846–2855. https://doi.org/10.1021/acsami.6b13625.

(33) Antti Sirviö, J.; Visanko, M.; Liimatainen, H. Deep Eutectic Solvent System Based on Choline Chloride-Urea as a Pre-Treatment for Nanofibrillation of Wood Cellulose. *Green Chemistry* **2015**, *17* (6), 3401–3406. https://doi.org/10.1039/C5GC00398A.

(34) Wu, X.; Moon, R. J.; Martini, A. Tensile Strength of Iβ Crystalline Cellulose Predicted by Molecular Dynamics Simulation. *Cellulose* **2014**, *21* (4), 2233–2245. https://doi.org/10.1007/s10570-014-0325-0.

(35) Iwamoto, S.; Kai, W.; Isogai, A.; Iwata, T. Elastic Modulus of Single Cellulose Microfibrils from Tunicate Measured by Atomic Force Microscopy. *Biomacromolecules* **2009**, *10* (9), 2571–2576. https://doi.org/10.1021/bm900520n.

(36) Fukuzumi, H.; Saito, T.; Iwata, T.; Kumamoto, Y.; Isogai, A. Transparent and High Gas Barrier Films of Cellulose Nanofibers Prepared by TEMPO-Mediated Oxidation. *Biomacromolecules* **2009**, *10* (1), 162–165. https://doi.org/10.1021/bm801065u.

(37) Wong, E. W.; Sheehan, P. E.; Lieber, C. M. Nanobeam Mechanics: Elasticity, Strength, and Toughness of Nanorods and Nanotubes. *Science* **1997**, *277* (5334), 1971–1975. https://doi.org/10.1126/science.277.5334.1971.

(38) Min-Feng, Y.; Lourie, O.; Dyer, M. J.; Moloni, K.; al, et. Strength and Breaking Mechanism of Multiwalled Carbon Nanotubes under Tensile Load. *Science; Washington* **2000**, *287* (5453), 637–640. https://doi.org/10.1126/science.287.5453.637.

(39) Diaz, J. A.; Ye, Z.; Wu, X.; Moore, A. L.; Moon, R. J.; Martini, A.; Boday, D. J.; Youngblood, J. P. Thermal Conductivity in Nanostructured Films: From Single Cellulose Nanocrystals to Bulk Films. *Biomacromolecules* **2014**, *15* (11), 4096–4101. https://doi.org/10.1021/bm501131a.

(40) Saito, T.; Kuramae, R.; Wohlert, J.; Berglund, L. A.; Isogai, A. An Ultrastrong Nanofibrillar Biomaterial: The Strength of Single Cellulose Nanofibrils Revealed via Sonication-Induced Fragmentation. *Biomacromolecules* **2013**, *14* (1), 248–253. https://doi.org/10.1021/bm301674e.

(41) Johnson, R.K., Zink-Sharp, A., Renneckar, S.H. and Glasser, W.G., 2009. A new bio-based nanocomposite: fibrillated TEMPO-oxidized celluloses in hydroxypropylcellulose matrix. *Cellulose*, *16*(2), pp.227-238.

(42) Li, W.; Wang, R.; Liu, S. Nanocrystalline Cellulose Prepared from Softwood Kraft Pulp via Ultrasonic-Assisted Acid Hydrolysis. *BioResources* **2011**, *6* (4), 4271- 4281.

(43) Chen, W.; Yu, H.; Liu, Y.; Chen, P.; Zhang, M.; Hai, Y. Individualization of Cellulose Nanofibers from Wood Using High-Intensity Ultrasonication Combined with Chemical Pretreatments. *Carbohydrate Polymers* **2011**, *83* (4), 1804–1811. https://doi.org/10.1016/j.carbpol.2010.10.040.

(44) Kim, J.-H.; Shim, B. S.; Kim, H. S.; Lee, Y.-J.; Min, S.-K.; Jang, D.; Abas, Z.; Kim, J. Review of Nanocellulose for Sustainable Future Materials. *Int. J. of Precis. Eng. and Manuf.-Green Tech.* **2015**, *2* (2), 197–213. https://doi.org/10.1007/s40684-015-0024-9.

(45) Jiang, F.; Hsieh, Y.-L. Super Water Absorbing and Shape Memory Nanocellulose Aerogels from TEMPO-Oxidized Cellulose Nanofibrils via Cyclic Freezing–Thawing. *J. Mater. Chem. A* **2014**, *2* (2), 350–359. https://doi.org/10.1039/C3TA13629A.

(46) Lavoine, N.; Bergström, L. Nanocellulose-Based Foams and Aerogels: Processing, Properties, and Applications. *Journal of Materials Chemistry A* **2017**, *5* (31), 16105–16117. https://doi.org/10.1039/c7ta02807e.

(47) Yuan, H.; Nishiyama, Y.; Wada, M.; Kuga, S. Surface Acylation of Cellulose Whiskers by Drying Aqueous Emulsion. *Biomacromolecules* **2006**, *7* (3), 696–700. https://doi.org/10.1021/bm050828j.

(48) Tang, L.; Huang, B.; Lu, Q.; Wang, S.; Ou, W.; Lin, W.; Chen, X. Ultrasonication-Assisted Manufacture of Cellulose Nanocrystals Esterified with Acetic Acid. *Bioresource Technology* **2013**, *127*, 100–105. https://doi.org/10.1016/j.biortech.2012.09.133.

(49) Jonoobi, M.; Harun, J.; Mathew, A. P.; Hussein, M. Z. B.; Oksman, K. Preparation of Cellulose Nanofibers with Hydrophobic Surface Characteristics. *Cellulose* **2010**, *17* (2), 299–307. https://doi.org/10.1007/s10570-009-9387-9.

(50) Parambath Kanoth, B.; Claudino, M.; Johansson, M.; Berglund, L. A.; Zhou, Q. Biocomposites from Natural Rubber: Synergistic Effects of Functionalized Cellulose Nanocrystals as Both Reinforcing and Cross-Linking Agents via Free-Radical Thiol–Ene Chemistry. *ACS Appl. Mater. Interfaces* **2015**, *7* (30), 16303–16310. https://doi.org/10.1021/acsami.5b03115.

(51) Goussé, C.; Chanzy, H.; Excoffier, G.; Soubeyrand, L.; Fleury, E. Stable Suspensions of Partially Silylated Cellulose Whiskers Dispersed in Organic Solvents. *Polymer* **2002**, *43* (9), 2645–2651. https://doi.org/10.1016/S0032-3861(02)00051-4.

(52) Goussé, C.; Chanzy, H.; Cerrada, M. L.; Fleury, E. Surface Silylation of Cellulose Microfibrils: Preparation and Rheological Properties. *Polymer* **2004**, *45* (5), 1569–1575. https://doi.org/10.1016/j.polymer.2003.12.028.

(53) Araki, J.; Wada, M.; Kuga, S. Steric Stabilization of a Cellulose Microcrystal Suspension by Poly(Ethylene Glycol) Grafting. *Langmuir* **2001**, *17* (1), 21–27. https://doi.org/10.1021/la001070m.

(54) Lasseuguette, E. Grafting onto Microfibrils of Native Cellulose. *Cellulose* **2008**, *15* (4), 571–580. https://doi.org/10.1007/s10570-008-9200-1.

(55) Johnson, R. K.; Zink-Sharp, A.; Glasser, W. G. Preparation and Characterization of Hydrophobic Derivatives of TEMPO-Oxidized Nanocelluloses. *Cellulose* **2011**, *18* (6), 1599–1609. https://doi.org/10.1007/s10570-011-9579-y.

(56) Shrestha, S.; Chowdhury, R. A.; Toomey, M. D.; Betancourt, D.; Montes, F.; Youngblood, J. P. Surface Hydrophobization of TEMPO-Oxidized Cellulose Nanofibrils (CNFs) Using a Facile, Aqueous Modification Process and Its Effect on Properties of Epoxy Nanocomposites. *Cellulose* **2019**, *26* (18), 9631–9643. https://doi.org/10.1007/s10570-019-02762-w.

(57) Dufresne, A. Nanocellulose: A New Ageless Bionanomaterial. *Materials Today* **2013**, *16* (6), 220–227. https://doi.org/10.1016/j.mattod.2013.06.004.

(58) Lin, N.; Huang, J.; Chang, P. R.; Feng, J.; Yu, J. Surface Acetylation of Cellulose Nanocrystal and Its Reinforcing Function in Poly(Lactic Acid). *Carbohydrate Polymers* **2011**, *83* (4), 1834–1842. https://doi.org/10.1016/j.carbpol.2010.10.047.

(59) Sassi, J.-F.; Chanzy, H. Ultrastructural Aspects of the Acetylation of Cellulose. *Cellulose* **1995**, *2* (2), 111–127. https://doi.org/10.1007/BF00816384.

(60) Habibi, Y. Key Advances in the Chemical Modification of Nanocelluloses. *Chem. Soc. Rev.* **2014**, *43* (5), 1519–1542. https://doi.org/10.1039/C3CS60204D.

(61) Morandi, G.; Heath, L.; Thielemans, W. Cellulose Nanocrystals Grafted with Polystyrene Chains through Surface-Initiated Atom Transfer Radical Polymerization (SI-ATRP). *Langmuir* **2009**, *25* (14), 8280–8286. https://doi.org/10.1021/la900452a.

(62) Yin, Y.; Tian, X.; Jiang, X.; Wang, H.; Gao, W. Modification of Cellulose Nanocrystal via SI-ATRP of Styrene and the Mechanism of Its Reinforcement of Polymethylmethacrylate. *Carbohydrate Polymers* **2016**, *142*, 206–212. https://doi.org/10.1016/j.carbpol.2016.01.014.

(63) Filpponen, I.; Argyropoulos, D. S. Regular Linking of Cellulose Nanocrystals via Click Chemistry: Synthesis and Formation of Cellulose Nanoplatelet Gels. *Biomacromolecules* **2010**, *11* (4), 1060–1066. https://doi.org/10.1021/bm1000247.

(64) Benkaddour, A.; Jradi, K.; Robert, S.; Daneault, C. Grafting of Polycaprolactone on Oxidized Nanocelluloses by Click Chemistry. *Nanomaterials* **2013**, *3* (1), 141–157. https://doi.org/10.3390/nano3010141.

(65) Braun, B.; Dorgan, J. R. Single-Step Method for the Isolation and Surface Functionalization of Cellulosic Nanowhiskers. *Biomacromolecules* **2009**, *10* (2), 334–341. https://doi.org/10.1021/bm8011117.

(66) J. Sobkowicz, M.; Braun, B.; R. Dorgan, J. Decorating in Green: Surface Esterification of Carbon and Cellulosic Nanoparticles. *Green Chemistry* **2009**, *11* (5), 680–682. https://doi.org/10.1039/B817223D.

(67) Huang, P.; Wu, M.; Kuga, S.; Wang, D.; Wu, D.; Huang, Y. One-Step Dispersion of Cellulose Nanofibers by Mechanochemical Esterification in an Organic Solvent. *ChemSusChem* **2012**, *5* (12), 2319–2322. https://doi.org/10.1002/cssc.201200492.

(68) Abitbol, T.; Rivkin, A.; Cao, Y.; Nevo, Y.; Abraham, E.; Ben-Shalom, T.; Lapidot, S.; Shoseyov, O. Nanocellulose, a Tiny Fiber with Huge Applications. *Current Opinion in Biotechnology* **2016**, *39*, 76–88. https://doi.org/10.1016/j.copbio.2016.01.002.

(69) Xu, H.; Xie, L.; Chen, Y.-H.; Huang, H.-D.; Xu, J.-Z.; Zhong, G.-J.; Hsiao, B. S.; Li, Z.-M. Strong Shear Flow-Driven Simultaneous Formation of Classic Shish-Kebab, Hybrid Shish-Kebab, and Transcrystallinity in Poly (Lactic Acid)/Natural Fiber Biocomposites. *ACS Sustainable Chem. Eng.* **2013**, *1* (12), 1619–1629. https://doi.org/10.1021/sc4003032.

(70) Khoshkava, V.; Kamal, M. R. Effect of Surface Energy on Dispersion and Mechanical Properties of Polymer/Nanocrystalline Cellulose Nanocomposites. *Biomacromolecules* **2013**, *14* (9), 3155–3163. https://doi.org/10.1021/bm400784j.

(71) Goffin, A.-L.; Raquez, J.-M.; Duquesne, E.; Siqueira, G.; Habibi, Y.; Dufresne, A.; Dubois, P. From Interfacial Ring-Opening Polymerization to Melt Processing of Cellulose Nanowhisker-Filled Polylactide-Based Nanocomposites. *Biomacromolecules* **2011**, *12* (7), 2456–2465. https://doi.org/10.1021/bm200581h.

(72) Floros, M.; Hojabri, L.; Abraham, E.; Jose, J.; Thomas, S.; Pothan, L.; Leao, A. L.; Narine, S. Enhancement of Thermal Stability, Strength and Extensibility of Lipid-Based Polyurethanes with Cellulose-Based Nanofibers. *Polymer Degradation and Stability* **2012**, *97* (10), 1970–1978. https://doi.org/10.1016/j.polymdegradstab.2012.02.016.

(73) Maiti, S.; Sain, S.; Ray, D.; Mitra, D. Biodegradation Behaviour of PMMA/Cellulose Nanocomposites Prepared by in-Situ Polymerization and Ex-Situ Dispersion Methods. *Polymer Degradation and Stability* **2013**, *98* (2), 635–642. https://doi.org/10.1016/j.polymdegradstab.2012.11.011.

(74) Zaaba, N. F.; Ismail, H. A Review on Tensile and Morphological Properties of Poly (Lactic Acid) (PLA)/ Thermoplastic Starch (TPS) Blends. *Polymer-Plastics Technology and Materials* **2019**, *58* (18), 1945–1964. https://doi.org/10.1080/25740881.2019.1599941.

(75) Zaaba, N. F.; Jaafar, M.; Ismail, H. Tensile and Morphological Properties of Nanocrystalline Cellulose and Nanofibrillated Cellulose Reinforced PLA Bionanocomposites: A Review. *Polymer Engineering & Science* **2021**, *61* (1), 22–38. https://doi.org/10.1002/pen.25560.

(76) Song, J. H.; Murphy, R. J.; Narayan, R.; Davies, G. B. H. Biodegradable and Compostable Alternatives to Conventional Plastics. *Philosophical Transactions of the Royal Society B: Biological Sciences* **2009**, *364* (1526), 2127–2139. https://doi.org/10.1098/rstb.2008.0289.

(77) Vroman, I.; Tighzert, L. Biodegradable Polymers. *Materials* **2009**, *2* (2), 307–344. https://doi.org/10.3390/ma2020307.

(78) Leja, K.; G, L. Polymer Biodegradation and Biodegradable Polymers - a Review. *Polish Journal of Environmental Studies* **2010**, *2* (19), 255–266.

(79) Kramschuster, A.; Turng, L.-S. An Injection Molding Process for Manufacturing Highly Porous and Interconnected Biodegradable Polymer Matrices for Use as Tissue Engineering Scaffolds. *Journal of Biomedical Materials Research Part B: Applied Biomaterials* **2010**, *92B* (2), 366–376. https://doi.org/10.1002/jbm.b.31523.

(80) Zhao, P.; Liu, W.; Wu, Q.; Ren, J. Preparation, Mechanical, and Thermal Properties of Biodegradable Polyesters/Poly(Lactic Acid) Blends. *Journal of Nanomaterials* **2010**, *2010*, e287082-e287089. https://doi.org/10.1155/2010/287082.

(81) Thepthawat, A.; Srikulkit, K. Improving the Properties of Polylactic Acid by Blending with Low Molecular Weight Polylactic Acid-g-Natural Rubber. *Polymer Engineering & Science* **2014**, *54* (12), 2770–2776. https://doi.org/10.1002/pen.23835.

(82) Li, M.; Liu, W.; Sun, J.; Xianyu, Y.; Wang, J.; Zhang, W.; Zheng, W.; Huang, D.; Di, S.; Long, Y.-Z.; Jiang, X. Culturing Primary Human Osteoblasts on Electrospun Poly (Lactic-Co-Glycolic Acid) and Poly(Lactic-Co-Glycolic Acid)/Nanohydroxyapatite Scaffolds for Bone Tissue Engineering. *ACS Appl. Mater. Interfaces* **2013**, *5* (13), 5921–5926. https://doi.org/10.1021/am401937m.

(83) Hijazi, N.; Le Moigne, N.; Rodier, E.; Sauceau, M.; Vincent, T.; Benezet, J.-C.; Fages, J. Biocomposite Films Based on Poly (Lactic Acid) and Chitosan Nanoparticles: Elaboration, Microstructural and Thermal Characterization. *Polymer Engineering & Science* **2019**, *59* (S1), e350–e360. https://doi.org/10.1002/pen.24983.

(84) da Cruz Faria, É.; Dias, M. L.; Ferreira, L. M.; Tavares, M. I. B. Crystallization Behavior of Zinc Oxide/Poly (Lactic Acid) Nanocomposites. *J Therm Anal Calorim* **2021**, *146* (4), 1483–1490. https://doi.org/10.1007/s10973-020-10166-3.

(85) Pei, A.; Zhou, Q.; Berglund, L. A. Functionalized Cellulose Nanocrystals as Biobased Nucleation Agents in Poly(l-Lactide) (PLLA) – Crystallization and Mechanical Property Effects. *Composites Science and Technology* **2010**, *70* (5), 815–821. https://doi.org/10.1016/j.compscitech.2010.01.018.

(86) Jonoobi, M.; Harun, J.; Mathew, A. P.; Oksman, K. Mechanical Properties of Cellulose Nanofiber (CNF) Reinforced Polylactic Acid (PLA) Prepared by Twin Screw Extrusion. *Composites Science and Technology* **2010**, *70* (12), 1742–1747. https://doi.org/10.1016/j.compscitech.2010.07.005.

(87) dos Santos, F. A.; Iulianelli, G. C. V.; Tavares, M. I. B. Effect of Microcrystalline and Nanocrystals Cellulose Fillers in Materials Based on PLA Matrix. *Polymer Testing* **2017**, *61*, 280–288. https://doi.org/10.1016/j.polymertesting.2017.05.028.

(88) Petinakis, E.; Liu, X.; Yu, L.; Way, C.; Sangwan, P.; Dean, K.; Bateman, S.; Edward, G. Biodegradation and Thermal Decomposition of Poly (Lactic Acid)-Based Materials Reinforced by Hydrophilic Fillers. *Polymer Degradation and Stability* **2010**, *95* (9), 1704–1707. https://doi.org/10.1016/j.polymdegradstab.2010.05.027.

(89) Sinha Ray, S.; Yamada, K.; Okamoto, M.; Fujimoto, Y.; Ogami, A.; Ueda, K. New Polylactide/Layered Silicate Nanocomposites. 5. Designing of Materials with Desired Properties. *Polymer* **2003**, *44* (21), 6633–6646. https://doi.org/10.1016/j.polymer.2003.08.021.

(90) Rasal, R. M.; Janorkar, A. V.; Hirt, D. E. Poly (Lactic Acid) Modifications. *Progress in Polymer Science* **2010**, *35* (3), 338–356. https://doi.org/10.1016/j.progpolymsci.2009.12.003.

(91) Svagan, A. J.; Åkesson, A.; Cárdenas, M.; Bulut, S.; Knudsen, J. C.; Risbo, J.; Plackett, D. Transparent Films Based on PLA and Montmorillonite with Tunable Oxygen Barrier Properties. *Biomacromolecules* **2012**, *13* (2), 397–405. https://doi.org/10.1021/bm201438m.

(92) Armentano, I.; Bitinis, N.; Fortunati, E.; Mattioli, S.; Rescignano, N.; Verdejo, R.; Lopez-Manchado, M. A.; Kenny, J. M. Multifunctional Nanostructured PLA Materials for Packaging and Tissue Engineering. *Progress in Polymer Science* **2013**, *38* (10), 1720–1747. https://doi.org/10.1016/j.progpolymsci.2013.05.010.

(93) Raquez, J.-M.; Habibi, Y.; Murariu, M.; Dubois, P. Polylactide (PLA)-Based Nanocomposites. *Progress in Polymer Science* **2013**, *38* (10), 1504–1542. https://doi.org/10.1016/j.progpolymsci.2013.05.014.

(94) Ali, U.; Karim, K. J. Bt. A.; Buang, N. A. A Review of the Properties and Applications of Poly (Methyl Methacrylate) (PMMA). *Polymer Reviews* **2015**, *55* (4), 678–705. https://doi.org/10.1080/15583724.2015.1031377.

(95) Pandey, N.; Khaling, R.; Verma, P.; Pendke, P.; Patel, A. Characterization of TiO2 Doped Poly (Methyl Methacrylate) PMMA Thin Films Using XRD. *AIP Conference Proceedings* **2019**, *2100* (1), 020151-020155. https://doi.org/10.1063/1.5098705.

(96) Fujimoto, K.; Tang, Z.; Shinoda, W.; Okazaki, S. All-Atom Molecular Dynamics Study of Impact Fracture of Glassy Polymers. I: Molecular Mechanism of Brittleness of PMMA and Ductility of PC. *Polymer* **2019**, *178*, 121570-121579. https://doi.org/10.1016/j.polymer.2019.121570.

(97) Ounas, O.; El Foulani, A. A.; Lekhlif, B.; Jamal-Eddine, J. Immobilization of TiO2 into a Poly Methyl Methacrylate (PMMA) as Hybrid Film for Photocatalytic Degradation of Methylene Blue. *Materials Today: Proceedings* **2020**, *22*, 35–40. https://doi.org/10.1016/j.matpr.2019.08.068.

(98) Benhabiles, O.; Galiano, F.; Marino, T.; Mahmoudi, H.; Lounici, H.; Figoli, A. Preparation and Characterization of TiO2-PVDF/PMMA Blend Membranes Using an Alternative Non-Toxic Solvent for UF/MF and Photocatalytic Application. *Molecules* **2019**, *24* (4), 724-743. https://doi.org/10.3390/molecules24040724.

(99) Boujemaoui, A.; Ansari, F.; Berglund, L. A. Nanostructural Effects in High Cellulose Content Thermoplastic Nanocomposites with a Covalently Grafted Cellulose–Poly (Methyl Methacrylate) Interface. *Biomacromolecules* **2019**, *20* (2), 598–607. https://doi.org/10.1021/acs.biomac.8b00701.

(100) Thomas, S.; Maria, H. J. *Progress in Rubber Nanocomposites*; Woodhead Publishing, 2016.

(101) Low, D. Y. S.; Supramaniam, J.; Soottitantawat, A.; Charinpanitkul, T.; Tanthapanichakoon, W.; Tan, K. W.; Tang, S. Y. Recent Developments in Nanocellulose-Reinforced Rubber Matrix Composites: A Review. *Polymers* **2021**, *13* (4), 550-584. https://doi.org/10.3390/polym13040550.

(102) Ibrahim, S.; Othman, N.; Sreekantan, S.; Tan, K. S.; Mohd Nor, Z.; Ismail, H. Preparation and Characterization of Low-Molecular-Weight Natural Rubber Latex via Photodegradation Catalyzed by Nano TiO2. *Polymers* **2018**, *10* (11), 1216-1232. https://doi.org/10.3390/polym10111216.

(103) Samsuri, A. Degradation of Natural Rubber and Synthetic Elastomers. In *Shreir's Corrosion*; 2010; Vol. 3, pp 2407–2438. https://doi.org/10.1016/B978-044452787-5.00117-7.

(104) Hakimi, N. M. F.; Lee, S. H.; Lum, W. C.; Mohamad, S. F.; Osman Al Edrus, S. S.; Park, B.-D.; Azmi, A. Surface Modified Nanocellulose and Its Reinforcement in Natural Rubber Matrix Nanocomposites: A Review. *Polymers* **2021**, *13* (19), 3241-3264. https://doi.org/10.3390/polym13193241.

(105) Karásek, L.; Sumita, M. Characterization of Dispersion State of Filler and Polymer-Filler Interactions in Rubber-Carbon Black Composites. *J Mater Sci* **1996**, *31* (2), 281–289. https://doi.org/10.1007/BF01139141.

(106) Hashim, A. S.; Azahari, B.; Ikeda, Y.; Kohjiya, S. The Effect of Bis(3-Triethoxysilylpropyl) Tetrasulfide on Silica Reinforcement of Styrene-Butadiene Rubber. *Rubber Chemistry and Technology* **1998**, *71* (2), 289–299. https://doi.org/10.5254/1.3538485.

(107) Wang, M.-J. Effect of Polymer-Filler and Filler-Filler Interactions on Dynamic Properties of Filled Vulcanizates. *Rubber Chemistry and Technology* **1998**, *71* (3), 520–589. https://doi.org/10.5254/1.3538492.

(108) Cao, L.; Huang, J.; Chen, Y. Dual Cross-Linked Epoxidized Natural Rubber Reinforced by Tunicate Cellulose Nanocrystals with Improved Strength and Extensibility. *ACS Sustainable Chem. Eng.* **2018**, *6* (11), 14802–14811. https://doi.org/10.1021/acssuschemeng.8b03331.

(109) De Vos, L.; Van de Voorde, B.; Van Daele, L.; Dubruel, P.;Van Vlierberghe, S. Poly (alkylene terephthalate)s: From current developments in synthetic strategies towards applications. *European Polymer Journal* **2021**, 161, p.110840. https://doi.org/10.1016/j.eurpolymj.2021.110840.

(110) Welle, F. The facts about PET. URL: https://www. petcore-europe. org/images/news/pdf/factsheet_the_facts_about_pet_dr_frank_welle_2018. pdf (Accessed June 13, 2021).

(111) Scheirs, J.; Long, T.E. Modern polyesters: chemistry and technology of polyesters and copolyesters. John Wiley & Sons. eds., 2005.

(112) Kargarzadeh, H.; Mariano, M.; Huang, J.; Lin, N., Ahmad, I.; Dufresne, A.; Thomas, S. Recent developments on nanocellulose reinforced polymer nanocomposites: A review. *Polymer* **2017**, 132, pp.368-393. https://doi.org/10.1016/j.polymer.2017.09.043.

(113) Zaman, M.; Liu, H.; Xiao, H.; Chibante, F.; Ni, Y. Hydrophilic modification of polyester fabric by applying nanocrystalline cellulose containing surface finish. *Carbohydrate polymers* **2013**, 91(2), pp.560-567. https://doi.org/10.1016/j.carbpol.2012.08.070.

(114) Bide, M.; Tao Zhong, M.; Ukponmwan, J.; Phaneuf, M.; Quist, W.; LoGerfo, F. Bifunctional Surface Modification of Polyester. *AATCC review* **2003**, 3(11).

(115) Bech, L.; Meylheuc, T.; Lepoittevin, B.; Roger, P. Chemical surface modification of poly (ethylene terephthalate) fibers by aminolysis and grafting of carbohydrates. *Journal of Polymer Science Part A: Polymer Chemistry* **2007**, 45(11), pp.2172-2183. https://doi.org/10.1002/pola.21983.

(116) Alakara, Ş.F.; Karakişla, M.; Saçak, M. Preparation of Poly (ethylene terephthalate)-g-Methacrylamide Copolymers Initiated by Azobisizobutyronitrile: Characterization and Investigation of Some Properties. *Journal of Macromolecular Science, Part A: Pure and Applied Chemistry* **2008**, 45(4), pp.276-280. https://doi.org/10.1080/10601320701863700.

(117) Morent, R.; De Geyter, N.; Verschuren, J.; De Clerck, K.; Kiekens, P.; Leys, C. Non-thermal plasma treatment of textiles. *Surface and coatings technology* **2008**, 202(14), pp.3427-3449. https://doi.org/10.1016/j.surfcoat.2007.12.027.

(118) Zhang, H.; Wang, X.; Liang, Y.; Preparation and characterization of a Lithium-ion battery separator from cellulose nanofibers. *Heliyon* **2015**, 1(2), p.e00032. https://doi.org/10.1016/j.heliyon.2015.e00032.

(119) Hasegawa, M.; Isogai, A.; Onabe, F.; Usuda, M. Dissolving states of cellulose and chitosan in trifluoroacetic acid. *Journal of applied polymer science* **1992**, 45(10), pp.1857-1863. https://doi.org/10.1002/app.1992.070451020.

(120) Rodrigues, B.V.; Ramires, E.C.; Santos, R.P.; Frollini, E. Ultrathin and nanofibers via room temperature electrospinning from trifluoroacetic acid solutions of untreated lignocellulosic sisal fiber or sisal pulp. *Journal of Applied Polymer Science* **2015**, 132(16). https://doi.org/10.1002/app.41826.

(121) de Oliveira Santos, R.P.; Rodrigues, B.V.M.; dos Santos, D.M.; Campana-Filho S.P.; Ruvolo-Filho, A.C.; and Frollini, E. Electrospun recycled PET-based mats: Tuning the properties by addition of cellulose and/or lignin. *Polymer Testing* **2017**, 60, pp.422-431. https://doi.org/10.1016/j.polymertesting.2017.04.023.

(122) Persano, L.; Camposeo, A.; Tekmen, C.; Pisignano, D. Industrial upscaling of electrospinning and applications of polymer nanofibers: a review. *Macromolecular materials and engineering* **2013**, 298(5), pp.504-520. https://doi.org/10.1002/mame.201200290.

(123) Xia, Y.; Larock, R. C. Vegetable Oil-Based Polymeric Materials: Synthesis, Properties, and Applications. *Green Chem.* **2010**, *12* (11), 1893-1909. https://doi.org/10.1039/c0gc00264j.

(124) Sain, S.; Åkesson, D.; Skrifvars, M. Synthesis and Properties of Thermosets from Tung Oil and Furfuryl Methacrylate. *Polymers* **2020**, *12* (2), 258-273. https://doi.org/10.3390/polym12020258.

(125) Johns, A.; Edwards, K.; Inglesby, S.; Quirino, R. L. Emulsion Polymerization of Tung Oil-Based Latexes with Asolectin as a Biorenewable Surfactant. *Coatings* **2016**, *6* (4), 56-67. https://doi.org/10.3390/coatings6040056.

(126) Li, F.; Hanson, M. V.; Larock, R. C. Soybean Oil–Divinylbenzene Thermosetting Polymers: Synthesis, Structure, Properties and Their Relationships. *Polymer* **2001**, *42* (4), 1567–1579. https://doi.org/10.1016/S0032-3861(00)00546-2.

(127) Türünç, O.; Billiet, S.; De Bruycker, K.; Ouardad, S.; Winne, J.; Du Prez, F. E. From Plant Oils to Plant Foils: Straightforward Functionalization and Crosslinking of Natural Plant Oils with Triazolinediones. *European Polymer Journal* **2015**, *65*, 286–297. https://doi.org/10.1016/j.eurpolymj.2014.12.013.

(128) Moreno, M.; Armentano, I.; Fortunati, E.; Mattioli, S.; Torre, L.; Lligadas, G.; Ronda, J. C.; Galià, M.; Cádiz, V. Cellulose Nano-Biocomposites from High Oleic Sunflower Oil-Derived Thermosets. *European Polymer Journal* **2016**, *79*, 109–120. https://doi.org/10.1016/j.eurpolymj.2016.04.018.

(129) Wik, V. M.; Aranguren, M. I.; Mosiewicki, M. A. Castor Oil-Based Polyurethanes Containing Cellulose Nanocrystals. *Polym Eng Sci* **2011**, *51* (7), 1389–1396. https://doi.org/10.1002/pen.21939.

(130) He, M.; Zhou, J.; Zhang, H.; Luo, Z.; Yao, J. Microcrystalline Cellulose as Reactive Reinforcing Fillers for Epoxidized Soybean Oil Polymer Composites. *Journal of Applied Polymer Science* **2015**, *132* (36). 42488-42496. https://doi.org/10.1002/app.42488.

(131) Bouaziz, K.; Ayadi, M.; Allouche, N.; Chemtob, A. Renewable Photopolymer Films Derived From Low-Grade Lampante and Pomace Olive Oils. *European Journal of Lipid Science and Technology* **2017**, *119* (12), 1700003-1700010. https://doi.org/10.1002/ejlt.201700003.

(132) Lazzari, M.; Chiantore, O. Drying and Oxidative Degradation of Linseed Oil. *Polymer Degradation and Stability* **1999**, *65* (2), 303–313. https://doi.org/10.1016/S0141-3910(99)00020-8.

(133) Hess, P. S.; O'Hare, G. A. Oxidation of Linseed Oil. *Ind. Eng. Chem.* **1950**, *42* (7), 1424–1431. https://doi.org/10.1021/ie50487a044.

(134) Veigel, S.; Lems, E.-M.; Grüll, G.; Hansmann, C.; Rosenau, T.; Zimmermann, T.; Gindl-Altmutter, W. Simple Green Route to Performance Improvement of Fully Bio-Based Linseed Oil Coating Using Nanofibrillated Cellulose. *Polymers* **2017**, *9* (9), 425-437. https://doi.org/10.3390/polym9090425.

(135) Diamante, L.M. and Lan, T., Absolute viscosities of vegetable oils at different temperatures and shear rate range of 64.5 to 4835 s− 1, *Journal of food processing*, *2014*. http://dx.doi.org/10.1155/2014/234583

(136) Sahasrabudhe, S.N.; Rodriguez-Martinez, V.; O'Meara, M.; Farkas, B.E. Density, viscosity, and surface tension of five vegetable oils at elevated temperatures: Measurement and modeling. *International Journal of Food Properties* **2017**, *20*(sup2), pp.1965-1981. https://doi.org/10.1080/10942912.2017.1360905

(137) Dankovich, T.A. and Hsieh, Y.L., Surface modification of cellulose with plant triglycerides for hydrophobicity. *Cellulose* **2007**, *14*(5), pp.469-480. https://doi.org/10.1007/s10570-007-9132-1

CHAPTER 2: Hydrophobic 2,7-Octadienyl Ether-Cellulose Nanofibrils Using Butadiene Sulfone as Both a Reagent and a Medium

2.1 Abstract

This is the first proof of concept of generating hydrophobic nanocelluloses by facile one-pot solventless telomerization using butadiene sulfone (BDS) to serve as a liquid reaction medium and as a source of 1,3-butadiene (1,3-BD). Optimal telomerization of 1,3-BD using 6 equivalents of 2,7-octadienyl ether (ODE) per to amorphous cellulose (anhydroglucose unit (AGU)) at 110 °C ("6ODE110"), followed by disintegration by shear force, yielded ca. 27-41 % hydrophobic nanocelluloses. These nanocelluloses were dispersible in dimethyl sulfoxide (DMSO), THF, and $CHCl_3$ at 3.7, 6.3, and 4.4 nm thickness, respectively. The surface ODE group was evidenced by methylene peaks at 2800-2980 cm^{-1} and C=C stretches at 1640-1704 cm^{-1} by FTIR. Solution state ^1H NMR elucidated the ODE structure (d_6-DMSO, δ:1.47, 1.95, 2.07 ppm for methylene protons, and 4.86, 5.29, 5.61, 5.90, 6.07 ppm for olefinic protons) along with cellulosic protons (δ: 4.12, 3.08, 3.28, 3.40, 3.53, 3.19, 3.93 ppm for H1, 2, 3, 4, 5, 6a, 6b, respectively), indicating a 30 % surface OH to ODE conversion. ODE-CNFs exhibited far superior thermal stability with a Tmax of 332 °C, 67 °C higher than that of TEMPO-CNFs. Most impressively, 1 % ODE-NC effectively converted hydrophilic solid mica and porous cellulose paper to hydrophobic surfaces with outstanding 102 ± 1° and 94 ± 2° water contact angles, respectively.

2.2 Introduction

Nanocelluloses (NCs) are the crystalline domains isolated by chemical, enzymatic, or mechanical means, or a combination thereof, from native cellulose, nature's most abundant biopolymer. The most commonly used method to isolate the crystalline NCs in the past decades has been either (1) removing the amorphous chains via sulfuric acid (H_2SO_4) hydrolysis[1] to the most crystalline (up to 91 %)[2] nanorod-like cellulose nanocrystals (CNCs) typically in low yields

(< 30 %)[2], (2) by regioselective TEMPO-mediated oxidation originally reported on glucans[3] to produce thinner and longer cellulose nanofibrils (CNFs) in much higher yields (*ca.* 90 %).[2,4,5] More recently, as a newly emerging method, Kontturi et al. reported isolation of unmodified and uncharged CNCs by using hydrochloric acid vapor with an impressive 97.4 % yield and increased crystallinity from cellulose.[6] The CNFs have an intrinsic tensile strength of 233 MPa[9] and a Young's modulus of 145 GPa[8], whereas the CNCs have an intrinsic tensile strength of 7.5 GPa[7] and a Young's modulus of 150 GPa[8], the highest among organic materials. Indeed, CNCs approach one-third of the 29 GPa[10] tensile strength, and half of the 270–950 GPa[11] Young's modulus of carbon nanotubes. Both H_2SO_4 hydrolyzed CNCs and TEMPO-oxidized CNFs carry negative charges via sulfate esters and carboxylates, respectively, to exhibit excellent aqueous dispersibility compared to uncharged and unmodified CNCs produced by HCl vapor[12], which are only dispersible in formic acid and *m*-cresol. Charged NCs find use in aqueous applications, such as reinforcing hydrophilic polymers[13], coating papers[14], hydrogels and aerogels[15,16]. However, none of these NCs can be dispersed in common organic solvents nor are they compatible with synthetic polymers.

To date, efforts to improve organic dispersibility or synthetic polymer compatibility have been practiced by surface modification of already-processed CNCs[17-20] and CNFs[21-25], or lengthy multi-step processes of cellulose functionalization followed by defibrillation[26]. For CNCs, further reactions, such as esterification with succinic anhydride[17] or 11-mercaptoundecanoic acid[18], silylation with alkyl chlorosilanes[19], or graft polymerization of styrene[20], were necessary to render them dispersible in dimethyl sulfoxide (DMSO)[17], 1,4-dioxane[17], toluene[18], and tetrahydrofuran (THF)[19], or to improve compatibility with PMMA[20]. In the case of CNFs, tannic acid priming and amidation with hexadecylamine improved its dispersibility in acetone, ethanol, DMF and toluene[21].

Graft-polymerization of butyl acrylate on CNFs renders them THF-dispersible[22] for epoxy[21] and PLA composites[22]. Amidation of CNFs mediated by 1-ethyl-3-(3-dimethylaminopropyl)-carbodiimide with octadecyl amine[23], amine-terminated polyethylene glycol[24], benzyl amine[25], hexylamine[25], or dodecylamine[25], renders the CNFs THF-disperisible[23] and $CHCl_3$-dispersible[24] upon freeze drying, or toluene-dispersible[25] by solvent exchange.

Acetylation was conducted directly on cotton linter cellulose[27,28] in an aqueous mixture of acetic acid and butyric acid with a catalytic amount of hydrochloric acid, followed by mechanical agitation in a blender (Waring) for 20 or 40 min, to produce acetylated CNCs with 25-50 nm diameters, 170-280 nm lengths, and DS of 0.02-0.12 mmol/g depending on blending (20 or 40 min), and reaction (4-20 h) time. The product from a 20 h reaction followed by 20 min blending formed a uniform opaque dispersion in ethyl acetate that lasted at least for 1 h. Kenaf cellulose was acetylated with acetic anhydride in pyridine, then mechanically blended in aqueous media, cryo-crushed, and homogenized by high-pressure (500 bar, 40 times) to produce 10-20 nm wide micrometer-length nanofibers with DS 1.16 (per 3 OH groups) which formed milky acetone and ethanol dispersions that were stable for two months.[26] Modification of cellulose followed by mechanical disintegration is more efficient than functionalizing already-processed CNCs or CNFs, however, it still involves time-consuming reactions and disintegrations. Therefore, better-streamlined and more sustainable approaches to produce more hydrophobic nanocellulose are critically needed.

This study, therefore, aims to develop a facile process for direct functionalization of cellulose followed by disintegration to generate novel nanocelluloses with more a hydrophobic hydrocarbon moiety. Particularly, CNFs that are characterized by large surface areas were the focus of this study. First and foremost, butadiene sulfone (BDS) was employed as both a solvent

and a reagent. BDS is solid at room temperature, and melts at 65 °C, and thus can serve as a reaction medium at the elevated temperature. Structurally, BDS is analogous to piperylene sulfone[29], which carries an extra C1 methyl group and has similar physical properties (dipole moment D = 5.32, dielectric constant ε = 42.6, and solvent polarity π*= 0.87) as DMSO (D = 4.27, ε = 46.7, π* = 1.00), a common solvent for diverse organic reactions. Above 90 °C, BDS undergoes reversible cheletropic degradation into gaseous 1,3-butadiene (1,3-BD) and sulfur dioxide (SO_2) which have been shown to revert back to liquid or solid BDS at up to 96 wt % of the original mass upon cooling in the presence of excess SO_2 and 1 wt % hydroquinone inhibitor in a sealed environment.[29,30] As a reagent, BDS has shown to be a safer source of 1,3-BD for Diels-Alder reactions between conjugated dienes and maleic anhydride[31] or 1,4-dihydronaphthalene[32], compared to the highly volatile (T_b = - 4.4 °C) 1,3-BD from a gas cylinder. In the presence of water, BDS could also supply sulfurous acid to simultaneously solubilize lignin and hydrolyze xylan in biorefining.[33,34]

With the chemical versatility and recyclability of BDS, the first effort is to telomerize 1,3-BD generated from BDS with cellulose isolated from rice straw (RS), the largest agricultural crop residue in the world[35], with a similar cellulose content as wood[36]. Telomerization of 1,3-BD has been well-documented with alcohols[37-39], carbohydrates[40,41], and starch[42,43] for the production of plasticizers[37], chemical building blocks[38,39], surfactants [40,41], and sizing agents for textile applications, or in pharmaceutical applications[42,43]. However, BDS as a precursor for telomerization of 1,3-BD has not been explored nor telomerization of 1,3-BD with cellulose. Most importantly, telomerization of 1,3-BD with cellulose to generate nanocelluloses is an original concept. Telomerization is a 100 % atom-efficient reaction, and produces C8 telomers of 2,7-octadienyl ether as a major product (> 95 %), branched iso telomers and 1,3,7-octatriene as minor

products (<5 %) when Pd/TOMPP (tris(2-methoxyphenyl)-phosphine) telomerization catalyst is used[41,44,45](**Scheme 2-1**). Depending on the ligand type used (TPPTS: trisodium salt of 3, 3',3''-phosphanetriyl benzene sulfonic acid), production of C12 and C24 telomers are also reported on ethylene glycol and MeOH[46]. The resulting 2,7-octadienyl ether linked to cellulose is more hydrophobic and less acid-labile than either ester or acetyl groups.

In the reaction, BDS serves as a reaction medium and as a source for 1,3-BD reagent to confer 2,7-octadienyl ether (ODE) functionality on cellulose by telomerization while obviating the need for an additional solvent. Telomerization was first optimized by considering the role of BDS in generating 1,3-BD and serving as a reaction medium. Kinetic analysis of BDS thermal decomposition showed that 10-22 wt % BDS decomposed into gaseous forms at 90-100 °C under sealed conditions.[47,48] Available 1,3-BD for the reaction was estimated based on a conservative 10 % conversion, whereas the remaining BDS functioned as a solvent for the reaction. Telomerization of 1,3-BD with cellulose was optimized at varying precursor BDS concentrations. This is expressed as the molar ratio of telomerized ODE to non-crystalline AGU in cellulose. The reaction temperatures were set at 90 °C, the break-down temperature of BDS into gaseous 1,3-BD and SO_2, and 110 °C, the onset temperature of the Diels-Alder reaction between the terminal alkene in the ODE group and 1,3-BD.[49,50] The optimal condition was evaluated by both the quantities and the qualities of ODE-NCs dispersible in aprotic DMSO, DMF, $CHCl_3$, and THF. These solvents' polarity and affinity to ODE-NC should be relative to the extent of ODE-substitution. The morphologies of organic-dispersible ODE-NC on hydrophilic mica and hydrophobic highly-oriented pyrolytic graphite (HOPG) were observed by AFM. The optimally-modified NCs were characterized by FTIR and ^{1}H NMR, their thermal properties by thermal gravimetric analyzer (TGA), and crystallinity by X-ray powder diffraction (XRD).

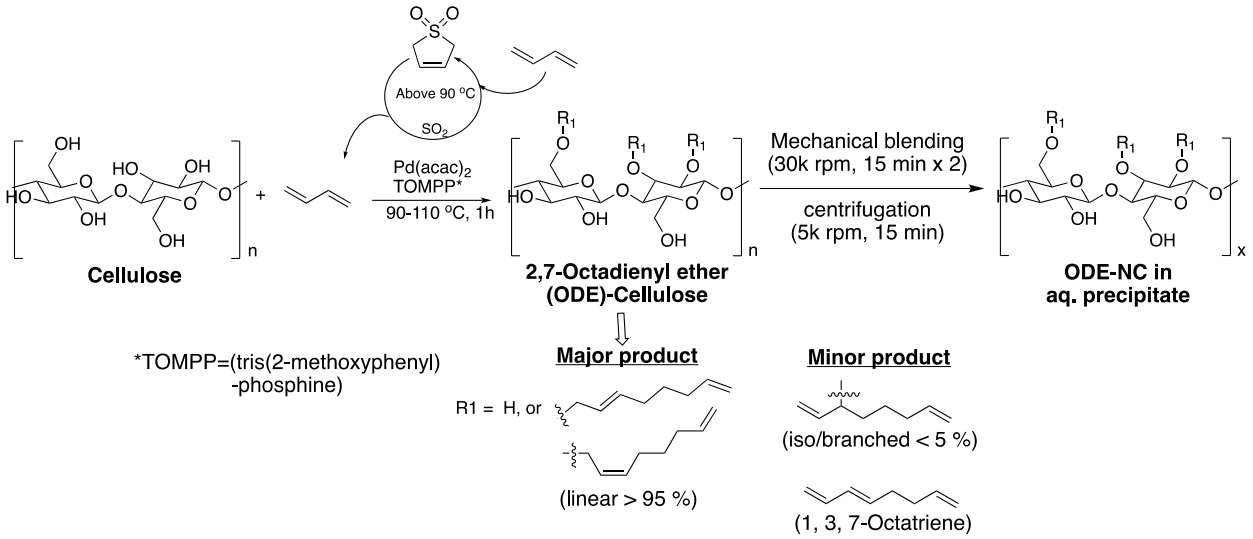

Scheme 2-1. The major product of 2,7-Octadienyl ether (ODE)-cellulose and minor products via telomerization of 1,3-BD using BDS as both a solvent and a source of reagent, followed by generation of ODE-nanocellulose (NC) by mechanical blending.

2.3 Experimental

2.3.1 Materials

Butadiene sulfone (BDS, 98%, ACROS Organics), palladium (II) acetylacetonate ($Pd(acac)_2$, 99 %, Sigma-Aldrich), TOMPP (96 %, Spectrum Chemicals & Laboratory Products), DMSO (certified), DMF (certified), acetone (HPLC grade), THF (histrogical grade), $CHCl_3$ (reagent grade), m-cresol (99 %, Sigma-Aldrich), toluene (certified), ethyl acetate (EtOAc, HPLC grade) and potassium bromide powder (KBr, FTIR grade, Neta Scientific, Inc.) were used as received without further purification. Water used was purified by the Milli-Q Advantage A-10 water purification system (Millipore Corporate, Billerica, MA). For imaging, mica (highest grade V1 mica discs, 10 mm, Ted Pella, Inc.) and HOPG (grade ZYB) were used for AFM, and carbon grids (300-mesh copper, formvar-carbon, Ted Pella Inc.) were used for TEM. For UV-vis spectrophotometry, quartz, silica and glass standard cell cuvettes (Fisher Scientific) were used.

Cellulose was isolated from rice straw (Calrose variety) using a previously reported three-step process of 2:1 v/v toluene/ethanol extraction, acidified $NaClO_2$ dissolution of lignin (1.4 %, 70 °C, 5 h), and alkaline dissolution of hemicellulose and silica (5% KOH, 90 °C for 2 h) in 36.0 wt % yield[2], close to the previously-reported 38.3 wt %[51]. The cellulose was frozen (-196 °C in liquid nitrogen) and freeze-dried (-48 °C, 3 d) to a fluffy white mass.

2.3.2 Telomerization to 2,7-octadienyl ether (ODE)-cellulose

All reactions were performed in a 100 mL stainless steel sealed autoclave reactor (HTR-100, Hydrion Scientific) in a temperature-controlled oil bath. Telomerization of 1,3-BD with cellulose was optimized at varying excesses of precursor BDS to AGU in non-crystalline cellulose at 90 °C and 110 °C for 1 h. The quantity of BDS was based on the most conservative 10 % 1,3-BD liberated from BDS at equilibrium[47, 48] and dimerization of two 1,3-BD into one 2,7-octadienyl ether (ODE). For each reaction, 100 mg cellulose (0.6 mmol, anhydroglucose unit (AGU)) was combined with 2.2 g, 3.5 g, or 4.6 g of BDS (19, 30, or 40 mmol, respectively), i.e., 1.0, 1.5, and 2.0 mmol ODE from 10 % conversion of liquid BDS to gaseous BDS. Using the reported 0.618 CrI for rice straw cellulose[36], amorphous AGU in 100 mg cellulose is 0.2 mmol. The ODE equivalent to the available AGU, or ODE:AGU ratios, became 4.0, 6.3 and 8.4, herein abbreviated as 4ODE, 6ODE and 8ODE. The minimal temperature was set at 90 °C, the onset temperature at which BDS generates 1,3-BD, the telomerizing reagent. At 120 °C, the Diels-Alder adduct was detected in the product by ^{1}H NMR (**Figure 2-1**), indicating further oligmerization of ODE. Preliminary trials were conducted to further optimize reaction variables (Table 2-1). As a result, telomerization was set at 90 °C and 110 °C for 1 h for 4ODE (designated as 4ODE90 and 4ODE110), and at 110 °C for the other two ODE equivalents (designated as 6ODE110 and 8ODE110). The palladium catalyst ($Pd(acac)_2$) required for coordination of two 1,3-BD into an

eight-carbon chain was as low as 0.023 mol% ([Pd] = 0.015 wt %). The amount of electron-rich TOMPP[41] ligand used to modulate Pd activity was 0.092 mol% per mol AGU. These amounts are equivalent to those employed for sugar alcohols and soluble carbohydrates[3]. The Pd loading (0.015 wt %) is also significantly lower than that used the used in telomerization of starch (0.04 wt %)[42]. After 1 h telomerization, where the pressure reached between 1.7 and 9.2 bar, the reactor was cooled in an ice bath and the reaction mixture was diluted with 10 mL acetone followed by vacuum filtration, then rinsed with 10 mL acetone in a centrifuge tube three times, vortexed (10 s), and vacuum filtered (3 times) to remove residual BDS, SO_2, and palladium complex.

The air-dried ODE-cellulose was suspended in 100 mL water (ca. 0.1 w/v %) and blended twice in a high-speed blender (Vitamix 5200) at 30k rpm for 15 min for a total of 30 min. Next, the mixture was centrifuged at 5k rpm for 30 min to collect aqueous precipitate (aq. ppt) that contained the defibrillated ODE-nanocelluloses, or ODE-NC. The control NCs were obtained by mechanically blending 90 mg pristine cellulose in 90 mL water (ca. 0.1 w/v %) and centrifugation to collect aq. ppt in the same manner as was done for ODE-cellulose. Subsequent to telomerization, the hydrolysis reaction can be conducted as necessary to obtain finer fibrils by addition of H_2O, following the work by deFrias and Feng[33,34] which used BDS in the presence of water to hydrolyze xylan before removal of lignin as a pretreatment of sugarcane bagasse and miscanthus towards the production of biofuels and chemicals.

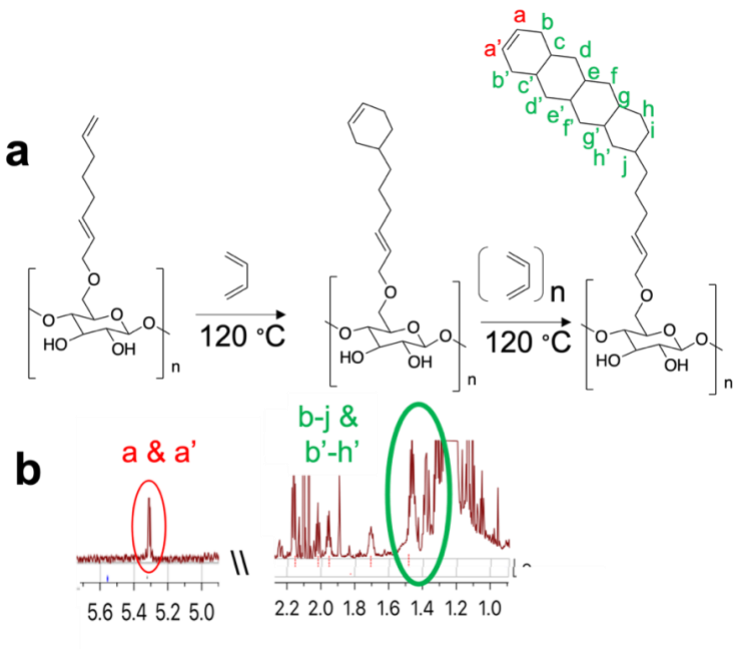

Figure 2-1. A side product formed by Diels-Alder reaction on ODE-cellulose: (a) reaction scheme during telomerization at 120 °C and (b) ^{1}H NMR of Diels-Alder side-product.

Table 2-1. Preliminary telomerization conditions.

ODE/Temperature	Reaction time	Variation in reaction condition	ODE-cellulose
4ODE110	2 h	n/a	dark brown product
4ODE90	2 h	n/a	dark brown product
4ODE110	1 h	46 mmol [Pd] per AGU	80 > p > 90 % in aq. ppt
6ODE120	1 h	n/a	Diels-Alder adduct
6ODE110	1 h	1.5 wt % H_2O added as a base	80 > p > 90 % in aq. ppt
6ODE110	1 h	Cellulose pre-treated in BDS at 70 °C for 2.5 h before telomerization	80 > p > 90 % in aq. ppt
6ODE110	1 h	5 mL DMF added as a co-solvent	80 > p > 90 % in aq. ppt

Where p represents for a product, and % abbreviates weight %.

2.3.3 Dispersion of ODE-cellulose in organic solvents

As general practice, the defibrillated ODE-cellulose is kept in an aqueous environment (never-dried aq. ppt) to maintain the swollen state of the fibrillar morphology[52]. After mechanical blending, the never-dried aq. ppt (90 mg) was solvent exchanged with acetone (5 mL x 3) followed by centrifugation (5 k rpm, 15 min) and decanting the acetone supernatant to collect the precipitate,

to which fresh acetone was added to repeat this process 2 more times to remove residual water. The final acetone precipitate was solvent exchanged again with DMSO, DMF, THF and $CHCl_3$ which have widely-varied dielectric constants, polarities and H-bonding abilities (**Table 2-2**).[53,54] Centrifugation of all organic dispersions was conducted at 1.5 k rpm for 15 min unless specified otherwise. Each organic dispersion was homogenized by brief 5 s ultra-sonication (40 kHz, 130 w, Branson 2510) and heated (55 °C, 24 h) to remove residual acetone, then centrifuged to collect CNFs in the organic supernatant (org sn). Each organic precipitate (org ppt) was vacuum-dried to quantify dry mass to calculate the weight of org sn. The $CHCl_3$ dispersion was left standing for 1 h after centrifugation to phase-separate gravitationally due to the close densities of $CHCl_3$ (ρ = 1.489 g/mL) and cellulose (ρ = 1.600 g/mL). The CNF control was collected from the aq. sn of unmodified cellulose by the same high-speed blending (30 k rpm, 30 min) and centrifugation (5 k rpm, 15 min). Herein, all mass percentage (wt %) are abbreviated as %, and the dried mass of org sn reflects the dispersibility of ODE-CNFs in the organic solvent. Light transmittance of 0.01 % ODE-NC in DMSO, DMF, THF and $CHCl_3$ supernatants from 6 ODE at 110 °C were measured from 300-800 nm using an Evolution 600 UV-vis spectrophotometer (Thermo Scientific, USA) with the respective solvent as reference.

Table 2-2. Physical properties of organic solvents.

	Dielectric constant (ε)	**H-bond donor (Hα)[a]**	**H-bond acceptor (Hβ)[b]**	**ρ (mg/mL)**	**γ (20 °C, dyn/cm)**
Water	80.1	1.17	0.47	0.998	72.8
DMSO	46.7	0	0.76	1.096	43.5
DMAc	37.8	n/a	n/a	0.937	32.4[c]
DMF	36.7	0	0.76	0.945	36.8
Acetone	20.7	0.08	0.43	0.788	23.5
m-cresol	11.5	n/a	n/a	1.030	n/a
THF	7.6	0	0.55	0.888	26.4
EtOAc	6.0	0	0.45	0.901	23.9
$CHCl_3$	4.8	0.2	0.10	1.489	26.7
Toluene	2.4	n/a	n/a	0.867	28.5

[a] from UV/vis spectrum of 4-nitroaniline that was sensitive to the hydrogen bond donation from the $-NH_2$ group.

[b] from dye studies in protic solvents by subtracting the polarity and polarizability effect.[53]
[c] at 30 °C.

2.3.4 Characterization

ODE-NCs in org sn, including CNFs and nanoparticles (NPs), were imaged by AFM and TEM. ODE-NCs (10 mL, ca. 0.0005 w/v %) were deposited onto freshly-cleaved hydrophilic mica or HOPG that had a reported water contact angle (WCA) of 70°[55,56], air-dried and scanned (Asylum Research MFP-3D, Santa Barbara, CA) in air under ambient conditions by tapping mode (28.98 N/m spring constant, ca. 297 kHz resonance frequency) with an OMCL-AC160TS standard silicon probe (Olympus Corp., Japan). The scan rate and image resolution were set to 1 Hz and 512 × 512 pixels, respectively, and the height images and profiles were processed with Igor Pro 6.21. The width and length of ODE-CNFs were measured from the images using TEM, JEOL JEM-1230. For TEM, ODE-CNFs (10 mL, ca. 0.0005 w/v %) were deposited onto glow-discharged or as-is carbon grids with the excess liquid being blotted by filter paper after 5 min. The specimens were then negatively stained with 2 % uranyl acetate or phosphotungstic acid, air-dried, and observed by TEM at a 40 or 80 kV accelerating voltage. The height and area ratios of CNFs/NPs were measured in AFM images, while width and length were measured in TEM images. These measurements were made on 30 - 100 ODE-CNFs and NPs in three to five images from different aliquots of the supernatant. An image analyzer (ImageJ, NIH, USA) was used to calculate the means and the standard deviations. ODE-microfibers in organic precipitates (ca. 0.1 w/v %, 10 μL) were deposited on glass slides and observed using a Leica DM2500 optical microscope equipped with a polarizer to measure their width and length (microfiber number (n) = 100 for both). Also, the averages with standard deviations were reported. The elemental composition of ODE-cellulose was evaluated using energy-dispersive X-ray spectroscopy (EDX, XMaxN Silicon Drift

Detector, Oxford Instruments, Abingdon, Oxfordshire, England) integrated into an SEM (XL 30-SFEG, FEI/Philips, USA). The sample was sputter-coated with gold for imaging and elemental analysis. ODE-CNFs and unmodified CNFs dried from the organic and the aq. sn, respectively, were analyzed as transparent KBr pellets (1:100, w/w) by a Thermo Nicolet 6700 FTIR with the transmittance spectra collected from an accumulation of 128 scans at a 4 cm^{-1} resolution over 4000–400 cm^{-1} at ambient conditions. The film surfaces of ODE-CNFs and unmodified CNFs (both dried from $CHCl_3$) were analyzed by FTIR-ATR spectra collected from 4000-400 cm^{-1} at a resolution of 4 cm^{-1} using a Nicolet iN10 microscope spectrometer (Thermo Fisher Scientific, USA). The thermal behavior of ODE-CNFs, ODE-cellulose, and cellulose were studied using a thermogravimetric analyzer (TGA-50, Shimadzu, Japan) from 25 °C to 500 °C at a 10 °C min^{-1} heating rate under N_2 purging (50 $mL \cdot min^{-1}$). The crystalline structures were determined by XRD using a PANalytical X'pert Pro powder diffractometer with a Ni-filtered Cu Kα radiation (λ = 1.5406 Å) at 45 kV anode voltage and 40 mA current. The samples were placed on a graphite stage using double-sided tape, and diffractograms were recorded from 5° to 40° at a scan rate of 2° per minute. The crystallinity index (CrI) was calculated by using the intensity of the 200 peak (I_{200}, 2θ = 22.6°) and the intensity minimum between the peaks at 200 and $1\bar{1}0$ (I_{am}, 2θ = 18.7°) as follows[57]:

$$\text{CrI} = \frac{I_{200} - I_{am}}{I_{200}} \times 100 \qquad \text{Eqn. 1}$$

The crystallite dimensions of these samples were calculated using the Scherrer equation[58],

$$D_{hkl} = \frac{0.9\,\lambda}{\beta 1/2\ cos\ \theta} \qquad \text{Eqn. 2}$$

where D_{hkl} is the crystallite dimension in the direction normal to the *h k l* lattice planes, l is the X-ray radiation wavelength (1.5406 Å). $\beta_{1/2}$ is the full width at half-maximum of the diffraction peak, and θ is the corresponding Bragg angle. $\beta_{1/2}$ was determined by multiple peak fitting in Origin software.

Solution state ^{1}H and ^{13}C NMR spectra of hydrolyzed ODE-CNFs (*h*ODE-CNFs) in d_6-DMSO were measured using a Bruker AVIII 800 MHz ^{1}H NMR spectrometer following a previously reported method[59], for CNFs with 2 nm or less lateral dimensions. Immediately after telomerization, ODE-cellulose was hydrolyzed (exfoliated) in-situ by sulfurous acid which was formed by a reaction of SO_2, the added 200 μL water and atmospheric O_2, followed by mechanical stirring at 110 °C for one hour. The resulting *h*ODE-cellulose was blended and centrifuged to collect the aq. ppt (ca. 5 mg) as previously described and solvent exchanged with acetone followed by rinsing (1.0 mL) and centrifugation to collect the acetone precipitate which were repeated three times, and then, solvent exchanged with 1 mL d_6-DMSO. The residual acetone was removed by heating (55 ºC, 2 d), and *h*ODE-CNFs in d_6-DMSO was centrifuged (5 k rpm, 10 min) to collect the supernatant with ca. 0.2 % *h*ODE-CNFs. 20 μL deuterated trifluoroacetic acid (TFA) was added to the sample immediately before the experiment to displace cellulosic OH peaks downfield to clear the olefinic proton region.[60,61] Percent conversion of surface OH groups was elucidated by quantitative integration of protons using an anomeric proton as an internal reference. This method was chosen over qualitative Br_2 titration using color change to indicate the presence of alkene. In our preliminary work, we had conducted Br_2 titration, but it showed inconsistent results. We concluded it does not give meaningful evidence nor is it practical for the 100 mg scale of our sample.

ODE-CNFs at 0.5 w/v supernatant, and 1 and 2 w/v % dispersion concentrated from 0.5 w/v % supernatant in THF and $CHCl_3$ supernatant (10 μL) were sonicated for 5 sec, then deposited on 1 cm diameter circular mica and cellulose filter paper (Whatman, 1 qualitative) (0.785 cm^2) at 0.5, 1, and 2 w/v % and allowed to air dry. Water contact angles (WCA, 5 μL) of sessile drops on these ODE-CNF covered surfaces were measured every 10 sec up to 80 sec and those values at 30 sec were reported. The median value of q_{right} and q_{left} of a sessile drop was obtained by using ImageJ contact angle plug-in software. WCA measurements were triplicated in different locations to average and derive the standard deviation. The surface coverage of mica by 10 μL ODE-CNFs in THF and $CHCl_3$ for their respective concentrations was analyzed by optical microscope, and the surface roughness was measured over a 5 μm x 5 μm area in triplicate by AFM. The average value and the standard deviation were reported.

2.4 Results and Discussion

2.4.1 Optimization of telomerization reaction

Telomerization of 1,3-BD into ODE on cellulose was conducted with three different quantities of BDS that served as both solvent and precursor to reagent at 90 °C and 110 °C for 1 h. Using a conservative 10% BDS to 1,3-BD conversion and amorphous AGU in rice straw cellulose, the equivalent ODE to non-crystalline AGU were at 4, 6 and 8 mole ratios. Coupled with reaction temperatures of 90 and 110 °C, four telomerization conditions designated as 4ODE90, 4ODE110, 6ODE110, 8ODE110 were studied. The telomerized ODE-cellulose averaged a 95 % yield at the reaction conditions, where 5 wt % loss was observed which could be attributed to exfoliated unmodified cellulose fragments (**Figure 2-2**). This is similar to the observation that pretreatment of miscanthus by BDS[34] is accompanied by a loss of glucan up to 10 wt %. Upon

blending (30k rpm, 30 min), aqueous precipitates (aq. ppt) that contained hydrophobic ODE-NCs were collected for further analyses. The aqueous supernatants (aq. sn) were observed to contain 2-6 % CNFs and CNF bundles, similar to the 4.8 % CNFs from 60 min blending[2]. The thickness and length of these CNFs slightly decreased with higher BDS ratios and temperatures, i.e., from 1.7 to 4.2 nm and 0.8 to 4.3 μm, respectively **(Figure 2-3)**. The quantities and dimensions of these hydrophilic CNFs as minor by-products were consistent with shear force processing.

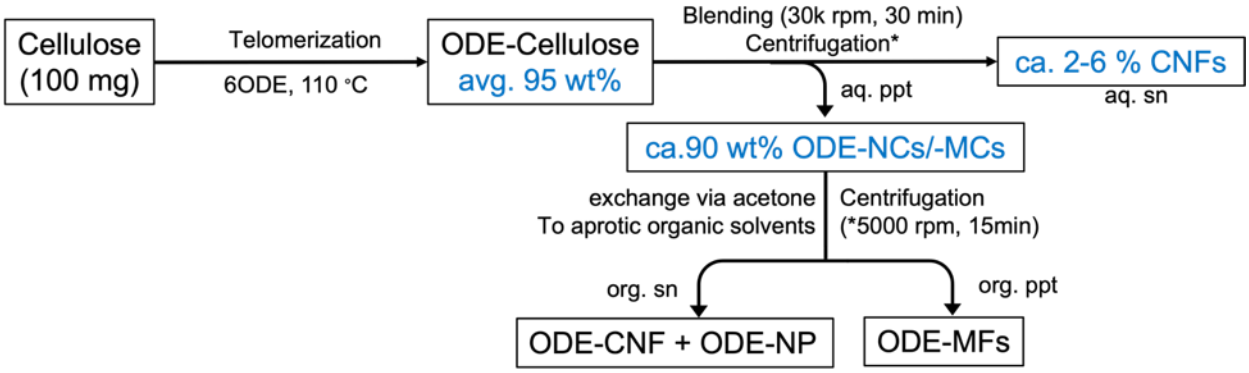

Figure 2-2. Telomerization reaction and process flow chart and products.

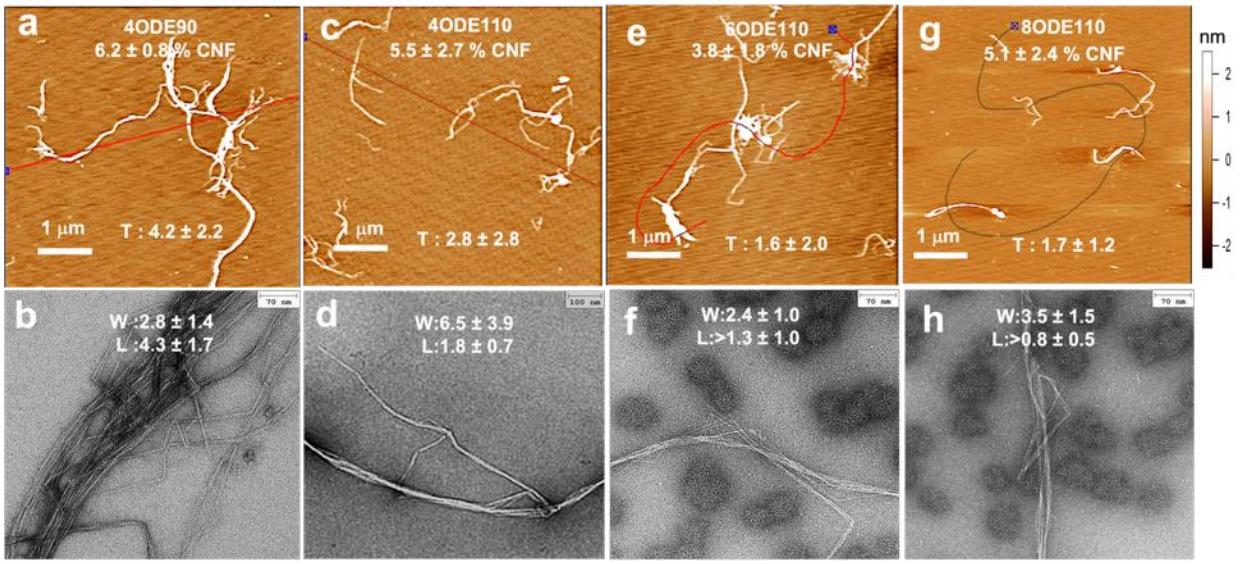

Figure 2-3. AFM (a, c, e, g) and TEM (b, d, f, h, all stained with 2% uranyl acetate) of CNFs in the aqueous supernatant (aq. sn) from telomerization (4, 6, and 8 ODE/AGU, 90 or 110 °C) and blending (30 k rpm, 30 min). Wt % CNFs, and their thicknesses (T, nm), widths (W, nm), and lengths (L, μm) were determined from 3, 100, 30 and 13 measurements, respectively.

The CrI of ODE-cellulose in the aq. ppt was 53.5, 57.5, 65.5 and 50.0 % respectively for 4ODE90, 4ODE110, 6ODE110, 8ODE110 (**Figure 2-4a**), retaining most of the crystallinity of the original cellulose (CrI = 60.3 %) except for the more crystalline 6ODE110. The never-dried aq. ppt from 6ODE110 was solvent exchanged with acetone, and then with DMSO, DMF, THF, and $CHCl_3$ to create homogenous opaque dispersions in polar DMSO and DMF but flocculated suspensions in the less polar THF and $CHCl_3$, immediately after 3 seconds of vortexing (**Figure 2-4b**). All were sedimented within 1 h, leaving a reasonably transparent top phase except for $CHCl_3$, which remained partly flocculated due to its close density (ρ = 1.489 g/cm^3) to cellulose. All phase-separated suspensions could be homogenously resuspended by brief hand shaking. The more homogenous DMSO and DMF dispersions of defibrillated ODE-cellulose demonstrated their solvent affinities through polar and H-bonding interactions, indicating the presence of remaining surface hydroxyls.

The ODE-NCs in organic supernatant varied from 7.0 % to 41.7 % of aq. ppt, increasing with higher BDS and temperatures, except for negligible differences among those in DMF and those from 8ODE110 in solvents other than DMSO **(Figure 2-4c**). The highest quantities of ODE-NCs from 6ODE110 in the less polar THF and $CHCl_3$, 27.3 % and 30.3 %, respectively, were ten times that of the control, indicating their highest hydrophobicity. For 4ODE90 and 4ODE110, their significantly lower dispersibility in the least polar $CHCl_3$ (7.0 % and 11%, respectively) indicated less effective telomerization at the lowest BDS mole ratio of 4ODE. While ODE-NC yields in DMF appeared unaffected by reaction conditions, yields in the more polar DMSO increased with increasing BDS and temperatures, resulting in the highest 40.1 and 41.7 % yields of ODE-NCs for 6ODE110 and 8ODE110, respectively. This may be due to a DMSO's structural characteristic which contains polar and non-polar functional groups to be able to associate with ODE-NCs with

the different extent of functionality. This suggests ODE-NCs in DMSO include all NCs, i.e., not only telomerized but also less-modified and even unmodified. As expected, the quantity of BDS consumed also increased with temperature and correlated with increasing ODE-NCs dispersed in organic solvents (**Figure 2-4c**). The proportionally higher BDS consumption from 6ODE110 to 8ODE110 along with obviously lowered ODE-NCs in THF and $CHCl_3$ will be discussed further in the AFM section. Clearly, telomerization of 1,3-BD from BDS was optimal at 6ODE110 to generate ODE-NCs of greatest dispersibility in organic solvents. Further characterization was thus focused on ODE-NCs from 6ODE110.

The organic precipitates consisted of microfibrils (**Figure 2-4d**) in 2.9-9.4 μm widths and 157-301 μm lengths (**Table 2-3**), all showing birefringence (**Figure 2-4e**), representing less telomerized or un-modified cellulose. The aq. ppt from 6ODE110 could also be dispersed in m-cresol and toluene supernatant to give 33.3 ± 4.7 % and 29.1 ± 13.0 % ODE-NCs (**Figure 2-4f, g**), respectively, mostly as particulates or branched fibrils (**Figure 2-4f, g**), but the aq. ppt gives < 10 % dispersibility in acetone and ethyl acetate supernatants (**Table 2-3**). Among these, *m*-cresol and toluene precipitates gelled (**Figures 2-4h, i**), which may be attributed to H-bonding between hydroxyls of ODE-NCs and *m*-cresol. Both gels exhibited shear thinning behaviors upon shaking, indicating their potential processibility, including coatings or inks for 3-D printing.

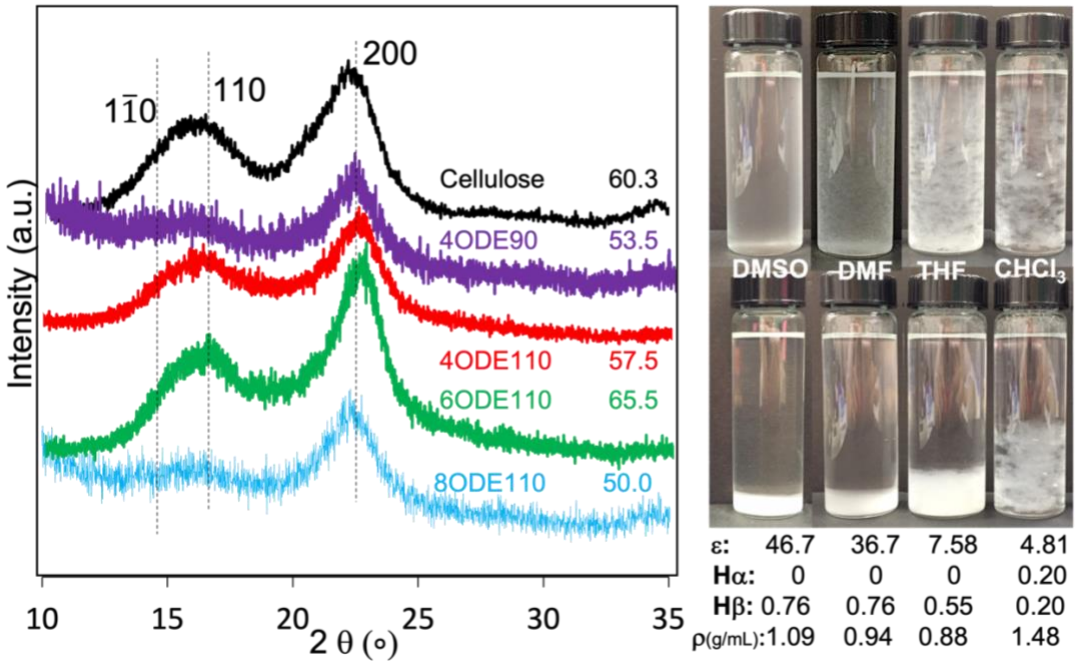

Figure 2-4. ODE-cellulose and ODE-NCs from 6ODE110: (a) XRD of ODE-cellulose; (b) organic dispersions (0.1 wt %) of the aq. ppt, immediately after vertexing (top) and after 1 h (bottom);

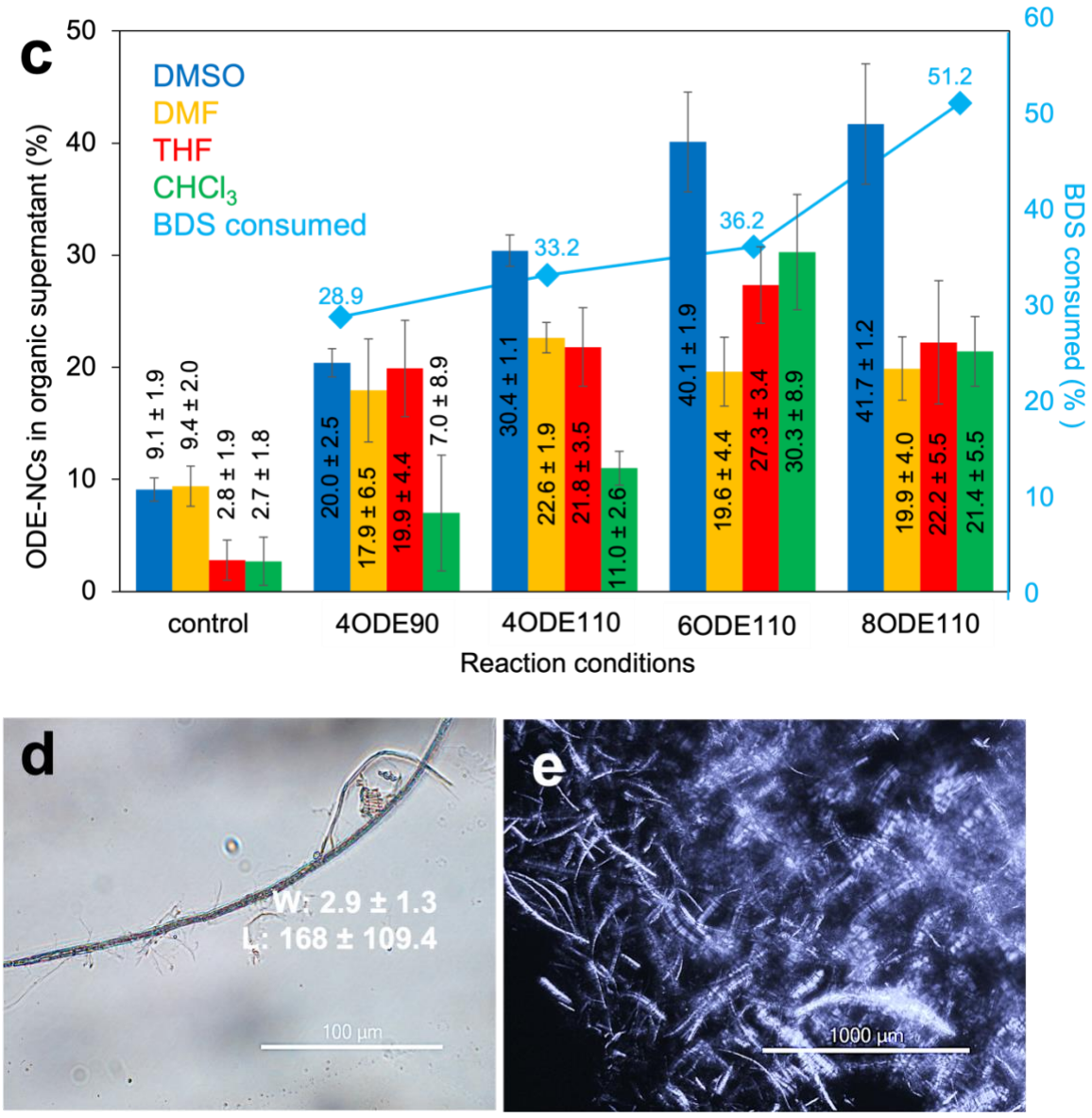

Figure 2-4, continued. (c) ODE-NCs in organic supernatant and consumption of BDS. Optical microscope images of representative microfibrils in DMSO (6ODE110) precipitate (1.5 k rpm,15 min); (d) transmission; (e) under cross-polarized light. Width (W, µm), and length (L, µm), were determined from 50-100 measurements;

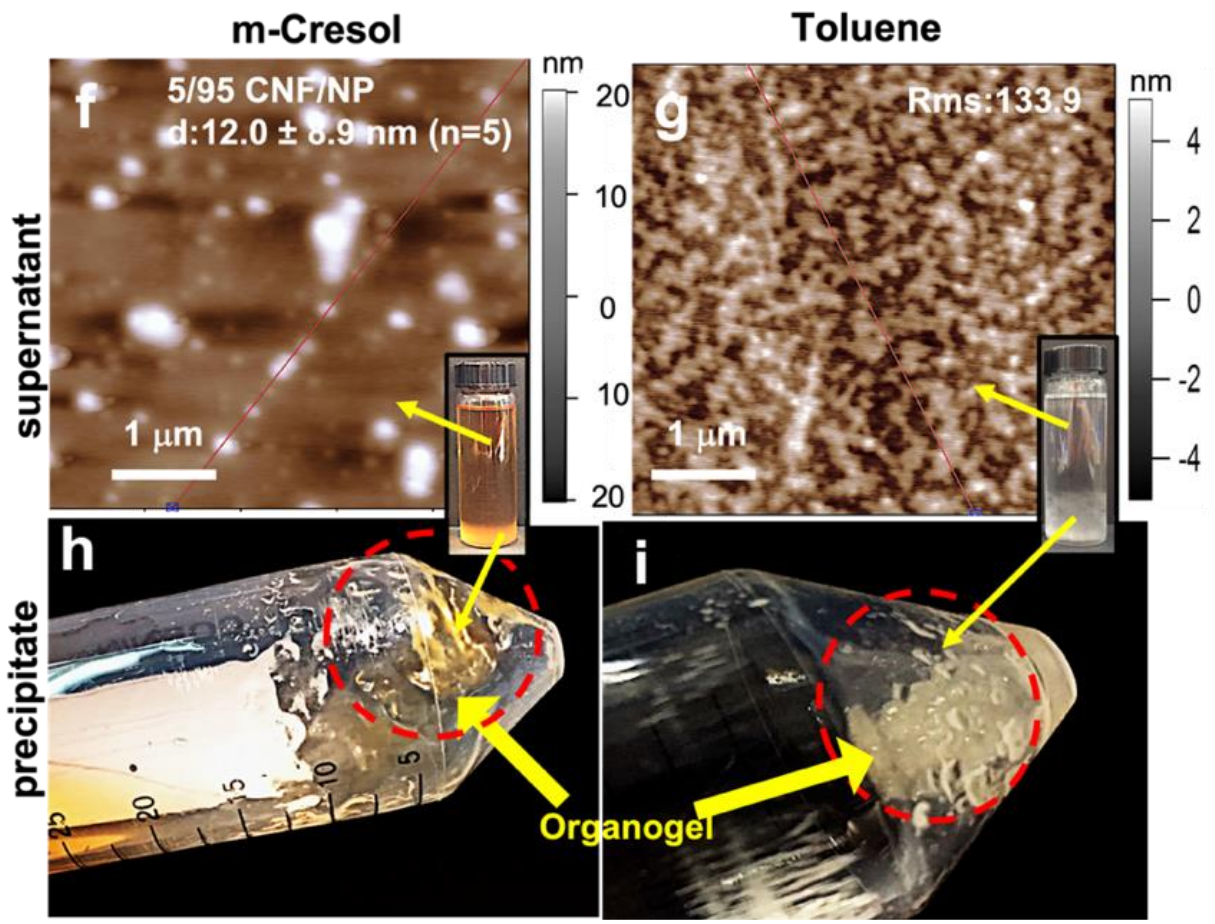

Figure 2-4, continued. The organic supernatant and gelled precipitate from 6ODE110 in m-cresol and toluene after centrifugation (1.5 k rpm, 15 min): AFM of supernatant (0.0005 w/v % on HOPG) in (f) m-cresol and (g) toluene. Photos of gelled precipitate in (h) m-cresol and (i) toluene. The insets are respective dispersion before centrifugation and resting for one hour after vertexing for 3 sec;

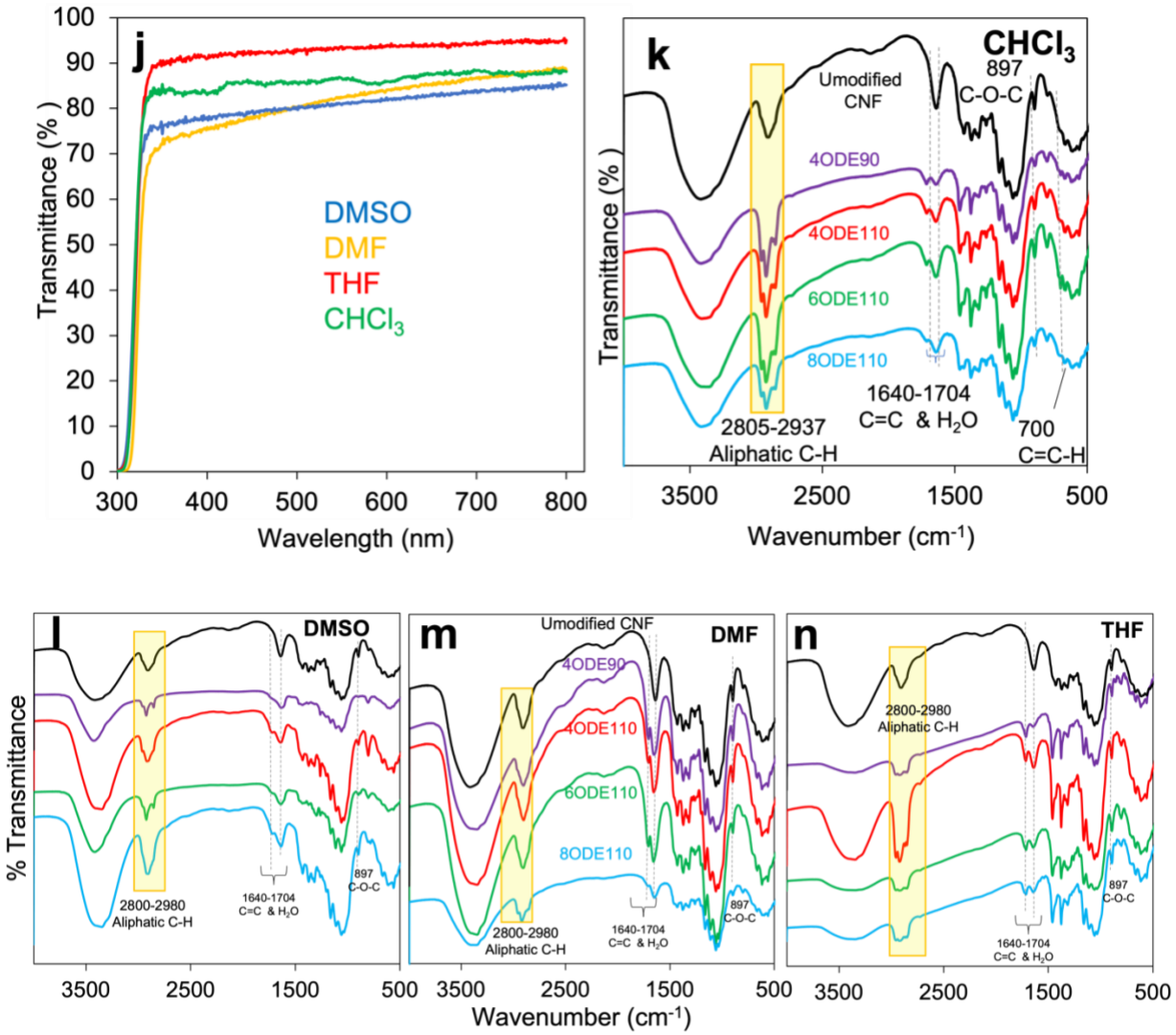

Figure 2-4, continued (j) UV-vis transmittance of 0.01 w/v % organic supernatants; FTIR ODE-NCs in (k) $CHCl_3$, (l) DMSO, (m) DMF, (n) THF.

Table 2-3. The mass and dimensions of ODE-CNFs and ODE-microfibrils in organic supernatant and precipitate from 6ODE110 (0.1 w/v %). Thicknesses and ratios of CNF/NP in ODE-NCs were based on AFM images. Widths and lengths of ODE-microfibrils were from optical microscopic images.

Solvents Used in Solvent Exchange	ODE-NCs in Supernatant			Microfibrils in Precipitate		
	Mass (wt %)	CNF Thickness (nm) n=20-50	CNF/NP (% area)	Mass (wt %)	Width (μm) n=50-100	Length (μm) n=50-100
DMSO	40.1 ± 1.0	3.7 ± 5.2	60/40	59.9 ± 1.0	3.7 ± 1.7	223 ± 167
DMF	19.6 ± 6.5	1.8 ± 1.3	30/70	80.4 ± 6.5	4.3 ± 1.7	25± 102
Acetone	<10	n/a	n/a	>90	5.2 ± 3.1	351 ± 185
m-Cresol	33.3 ± 4.7	n/a	5/95	66.7 ± 4.7	9.4 ± 4.4	157 ± 101
THF	27.3 ± 3.4	6.3 ± 2.4	60/40	72.7 ± 3.4	3.3 ± 1.6	301 ± 149
Ethyl acetate	<10	n/a	n/a	>90	4.7 ± 2.0	240± 105
$CHCl_3$	30.3 ± 8.9	4.4 ± 2.2	70/30	69.7 ± 8.9	4.1 ± 1.6	235± 116
Toluene	28.1 ± 13.0	n/a	n/a	71.9 ± 13.0	4.2 ± 1.4	235± 112

The THF and $CHCl_3$ supernatants (0.01 w/v %) from 6ODE110 showed higher UV-vis transmittance than the DMSO and DMF supernatants, indicating that those ODE-NCs in THF and $CHCl_3$ are smaller and/or more compatible with these less polar solvents, thus more hydrophobic (**Figure 2-4j**). FTIR of all ODE-NCs exhibited equally sharp cellulose peaks at 897 cm^{-1}, at 1640 cm^{-1}, 2898 cm^{-1} and 3394 cm^{-1}, representing the β-glycosidic C_1-O-C_4 deformation, residual water, and aliphatic C-H and OH groups (**Figure 2-4 l-n**). ODE-NCs dried from $CHCl_3$ supernatant contained the most distinguishable ODE characteristics regardless of reaction conditions. The methylene and allylic C-H stretching at 2800-2980 cm^{-1}, C=C stretching at 1640-1704 cm^{-1} and C=C-H bending at 700 cm^{-1} were more resolved and intense (**Figure 2-4k**), indicating higher hydrophobic ODE contents for those ODEs dispersed in $CHCl_3$ than in other solvents, and also indicating their higher hydrophobicity.

2.4.2 Morphologies of ODE-nanocelluloses

ODE-NCs in organic supernatants from 6ODE110 were further observed by AFM and TEM. ODE-NCs in THF or $CHCl_3$ appeared as individually separated straight fibrils on HOPG or carbon (**Figure 2-5c-e, g, h**), clear evidence of their uniformly hydrophobic surfaces and strong affinity to the hydrophobic surfaces. This contrasts with their appearance as sub-micron particulates on hydrophilic mica (**Figure 2-5a-b)** and the unmodified control nanoparticulates (NPs) in $CHCl_3$ on HOPG (**Figure 2-5f**). AFM images further revealed that the majority of ODE-NCs in THF and $CHCl_3$ supernatants were mostly CNFs, i.e., 60/40 CNF/NP with 6.3 ± 2.4 nm thickness for CNFs in THF (**Figure 2-5c**), 70/30 CNF/NP with 4.4 ± 2.2 nm thickness, 4.1 ± 1.8 nm width, and 1.7 ± 0.4 μm length for CNFs in $CHCl_3$ (**Figure 2-5d, e**). The higher proportion of smaller ODE-CNFs in $CHCl_3$ indicate their higher hydrophobicity in $CHCl_3$ than in THF. ODE-NCs from 8ODE110 in $CHCl_3$ were also mostly fibrillar (60/40 CNF/NP), with a similar 4.2 nm thickness as those from 6ODE110 but a much shorter length at 0.8 μm (**Figure 2-5g, h**). The shorter and the lower yield of nanocellulose from 8ODE110 than from 6ODE110, in combination with the highest BDS consumption to form 8ODE110 (**Figure 2-4c**), point to acid hydrolysis of ODE-CNFs by sulfurous acid which is formed by a reaction of SO_2 from BDS with residual water and atmospheric oxygen as indicated in hydrolysis of xylan during pretreatment of sugarcane bagasse[33] and miscanthus[34] with BDS and water.

While ODE-NCs in DMSO had the same 60/40 CNF/NP ratio (**Figure 2-5k)** as those in THF, some were nearly four times thicker and appeared as bundles (**Figure 2-5k inset**), suggesting they were less telomerized and/or less hydrophobic. Significantly fewer CNFs (30/70 CNF/NP) in DMF (**Figure 2-5n)** with mainly NPs and aggregates (>90 %) from 4ODE90 and 4ODE110 by the AFM images on HOPG indicates less hydrophobic surface chemistry of ODE-NCs, thus more

unreacted or less functionalized OHs (**Figure 2-5 i, j, l, m**). These morphological observations further confirm that the 6ODE110 telomerization conditions defined earlier produce the most hydrophobic ODE-NCs in the highest quantities. The proportions of CNFs and NPs in ODE-NCs depend on the organic liquids, i.e., 70 % CNFs in $CHCl_3$ and 60 % CNFs in THF and DMSO. The CNFs in $CHCl_3$ were the most hydrophobic, the thinnest (4.4 ± 2.2 nm, 4.1 ± 1.8 nm wide) and the longest (1.7 ± 0.4 μm), with the highest aspect ratio of ca. 400.

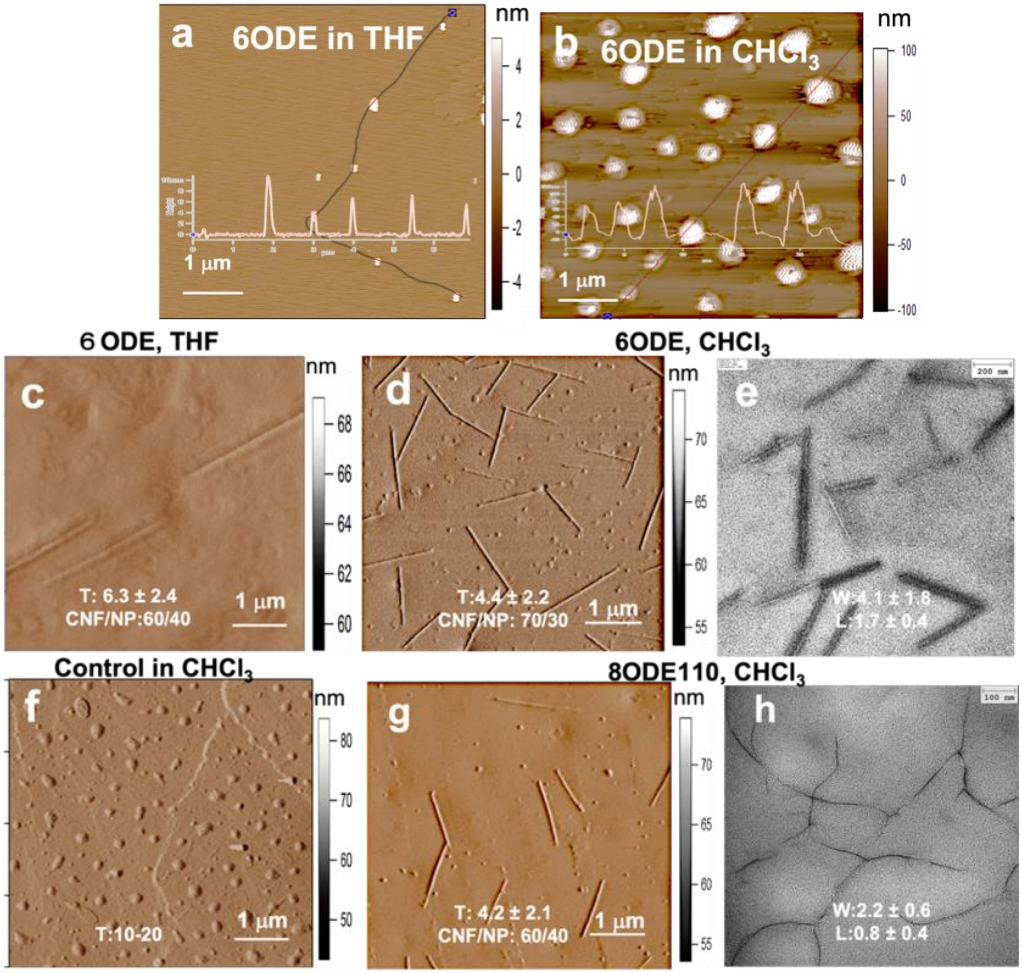

Figure 2-5. AFM (a and b on mica, c, d, f and g on HOPG) and TEM (e and h on carbon) images of ODE-CNFs from: (a-e) 6ODE110; (f) unmodified CNF control; (g and h) 8ODE110. At 0.0005 w/v % in THF or $CHCl_3$ supernatants. The specimen for TEM was negatively stained with (e) 2 % uranyl acetate or (h) phosphotungstic acid. Measurements for thicknesses, widths and lengths were based on n=100 for thickness (T, nm), and n=30 for width (W, nm) and length (L, μm). Area percent nanofibrils and nanoparticles (CNF/NP) were indicated;

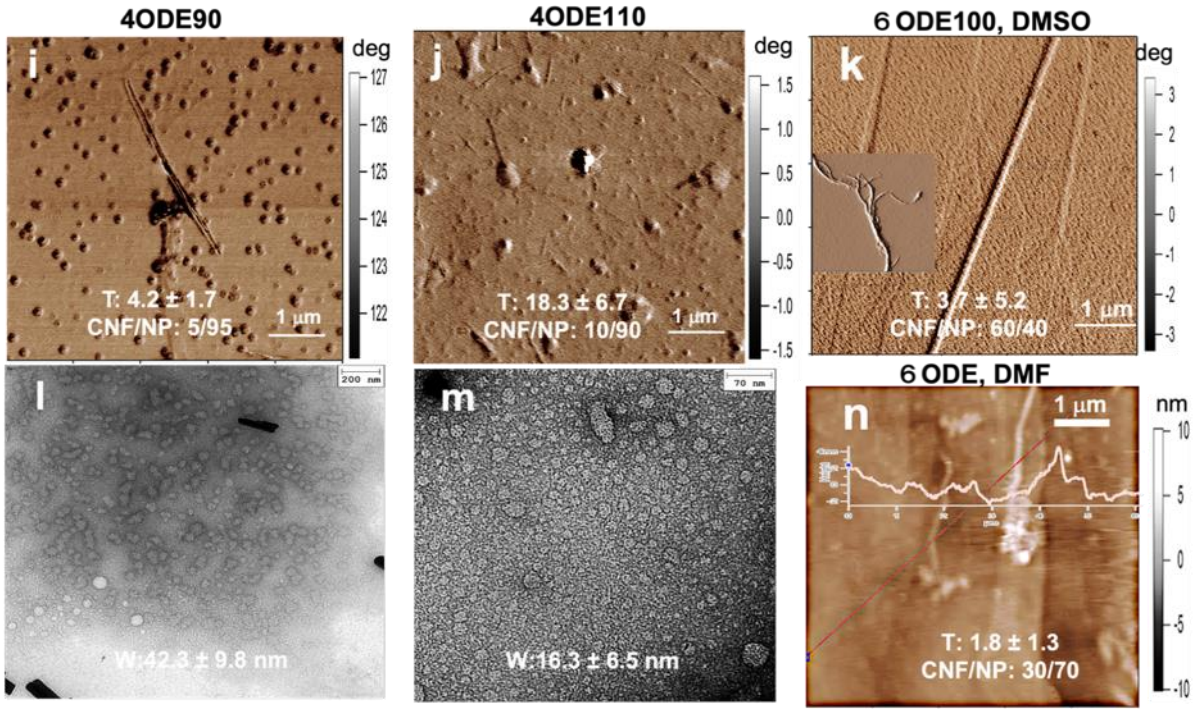

Figure 2-5, continued. AFM (i-k and n) and TEM (l, m) images of ODE-NCs stained with 2% phosphotangstic acid from (i, l) 4ODE90 and (j, m) 4ODE110 dispersed in $CHCl_3$; (k) 6ODE110 dispersed in DMSO, and the inset shows CNF bundles; (n) 6ODE110 dispersed in DMF. Measurements for thicknesses, widths and lengths were based on n=100 for thickness (T, nm), and n=30 for width (W, nm) and length (L, μm). Area percent nanofibrils and nanoparticles (CNF/NP) were indicated.

2.4.3 Surface characterization by the solution state ^{1}H NMR

In-situ hydrolysis of ODE-cellulose was done by simply adding water to generate sulfurous acid from the SO_2 precursor followed by blending to produce thinner *h*ODE-CNFs (**Figure 2-6a, b**) to improve spectral sensitivity as we previously demonstrated[59]. Solution state ^{1}H NMR of *h*ODE-CNFs from 6ODE110 showed cellulosic protons (**Figure 2-6c**) as did those from both 4ODE110 and 8 ODE110 (**Figure 2-6d, e**), but not 4ODE90, which had poor peak resolution (not shown) attributed to thick and branched fibrillar structures even after hydrolysis. The most distinguishable signals for ODE-groups were observed in that of *h*ODE-CNFs from 6ODE110, indicating higher ODE substitution of OH groups. The downfield peak at δ 4.27 is assigned to the

cellulosic anomeric proton (H1) that is close to the chemical shift at δ 4.45 for TEMPO-oxidized CNFs.[59] The furthest upfield triplet at δ 3.08 ppm coincides with the chemical shift of H2 at δ 3.05 ppm for cellulose dissolved in DMA-*d*9/LiCl.[62] Peaks present at δ 3.28, δ 3.40, δ 3.53 ppm, and δ 3.19, δ 3.93 ppm are assigned for H3, H4, H5 and each of the diastereotopic H6 protons, respectively, which are in close proximity to the chemical shifts of H3, H4, H5 at δ 3.52, δ 3.66, δ 3.75 ppm, and those of H6 at δ 4.04 and δ 3.30 ppm for TEMPO-CNFs. The upfield multiplets at δ 1.47, δ 1.95, and δ 2.07 ppm are assigned to methylene protons, and peaks at δ 6.07 (1H), δ 5.61 (2H), δ 5.29 (1H) ppm belong to olefinic protons for ODE-CNFs. The integration values of all 13 ODE protons were averaged and normalized to the reference anomeric proton at δ 4.27 to obtain the degree of substitution (DS) of ODE/AGU because only surface nuclei could be detected by ^{1}H NMR of nanocellulose.[51] In comparison, the spectrum of as-is CNFs (**Figure 2-6c inset**) exhibited considerably lower peak intensity of alkene protons in ODE groups evidenced by the integration values.

$$\text{ODE/AGU} = \frac{(a+b+c+\ldots\ldots\ldots+m)/13}{H1} \qquad \text{Eqn. 3}$$

^{13}C NMR is as follows (800 MHz, d_6-DMSO, 25 °C, tetramethylsilane (TMS)) in **Table 2-4** (**Figure 2-6f**).

Table 2-4. Chemical shift of carbons in ODE-CNFs.

ppm	29.2	30.2	31.1	63.7	73.0	74.4	75.7	79.4	83.3	102.2	129.2	133.2	134.8	138.0
C#	C11	C12	C10	C6	C5	C2	C3	C4	C7	C1	C14	C13	C9	C8

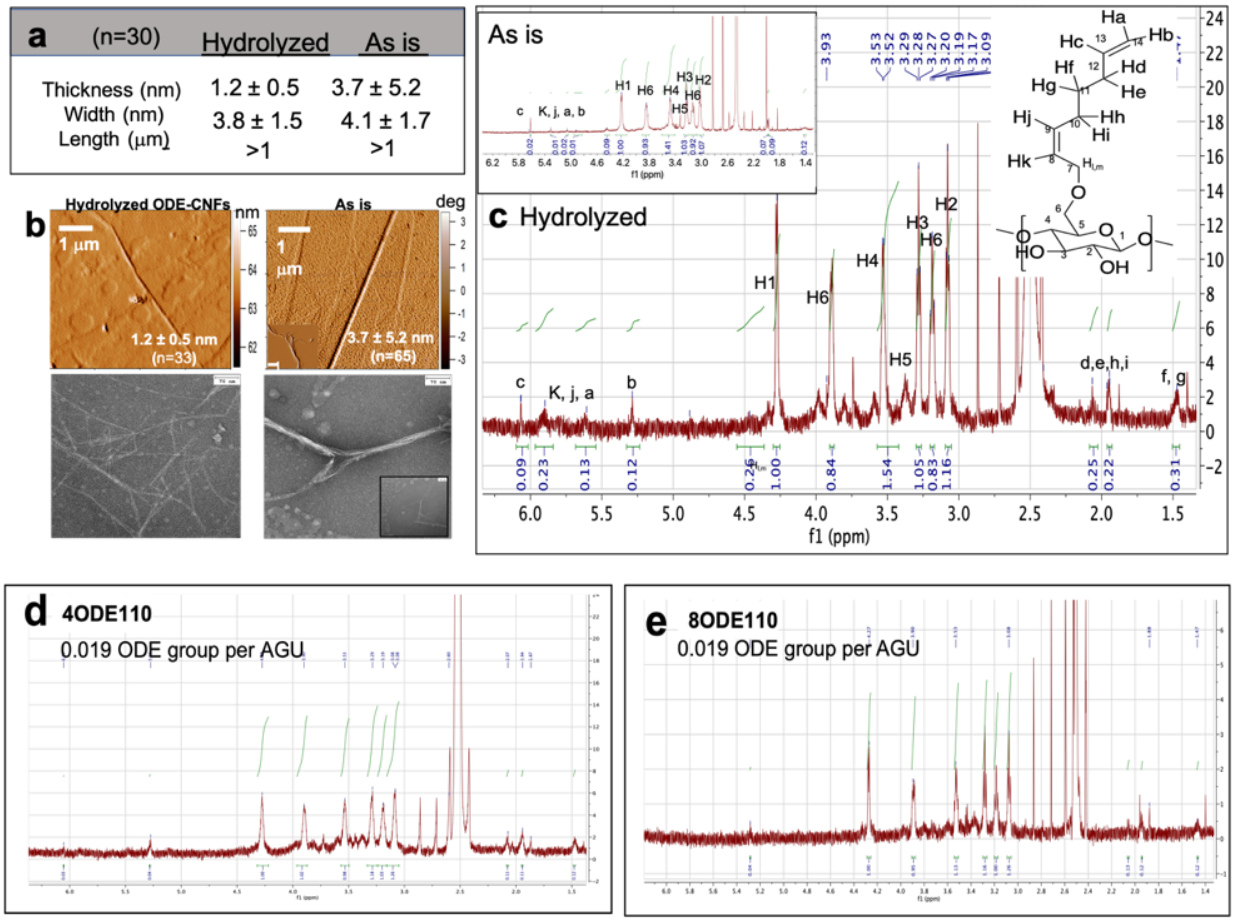

Figure 2-6. Surface characterization of *h*ODE-CNFs (from 6ODE110): (a) AFM of *h*ODE-CNFs in d_6-DMSO supernatant on HOPG (0.0005 %); (b) thickness distribution. ^{1}H NMR spectra for *h*ODE-NCs from (c) 6ODE110, inset spectrum is for as is ODE-NCs; (d) 4ODE110; (e) 4ODE90;

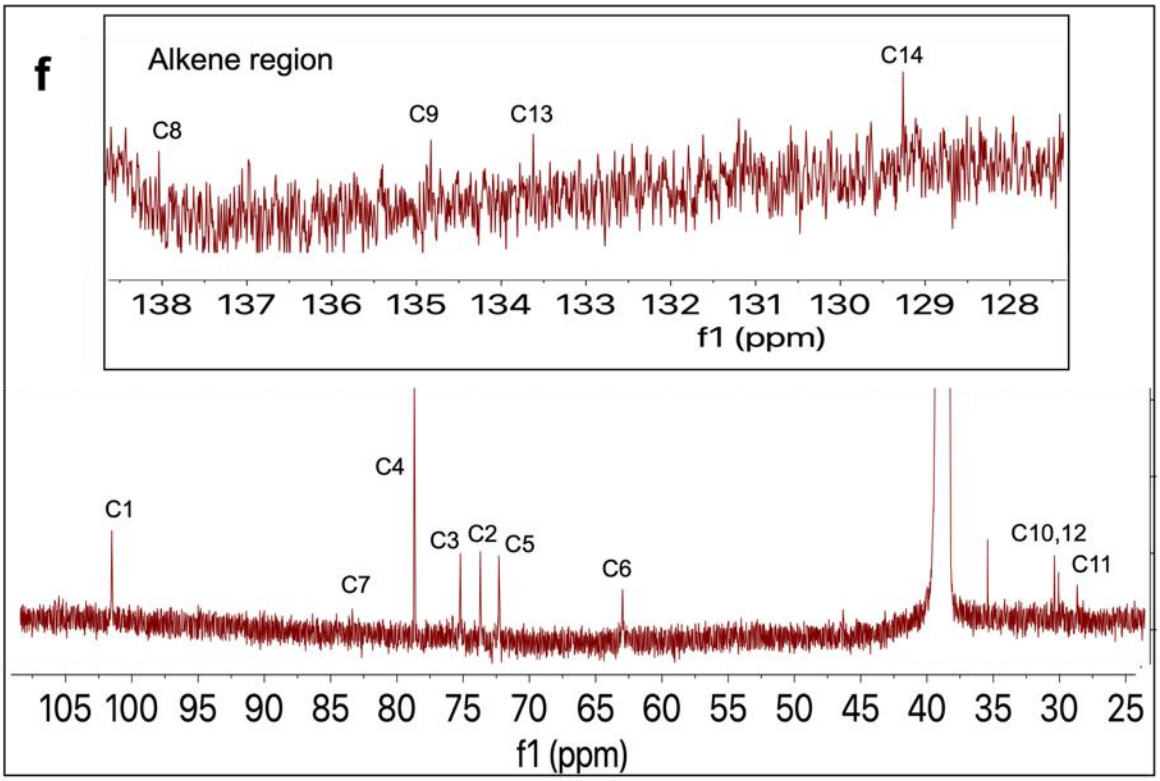

Figure 2-6, continued. (f) ^{13}C spectrum of *h*ODE-NCs from 6ODE110 in d_6-DMSO.

2.4.4 Surface ODE groups based on crystalline structure

To estimate the total number of OH groups on CNF surfaces, a simplified nanofibril cross-section model (**Figure 6a**) that depicts the hydrophobic (200) crystalline planes as the width (W) and the hydrophilic surfaces with hydroxyls and ODE groups as the thickness (T) along the respective b and a axes of the unit cell (**Figure 2-7a, b)** was created based on thorough observations and analyses of individual ODE-CNFs by AFM and TEM. Our cross-sectional shape is based on the morphology of ODE-nanofibrils which appeared completely straight on hydrophobic HOPG (**Figures 2-5d**) and carbon grids (**Figures 2-5e**). The absence of any kinks or bends means the surfaces of fibrils attached to HOPG is uniformly compatible with the HOPG surface, thus they are most likely the (200) planes. Bending or rotating of ODE-CNFs should be observed when the ununiformly functionalized $(1\bar{1}0)$ (110) planes are attached to HOPG.

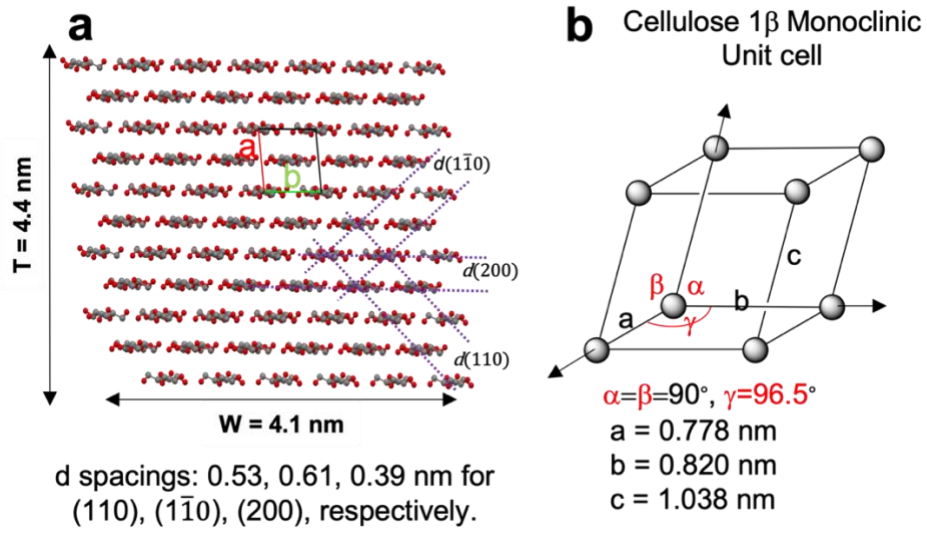

Figure 2-7. Hydrophobic ODE-CNF cross-sectional models (a) representing (200) plane on hydrophobic HOPG or carbon surfaces with d-spacings noted and (b) cellulose 1β monoclinic unit cell with lattice dimensions noted.

In this model, surface OH groups are the surface AGU (N_s) over total AGU (N_t) multiplied by $\frac{3}{2}$ since there are 3 OHs exposed on either each surface cellobiose or on 2 AGUs (Eqn. 4). N_s are those on two sides (2x) along the thickness (T) spaced by $d(200)$ plus one (Eqn. 5). The total number of AGUs are simply the product of multiplying those in the T and W directions (Eqn. 6). Thus, the percent of ODE over total surface OHs is expressed by Eqn. 7 in which ODE/AGU derived from ^{1}H NMR integration calculation (Eqn. 3) is divided by total surface OHs from Eqn. 4. This operation led to 30.0 % conversion of CNF surface OHs to ODE-groups, equivalent to 0.74 mmol ODE/g-cell.

$$\text{surface OH} = \frac{3}{2} \cdot \frac{Ns}{Nt} = \frac{3b}{W+b} \qquad \text{Eqn. 4}$$

$$\text{where } N_s = 2 \cdot \{\frac{T}{d(200)} + 1\} \qquad \text{Eqn. 5}$$

$$N_t = \{\frac{T}{d(200)} + 1\} \cdot \{\frac{W}{b} + 1\} \qquad \text{Eqn. 6}$$

$$\text{ODE / surface OH} = \frac{(\text{eq. 2})}{(\text{eq. 3})} \qquad \text{Eqn. 7}$$

2.4.5 Physical properties of 6ODE110 ODE-CNFs from $CHCl_3$

ODE-CNFs exhibited the distinctive cellulose characteristic Iβ peaks at 14.7°, 16.8° and 22.7° corresponding to the $(1\,\bar{1}\,0)$ (110) and (200) monoclinic cellulose Iβ lattice planes, respectively (**Figure 2-8a**). For ODE-CNFs, the CrI of 52.3 % (calculated from their XRD patterns) and the crystallite dimension of 2.67 nm (calculated from the Scherrer equation) showed substantial retention of the crystalline core of original pure rice straw cellulose (CrI = 60.2 %, D_{hkl} = 3.46 nm). The CrI and the crystallite dimension of unmodified CNFs (those produced by only mechanical blending) increased to 65.5 % and 4.05 nm respectively (**Figure 2-8b**), indicating removal of amorphous regions. The slightly lower crystallinity and the smaller crystallite dimension of ODE-CNFs indicate that hydroxyl groups in the inter-fibrillar regions involved in telomerization facilitate their dispersion in organic liquids.

As shown in **Figure 2-8c**, ODE-CNFs have a negligible moisture absorption of 0.8 % (as measured by TGA), compared to 4.9 % for unmodified CNFs and 6.3 % for the original cellulose, giving clear evidence of the surface OH to ODE conversion. ODE-CNFs also decompose differently from unmodified CNFs and the original cellulose, losing some mass over the broad temperature range of 160-306°, then showing a greater mass loss in the narrow 325-335 °C range. The first loss is attributed to the decomposition of surface ODE which may be akin to structurally similar fatty acid alkene degradation.[63,64] The second mass loss at Tmax of 332 °C is slightly higher than for unmodified CNFs (325 °C). Both losses are lower than the original cellulose due to their nanoscale dimensions. Most significantly, Tmax of ODE-CNFs at 332 °C is 67 °C higher than the 265 °C Tmax of TEMPO-CNF[2]. The significantly, the higher thermal stability of ODE-CNFs reflects the decoupled surface-versus-core decomposition and is a clear advantage over TEMPO-

CNFs that decompose by decarboxylation of surface carboxylates followed by concurrent solid-to-gas breakdown of the cellulose core[2].

FTIR-ATR of the dried ODE-CNF surface (**Figure 2-8d**) showed =C-H stretch at 3023 cm^{-1}, methylene groups at 2800-2980 cm^{-1} and C=C at 1640-1704 cm^{-1}(**Figure 2-4k)**.

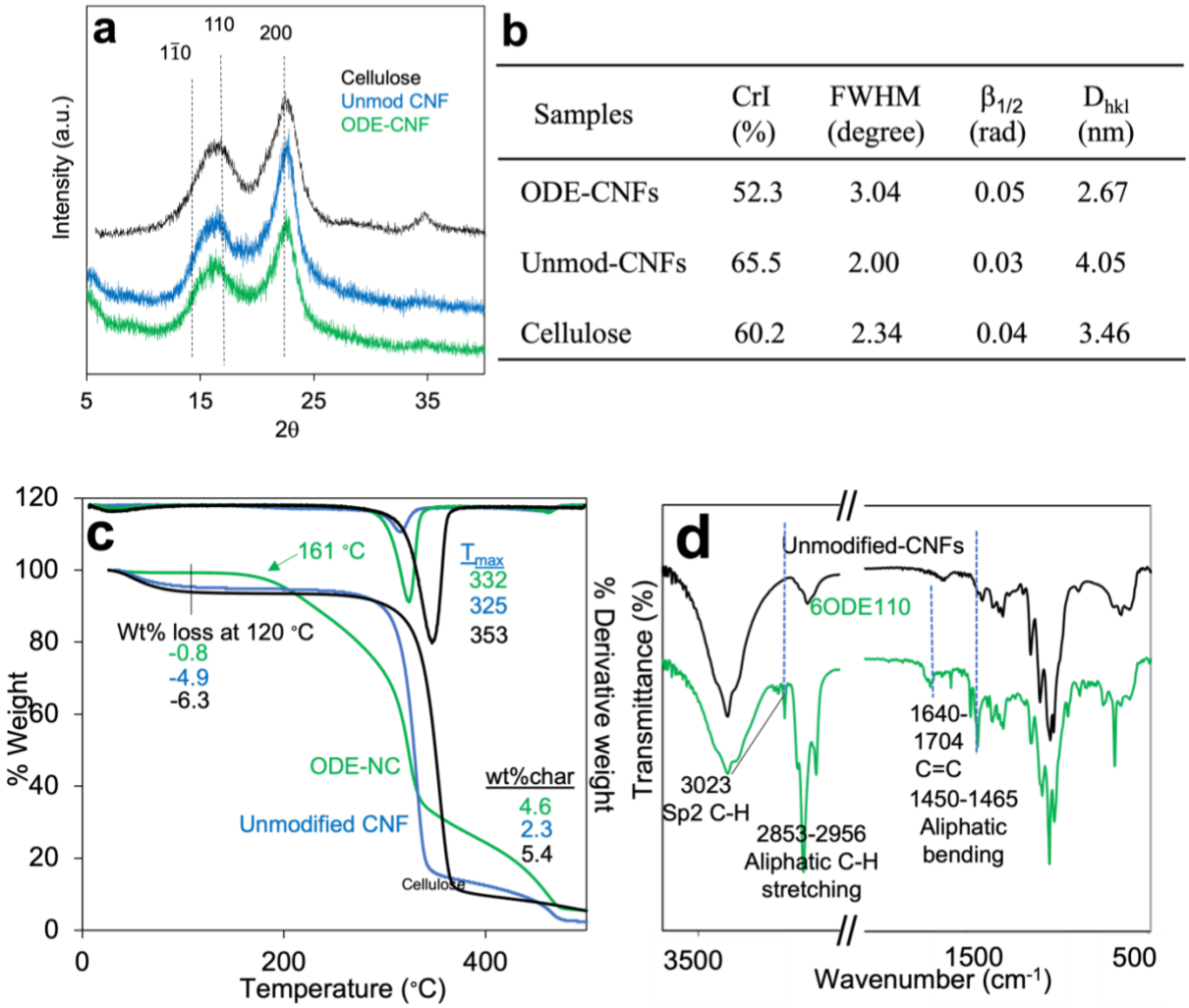

Samples	CrI (%)	FWHM (degree)	$\beta_{1/2}$ (rad)	D_{hkl} (nm)
ODE-CNFs	52.3	3.04	0.05	2.67
Unmod-CNFs	65.5	2.00	0.03	4.05
Cellulose	60.2	2.34	0.04	3.46

Figure 2-8. Characteristics of air-dried ODE-CNFs (6ODE110) from $CHCl_3$: (a) XRD; percent crystallinity; (b) the respective crystallite size based on the Scherrer equation; (c) TGA and derivative-TGA; (d) FTIR-ATR.

The ability of ODE-CNFs in THF and $CHCl_3$ supernatants to spread, coat, and change the surface wettability of hydrophilic solid and porous surfaces was investigated. Freshly cleaved mica

was smooth (root mean square (RMS): *ca.*1-2 nm), displaying 0° WCA, and remained similarly wettable when 10 μL of either THF or $CHCl_3$ was spread and dried (**Figure 2-9a**). With 0.5 w/v % ODE-CNFs, 10 μL of either THF and $CHCl_3$ were spread and dried to similar-sized area to ca. 0.1 mg/cm^2 (**Table 2-5**), rendering surfaces hydrophobic with WCAs of 61 ± 2° and 82 ± 7°, respectively (**Figure 2-9b, c, insets**). However, optical microscopy showed numerous areas of exposed mica surfaces which is demonstrated by the surface roughness measurements (root mean square, RMS) of 108 nm (THF) and 93 nm ($CHCl_3$) by AFM in comparison to smooth mica surface (2 nm). This indicates insufficient coverage by ODE-CNFs at 0.5 %. Doubling ODE-CNF concentration in THF and $CHCl_3$ to 1 % not only further enhanced the hydrophobicity to WCA of 78 ± 4° (THF) and 102 ± 1° ($CHCl_3$), but also reduced roughness to 78 and 59 nm, respectively (**Figure 2-9 b, c, insets**), indicating more uniform coverage. The reduced area coverage of CNFs on mica dried from 1.0 % THF and $CHCl_3$ dispersions (**Figure 2-9 b, c, insets**) led to higher area densities of ca. 0.36 mg/cm^2 (THF) and 0.50 mg/cm^2 ($CHCl_3$) which reflect the increased liquid surface tensions due to the presence of hydrophobic ODE-CNFs (**Table 2-5**). The smaller area covered by ODE-CNFs in $CHCl_3$ than THF is also consistent with the more hydrophobic nature of those in $CHCl_3$ as observed earlier. The fact that 2 % ODE-CNFs in either solvent did not induce further hydrophobicity (**Figure 2-9d**) suggests that 1 % ODE-CNFs is an effective concentration to cover and convert the hydrophilic mica surface to hydrophobic. All sessile drops stabilized in ca. 80 sec on coated mica (**Figure 2-9e**), demonstrating the low energy of ODE-CNF covered surfaces.

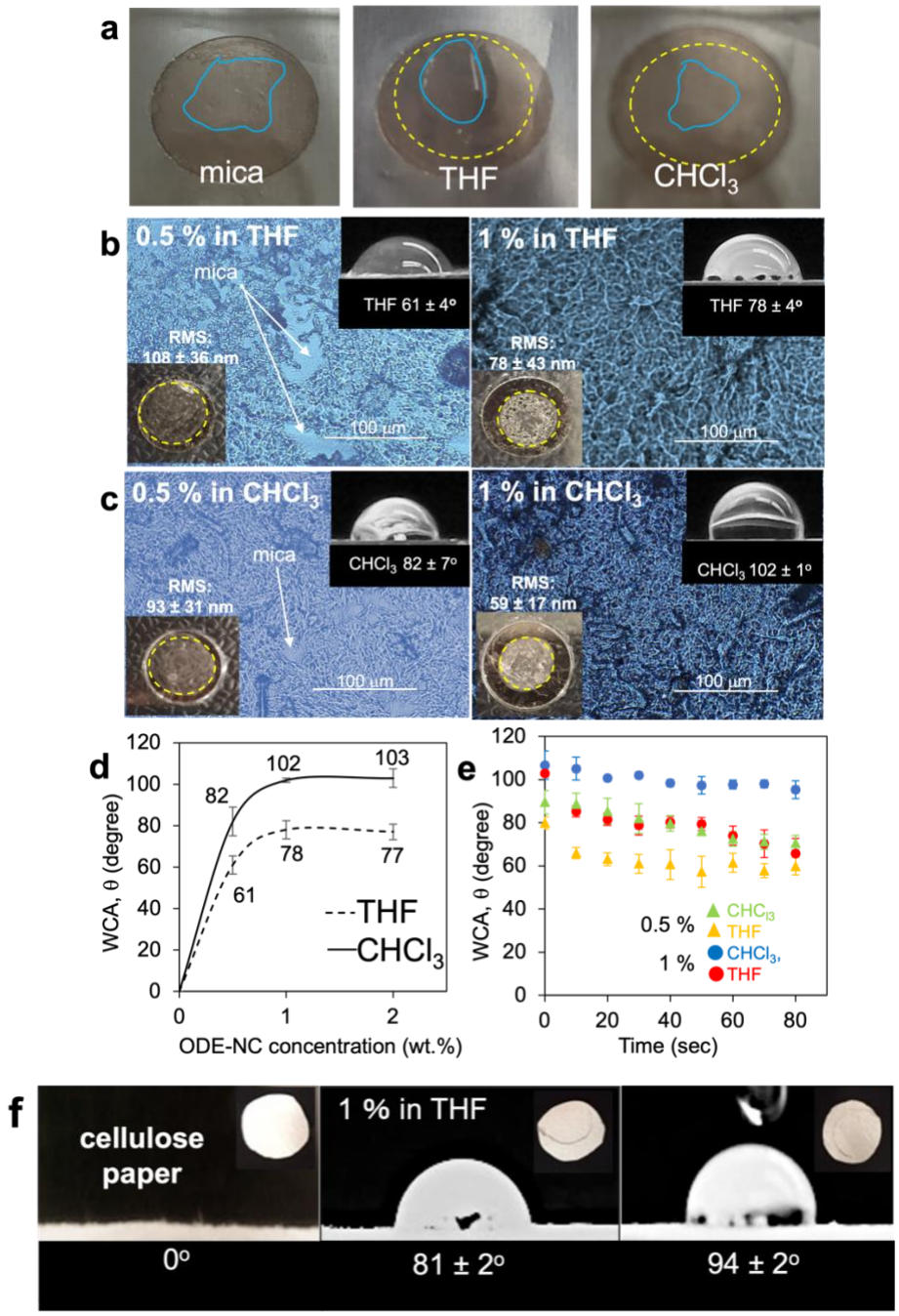

Figure 2-9. Water contact angles (5 µL sessile drop) on hydrophilic mica and cellulose paper as affected by air dried ODE-CNFs (6ODE110) in THF and $CHCl_3$ (10 µL): (a) top views of water spreading (blue lines) on mica as-is and mica covered with 10 µL THF and $CHCl_3$ and dried (yellow dash lines); optical microscopic images of mica coated with 0.5 % (left) and 1 % (right) ODE-CNFs in (b) THF and (c) $CHCl_3$ with their respective WCA (at 30 s); (d) WCA as a function of concentration; (e) WCA as a function of time; (f) WCA (at 2 s) over cellulose paper as-is and covered with 1 % ODE-CNFs in THF and $CHCl_3$ and dried.

Table 2-5. Coating characteristics of ODE-NC from THF and $CHCl_3$ dispersion over mica and cellulose paper.

	Surface tension @20 oC (mN/m)	Density (g/mL)	dielectric Constant, ε	b_p (°C)	ODE-NC coated mica				Cellulose paper
					Conc. (v/w%)	WCA (θ, degree)	Area ODE-NCs (mg/cm²)	Surface roughness (rms, nm)	Weight gain (wt%)
THF	26.4	0.89	7.58	66.0	0.5	61 ± 4	0.10	108 ± 36	1.7 ± 0.1
					1.0	78 ± 4	0.36	78 ± 43	1.9 ± 0.1
$CHCl_3$	27.1	1.49	4.81	61.2	0.5	82 ± 7	0.10	93 ± 31	5.1 ± 0.1
					1.0	102 ± 1	0.50	59 ± 17	5.7 ± 0.1

The hydrophilic cellulose filter paper (qualitative, grade 1) absorbed water instantaneously and a 5 μL water droplet wetted the entire area, whereas those coated with 1 % ODE-CNFs from THF and $CHCl_3$ displayed 81 ± 2° and 94 ± 2° WCA, respectively, for the initial two seconds (**Figure 2-9g**). After 3 seconds, the water droplet spread to cover ca. 60 % of the coated area, suggesting incomplete coverage of ODE-CNFs on the more porous cellulose paper. These preliminary results demonstrated the promise of ODE-NCs as a highly effective hydrophobic surface coating for solid surfaces.

2.5 Conclusions

Hydrophobic nanocelluloses have been successfully prepared by telomerization achieved by using butadiene sulfone (BDS) as both a reagent (1,3-BD) and a reaction medium, followed by mechanical disintegration (30k rpm, 30 min), and organic solvent dispersion. The optimal reaction condition with 6ODE at 100 °C produced 41.6 %, 27.3 %, and 30.3 % 2,7-octadienyl ether (ODE)-CNFs in DMSO, THF, and $CHCl_3$ supernatants with 3.7 nm, 6.3 nm, and 4.4 nm thicknesses, respectively, while retaining significant crystallinity. The presence of ODE-groups in ODE-CNFs was confirmed by FTIR and ATR-FTIR, showing =C-H stretching at 3023 cm^{-1}, methylene groups at 2800-2980 cm^{-1} and C=C at 1640-1704 cm^{-1}. The solution phase ^1H NMR in d_6-DMSO elucidated surface protons of ODE-CNFs at δ1.47, 1.95, 2.07, 3.08, 3.19, 3.28, 3.40, 3.53, 3.93,

4.12, 4.86, 5.29, 5.61, 5.90, and 6.07 ppm. A 30 % conversion of surface OH to ODE was estimated based on the integration value of the average ODE proton normalized to that of anomeric proton on cellulose backbone. ODE-CNFs were nearly as thermally stable as un-modified CNF, and exceedingly superior in thermal stability (Tmax = 332 °C) compared to TEMPO-oxidized CNFs (Tmax = 265 °C). These ODE-CNFs were hydrophobic, absorbing negligible moisture, and their deposition at a mere 1 w/v % on hydrophilic mica and porous cellulose paper (WCA= 0°) instilled impressive hydrophobicity of 102° and 94° WCAs, respectively. These organic solvent compatible, thermally stable, and high aspect ratio ODE-CNFs are the most hydrophobic reported to date. ODE-CNFs generated from this facile process hold great promise toward numerous hydrocarbon and synthetic polymer compatible applications.

2.6 Acknowledgments

Financial support from the California Rice Research Board (Project RU-9), the American Association of Textile Chemists and Colorists, and the Henry A. Jastro Research Award, University of California, Davis are greatly appreciated.

2.7 References

(1) Beck-Candanedo, S.; Roman, M.; Gray, D. G. Effect of Reaction Conditions on the Properties and Behavior of Wood Cellulose Nanocrystal Suspensions. *Biomacromolecules* **2005**, *6* (2), 1048–1054.

(2) Jiang, F.; Hsieh, Y.-L. Chemically and Mechanically Isolated Nanocellulose and Their Self-Assembled Structures. *Carbohydrate Polymers* **2013**, *95* (1), 32–40.

(3) de Nooy, A. E. J.; Besemer, A. C.; van Bekkum, H. Highly Selective Nitroxyl Radical-Mediated Oxidation of Primary Alcohol Groups in Water-Soluble Glucans. *Carbohydrate Research* **1995**, *269* (1), 89–98.

(4) Isogai, A.; Saito, T.; Fukuzumi, H. TEMPO-Oxidized Cellulose Nanofibers. *Nanoscale* **2011**, *3* (1), 71–85.

(5) Saito, T.; Kimura, S.; Nishiyama, Y.; Isogai, A. Cellulose Nanofibers Prepared by TEMPO-Mediated Oxidation of Native Cellulose. *Biomacromolecules* **2007**, *8* (8), 2485–2491.

(6) Kontturi, E.; Meriluoto, A.; Penttilä, P.A.; Baccile, N.; Malho, J.M.; Potthast, A.; Rosenau, T.; Ruokolainen, J.; Serimaa, R.; Laine, J.; Sixta, H. Degradation and crystallization of cellulose in hydrogen chloride vapor for high-yield isolation of cellulose nanocrystals. *Angewandte Chemie International Edition* **2016**, *55*(46), 14455-14458.

(7) Wu, X.; Moon, R. J.; Martini, A. Tensile Strength of Iβ Crystalline Cellulose Predicted by Molecular Dynamics Simulation. *Cellulose* **2014**, *21* (4), 2233–2245.

(8) Iwamoto, S.; Kai, W.; Isogai, A.; Iwata, T. Elastic Modulus of Single Cellulose Microfibrils from Tunicate Measured by Atomic Force Microscopy. *Biomacromolecules* **2009**, *10* (9), 2571–2576.

(9) Fukuzumi, H.; Saito, T.; Iwata, T.; Kumamoto, Y.; Isogai, A. Transparent and High Gas Barrier Films of Cellulose Nanofibers Prepared by TEMPO-Mediated Oxidation. *Biomacromolecules* **2009**, *10* (1), 162–165.

(10) Wong, E. W.; Sheehan, P. E.; Lieber, C. M. Nanobeam Mechanics: Elasticity, Strength, and Toughness of Nanorods and Nanotubes. *Science* **1997**, *277* (5334), 1971–1975.

(11) Min-Feng, Y.; Lourie, O.; Dyer, M. J.; Moloni, K.; Strength and Breaking Mechanism of Multiwalled Carbon Nanotubes under Tensile Load. *Science; Washington* **2000**, *287* (5453), 637–640.

(12) Lorenz, M.; Sattler, S.; Reza, M.; Bismarck, A.; Kontturi, E. Cellulose nanocrystals by acid vapour: towards more effortless isolation of cellulose nanocrystals. *Faraday Discussions* **2017**, *202*, 315-330.

(13) Kim, J.-H.; Shim, B. S.; Kim, H. S.; Lee, Y.-J.; Min, S.-K.; Jang, D.; Abas, Z.; Kim, J. Review of Nanocellulose for Sustainable Future Materials. *Int. J. of Precis. Eng. and Manuf.-Green Tech.* **2015**, *2* (2), 197–213.

(14) Hubbe, M. A.; Rojas, O. J.; Lucia, L. A.; Sain, M. Cellulosic Nanocomposite: A Review. *BioResources* **2008**, 3(3), 929-980.

(15) Jiang, F.; Hsieh, Y.-L. Amphiphilic Superabsorbent Cellulose Nanofibril Aerogels. *J. Mater. Chem. A* **2014**, *2* (18), 6337–6342.

(16) Lavoine, N.; Bergström, L. Nanocellulose-Based Foams and Aerogels: Processing, Properties, and Applications. *Journal of Materials Chemistry A* **2017**, *5* (31), 16105–16117.

(17) Yuan, H.; Nishiyama, Y.; Wada, M.; Kuga, S. Surface Acylation of Cellulose Whiskers by Drying Aqueous Emulsion. *Biomacromolecules* **2006**, *7* (3), 696–700.

(18) Parambath Kanoth, B.; Claudino, M.; Johansson, M.; Berglund, L. A.; Zhou, Q. Biocomposites from Natural Rubber: Synergistic Effects of Functionalized Cellulose Nanocrystals as Both Reinforcing and Cross-Linking Agents via Free-Radical Thiol–Ene Chemistry. *ACS Appl. Mater. Interfaces* **2015**, *7* (30), 16303–16310.

(19) Goussé, C.; Chanzy, H.; Excoffier, G.; Soubeyrand, L.; Fleury, E. Stable Suspensions of Partially Silylated Cellulose Whiskers Dispersed in Organic Solvents. *Polymer* **2002**, *43* (9), 2645–2651.

(20) Yin, Y.; Tian, X.; Jiang, X.; Wang, H.; Gao, W. Modification of Cellulose Nanocrystal via SI-ATRP of Styrene and the Mechanism of Its Reinforcement of Polymethylmethacrylate. *Carbohydrate Polymers* **2016**, *142*, 206–212.

(21) Shrestha, S.; Chowdhury, R. A.; Toomey, M. D.; Betancourt, D.; Montes, F.; Youngblood, J. P. Surface Hydrophobization of TEMPO-Oxidized Cellulose Nanofibrils (CNFs) Using a Facile, Aqueous Modification Process and Its Effect on Properties of Epoxy Nanocomposites. *Cellulose* **2019**, *26* (18), 9631–9643.

(22) Song, Z.; Xiao, H.; Zhao, Y. Hydrophobic-modified nano-cellulose fiber/PLA biodegradable composites for lowering water vapor transmission rate (WVTR) of paper. *Carbohydrate polymers* **2014**, *111*, 442-448.

(23) Johnson, R.K.; Zink-Sharp, A.; Glasser, W.G. Preparation and characterization of hydrophobic derivatives of TEMPO-oxidized nanocelluloses. *Cellulose* **2011**, *18*(6), 1599-1609.

(24) Araki, J.; Wada, M.; Kuga, S. Steric stabilization of a cellulose microcrystal suspension by poly (ethylene glycol) grafting. *Langmuir* **2001**, *17*(1), 21-27.

(25) Lasseuguette, E. Grafting onto microfibrils of native cellulose. *Cellulose* **2008**, *15*(4), 571-580.

(26) Jonoobi, M.; Harun, J.; Mathew, A. P.; Hussein, M. Z. B.; Oksman, K. Preparation of Cellulose Nanofibers with Hydrophobic Surface Characteristics. *Cellulose* **2010**, *17* (2), 299–307.

(27) Braun, B.; Dorgan, J. R. Single-Step Method for the Isolation and Surface Functionalization of Cellulosic Nanowhiskers. *Biomacromolecules* **2009**, *10* (2), 334–341.

(28) J. Sobkowicz, M.; Braun, B.; R. Dorgan, J. Decorating in Green: Surface Esterification of Carbon and Cellulosic Nanoparticles. *Green Chemistry* **2009**, *11* (5), 680–682.

(29) Vinci, D.; Donaldson, M.; Hallett, J. P.; John, E. A.; Pollet, P.; Thomas, C. A.; Grilly, J. D.; Jessop, P. G.; Liotta, C. L.; Eckert, C. A. Piperylene Sulfone: A Labile and Recyclable DMSO Substitute. *Chem. Commun.* **2007**, No. 14, 1427.

(30) Huang, Y.; Ureña-Benavides, E. E.; Boigny, A. J.; Campbell, Z. S.; Mohammed, F. S.; Fisk, J. S.; Holden, B.; Eckert, C. A.; Pollet, P.; Liotta, C. L. Butadiene Sulfone as 'Volatile', Recyclable Dipolar, Aprotic Solvent for Conducting Substitution and Cycloaddition Reactions. *Sustain Chem Process* **2015**, *3* (1), 1-10.

(31) Sample, T. E.; Hatch, L. F. 3-Sulfolene: A Butadiene Source for a Diels-Alder Synthesis: An Undergraduate Laboratory Experiment. *J. Chem. Educ.* **1968**, *45* (1), 55.

(32) Filatov, M. A.; Baluschev, S.; Ilieva, I. Z.; Enkelmann, V.; Miteva, T.; Landfester, K.; Aleshchenkov, S. E.; Cheprakov, A. V. Tetraaryltetraanthra[2,3]Porphyrins: Synthesis, Structure, and Optical Properties. *J. Org. Chem.* **2012**, *77* (24), 11119–11131.

(33) Atilio de Frias, J.; Feng, H. Pretreatment of Furfural Residues with Switchable Butadiene Sulfone in the Sugarcane Bagasse Biorefinery. *Green Chem.* **2014**, *16* (5), 2779-2787.

(34) de Frias, J. A.; Feng, H. Switchable Butadiene Sulfone Pretreatment of Miscanthus in the Presence of Water. *Green Chem.* **2013**, *15* (4), 1067-1078.

(35) Smil, V. Crop Residues: Agriculture's Largest Harvest Crop Residues Incorporate More than Half of the World's Agricultural Phytomass. *BioScience* **1999**, *49* (4), 299–308.

(36) Lu, P.; Hsieh, Y.-L. Preparation and Characterization of Cellulose Nanocrystals from Rice Straw. *Carbohydrate Polymers* **2012**, *87* (1), 564–573.

(37) Bouquillon, S.; Muzart, J.; Pinel, C.; Rataboul, F. Palladium-Catalyzed Telomerization of Butadiene with Polyols: From Mono to Polysaccharides. *Carbohydrates in Sustainable Development II*; Rauter, A. P., Vogel, P., Queneau, Y., Eds.; Springer Berlin Heidelberg: Berlin, Heidelberg, **2010**; Vol. 295, 93–119.

(38) Palkovits, R.; Nieddu, I.; Klein Gebbink, R. J. M.; Weckhuysen, B. M. Highly Active Catalysts for the Telomerization of Crude Glycerol with 1,3-Butadiene. *ChemSusChem* **2008**, *1* (3), 193–196.

(39) Palkovits, R.; Parvulescu, A. N.; Hausoul, P. J. C.; Kruithof, C. A.; Klein Gebbink, R. J. M.; Weckhuysen, B. M. Telomerization of 1,3-Butadiene with Various Alcohols by Pd/TOMPP Catalysts: New Opportunities for Catalytic Biomass Valorization. *Green Chem.* **2009**, *11* (8), 1155-1160.

(40) Desvergnes-Breuil, V.; Pinel, C.; Gallezot, P. Green Approach to Substituted Carbohydrates: Telomerisation of Butadiene with Sucrose. *Green Chem.* **2001**, *3* (4), 175–177.

(41) Hausoul, P. J. C.; Bruijnincx, P. C. A.; Klein Gebbink, R. J. M.; Weckhuysen, B. M. Base-Free Pd/TOMPP-Catalyzed Telomerization of 1,3-Butadiene with Carbohydrates and Sugar Alcohols. *ChemSusChem* **2009**, *2* (9), 855–858.

(42) Mesnager, J.; Quettier, C.; Lambin, A.; Rataboul, F.; Pinel, C. Telomerization of Butadiene with Starch under Mild Conditions. *ChemSusChem* **2009**, *2* (12), 1125–1129.

(43) Mesnager, J.; Quettier, C.; Lambin, A.; Rataboul, F.; Perrard, A.; Pinel, C. Telomerization of Butadiene with Starch in Water: Role of the Surfactants. *Green Chem.* **2010**, *12* (3), 475-482.

(44) Hausoul, P.J.; Parvulescu, A.N.; Lutz, M.; Spek, A.L.; Bruijnincx, P.C.; Klein Gebbink, R.J.; Weckhuysen, B.M. Mechanistic Study of the Pd/TOMPP-Catalyzed Telomerization of 1, 3-Butadiene with Biomass-Based Alcohols: On the Reversibility of Phosphine Alkylation. *ChemCatChem* **2011**, *3*(5), 845-852.

(45) Palkovits, R.; Nieddu, I.; Kruithof, C.A.; Klein Gebbink, R.J.; Weckhuysen, B.M. Palladium-Based Telomerization of 1, 3-Butadiene with Glycerol Using Methoxy-Functionalized Triphenylphosphine Ligands. *Chemistry–A European Journal* **2008**, *14*(29), 8995-9005.

(46) Parvulescu, A.N.; Hausoul, P.J.C.; Bruijnincx, P.C.A.; Korhonen, S.T.; Teodorescu, C.; Klein Gebbink, R.J.M.; Weckhuysen, B.M. Telomerization of 1, 3-butadiene with biomass-derived alcohols over a heterogeneous Pd/TPPTS catalyst based on layered double hydroxides. *ACS Catalysis* **2011**, *1*(5), 526-536.

(47) Drake, L. R.; Stowe, S. C.; Partansky, A. M. Kinetics of the Diene Sulfur Dioxide Reaction. *J. Am. Chem. Soc.* **1946**, *68* (12), 2521–2524.

(48) Minoura, Y.; Nakajima, S. Polymerization of Butadiene Sulfone. *Journal of Polymer Science Part A-1: Polymer Chemistry* **1966**, *4* (12), 2929–2944.

(49) Vollmüller, F.; Krause, J.; Klein, S.; Mägerlein, W.; Beller, M. Control of Chemo- and Regioselectivity in the Palladium-Catalyzed Telomerization of Butadiene with Methanol − Catalysis and Mechanism. *European Journal of Inorganic Chemistry* **2000**, *2000* (8), 1825–1832.

(50) Huo, C.-F.; Jackstell, R.; Beller, M.; Jiao, H. Mechanistic Study of Palladium-Catalyzed Telomerization of 1,3-Butadiene with Methanol. *J Mol Model* **2010**, *16* (3), 431–436.

(51) Hessien, M. M.; Rashad, M. M.; Zaky, R. R.; Abdel-Aal, E. A.; El-Barawy, K. A. Controlling the Synthesis Conditions for Silica Nanosphere from Semi-Burned Rice Straw. *Materials Science and Engineering: B* **2009**, *162* (1), 14–21.

(52) Kontturi, E. and Vuorinen, T., 2009. Indirect evidence of supramolecular changes within cellulose microfibrils of chemical pulp fibers upon drying. *Cellulose*, *16*(1), pp.65-74.

(53) Anslyn, E. V.; Dougherty, D. A. *Modern Physical Organic Chemistry*; University Science Books, 2006.

(54) Liu, X.; Hsieh, Y.-L. Amphiphilic Protein Microfibrils from Ice-Templated Self-Assembly and Disassembly of Pickering Emulsions. *ACS Appl. Bio Mater.* **2020**, 3(4), 2473-2481.

(55) Gu, J.; Hsieh, Y.-L. Surface and Structure Characteristics, Self-Assembling, and Solvent Compatibility of Holocellulose Nanofibrils. *ACS Appl. Mater. Interfaces* **2015**, *7* (7), 4192–4201.

(56) Yang, H.; Fung, S.-Y.; Pritzker, M.; Chen, P. Modification of Hydrophilic and Hydrophobic Surfaces Using an Ionic-Complementary Peptide. *PLoS ONE* **2007**, *2* (12), e1325.

(57) Segal, L.; Creely, J. J.; Martin, A. E.; Conrad, C. M. An Empirical Method for Estimating the Degree of Crystallinity of Native Cellulose Using the X-Ray Diffractometer. *Textile Research Journal* **1959**, *29* (10), 786–794.

(58) Scherrer, P. (1918). Estimation of the size and internal structure of colloidal particles by means of Röntgen rays. Nachrichten von der Gesellschaft der Wissenschaften zu Göttingen, 96–100.

(59) Jiang, F.; Dallas, Jerry. L.; Ahn, B. K.; Hsieh, Y.-L. 1D and 2D NMR of Nanocellulose in Aqueous Colloidal Suspensions. *Carbohydrate Polymers* **2014**, *110*, 360–366.

(60) Ross, S. A.; Lowe, G. Downfield Displacement of the NMR Signal of Water in Deuterated Dimethylsulfoxide by the Addition of Deuterated Trifluoroacetic Acid. *Tetrahedron Letters* **2000**, *41* (17), 3225–3227.

(61) Tizzotti, M. J.; Sweedman, M. C.; Tang, D.; Schaefer, C.; Gilbert, R. G. New ^{1}H NMR Procedure for the Characterization of Native and Modified Food-Grade Starches. *J. Agric. Food Chem.* **2011**, *59* (13), 6913–6919.

(62) Nardin, R.; Vincendon, M. Homo- and Heteronuclear Two-Dimensional Correlated Nuclear Magnetic Resonance Spectra of Cellulose. *Macromolecules* **1986**, *19* (9), 2452–2454.

(63) Izzo, F. C.; Zendri, E.; Biscontin, G.; Balliana, E. TG–DSC Analysis Applied to Contemporary Oil Paints. *Journal of Thermal Analysis and Calorimetry* **2011**, *104* (2), 541–546.

(64) Lazzari, M.; Chiantore, O. Drying and Oxidative Degradation of Linseed Oil. *Polymer Degradation and Stability* **1999**, *65* (2), 303–313.

(65) Smutny, E. J. Linear Telomerization of Conjugated Dienes. *Ann NY Acad Sci* **1973**, *214* (1), 125–142.

CHAPTER 3: A Method for Preparing Samples of Colloidal State Hydrophobic Nanofibrils in a d_6-DMSO Solution for Phase 1D and 2D NMR Analysis

3.1 Abstract

This chapter covers surface structural elucidation of individual ODE-CNFs as colloidal suspensions in d_6-DMSO by ^{1}H and ^{13}C nuclear magnetic resonance spectroscopy (NMR), 2D heteronuclear single quantum coherence (2D HQSC), and homonuclear correlation spectroscopy (COSY). "As-is" ODE-CNFs (thickness: 3.7 ± 5.2 nm, width: 4.1 ± 1.7 nm) were obtained from telomerization of butadiene produced from butadiene sulfone with rice straw cellulose, followed by mechanical disintegration. The *h*ODE-CNFs (T:1.2 ± 0.5 nm, W:3.8 ± 0.5 nm) were obtained from the subsequent hydrolysis. Their ^{1}H spectra were identical except *h*ODE-CNFs showed improved peak intensity[1] in agreement with ^{1}H and HSQC NMR of TEMPO-CNF[20]. The integration area of the proton peaks gave H2:H1 ratios of 1.16:1, close to the theoretical 1:1 value for cellulose, enabling quantitative calculation of surface functionalization (0.13) per AGUs. The chemical shifts of *h*ODE-CNFs in ^{1}H NMR and ^{13}C NMR are as follows: δ = 1.5, 2.0, 2.1, 3.1, 3.2, 3.3, 3.4, 3.5, 3.9, 4.1, 4.9, 5.3, 5.6, 5.9, 6.1, and δ = 29.2, 30.2, 31.1, 63.7, 73.0, 74.4, 75.7, 75.7, 83.3, 102.2, 129.2, 133.2, 134.8, 138.0 ppm, respectively. 2D HSQC and COSY clearly elucidated spatial connectivity of cellulosic H-C and vicinal hydrogens in ODE-CNF structure.

3.2 Introduction

Nanocelluloses are the highly crystalline nanoscale domains isolated from cellulose, the most abundant and renewable biopolymer on earth originating from sources such as plants, wood, and tunicates, and characterized by strength and biocompatibility. Nanocelluloses have been most commonly derived by chemical means in combination with mechanical forces. Sulfuric acid hydrolysis[2] generates highly crystalline, short rod-shaped CNCs, while TEMPO-mediated oxidation[3–5], combined with mechanical disintegration, produces CNFs with a high aspect ratio.

Nanocelluloses have an intrinsic tensile strength of 7.5 GPa[6] and Young's modulus of 150 GPa[7] for CNCs (the highest among organic materials), and 233 MPa[8] and 145 GPa[7] for CNFs, respectively. They are both aqueous-compatible due to surface negative charges; however, they are not suitable for hydrophobic processing. To produce nanocelluloses compatible with organic solvents and hydrophobic polymers, chemical modifications of CNCs and CNFs are typically employed, by silylation[9,10], acylation[11], or etherification[12] for CNCs, and amidation[13,14] for CNFs. Less frequently, surface modification of cellulose, by acetylation[15] and telomerization[1], followed by mechanical defibrillation, is also practiced.

Analytical techniques such as FTIR, X-ray photoelectron spectroscopy (XPS), and energy dispersive X-ray analysis (EDX) discern qualitative characteristics of surface functional groups on molecules in solution and solid state, while NMR can provide both qualitative and quantitative information. Solution state NMR analysis is particularly important for nanocelluloses because it elucidates molecular structures, the connectivity of atoms, and their interactions based on individual fibrillar morphology. This cannot be accomplished by solid-state NMR techniques, such as cross-polarization/magic-angle-spinning (CP/MAS)[16] and dynamic nuclear polarization (DNP)[17], due to the sample preparation method of drying and grinding that leads to agglomeration of fibrils or disintegration of crystalline structures. The structure of aqueous soluble TEMPO-oxidized polyglucuronic acids, derived from microcrystalline cellulose and cotton linter, has been elucidated in 9 % aqueous NaOH[18] and D_2O[19], respectively. More recently, the first ^1H and 2D HSQC NMR on CNCs and CNFs as colloidal suspensions elucidated their surface chemical structure[20]. Quantitatively, conversion of C6 primary hydroxyl to carboxylate on CNFs, as analyzed by 2D HSQC NMR, was proven to be consistent with, but more sensitive than, those conversions obtained by conductometric titration. Thus, NMR in solution state can offer superior

structural and quantitative information on individual nanocelluloses, especially when the CNF dimension is 2 nm or thinner to maximize spectral sensitivity due to the faster tumbling and reorientation of the thinner fibrils. However, the above analyses were performed on hydrophilic nanocelluloses in D_2O, and there is no previous report of partially hydrophobized CNFs with low degrees of substitution analyzed in a single organic solvent by NMR. Fully functionalized microcrystalline cellulose with acetyl and amino groups with DS = 3 (per 3 OH groups) was soluble in $CDCl_3$ and the surface chemistry was successfully elucidated by solution state ^{13}C NMR analysis[21]. On the other hand, nanocelluloses with lower degrees of substitution are insoluble in all organic solvents, and direct methods to characterize their surface chemistry are severely limited. For example, CNCs grafted with PMMA (surface DS = 0.096 per 3 OH groups) in acetone were solvent exchanged to the combination solvents of tetraalkylphosphonium acetate ionic liquid ([P4444][OAc]): d_6-DMSO, then analyzed by 1D and 2D HSQC NMR[22]. Ionic liquid dissolves nanocellulose into individual chains that provide only indirect information about crystalline CNCs. Also, it exhibits multiple solvent peaks likely to interfere with the peaks of the interest.

There is a dire need of a simple solution state NMR analysis in a single organic solvent for hydrophobized CNFs with low DS. Therefore, in this study, hydrophobic CNFs functionalized with octadienyl ether were probed using 1D and 2D NMR to demonstrate their suitability for direct characterization of the surfaces of individual CNFs in d_6-DMSO in the colloidal state.

3.3 Experimental

3.3.1 Materials

Please refer to Chapter 2, Section 2.3.1.

3.3.2 Derivation of ODE-CNFs and hODE-CNFs

For telomerization of cellulose, hydrolysis of ODE-cellulose, and defibrillation of them into ODE-CNFs and ODE-*h*CNFs, please refer to Chapter 2, Section 2.3.2.

3.3.3 NMR sample preparation of ODE-CNFs and hODE-CNFs

Solution state ^{1}H and ^{13}C NMR, was conducted to avoid drying and potential agglomeration of fibrils which may lead to inaccurate surface information. The sample preparation of ODE-CNFs and hODE-CNFs in d_6-DMSO is briefly described in Chapter 2, Section 2.3.4. In more detail, the aqueous precipitates were rinsed with acetone to precipitate more hydrophobic as-is ODE-CNFs and *h*ODE-CNFs, followed by centrifugation to remove the top clear phase. This was repeated 3 times (**Figure 3-1**). To the last precipitate in acetone that contains *ca.*10 mg (dried weight) of as-is ODE-CNFs or *h*ODE-CNFs, 1 mL d_6-DMSO was added, and then, the residual acetone in d_6-DMSO was removed in an oven at 55-60 ºC for 3 d with occasional stirring. This was followed by centrifugation at 11k rpm for 10 min to collect the clear d_6-DMSO supernatant, from which 600 μL was transferred to a NMR tube for the analysis with the final concentration ca. 0.5 %. As the final step in sample preparation, immediately before the experiments, about 10 vol % of TFA was added to the sample to displace cellulosic OH peaks out of the olefinic proton region by H-bonding the OHs with the TFA.

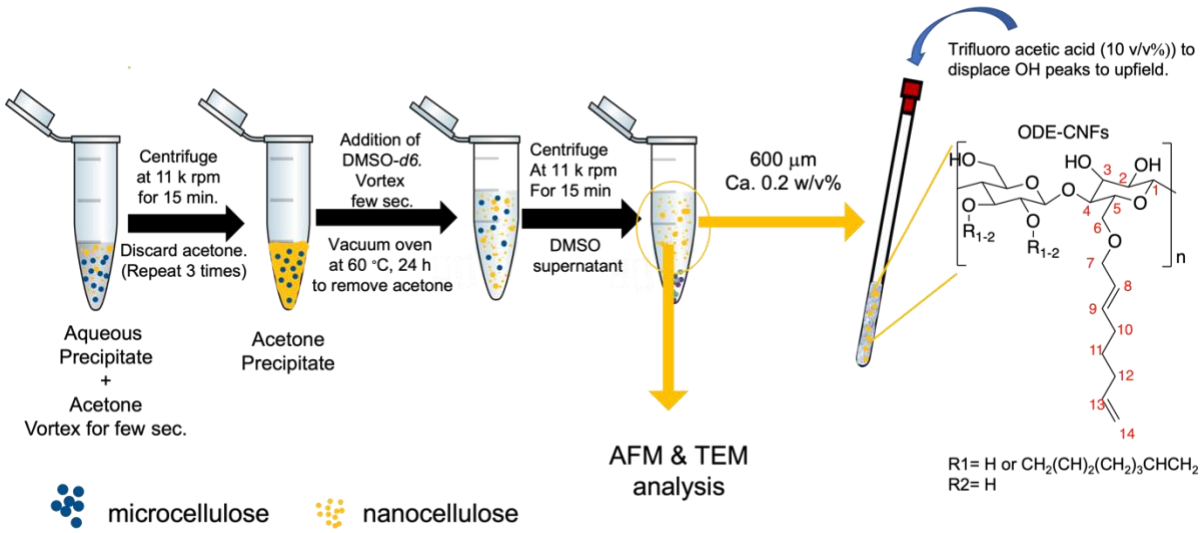

Figure 3-1. Solution state NMR sample preparation process.

3.3.4 Surface characterization of ODE-CNFs and hODE-CNFs by NMR, AFM and TEM.

For surface characterization information for NMR, AFM and TEM, please refer to Chapter 2, Section 2.3.4.

3.4 Results and Discussion

3.4.1 Characterization of hODE-CNFs and as-is ODE-CNFs

Figures 3-2 a & b show that the thickness of *h*ODE-CNFs (1.2 ± 0.5 nm) had been significantly reduced during hydrolysis of the "as is" ODE-CNFs (3.7 ± 5.2 nm). The lower thickness of *h*ODE-CNFs can improve spectral sensitivity, as concluded in our previous publication[20]. NMR analysis is meaningful especially when the CNF dimension is 2 nm or thinner to maximize spectral sensitivity due to faster tumbling and reorientation of the thinner fibrils. The inversion recovery curves of H2 (**Figure 3-2c**) show faster recovery (1.48 s) of *h*ODE-CNFs than

that (4.67 s) of ODE-CNFs, which is consistent with the much thinner *h*ODE-CNFs than ODE-CNFs to produce more highly-resolved spectral peaks, which is consistent with TEMPO-CNFs[20].

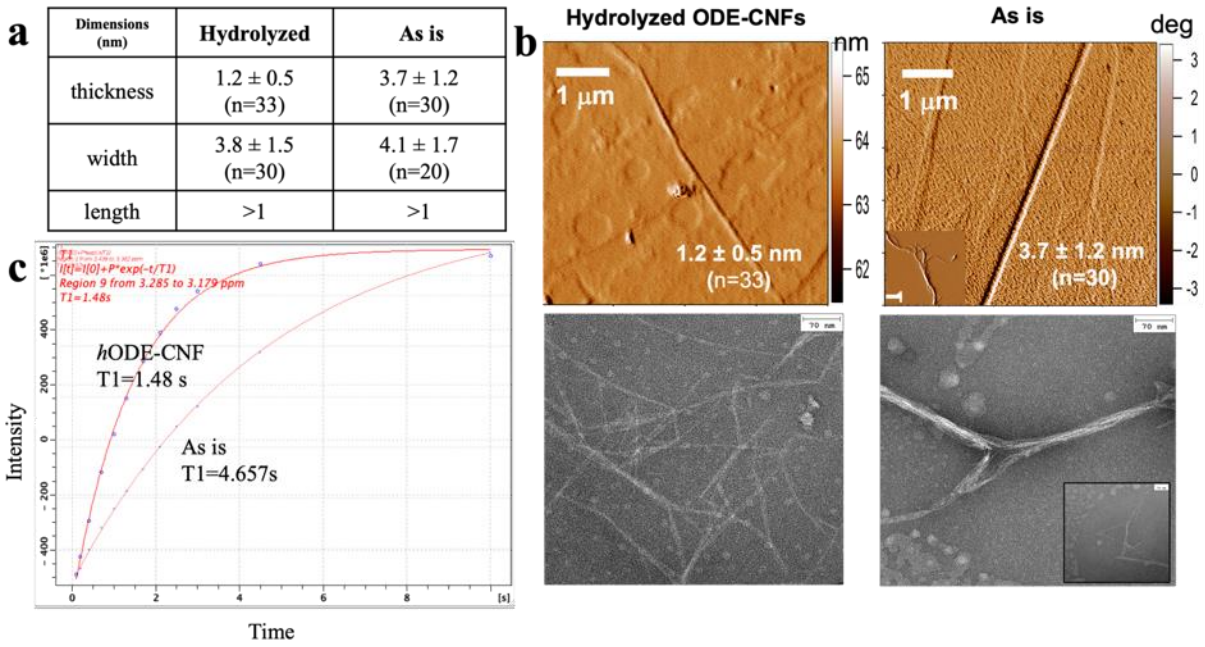

Figure 3-2. Surface characterization and sensitivity comparison of *h*ODE-CNFs and "as is" ODE-CNFs: (a) fibril dimensions; (b) AFM and TEM of respective ODE-CNFs; (c) recovery time (T1) inversion recovery of respective ODE-CNFs.

For ^{1}H NMR and ^{13}C NMR spectra, the chemical shifts of protons and carbons for ODE-CNFs and the peak integration analysis, please go to Chapter 2, Section 2.4.3.

3.4.2 Heteronuclear single quantum coherence spectroscopy (HSQC)

Heteronuclear single quantum coherence spectroscopy (HSQC) is used to correlate the chemical shift of protons (displayed on the F2 axis) to the ^{13}C chemical shift (on the "indirect," F1 axis) of their directly-attached carbons.

For cellulosic protons, the H1 proton is coupled to the anomeric carbon at 102 ppm **(Figure 3-3)**. Diastereotopic protons spaced apart from each other at δ 3.19 and δ 3.93 are both attached to C6 at 63.65 ppm. H2, H3, H4, and H5 are coupled to the carbons at 73.01, 74.39, 75.72, and 79.39

ppm, respectively. All of these are in proximity to, or consistent with, the TEMPO-oxidized cellulosic protons reported previously[20].

For ODE-groups, two sets of allylic peaks and one methylene peak were coupled with the upfield carbon at 28.5, 30.0, and 31.0 ppm, although the intensity was very low, and the carbon connection with olefinic protons was not as clear, due to the low degree of substitution.

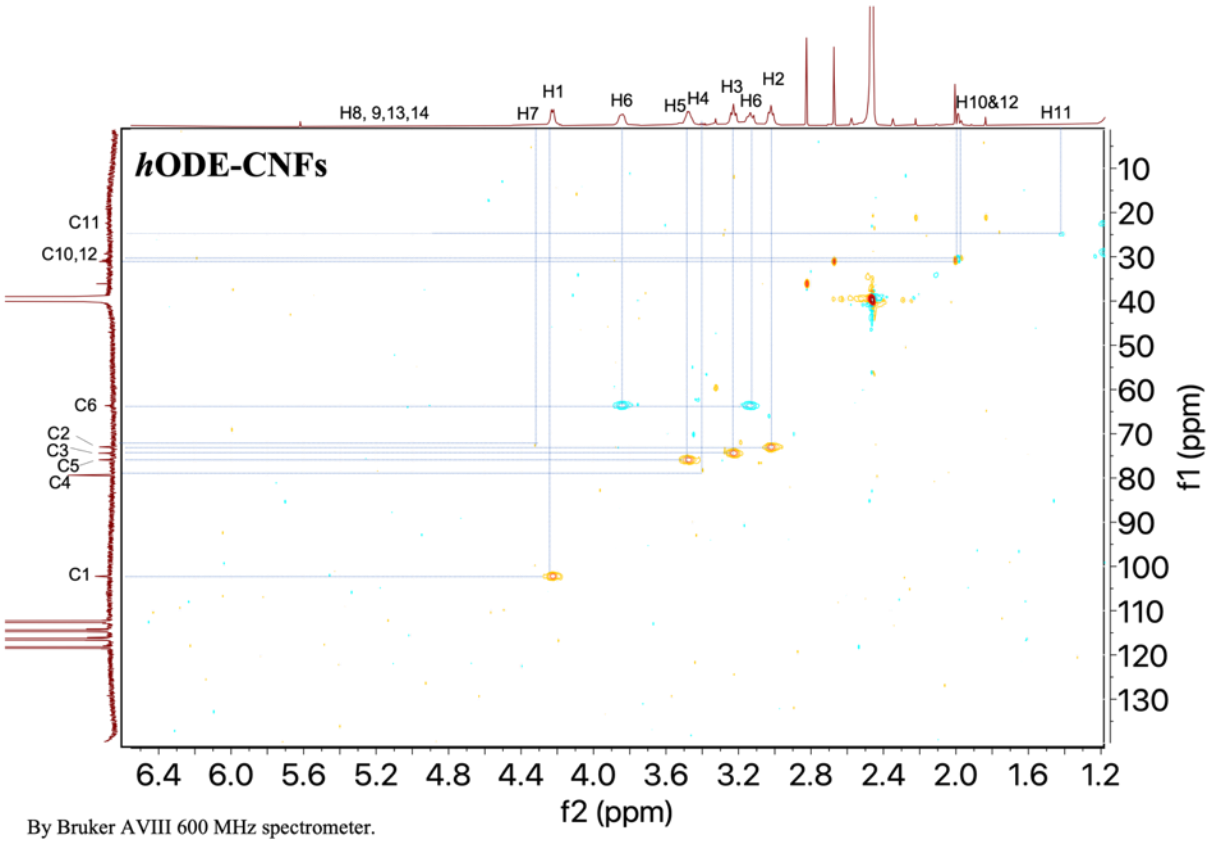

Figure 3-3. HSQC spectrum of *h*ODE-CNFs.

3.4.3 Homonuclear correlation spectroscopy (COSY)

Homonuclear Correlation Spectroscopy (COSY) identifies spins of vicinal hydrogens which are coupled with each other. The assignments of protons in the cellulose backbone for ODE-CNFs in COSY are as follows (**Figure 3-4**): H1 and H2 are coupled with each other at 4.27 and 3.17 ppm, H2 and H3 are at 3.17 and 3.28 ppm, H3 and H4 are at 3.28 and 3.40 ppm, H4 and H5

are at 3.40 and 3.53 ppm, H5 and H6a are at 3.53 and 3.20 ppm, and H5 and H6b are at 3.53 and 3.93 ppm. Peaks from H4 and H5 appear only in the center, indicating that they overlap each other due to being in the same environment. Therefore, all vicinal protons which are coupled with each other were identified.

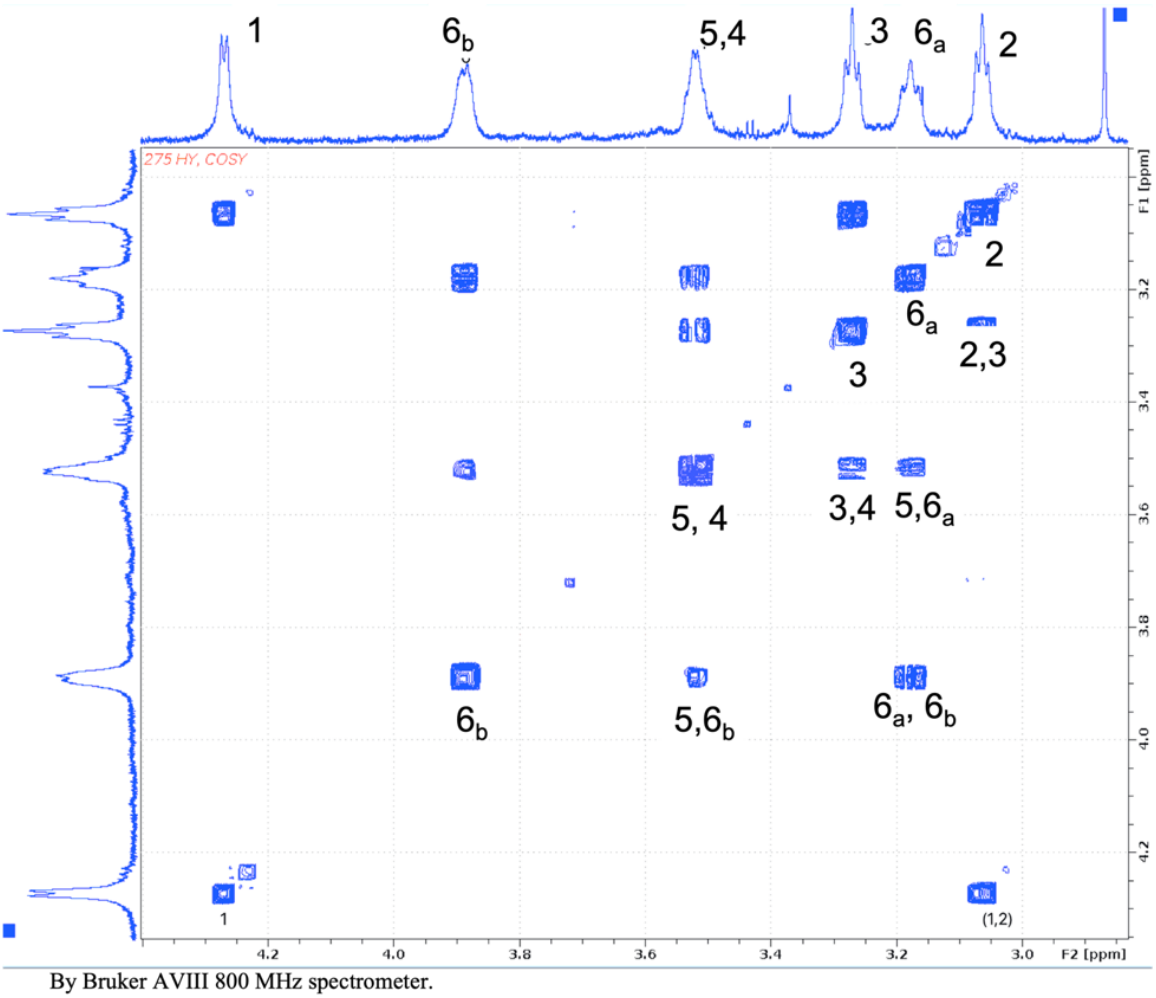

Figure 3-4. COSY spectrum of *h*ODE-CNFs.

3.5 Conclusions

Surface chemistries of hydrophobic ODE-CNFs have been successfully characterized by solution state NMR of their colloidal suspensions in d_6-DMSO, following the never-dried sample preparation method for TEMPO-oxidized CNFs in D_2O[20]. Cellulose was extracted from rice straw,

functionalized by telomerization of butadiene derived from butadiene sulfone with cellulose hydroxyls, followed by mechanical blending to obtain hydrophobic ODE-CNFs ("as-is") with dimensions of 3.7 ± 5.2 nm thickness and 4.1 ± 1.7 nm width. To produce thinner fibrils to obtain sharper signals, hydrolysis was conducted to generate *h*ODE-CNFs with the dimension of 1.2 ± 0.5 nm thickness and 3.8 ± 0.5 nm width. ^{1}H and ^{13}C NMR of *h*ODE-CNFs was used to elucidate the surface protons and carbons even for those from ODE-groups with low substitution on individual ODE-CNF at δ = 1.47, 1.95, 2.07, 3.08, 3.19, 3.28, 3.40, 3.53, 3.93, 4.12, 4.86, 5.29, 5.61, 5.90, 6.07, and δ = 29.24, 30.20, 31.09, 63.65, 73.01, 74.39, 75.72, 75.72, 83.33, 102.21, 129.24, 133.23, 134.81, 138.02 ppm, respectively. Chemical shifts for the ^{1}H and ^{13}C peaks of the ODE-CNF backbone were consistent with those of TEMPO-CNFs[20]. Also, the integration area of the proton peak gave H2:H1 ratios of 1.16:1, close to the theoretical 1:1 value for cellulose. 2D HSQC clearly provided structural information on cellulosic protons by showing spatial connectivity between protons and carbons. 2D COSY identified vicinal hydrogens which are coupled with each other. These findings verified that solution-state NMR of hydrophobic CNFs in d_6-DMSO can provide direct analysis of CNFs in 1D and 2D NMR, offering surface chemistry elucidation of individual CNFs not only in D_2O but also in d_6-DMSO.

3.6 Acknowledgements

Financial support from the California Rice Research Board (Project RU-9) and the Henry A. Jastro Research Award, University of California, Davis is greatly appreciated.

3.7 References

(1) Fukuda, J.; Hsieh, Y.-L. Hydrophobic 2,7-Octadienyl Ether-Cellulose Nanofibrils Using Butadiene Sulfone as the Dual Reagent and Medium. *ACS Sustainable Chem. Eng.* **2021**, *9* (18), 6489–6498. https://doi.org/10.1021/acssuschemeng.1c02092.

(2) Beck-Candanedo, S.; Roman, M.; Gray, D. G. Effect of Reaction Conditions on the Properties and Behavior of Wood Cellulose Nanocrystal Suspensions. *Biomacromolecules* **2005**, *6* (2), 1048–1054. https://doi.org/10.1021/bm049300p.

(3) de Nooy, A. E. J.; Besemer, A. C.; van Bekkum, H. Highly Selective Nitroxyl Radical-Mediated Oxidation of Primary Alcohol Groups in Water-Soluble Glucans. *Carbohydrate Research* **1995**, *269* (1), 89–98. https://doi.org/10.1016/0008-6215(94)00343-E.

(4) Isogai, A.; Saito, T.; Fukuzumi, H. TEMPO-Oxidized Cellulose Nanofibers. *Nanoscale* **2011**, *3* (1), 71–85. https://doi.org/10.1039/C0NR00583E.

(5) Jiang, F.; Han, S.; Hsieh, Y.-L. Controlled Defibrillation of Rice Straw Cellulose and Self-Assembly of Cellulose Nanofibrils into Highly Crystalline Fibrous Materials. *RSC Adv.* **2013**, *3* (30), 12366-12375. https://doi.org/10.1039/c3ra41646a.

(6) Wu, X.; Moon, R. J.; Martini, A. Tensile Strength of Iβ Crystalline Cellulose Predicted by Molecular Dynamics Simulation. *Cellulose* **2014**, *21* (4), 2233–2245. https://doi.org/10.1007/s10570-014-0325-0.

(7) Iwamoto, S.; Kai, W.; Isogai, A.; Iwata, T. Elastic Modulus of Single Cellulose Microfibrils from Tunicate Measured by Atomic Force Microscopy. *Biomacromolecules* **2009**, *10* (9), 2571–2576. https://doi.org/10.1021/bm900520n.

(8) Fukuzumi, H.; Saito, T.; Iwata, T.; Kumamoto, Y.; Isogai, A. Transparent and High Gas Barrier Films of Cellulose Nanofibers Prepared by TEMPO-Mediated Oxidation. *Biomacromolecules* **2009**, *10* (1), 162–165. https://doi.org/10.1021/bm801065u.

(9) Goussé, C.; Chanzy, H.; Excoffier, G.; Soubeyrand, L.; Fleury, E. Stable Suspensions of Partially Silylated Cellulose Whiskers Dispersed in Organic Solvents. *Polymer* **2002**, *43* (9), 2645–2651. https://doi.org/10.1016/S0032-3861(02)00051-4.

(10) Saini, S.; Belgacem, M. N.; Bras, J. Effect of Variable Aminoalkyl Chains on Chemical Grafting of Cellulose Nanofiber and Their Antimicrobial Activity. *Materials Science and Engineering: C* **2017**, *75*, 760–768. https://doi.org/10.1016/j.msec.2017.02.062.

(11) Yuan, H.; Nishiyama, Y.; Wada, M.; Kuga, S. Surface Acylation of Cellulose Whiskers by Drying Aqueous Emulsion. *Biomacromolecules* **2006**, *7* (3), 696–700. https://doi.org/10.1021/bm050828j.

(12) Tingaut, P.; Hauert, R.; Zimmermann, T. Highly Efficient and Straightforward Functionalization of Cellulose Films with Thiol-Ene Click Chemistry. *J. Mater. Chem.* **2011**, *21* (40), 16066–16076. https://doi.org/10.1039/C1JM11620G.

(13) Johnson, R. K.; Zink-Sharp, A.; Glasser, W. G. Preparation and Characterization of Hydrophobic Derivatives of TEMPO-Oxidized Nanocelluloses. *Cellulose* **2011**, *18* (6), 1599–1609. https://doi.org/10.1007/s10570-011-9579-y.

(14) Shrestha, S.; Chowdhury, R. A.; Toomey, M. D.; Betancourt, D.; Montes, F.; Youngblood, J. P. Surface Hydrophobization of TEMPO-Oxidized Cellulose Nanofibrils (CNFs) Using a Facile, Aqueous Modification Process and Its Effect on Properties of Epoxy Nanocomposites. *Cellulose* **2019**, *26* (18), 9631–9643. https://doi.org/10.1007/s10570-019-02762-w.

(15) Jonoobi, M.; Harun, J.; Mathew, A. P.; Hussein, M. Z. B.; Oksman, K. Preparation of Cellulose Nanofibers with Hydrophobic Surface Characteristics. *Cellulose* **2010**, *17* (2), 299–307. https://doi.org/10.1007/s10570-009-9387-9.

(16) Gicquel, E.; Martin, C.; Heux, L.; Jean, B.; Bras, J. Adsorption versus Grafting of Poly(N-Isopropylacrylamide) in Aqueous Conditions on the Surface of Cellulose Nanocrystals. *Carbohydrate Polymers* **2019**, *210*, 100–109. https://doi.org/10.1016/j.carbpol.2019.01.022.

(17) Kumar, A.; Durand, H.; Zeno, E.; Balsollier, C.; Watbled, B.; Sillard, C.; Fort, S.; Baussanne, I.; Belgacem, N.; Lee, D.; Hediger, S.; Demeunynck, M.; Bras, J.; Paëpe, G. D. The Surface Chemistry of a Nanocellulose Drug Carrier Unravelled by MAS-DNP. *Chemical Science* **2020**, *11* (15), 3868–3877. https://doi.org/10.1039/C9SC06312A.

(18) Tahiri, C.; Vignon, M. R. TEMPO-Oxidation of Cellulose: Synthesis and Characterisation of Polyglucuronans. *Cellulose* **2000**, *7* (2), 177–188. https://doi.org/10.1023/A:1009276009711.

(19) Hirota, M.; Tamura, N.; Saito, T.; Isogai, A. Oxidation of Regenerated Cellulose with NaClO2 Catalyzed by TEMPO and NaClO under Acid-Neutral Conditions. *Carbohydrate Polymers* **2009**, *78* (2), 330–335. https://doi.org/10.1016/j.carbpol.2009.04.012.

(20) Jiang, F.; Dallas, Jerry. L.; Ahn, B. K.; Hsieh, Y.-L. 1D and 2D NMR of Nanocellulose in Aqueous Colloidal Suspensions. *Carbohydrate Polymers* **2014**, *110*, 360–366. https://doi.org/10.1016/j.carbpol.2014.03.043.

(21) Fox, S. C.; Edgar, K. J. Staudinger Reduction Chemistry of Cellulose: Synthesis of Selectively O-Acylated 6-Amino-6-Deoxy-Cellulose. *Biomacromolecules* **2012**, *13* (4), 992–1001. https://doi.org/10.1021/bm2017004.

(22) King, A. W. T.; Mäkelä, V.; Kedzior, S. A.; Laaksonen, T.; Partl, G. J.; Heikkinen, S.; Koskela, H.; Heikkinen, H. A.; Holding, A. J.; Cranston, E. D.; Kilpeläinen, I. Liquid-State NMR Analysis of Nanocelluloses. *Biomacromolecules* **2018**, *19* (7), 2708–2720. https://doi.org/10.1021/acs.biomac.8b00295.

CHAPTER 4: Tunable Hydrophobic Octadienyl-Ether Nanocellulose Derived by Ultra-Sonication: Scale-Up, Optimization and Applications

4.1 Abstract

2,7-Octadienyl-ether cellulose (ODE-NC) previously obtained with the optimal condition (0.1 g scale)[1] was sonicated to prove that ultra-sonication in organic media could produce ODE-NC, and further improve yields. Wetting and 5 sec. vortexing of ODE-cellulose in tert-butanol (TB) prior to sonication improved the yield of ODE-NC in THF, $CHCl_3$, LO, and toluene to 28, 52, 66, and 37 %, respectively. Scale-up (0.5 g cellulose) telomerization with 6ODE equivalence per AGU at 110 °C resulted in a DS of 0.67 mmol ODE/g-cell, in relative agreement with 0.74 mmol ODE/g cell obtained at 0.1 g cellulose scale, which validated the scale-up reaction. Sonicating cellulose (50 % amplitude (*A*), 3 min) in DMF prior to telomerization separated cellulose bundles into individual fibers and produced ODE-cellulose with DS 1.2 and 1.8 mmol ODE/g-cell (1.2ODE-cell and 1.8ODE-cell, respectively). Sonication (50 % *A*, 20 min) of 1.2ODE-cell and 1.8ODE-cell yielded 45.5 % 1.2ODE-NC in toluene and 73.3 % 1.8ODE-NC in LO. A cast film formed from sonicated 1.2ODE-cell combined with polybutadiene (PBD) in toluene exhibited an outstanding modulus (2.23 ± 0.34 MPa) and yield strength (0.15 ± 0.04 MPa), over six- and two-fold higher than those of the PBD control, respectively. Furthermore, a film formed by a thorough 5 h mixing of 2 wt % 1.2ODE-microcellulose/nanocellulose (MC/NC) and poly(styrene-blk-isoprene-blk-styrene) (PSIS) in toluene showed a strength of 17.3 ± 3.3 MPa, ca. three-fold higher than those of the control film and the film formed by cross-linking between alkenes in ODE-groups and isoprene. Cellulose paper (CP) was optimally reinforced by coating with 0.07 v/v.% 1.8ODE-NC mixed with LO (85 wt % add-on) and heating at 70 ºC for 16 h, showing improved strength by 2.6-fold with respect to CP. The coated CP surface after rinsing off the unbound reaction residues (11 %) was hydrophobic (WCA 91~117º) and water repellent for 3h, due to fatty acids (FAs) covalently bound to CP via transesterification, and cross-linked

FAs and ODE-NC. This report has demonstrated a streamlined approach to directly disintegrating ODE-cellulose in organic solvents and/or plant oil by sonication into ODE-NC. The excellent compatibility of the optimized 1.2ODE-NC with PBD and PSIS in toluene, and 1.8ODE-NCs with bio-degradable LO, suggests broad areas of future applications in material fabrication and food packaging.

4.2 Introduction

In Chapter 2, hydrophobization of cellulose by telomerization of 1,3-BD with hydroxyl groups was demonstrated by using butadiene sulfone (BDS) as both a reagent (1,3-BD) and a solvent.[1] ODE-cellulose was mechanically blended in water to produce ODE-NC-containing precipitate which was solvent-exchanged with polymer solvents to obtain 27.3 %, 30.3 % and 28.1 % yield of ODE-NC in respective THF, $CHCl_3$, and toluene dispersions. ODE-NC in THF and $CHCl_3$ contained more nanofibrils (ODE-CNFs) than nanoparticles (**Table 4-1**), while ODE-NC in toluene contained no separated nanofibrils. With the DS of 0.74 mmol ODE/g-cell as measured by solution state ^{1}HNMR, ODE-NC absorbed negligible moisture and exhibited impressive hydrophobicity by WCA of 102° and 94° when deposited (1% in $CHCl_3$) over freshly-cleaved hydrophilic mica (WCA = 0°) and cellulose paper, respectively. However, the yields and the DS of ODE-NC needs to be further improved.

Table 4-1. Dispersion of ppt from aq. blending of ODE-cellulose (0.74 mmol/g-cell, 6ODE110 1 h).[1]

	DMSO	**DMF**	**m-Cresol**	**THF**	**$CHCl_3$**	**Toluene**
ODE-NC (wt %)	40.1	19.6	33.3	27.3	30.3	28.1
CNF/NP	60/40	30/70	5/95	60/40	70/30	*

*virtually no separated nanofibrils

This study focused on scaling up the one-pot synthesis of ODE-cellulose (ODE-cell), optimizing functionalization and yield, and streamlining the disintegration of ODE-NC by direct sonication in organic liquids (**Scheme 4-1**). Ultra-sonication refers to the acoustic cavitation caused by the nucleation, growth, oscillation, and transient collapse of gas bubbles to generate the localized elevated temperatures (ca. 5000 °C)[2] and/or pressures (ca. 500 atm)[3] utilized to disintegrate aggregated polymers or homogenize reagents. Sonication has been used to disintegrate TEMPO-oxidized or sulfuric acid hydrolyzed cellulose in water into CNCs and CNFs[4-6], but it is less common to apply sonication to produce nanocellulose in organic liquids. Cellulose was sonicated in DMF which is compatible with cellulose as well as BDS, 1,3-BD, and the catalyst, prior to telomerization to determine if the diffusion of 1,3-BD into the cellulose can improve telomerization. Pretreating OCE-cell with *tert*-butanol (TB) was examined to help disintegration of ODE-cell by sonication by reducing inter-fibrillar association among hydroxyls in ODE-cell via hydrogen bonding[7].

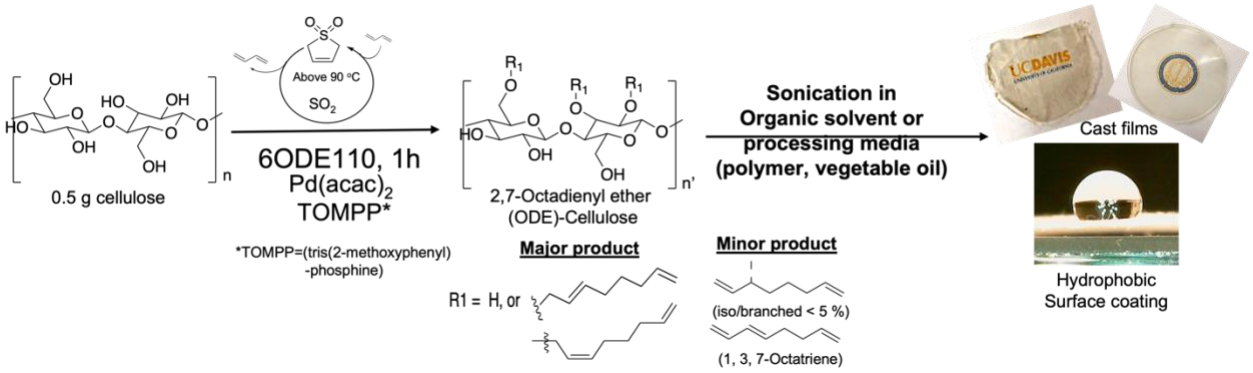

Scheme 4-1. Telomerization with 6ODE, 1h at 90-110 ºC at 0.5 g cellulose scale.

The effect of ODE groups in reinforcing polybutadiene (PBD) nanocomposite films with ODE-microcellulose/nanocellulose (MC/NC) with a DS of 1.2 mmol ODE/g-cell (1.2ODE) was investigated by varying the mixing methods of nanocomposite solutions. Also the effect of 1.2ODE-MC/NC in nanocomposite films of poly(styrene-blk-isoprene-blk-styrene) (PSIS) was

investigated by mixing or cross-linking with PSIS using a metal-free radical initiator, azobisisobutyronitrile (AIBN).

Disintegration of ODE-cellulose with DS of 1.8 mmol/g-cell (1.8ODE-cell) into 1.8ODE-NC in LO followed by homogenization using sonication was investigated by using the mixture as a hydrophobic reinforcing coating for cellulose paper (CP) under varying temperatures and lengths of heating.

LO not only has structural similarity with ODE groups but also contains three bis-allylic hydrogen atoms (**Figure 4-1**), which are potentially capable of initiating oxidation-induced cross-linking among alkenes in FAs and ODE-NC.[8,9] Also, transesterification between FAs in LO and hydroxyls in CP and ODE-NC create a covalently-bonded surface coating on CP. Therefore, the mechanical strength of the coated paper was probed in connection with transesterification and cross-linking reactions among CP, LO and ODE-NC.

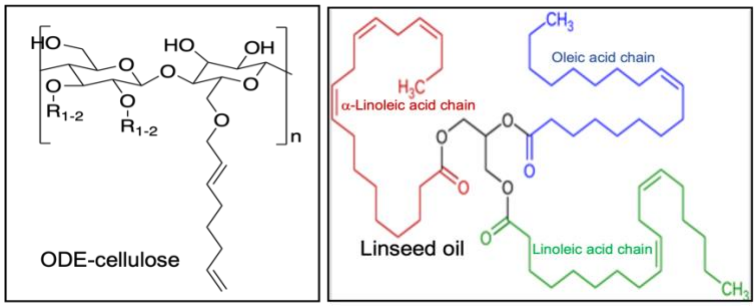

Figure 4-1. Structure of ODE-CNF and linseed oil.

4.3 Experimental

4.3.1 Materials

linseed oil (LO, Aldrich), PBD (MW200k-300k, Aldrich), PSIS (78% isoprene, Aldrich) were used as received without further purification were used as received without further purification. For other materials, please refer to Chapter 2, Section 2.3.1.

4.3.2 Telomerization Scale-Up

All telomerizations with 0.5 g cellulose were performed in a 500 mL stainless steel sealed autoclave reactor (HTR-00, Hydrion Scientific) equipped with a pressure gauge (200 psi max) and a digital temperature control with two thermocouples, one for the external temperature and the other for the internal liquid BDS temperature (**Figure 4-2**).

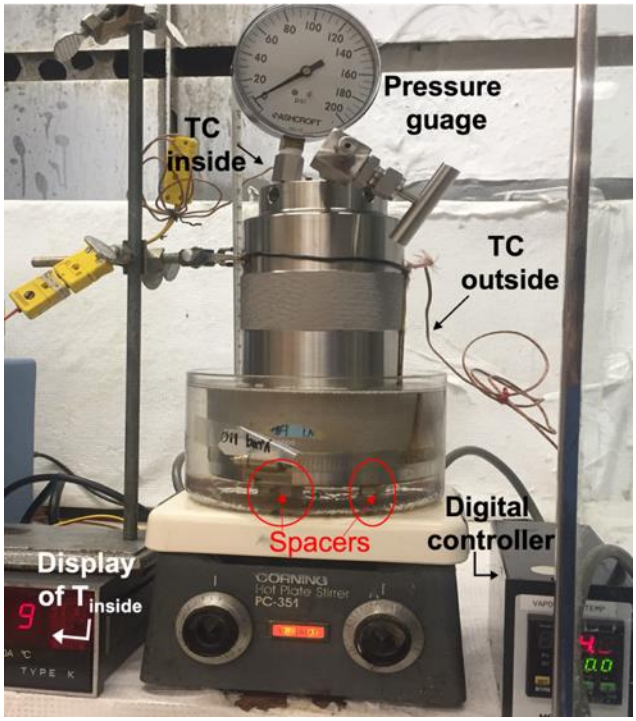

Figure 4-2. Set-up of temperature-controlled autoclave reactor for 0.5 g scale telomerization.

The optimal condition for telomerization of 1,3-BD with cellulose to generate ODE-cellulose reported in Chapter 2 was replicated in 0.5 g scale to reproduce the DS of 0.74 mmol ODE/g-cell. To optimize DS, 7 mL DMF was added to 0.5 g cellulose and the mixture was sonicated for 3 min at 50 % amplitude (*A*, ca. 7 kJ) in a 20 mL vial, then transferred to a Teflon reaction vessel with an extra 1 mL DMF to rinse the vial. For each reaction, 0.5 g cellulose (3

mmol AGU) was combined with 16.6 g of BDS (141 mmol), i.e., 7 mmol ODE (2 x 1,3-BD) from the conservatively-estimated 10 % conversion of BDS[1] to 1,3-BD. Using the reported 61.8 % CrI for rice straw cellulose[10], amorphous AGU in 0.5 g cellulose was *ca.*1 mmol. The ODE equivalence to the available AGU, or ODE:AGU ratio, became 6 and herein is abbreviated as 6ODE. The temperature was 100-110 °C at which BDS generates gaseous 1,3-BD (the telomerizing reagent) at a higher rate than at 90 °C. The palladium catalyst ($Pd(acac)_2$) used for coordination of two 1,3-BD into an eight-carbon chain, and the electron-rich TOMPP ligand used to modulate Pd activity, were as low as 0.023 mol% ([Pd] = 0.015 wt % of cellulose) and 0.092 mol% per mol AGU, respectively. Thus, the Pd needed is significantly lower than the 0.04 wt % used in telomerization of starch[11]. Upon 1 h telomerization where the pressure reached between 2.3-6.2 atm, the reactor was cooled in an ice bath and the reaction mixture was diluted with 30 mL acetone followed by vacuum filtration to obtain the product, ODE-cellulose. This product was then rinsed with 30 mL acetone in a centrifuge tube three times, vortexed (10 sec) and vacuum-filtered (3 times) to remove residual BDS, SO_2, and palladium complex. DS was calculated from the mass gain of ODE-cellulose (W_{ODE}) based on the average mass of cellulose obtained from heating BDS, without catalyst, under pressure at varying temperatures for 1 h. Exfoliation of cellulose removed 6.3 ± 1.3 wt %, leaving 93.3 ± 1.3 wt % or the base weight (W_{CB}) to calculate the yields from telomerization.

$$\text{DS (mmol ODE /g-cell)} = \left(\frac{\frac{W(ODE)-W(CB)}{MW(ODE)} x \frac{1000\ mmol}{mol}}{W(CB)} \right) \qquad \text{Eqn. 1}$$

Where weight (W) is expressed in grams (g), and MW(ODE) is 109 g/mol.

ODE-celluloses with the designated DS of 0.67 mmol ODE/g-cell, 1.2 mmol ODE/g-cell and 1.8 mmol ODE/g-cell are denoted as 0.67ODE-cell, 1.2ODE-cell, and 1.8ODE-cell.

4.3.3 Sonication

ODE-cellulose suspended in organic solvents (DMF, THF, $CHCl_3$, LO, toluene) was disintegrated by Q 700 (Q SONICA, LLC., output frequency 20 kHz), at 50 % *A* for the designated length of time. Volume of the organic solvents and the concentration of ODE-cellulose in the dispersions were kept constant in each experiment. Power (watt, W) was relatively constant between 40-50 W for all organic solvents except LO (50-60 W) for the designated amplitude (50 %). Ice bath was used to maintain the constant temperature at 25~30 ºC.

4.3.4 Characterization

The height of ODE-NC in $CHCl_3$ (10 mL, ca. 0.0005 w/v %) obtained from sonication (35-75 % *A*, 7-26 kJ) were measured by AFM on HOPG. $CHCl_3$ was selected as a sonication medium because the optimized ODE-NC[20] from blending were most compatible with $CHCl_3$, producing the highest quantity of ODE-NC and the highest ratio of CNFs/NPs by AFM (Asylum Research MFP-3D, Santa Barbara, CA). Please refer to Chapter 2, Section 2.3.4, for more detailed information about AFM imaging, and characterization of ODE-cellulose, cellulose paper and cellulose paper coated with ODE-CNFs/linseed oil by FTIR, TGA, XRD.

Crystallinity Index (CrI) was calculated by using the intensity of the 200 peak (I_{200}, 2θ = 22.6°) and the intensity minimum between the peaks at 200 and $1\bar{1}0$ (I_{am}, 2θ = 18.7°) as follows[12]:

$$\text{CrI} = \frac{I_{200} - I_{am}}{I_{200}} \times 100 \qquad \text{Eqn. 2}$$

4.3.5 tert-Butanol treatment

10 mg of ODE-cellulose (0.7 mmol ODE /g-cell) was wetted with 200 μL of tert-butanol (TB) and vortexed for 3 sec, followed by the addition of 10 mL $CHCl_3$, then sonicated at 50 % *A* for 20 min. 0.3 g ODE-cellulose was suspended and sonicated in 30 mL TB (at 50 % *A*, 20 min,

38 kJ), then lyophilized to produce a fluffy mass, which was vortexed in various solvents (THF, LO, toluene, and $CHCl_3$,). For the first three solvents, the next step was centrifugation to collect the supernatant, but for $CHCl_3$, gravitational separation was used.

4.3.6 Polymer nanocomposites

For film reinforcement, 3.3 g (i) polybutadiene (PBD) and (ii) PSIS were combined with previously sonicated (50 % *A*, 20 min, 45 kJ), 2 wt % 1.2ODE-cellulose (0.066 g, 0.079mmol ODE groups) and unmodified-cellulose (unmod-cell, 0.066 g) in toluene. Sonicated 1.2ODE-cellulose and unmod-cell were used as is (without separating into supernatant and precipitate) and are denoted as 1.2ODE-MC/NC or unmod-MC/NC, respectively. The amount of toluene used for the final cast solution was 33 mL and was evaporated in an oven at 70 °C overnight unless otherwise noted. For coating and reinforcement of cellulose paper, iii) 0.05 g of 1.8ODE-cellulose or unmod-cell was sonicated (50 % *A*, ca. 80 kJ) in 50 g LO for 20 min, and centrifuged (1.5 k rpm for 10 min) to collect the supernatant that contained 0.07 wt % 1.8ODE-NC or unmod-NC in LO to coat cellulose paper. Herein, all mass percentage (wt %) are abbreviated as %. Stress–strain tensile measurements of 1.5 cm x 5 cm rectangular specimens were performed on an Instron 5566, equipped with a 5.0 kN load cell, at a rate of 20 mm per min.

i) PBD

Cast films of PBD with 2 % 1.2ODE-NC/MC, 2% unmod-NC/MC and the control were prepared in toluene by varying sonication times for PBD as shown in Table 4-2.

Table 4-2. Reaction conditions for cast films using PBD.

Ingredients/Conditions	Abbreviation
PBD (10.0 w/v % in 33 mL toluene)	control
PBD (16.5 w/v % in 22 mL toluene), unmod-MC/NC in 11 mL toluene, stir 5 h	unmod20/PBD0
PBD (in 22 mL toluene), 1.2ODE-MC/NC in 11 mL toluene, stir 5 h	1.2ODE20/PBD0
PBD (in 22 mL toluene), 1.2ODE-MC/NC*	1.2ODE10/PBD10

PBD (in 33 mL toluene), dry 1.2ODE-cell**	ODE-cell/PBD20

* from sonicating 1.2ODE-cell (50 % *A*, 10 min, 23 kJ) in 11 mL toluene to produce 1.2ODE-MC/NC, then co-sonicating with PBD for 10 min
**co-sonicated (50 % *A*, 20 min, 74 kJ)

ii) Styrene-blk-isoprene-blk-styrene tri-block copolymer (PSIS)

Table 4-3 presents the variables and detailed processing methods used to examine the effect of ODE groups on reinforcing PSIS nanocomposite film with 1.2ODE-MC/NC by mixing or cross-linking with PSIS using AIBN.

The first set of conditions covered three controls, as detailed in Table 4-3. Pristine PSIS is denoted as control 1a; PSIS cross-linked with AIBN (6 mg, 0.037 mmol or 1:1 FR/ *t*-ene) is denoted as control 1b; PSIS mixed with the unmod-MC/NC is denoted as control 1c.

The second set of conditions was examined to determine the optimal amount of AIBN. Assuming the terminal alkenes (*t*-enes) at C7 of ODE groups in 1.2ODE-NC (0.079 mmol ODE) are more reactive than the internal alkenes at C2 of ODE groups, varied amounts of free radicals (FR) 0.036, 0.074 and 0.15 mmol, equivalent to 0.018, 0.037 and 0.073 mmol AIBN, were used to cross link all *t*-enes (0.079 mmol) with 0.2 % of isoprene-alkenes (38 mmol, *i*-enes) in 3.3 g PSIS. Thus, their mole ratio was presented as 0.5:1, 1:1 and 2:1 FR/*t*-ene, respectively, and denoted by **2a**, **2b** and **2c**. All cross-linking reactions with AIBN were performed under N_2.

The third variable was activation time of *t*-enes in 1.2ODE-NC (10 min, 1h) followed by the addition of PSIS to ensure that cross-linking takes place between *t*-enes and *i*-enes. Mixing AIBN (1:1 FR/*t*-ene) with ODE-MC/NC for 15 min was denoted as **3a**, and for 1h was denoted as **3b**.

The fourth variable was mixing time of ODE-MC/NC and PSIS in toluene with a stir bar.

The mixing times of 0.5 h, 5 h and 16 h were denoted as **4a**, **4b**, **4c**. The fifth condition was 3 % ODE-MC/NC in PSIS mixed for 16 h at r.t., denoted by **5**.

Table 4-3. Preparation and conditions for incorporating 1.2ODE-cell (2 %, 0.066 g) and unmod-cell in PSIS (98 w%, 3.3 g) in toluene (33.3 mL). Sonication of ODE-cell alone, and with PSIS, was performed at a constant amplitude, 50 % *A*, 20 min. AIBN cross-linking was conducted at 85 °C for 3 h unless otherwise noted.

Purpose	Variable	Method
1. Control	none	a) Stir PSIS at room temperature for 2h, then dry at 70 °C.
	AIBN	b) Stir & heat PSIS at 85 °C, add 6 mg AIBN (1:1 FR/*t*-ene), stir at 85 °C, 3h, dry at 70 °C.
	unmod-MC/NC, 0.5 h mix	c) Add unmod-MC/NC in 11 mL toluene to PSIS in 22 mL toluene at r.t. and mixing at r.t. for 0.5 h.
With 1.2ODE-MC/NC:		
2. **One-Pot x-linking:** To find an optimal AIBN amount	AIBN in 1~3 mL toluene	a) Add 3 mg AIBN (0.5:1 FR/*t*-ene) to the co-sonicated 1.2ODE-cell and PSIS in toluene, stir at 85 °C for 3h. b) Same as (2a) but with 6 mg AIBN (1:1 FR/*t*-ene) c) Same as (2a) but with 12 mg AIBN (0.5:1 FR/*t*-ene)
3. **Activation of *t*-enes / x-linking with *i*-enes:** To x-link *t*-enes and *i*-enes selectively (not to x-link among *i*-enes)	Activation time of *t*-enes	Add 6 mg AIBN (1:1 FR/*t*-ene) to 1.2ODE-MC/NC at 85 °C, then a) 10 min activation mixing, then adding PSIS to x-link for 2 h 50 min. b) 1 h activation mixing, then adding PSIS to x-link for 2 h.
4. Mixing by a stir bar: To examine a mixing effect without AIBN addition	Mixing time	a) Add 1.2ODE-MC/NC in 11 mL to PSIS in 22 mL in toluene and mix at r.t. for 0.5 h. b) Same as 4a, but mix at r.t. for 5 h c) Same as 4a, but mix at r.t. for 16 h
5. Same as 4	3 % ODE-MC/NC	Same as 4c, but with 3 % ODE-MC/NC in PSIS

iii) Cellulose paper coating with 0.07% ODE-NC in linseed oil

Cellulose filter paper (Whatman, qualitative, grade 1, ρ = 1.541 g/cm^3) (CP) was cut into 1.5 cm x 5 cm strips. CP strips were either as is, or covered with 500 mL of LO or 0.07 % unmodified-NC in LO. The excess LO was blotted by Kimwipes followed by drying at 70 °C for 8 h. Both were designated as controls. The experimental CP strips were immersed in 0.07 % ODE-NC, blotted, and dried at 70 °C for 8h, 16 h, 32 h, 64 h or dried for 16 h at 100 °C or 120 °C. CP strips were also immersed in 2.0 % ODE-MC/NC then dried at 85 °C for 16 h.

Unbound residual LO on CP was removed by rinsing with ethanol (five strips in 20 mL) by orbital shaker for 5 min. This was repeated with fresh ethanol each time until weight loss ceased. Typically, this took six to seven cycles. Acetone rinsing was conducted in the same manner. AFM samples of ODE-NC in LO were prepared by diluting 0.07 ODE/LO in toluene to 0.0005 w/v %. Water contact angles (WCA, 5 mL) of sessile drops on coated strips (control 2, 4a, 4b) were measured at 3 sec, 3 min and 20 min. The median value of q_{right} and q_{left} of a sessile drop was obtained by using ImageJ software, with contact angle plug-in software. WCA was triplicated in different locations to derive the average and the standard deviation. The density (ρ) of CP was calculated from the weighed mass and volume of a strip; porosity (ϕ) of the coated CP was calculated as:

$$\text{porosity } (\phi) = \left(1 - \frac{\rho_{ODE\text{-}LO}}{\rho(cell)} \right) \text{ x } 100\ \% \qquad \text{Eqn. 3}$$

Where ρ_{cell} is the density of pulp cellulose: 1.541 cm^3/g

Maximum absorption capacity was calculated based on porosity as follows:

$$Cm = \frac{\rho_{LO}}{\rho_{cell}} \cdot \frac{\phi}{1-\phi} \cdot 100\ \% \qquad \text{Eqn. 4}$$

Stress–strain tensile measurements of the 1.5 cm x 5 cm rectangular cellulose paper, and all ODE+LO coated cellulose paper strips, were performed in the same manner as those of PBD or PSIS composites.

4.4 Results and Discussion

4.4.1. ODE-cellulose disintegration into ODE-NC (0.74 mmol/g-cell) by sonication

The effect of sonication on disintegration of ODE-cellulose (0.74 mmol/g-cell) that was synthesized under the optimal condition of six mole equivalence of ODE at 110 ºC (6ODE110) for 1 h (100 mg scale)[1] in $CHCl_3$ was evaluated at 35, 50, and 75 % amplitudes for 5 and 10 min. At 5 min, as sonication energy increased (35-75 *A*, 7 kJ to 13 k), more nanoparticles (NPs, 60-90 %) with decreasing diameters (12.2-6.1 nm) and decreasing quantities of CNFs (40-10 %) with similar dimensions (T: 8.2 nm - 12.5 nm, L:1.9 - 2.0 μm) were produced (**Figure 4-3a, b**). At 10 min sonication, as energy increased (35-75 % *A*, 17 kJ to 26 kJ), the thickness of CNFs reduced to half (6.1 to 3.3 nm) and length reduced by two-thirds (1.7 to 0.5 μm), while the diameters of NPs stayed statistically constant between 2.9 ± 1.3 nm and 5.0 ± 2.0 nm (**Figure 4-3a, b**). This is consistent with the observation elsewhere that there is a minimum nanoparticle size below which degradation does not take place by sonication[13]. At 17 kJ sonication (50 % *A*), the submicron particulates (diameter of ca. 35.8 nm) are observed in the AFM image at ~60 % of the area compared to 40 % combined CNFs and NPs. However, at 20-26 kJ, the submicron particulates were no longer observed and the ratio of NPs to CNFs had dropped to 50 %/50 %, indicating their disintegration.

The corresponding precipitates contained microfibers which also showed reduced width and length as energy increased from 10 to 26 kJ (**Figure 4-3c, d**). These results proved the concept

that ODE-cellulose could be disintegrated by direct sonication (35-100 *A*, 5 or 10 min) in $CHCl_3$ into ODE-NC. However, the ODE-NC yields were low at 13, 13, and 18 % at the relatively low energies of 17, 20, and 26 kJ, respectively.

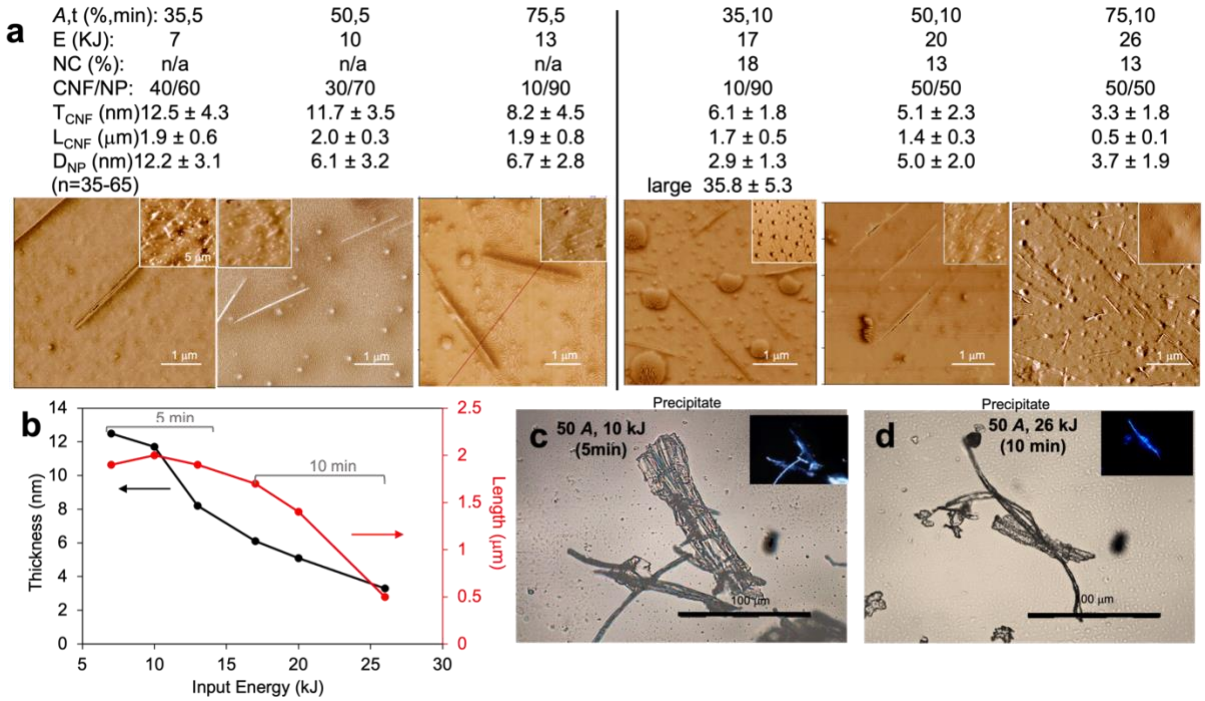

Figure 4-3. Effect of sonication on ODE-cellulose (6ODE110, 0.74 mmol ODE/g-cell synthesized by 0.1 cellulose scale) in $CHCl_3$ (0.1 w/v %): (a) AFMs of ODE-NC (CNF/NP) (0.001 w/v % for 5 min and 0.0005 w/v % for 10 min) on HOPG; (b) ODE-CNF thicknesses (T) and lengths (L) based on AFM images (n=30-100) as a function of sonication energy; (c) optical microscopic images of precipitates from sonication at 10 kJ and 26 kJ.

4.4.2 Scale-up

The synthesis of ODE-cellulose was optimized and scaled up from 0.1 g cellulose in 100 mL to 0.5 g cellulose in a 500 mL autoclave reactor. (**Figure 4-2**)

First, the decomposition rates of 16 g BDS in the presence of 0.5 g cellulose in the sealed reactor without the catalyst was determined by the percentage of the internal pressure over the maximum possible pressure (19 atm) upon heating at each temperature for 1 h. In a typical reaction, the pressure started to rise at around 95 °C and the rate of BDS decomposition accelerated between

100 and 105 °C and then plateaued at 106 °C, showing a linear BDS decomposition rate with increasing temperatures to a maximum 35.4 % at 106 °C. The temperature reached 90 °C in 20 min, at which point evolution of 1,3-BD became rapid, and the telomerization reaction was carried out for 40 min. This length of time is ample, consistent with the reported time needed for telomerization of 1,3-BD with carbohydrates and sugar alcohols[14].

By heating cellulose with BDS at varying temperatures without Pd in situ for 1 h (blank telomerization), 6.3 ± 1.3 % mass loss of cellulose was observed (**Figure 4-4a**) due to exfoliation, leaving 93.7 ± 1.3 % or the base weight to calculate the yields from telomerization with Pd. The yield of ODE-cellulose increased with increasing temperatures from 100 to 113 °C which corresponds to the availability of 1,3-BD, reaching up to 113 wt % with the degree of substitution (DS) with 1.2 mmol ODE/g-cell (**Figure 4-4b**) by mass gain (**Eqn. 1**). DS was derived by mass gain of ODE-cellulose based on the base weight, divided by MW of ODE (109 g), then further divided by the base weight. (**Eqn. 1**). However, the product with 1.2 mmol ODE/g-cell were brownish due to decomposed carbohydrates, thus the product with 0.67 mmol/g-cell (0.67ODE-cell) obtained at the average temperature of 107 °C is optimal. This DS is 10 % lower than the 0.74 mmol ODE/g-cell from the 0.1 g scale reaction under the same conditions, demonstrating the validity of the scale-up reaction.

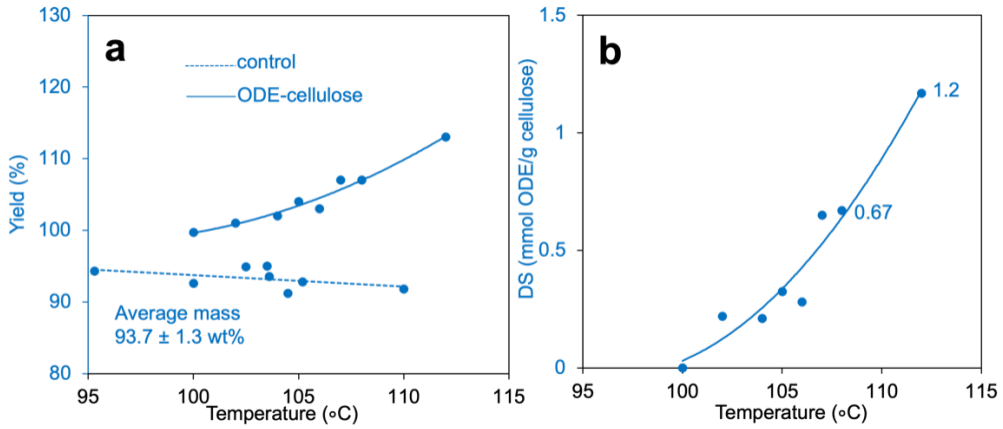

Figure 4-4. Effect of telomerization temperature on scale-up telomerization of 0.5 g cellulose: (a) % mass yield of control (no Pd) and ODE-cellulose; (b) degree of substitution (DS) of ODE-cellulose.

4.4.3 Optimization of disintegration by sonication

Direct sonication (50 % *A*) of 0.1 w/v % 0.67ODE-cell in THF, $CHCl_3$, linseed oil (LO) and toluene produced increasing quantities of ODE-NC with increasing sonication energy and time. Also, at 42 kJ (50*A*) for 20 min and 62 kJ (50*A*) for 30 min, quantities were greater using $CHCl_3$ than THF. $CHCl_3$ and toluene produced a similar quantity of ODE-NC, but for a given sonication time, toluene required more energy (62 kJ instead of 42 kJ at 20min, and 95 kJ instead of 62 kJ at 30 min, 50*A*) (**Figure 4-5a**). The higher quantity of ODE-NC in THF at 10 min may indicate that less functionalized ODE-NC was exfoliated in the first 10 min. Most importantly, sonication produced the same quantity of ODE-NC in $CHCl_3$ and toluene in shorter time (20 min) and in one step as those dispersed from blended aq. precipitate for 30 min[1] (**Figure 4-5b, c**). Thus, direct sonication in organic liquids was proven more effective than aq. blending.

Sonicating (20 min, 42-84 kJ) tert-butanol (TB) wetted ODE-cellulose in THF, $CHCl_3$, LO, and toluene (ca. 2 v/v% TB) improved ODE-NC yields to 28, 52, 66, and 37 % as compared to 18, 31, 47, and 30 % by direct sonication in the respective solvents (**Figure 4-5b, c**) with the highest increase in LO by 19 %. Pre-wetting with 5 v/v% TB did not further improve the ODE-NC yields. ODE-cellulose was also sonicated in TB (50 % *A*, 20 min, 38 kJ) and lyophilized to a fluffy mass, then vortexed in THF, $CHCl_3$, LO, and toluene to disperse 31, 57, 65, and 41 % ODE-NC, similar to those pre-wetted with TB (**Figure 4-5c**). Despite some advantages of lyophilized powdery nanocelluloses (they are readily dispersible in any liquids and convenient to transport), the lyophilization process requires more energy. Thereby, simply pre-wetting ODE-cellulose with TB

at ca. 2 v/v% was the optimal condition for improving the yield of ODE-NC in moderately to more hydrophobic organic solvents, and most impressively in LO.

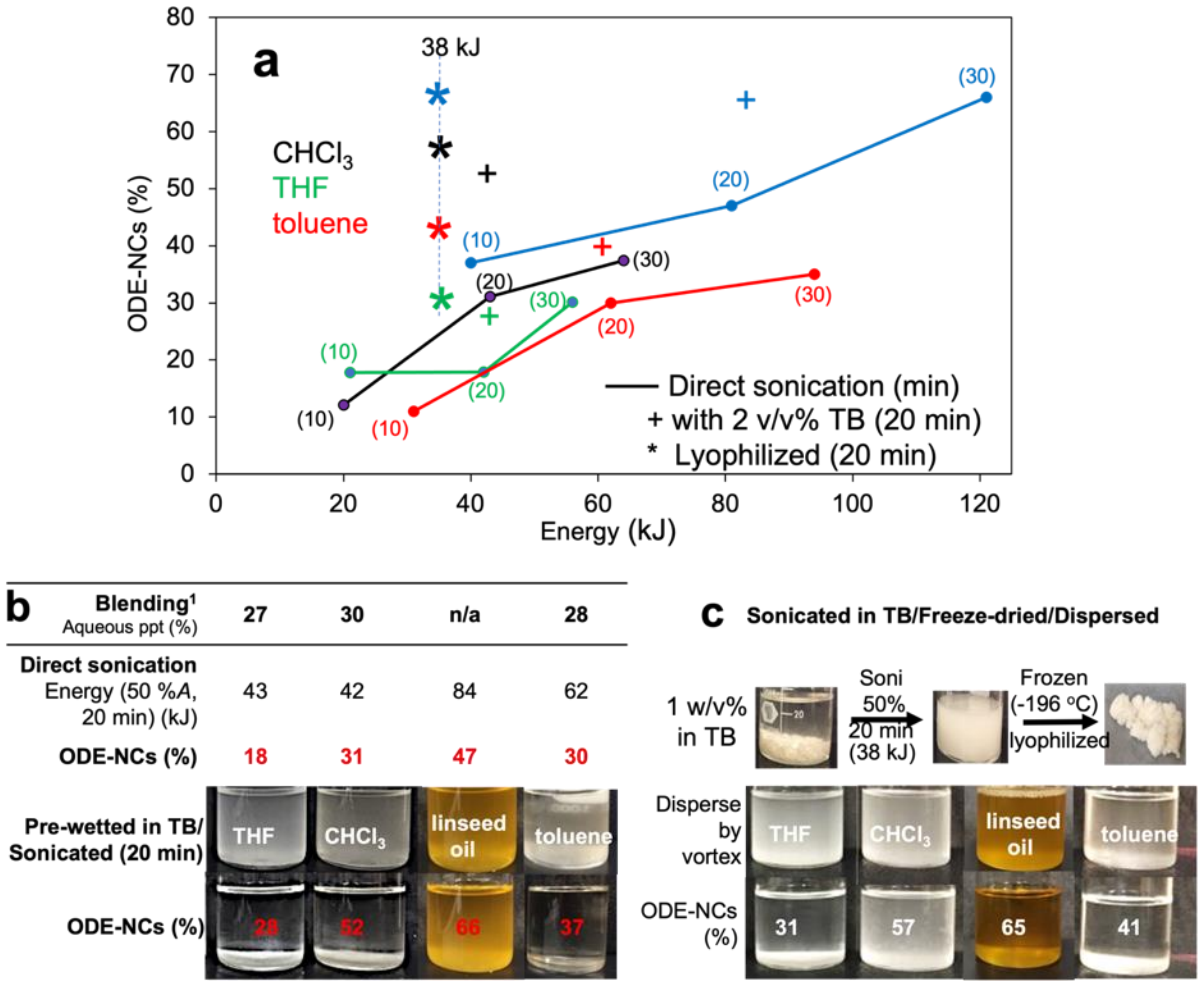

Figure 4-5. Optimization in generation of ODE-NC (0.1 w/v %) in organic liquids by sonication (50 % *A*, 10, 20, 30 min) of ODE-cellulose (6BED110, 0.67ODE) directly, pre-wetted with 2 v/v%: (a) % ODE-NC as a function of sonication energy (kJ), TB (+), or sonicated in TB & lyophilized (*). % ODE-NC dispersible in the organic liquids:(c) from direct sonication, from sonication of pre-wetted ODE-cellulose with 2 v/v%, (d) from sonication of ODE-cellulose in 100% TB and lyophilization.

4.4.4 Optimization of DS by pre-sonication of cellulose

Sonication (50 *A*, 3 min, 70 kJ) of cellulose in DMF reduced the 100+ μm wide fiber bundles to ca. 10 μm wide fibers in 1 min, then to single swollen fibers in 3 min (**Figure 4-6 inset photo**).

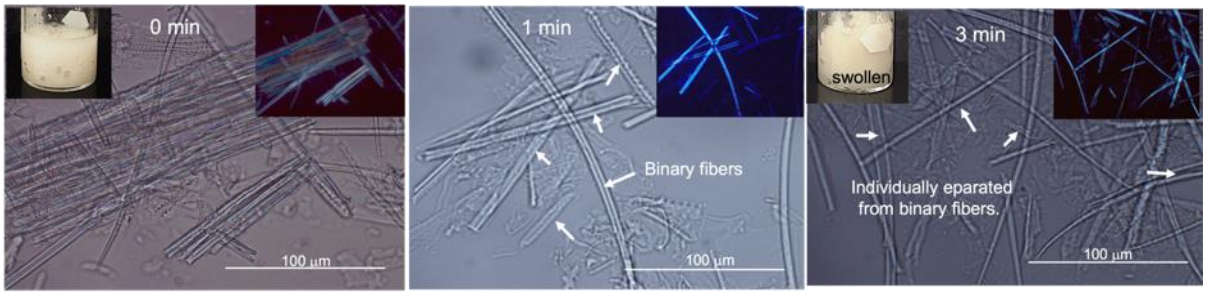

Figure 4-6. Optical microscopic images of cellulose (0.5 g) sonicated (50 % *A*, 0, 1 or 3 min, 2 or 7 kJ) in DMF (7 mL) with arrows indicating separated binary (middle) and individual fibers (right).

The yields from blank telomerization of pre-sonicated cellulose was 91.2 ± 2.1 wt % which was ca. 2% less than those from telomerization of cellulose without pre-sonication under the same conditions due to the increased exfoliation. This yield was used as the base weight to calculate yields. ODE-cellulose mass increased rapidly and more significantly as temperature increased, reaching higher yields than those without pre-sonication at similar temperatures (**Figure 4-7a**). Telomerization of cellulose briefly sonicated in DMF resulted in a much higher DS of 1.2 mmol ODE/g-cell (1.2ODE-cell) and 1.8 mmol ODE/g-cell (1.8ODE-cell) at the average temperature range between 103 and 110 ºC, respectively, as compared to 0.67 mmol/g-cell (0.67ODE) obtained at 107 ºC without pre-sonication. Moreover, longer reaction times of 1.5 h and 2 h at 110 ºC increased the DS to 3.1ODE-cell and 4.1ODE-cell, respectively (**Figure 4-7b**). This confirms that pre-sonication in DMF separated and swelled individual fibers, thus improving diffusion of reagents deep into the fibrils.

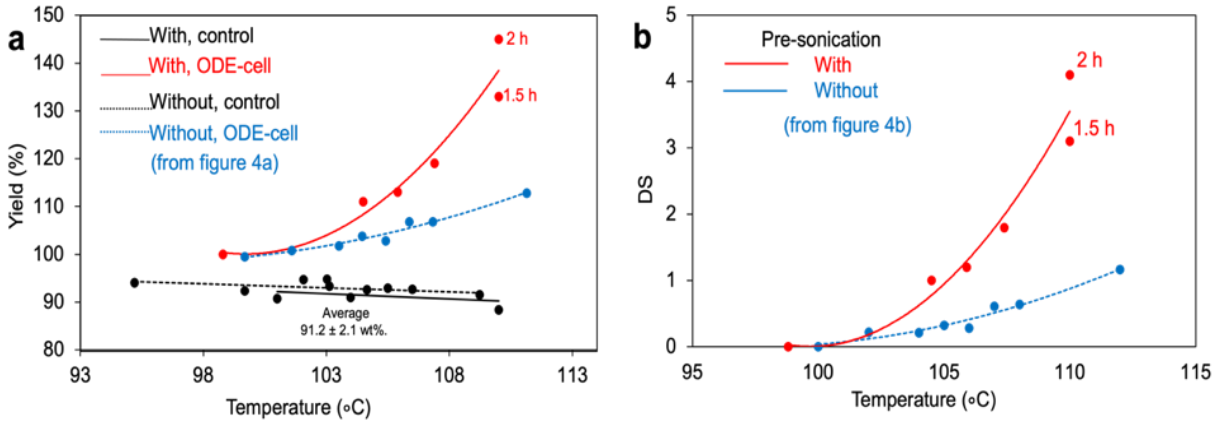

Figure 4-7. Effect of pre-sonication of cellulose in DMF on telomerization (6ODE, 1h) to ODE-cellulose on: (a) % mass yield of control (no Pd) and ODE-cellulose with or without pre-sonication; (b) DS of ODE-cellulose with or without pre-sonication.

In the FTIR, the presence of ODE groups with ether linkages to cellulose was shown by C-O-C bend at 1100 cm^{-1}, and =C-H stretch at 3049 cm^{-1}. All intensified with increasing DS, while a very small shoulder peak for the C=C stretch appeared next to the water peak at between 1640-1704 cm^{-1} (**Figure 4-8a**). Sharp peaks distinctive to cellulose are seen at 897 cm^{-1}, 1640 cm^{-1}, 2896 cm^{-1}, and 3363 cm^{-1}, representing the β-glycosidic C1-O-C4 deformation, residual water, aliphatic C-H, and OH groups, respectively. In XRD, the CrI of the most highly telomerized 3.1ODE-cell and 4.1ODE-cell was significantly reduced to 25.0 % and 9.8 %, respectively, from the 60.3 % CrI of the original cellulose (**Figure 4-8b**). Furthermore, the cellulose Iβ characteristic peaks at 14.7º, 16.8º, and 22.6º disappeared, while an emerging peak coincided with the regenerated cellulose II[15] at 20.5º, showing loss of cellulose Iβ to possibly cellulose II crystalline structure as a result of high substitution. 1.8ODE-cell preserved the majority of the crystallinity (CrI = 43.8 %) of the original cellulose, and a small sign of an evolving peak at 20.5º suggests that this is the highest DS with cellulose Iβ crystalline form. The moisture contents of ODE-cellulose were also reduced to 0.8 and 2.5 % for 1.8ODE-cell and 1.2ODE-cell, respectively, consistent with the less hygroscopic nature of ODE groups as their quantity increases. Similarly, the Tmax of cellulose (353 ºC) was

lowered to 320 ºC and 310 ºC for 1.2ODE-cell and 1.8ODE-cell, respectively, reflecting the heat labile nature of ether linkage at the elevated temperature. However, the Tmax is much higher than the 265 °C Tmax of TEMPO-CNF[16] (**Figure 4-8c**). Brief 3 min sonication of cellulose in DMF was highly effective in improving telomerization of 1,3-BD with cellulose, reaching a DS of up to 1.8 mmol ODE/g-cell with largely-preserved crystallinity and negligible moisture absorption.

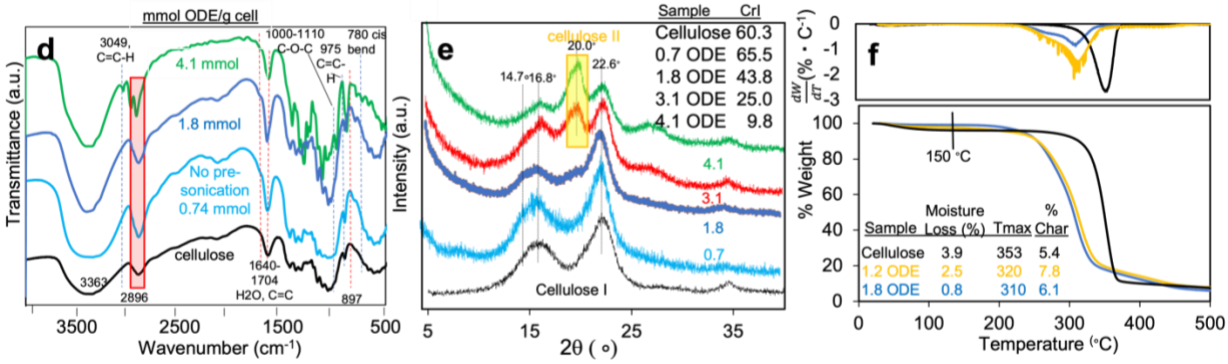

Figure 4-8. Characteristics of ODE-cellulose from telomerization of pre-sonicated cellulose: (a) FTIR; (b) XRD; (c) TGA and *d*TGA.

4.4.5 1.2ODE-NC by sonication in toluene

Sonication (50 % *A*) of 1.2ODE-cell and 1.8ODE-cell (0.1 w/v %) in toluene, a common solvent for PBD and PSIS elastomers, produced increasing yield of 1.2ODE-NC with increasing time and energy. As **Figure 4-9a** shows, the yield increase of 1.2ODE-NC was especially impressive for the increase in time from 10 min (31 kJ, 50 *A*) to 20min (62 kJ, 50 *A*).

The microfibers in the precipitate appeared individually separated in toluene, but aggregated as they dried on the hydrophilic glass, indicating their functionalized surfaces (**Figure 4-9b, inset**).

In AFM images, 1.2ODE-NC obtained from 20 min sonication (60 kJ, 50 *A*) appeared as 10-40 nm diameter particulates on hydrophilic mica (**Figure 4-9c**), indicating their hydrophobicity and incompatibility with mica. On more hydrophobic HOPG, four morphologies were observed.

Three of the four (ca. 75 % by area) were either (1) as an inter-connecting fibrillar network (T:1.0 ± 0.3 nm) (**Figure 4-9d**)**,** or (2) as individual straight and curly CNFs (T:1.3 ± 0.5 nm) **(Figure 4-9e**), or (3) as much thicker, wiggly CNFs (T:12.8 ± 3.3 nm) due possibly to multiple fibrils stacking up (**Figure 4-9f**). The fourth morphology, i.e., the remaining ca. 25 % of 1.2ODE-NC, were NPs (diameter 8.6 ± 2.9 nm), indicating a less hydrophobic surface than the other fibrils (**Figure 4-9g**). The varied thicknesses of ODE-CNFs (1.0 ~ 12.8 nm) and a tendency of curling may be attributed to unevenly distributed ODE groups on 1.2ODE-CNF surfaces. The product using sonication in toluene has far more 1.2ODE-CNFs than NPs (ratio 75:25), thus it is a far higher quality product than the 0.74ODE-NC[1] (with virtually no CNFs) obtained by mechanical blending (**Table 4-1**).

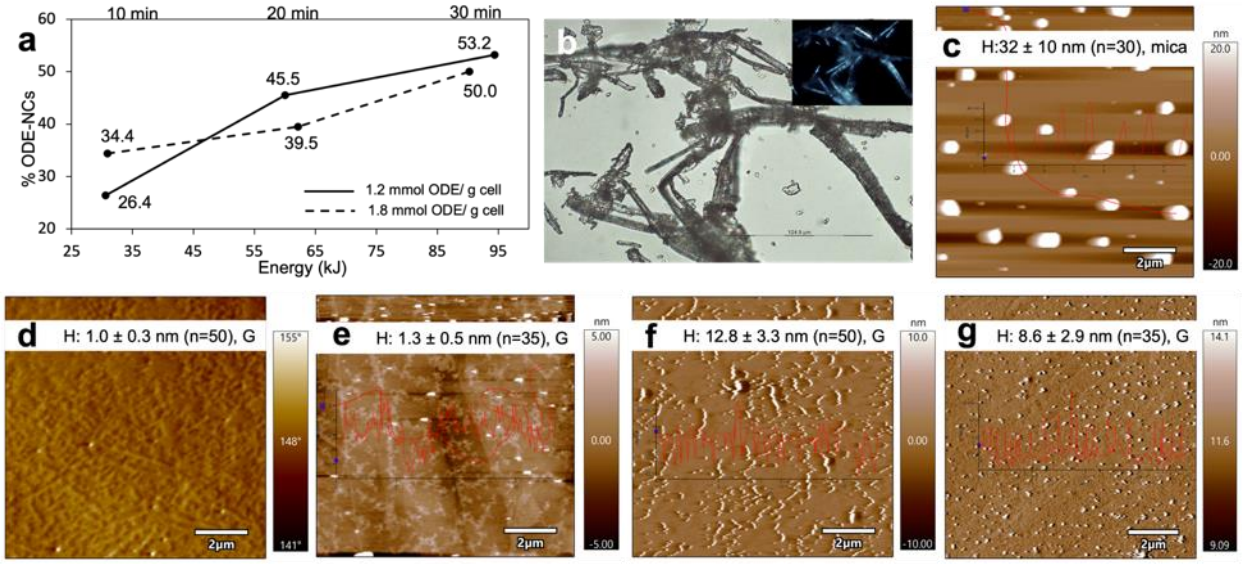

Figure 4-9. Sonication (50 % *A*, 10, 20 and 30 min) of 1.2ODE-cell and 1.8ODE-cell in toluene: (a) % 1.2ODE-NC in toluene as a function of sonication energy at 30, 60, 90 kJ. (b) optical microscope image of the precipitate from the sonicated (20 min) 1.2 ODE-cell, dried on glass. Inset images were taken by crossed polars. AFM images of 1.2ODE-NC: (c) on mica at 0.001 w/v %; (d, e) on HOPG at 0.05 %; (f, g) on HOPG at 0.001 %.

4.4.6 Effects of ODE-NC on mechanical strength of polymer composite

To examine the effect of ODE groups in 1.2ODE-MC/NC on reinforcing a PBD nanocomposite film, 1.2ODE-MC/NC was combined with PBD (sonicated at 50 *A* for 0, 10, and 20 min) (**Figure 4-10**), and designated as 1.2ODE20/PBD0, 1.2ODE10/PBD10, and 1.2ODE-cell/PBD20.

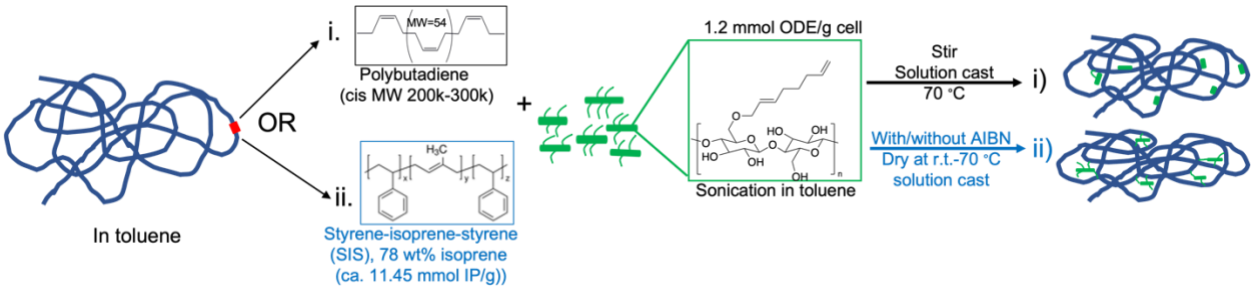

Figure 4-10. Nanocomposite film of 2 % 1.2ODE-NC in PBD or PSIS.

1.2ODE20/PBD0 exhibited the highest modulus (2.23 ± 0.34 MPa) and yield strength (0.15 ± 0.04 MPa), over 6- and 2-fold higher than those of the control, respectively, without sacrificing the strain (**Figure 4-11, Table 4-4**). While the unmod20/PBD0 film exhibited an excellent modulus (0.63 ± 0.07 MPa) and yield strength (0.11 ± 0.07 MPa), these were only a fraction of those from 1.2ODE20/PBD0, evidence of the enhanced interfacial affinity between 1.2ODE-MC/NC and PBD due to the surface ODE groups via overall Van Der Waals/London dispersion interactions.

As PBD sonication time increased to 20 min (1.2ODE-cell/PBD20), the modulus doubled and the ultimate strength tripled, compared to that of the control, but the strain was only a fraction of the control. The resulting plastic characteristics (**Figure 4-11b**) suggested chain scission of PBD due to extended sonication (23~74 kJ). This also agrees with the clearer film appearance of 1.2ODE-cell/PBD20 compared to that of 1.2ODE20/PBD0 or the control (**Figure 4-11b inset).**

These data suggest that sonication longer than 10 min (50 *A*) may damage polymers, and ODE-MC/NC is effectively homogenized with PBD by stirring without using sonication energy.

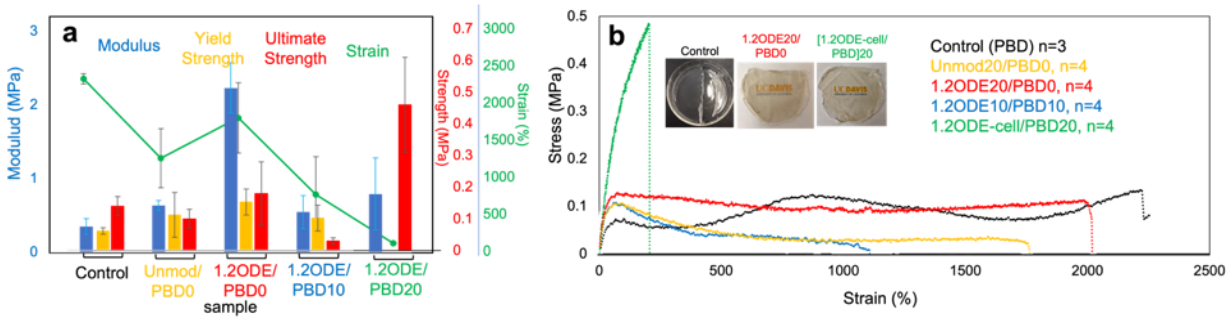

Figure 4-11. Effect of 2 % 1.2ODE-NC on the tensile properties of 1.2ODE-NC/PBD nanocomposites: (a) modulus, yield strength, ultimate strength, and strain; (b) representative stress-strain curves.

Table 4-4. Tensile properties of PBD nanocomposite with 2 % 1.2ODE-MC/NC.

PBD (Sonication Time)	Modulus (MPa)	Strength (MPa)		Strain (%)
		Yield	ultimate	
PBD	0.35± 0.11	0.06 ± 0.01	1) 0.13 ± 0.08 2) 0.14 ±0.03	2200 ± 70
Unmod20/PBD0	0.63 ± 0.07	0.11 ± 0.07	0.10 ± 0.03	1300 ± 400
1.2ODE20/PBD0	2.23 ± 0.34	0.15 ± 0.04	0.18 ± 0.10	1800 ± 500
1.2ODE10/PBD10	0.55 ± 0.23	0.10 ± 0.04	0.03 ± 0.01	800 ± 500
1.2ODE-cell/PBD20	0.79 ± 0.49	n/a	0.46 ± 0.15	110 ± 5

Table 4-4 is based on the average of three experimental results.

1.2ODE-MC/NC was also incorporated with PSIS at 2 % with a varied amount of metal-free radical initiator, AIBN (**Table 4-5**). With increased AIBN from 0.5:1 to 1:1 FR/*t*-ene molar ratio, the modulus (8.0 ± 1.6 MPa) increased by 27.0 % with respect to that of 1:0.5 FR/*t*-ene (6.3 ± 1.9 MPa), and by 63 % in comparison to those of both controls, control 1a (4.8 ± 0.6 MPa) and control 1b (4.9 ± 0.6 MPa), respectively, while the ultimate strength and the strain were unaffected statistically, indicating improved cross-linking between 1.2ODE-NC and PSIS by 1:1 FR/*t*-ene **(Figure 4-12a, c**). Further increasing AIBN to 2:1 FR/ *t*-ene produced a very sticky glass-adhering

film with a fraction of the strength and the strain of the control, without affecting the modulus (**Table 4-5**), possibly due to AIBN-induced PSIS decomposition[17] and chain scission of PSIS by excess AIBN. Thus, the optimal AIBN quantity was 1:1 FR/*t*-ene molar ratio (**Table 4-5**).

Table 4-5. Moles of alkenes in 1.2ODE group and PSIS.

AIBN **3mg: 0.02 mmol** **6mg: 0.04 mmol** **12mg: 0.08 mmol**	**Mass (g)**	**ODE group or I (mmol)**	**Total alkenes (mmol)**	***t*-enes, *i*-enes (mmol)**	**FR/t-ene or FR/i-ene**		
					0.04 mmol FR	**0.08 mmol FR**	**0.15 mmol FR**
1.2 mmol ODE/g -cell	0.07	0.08	0.16	0.08	0.5:1	1:1	2:1
PSIS (78 % isoprene = I)	PSIS: 3.3 I: 2.6	38	38	38	0.001:1	0.002:1	0.004:1

$MW_{(AIBN)}$ = 164 g/mol; $MW_{(I)}$ = 68.1 g/mol
FR: free radical, *t*-enes: terminal alkenes in 1.2ODE group's, *i*-enes: alkenes in isoprene.

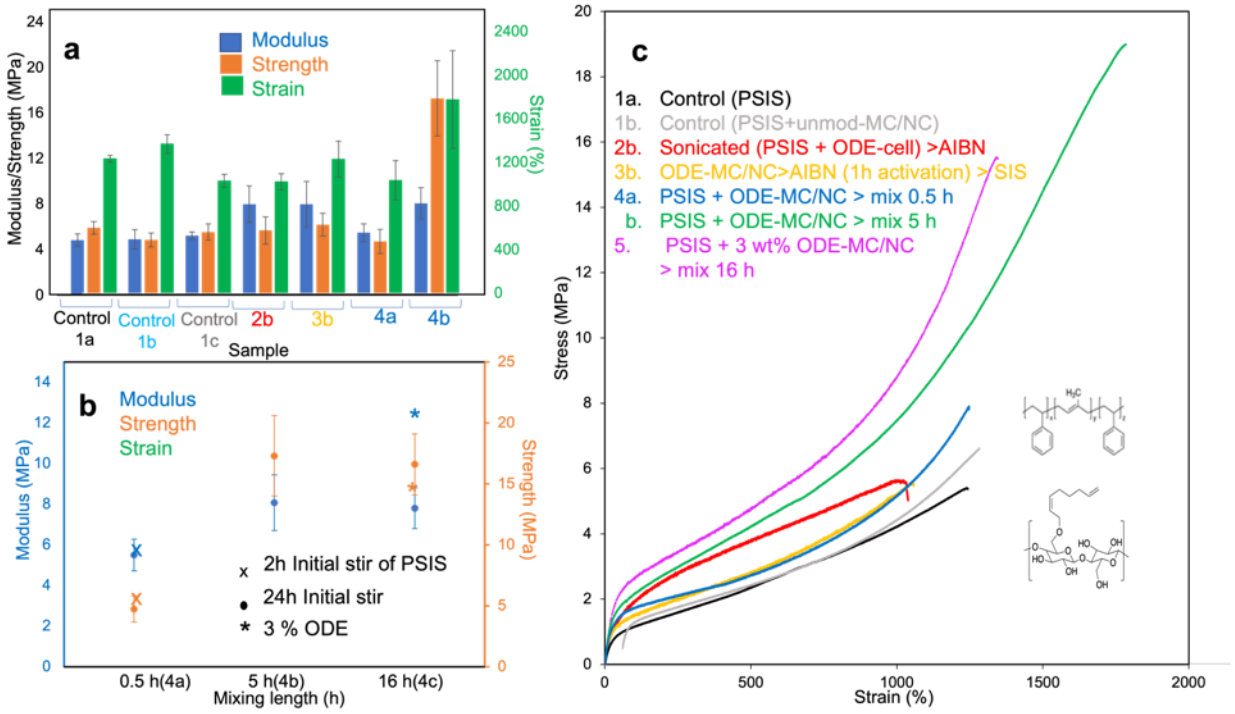

Figure 4-12. Effect of the sonicated 1.2ODE-cellulose with PSIS: (a) mol ratios of 1.2ODE-alkene and PSIS-alkene; (b) varied processing methods; (c) varied mixing lengths; (d) typical stress-strain curves.

Table 4-6. Stress-strain characteristics of 1.2ODE-NC/MC effects on PSIS copolymers with and without initiator AIBN and from different preparation conditions.

Purpose	Condition	Modulus (MPa)	Strength (MPa)	Strain (%)
1. Control	a. Pristine	4.8 ± 0.6	5.9 ± 0.6	1200 ± 30
	b. AIBN	4.9 ± 0.9	4.9 ± 0.6	1400 ± 90
	c. Unmod, (0.5 h mix)	5.3 ± 0.3	5.6 ± 0.7	1000 ± 60
With 2 % 1.2ODE-MC/NC:				
2. Optimum AIBN in x-linking	a. 0.5:1 FR/t-enes	6.3 ± 1.9	6.0 ± 1.0	1200 ± 50
	b. 1:1 FR/t-enes	8.0 ± 1.6	5.7 ± 1.2	1000 ± 70
	c. 2:1 FR/t-enes	5.1 ± 1.0	1.0 ± 0.1	300 ± 50
3. x-linking between *t*-enes and *i*-enes	a. 10 min	3.34	0.836	400
	b. 1 h	8.0 ± 2.0	6.2 ± 1.0	1200 ± 200
4. Effect of mixing.	a. 0.5 h	5.8 ± 0.9	4.2 ± 1.3	1000 ± 80
	b. 5 h	8.1 ± 1.4	17.3 ± 3.3	1800 ± 48
	c. 16 h	7.8 ± 1.0	16.6 ± 2.5	1800 ± 400
5. 3 % 1.2ODE-MC/NC	16 h mixing	13.5 ± 0.5	15.2 ± 1.5	1200 ± 100

t-Enes in 1.2ODE-MC/NC were activated for varied times (10 min and 1h) with the optimal amount of AIBN (1:1 FR/*t*-ene) at 85 °C for 15 min, followed by the addition of PSIS. The short 10 min mixing produced a very sticky glass-adhering mass with a fraction of the strength and the strain shown by control 1a and control 1b. On the other hand, increasing mixing time to 1 h increased the modulus (8.0 ± 2.0 MPa) by 67 % and the strength (6.2 ± 1.0 MPa) by 5 %**,** similar to the results from 2b (**Table 4-6.2)**, but with 20 % higher strain. This observation may indicate that the AIBN activation of *t*-enes for 1 h followed by PSIS addition, and the addition of AIBN to the mixture of 1.2ODE-MC/NC and PSIS, resulted in similar reinforcement, implying that *t*-enes may be more reactive toward AIBN than *i*-enes. Increasing AIBN to 2:1 FR/*t*-ene, keeping 1 h mixing constant, resulted in a sticky mass consistent with the observation of 2c (**Table 4-6.2)**. Thus, activation of *t*-enes by 1:1 FR/*t*-ene AIBN for 1 h (**Table 4-6.3)** showed the optimum reinforcing effect.

Mixing 1.2ODE-MC/NC and PSIS in toluene without AIBN for a short time (0.5 h) improved the modulus by 20.8 % with respect to that of the control 1a, and by 9.4 % compared with that of control 1c, without affecting the strength and strain, indicating the better interfacial adhesion of 1.2ODE-MC/NC compared with unmod-MC/NC surface with PSIS. A remarkable improvement was observed at the longer 5 h mixing time (**Table 4-6.4**), i.e., longer mixing time nearly tripled the strength to 17.3 ± 3.3 MPa compared with the two controls (0.5 h mixing), and the modulus and the strain improved to 8.1 ± 1.4 MPa and 1800 ± 400 %, respectively. Further lengthening the mixing time to 16 h (**Figure 4-12b**) did not lead to further improvement. Increasing 1.2ODE-MC/NC content to 3 % with 16 h mixing further improved the modulus (13.5 ± 0.5 MPa) by 66.7 % with respect to that of 5 h mixing, but the strength and the strain did not improve. Mixing for 5 h was deemed the optimal mixing time. Clearly, longer mixing improved the reinforcement of the PSIS nanocomposite films with 1.2ODE-MC/NC, likely by separation and re-orientation of polymer chains, forming the homogenized mixture with 1.2ODE-MC/NC.

4.4.7 Dispersibility and morphology of 1.8ODE-NCs in linseed oil

Sonication (50% *A*, 20 min, 84 kJ) of 1.2ODE-cell in LO yielded 52.9 % ODE-NC, higher than the 47 % from 0.67ODE-cell but lower than the 66 % from TB wetted 0.67ODE-cell (**Figure 4-5f, g**). Sonication (50 % *A*) of 1.8ODE-cell yielded a remarkable 67.9 % of 1.8ODE-NC in only 10 min. The yield increased moderately to 73.3 % at 20 min (84 kJ) and plateaued at 76.1 % at 30 min (120 kJ) (**Figure 4-13a**). The precipitate from 20 min sonication showed the most individually-separated (least aggregated) microfibers when diluted in toluene, compared to acetone and ethanol (**Figure 4-13, b-d**). AFM images of 1.8ODE-NC in LO, created by dilution in toluene to 0.0005 w/v % and deposition on HOPG (**Figure 4-13e, f**), showed residual LO-covered

nanofibrils with 15.0 ± 5.8 nm (n=50) thickness. By subtracting the thickness of LO droplets (11.6 ± 2.6 nm, n=20) prepared in the same manner, 1.8ODE-NC has an estimated thickness of ca. 3.4 nm.

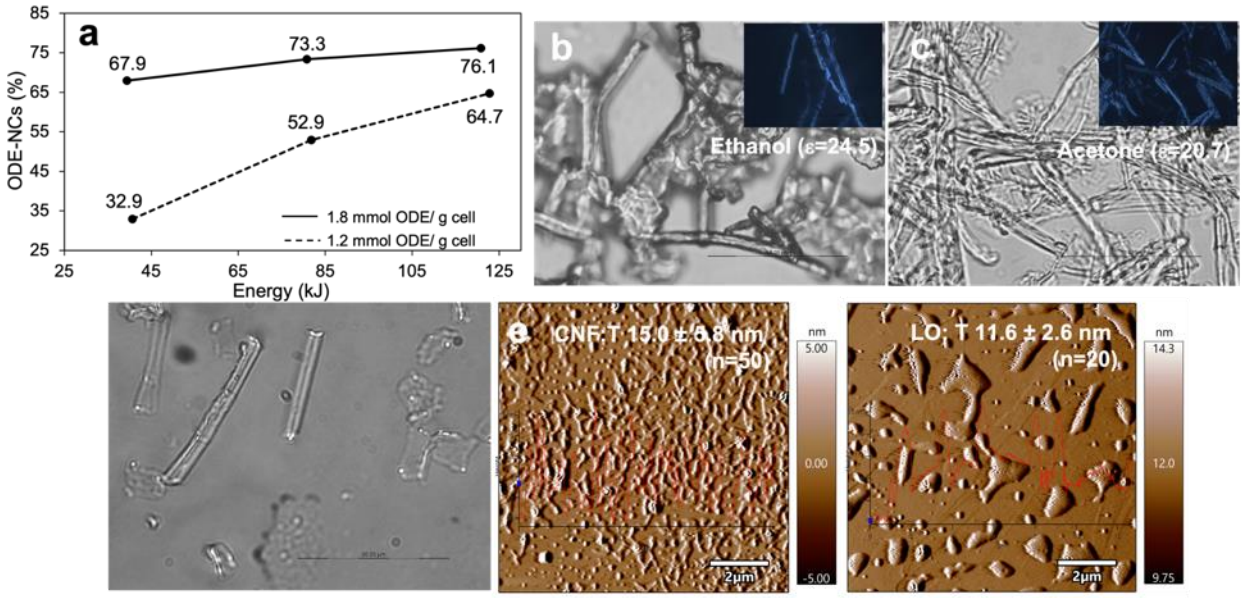

Figure 4-13. Sonication (50 % *A*) of 1.2ODE-cell and 1.8ODE-cell in linseed oil (LO): (a) weight % 1.2ODE-NC and 1.8ODE-NC from 10, 20 and 30 min or 40, 84, 120 kJ; optical microscopic images of precipitate from sonication (20 min; 84 kJ) of 1.8ODE-cell diluted in (b) ethanol, (c) acetone and (d) toluene; AFM images of ODE-CNFs (e) and LO (f) both diluted in, and dried from, toluene (0.0005 w/v %) on HOPG.

4.4.8 Reinforcing effect of 1.8ODE-NC in LO for cellulose paper

The mechanical strength and surface hydrophobicity of the paper coated with 1.8ODE-NC in LO were studied in connection with transesterification and cross-linking reactions among CP, LO and 1.8ODE-NC. CP imbedded with 0.07 % 1.8ODE-NC/LO (*ca.* 85 % add-on weight of NC/LO on CP) and heated under various temperatures (70-120 °C) for varied times improved the modulus, strength, and strain (**Table 4-7**). The LO-coated CP (control 2) showed some improvement in strength and strain in comparison with CP (control 1), indicating the reinforcing effect of LO by itself (**Figure 4-14a**). By adding 0.07 % 1.8ODE-MC/NC to LO, a significant improvement in strength (24.6 ± 0.5 MPa) and strain (6.4 ± 0.4 %) over those of control 2 was

observed. Doubling the heating time to 16 h increased the modulus and the strength further to 1.16 ± 0.09 GPa and 26.7 ± 0.8 MPa, respectively. On the other hand, the unmod-NC (control 3, 8 h heat) resulted in much lower strength and strain than those of 4a and 4c in **Table 4-7**, indicating 1.8ODE-NC's superior interfacial adhesion to FAs in LO compared with unmod-NC. Also, the lower strength of unmod-NC/LO (control 3) compared to LO (control 2) may suggest unmod-NC interfered with possible cross-linking among FA in LO. Neither increasing heating time nor temperature showed any noteworthy improvement (**Figure 4-14, b-d**). Heating under a N_2 environment (**Table 4-7**) decreased the strength and the strain by 14 % and 9 %, indicating a cross-linking effect by oxidative degradation[29] of FAs shown in Scheme 1-2 in Chapter 1. Further increasing 1.8ODE-NC from 0.07 % to 2.0 % and heating at a 15 °C higher temperature increased the modulus, strength, and strain to 1.39 ± 0.08 GPa, 31.0 ± 3.3 MPa and 9.6 ± 1.3 %, respectively. These increases were not proportional to the increase in 1.8ODE-NC concentration. Thus, heating 0.07 % 1.8ODE-NC in LO at 70 °C for 8-16 h is the optimal condition for CP coating for strength enhancement.

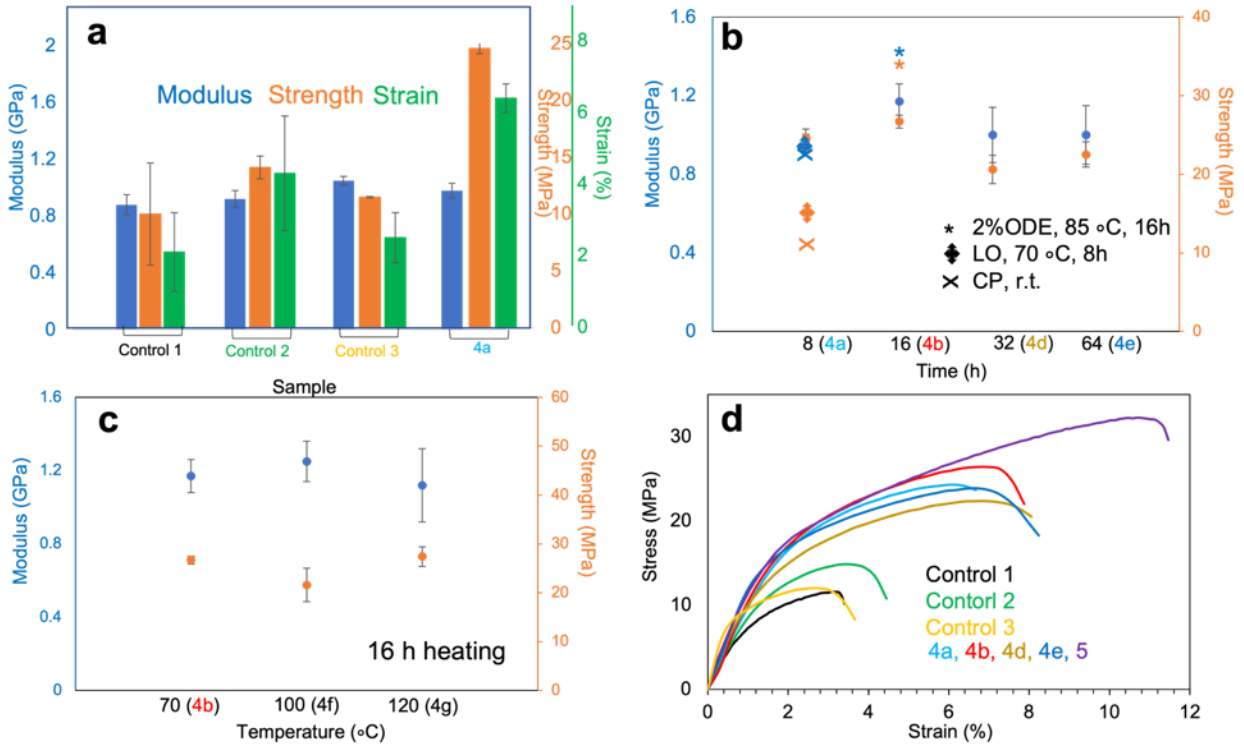

Figure 4-14. Tensile properties of CP coated with 0.07 % 1.8ODE-NC in LO: effect of (a) LO alone, with unmodified NC or 1.8ODE-NC heated at 70 °C for 8 h; (b) lengths of heating at 70 °C; (c) heating temperatures for 16h; (d) typical stress-strain curves.

Table 4-7. Effect of 0.07 and 2.0 % 1.8ODE-NC in LO coating of CP on mechanical strength.

Coating		Reaction condition	Modulus (GPa)	Strength (MPa)	Strain (%)
Controls	1. None (n=3)	n/a	0.88 ± 0.07	10.0 ± 4.5	2.1 ± 1.1
	2. LO only (n=3)	70 °C, 8h	0.92 ± 0.06	14.1 ± 1.0	4.3 ± 1.6
	3. 0.07 % unmod-NC in LO (n=3)	70 °C, 8h	1.05± 0.03	11.5 ± 0.7	2.5 ± 0.7
4. 0.07 % 1.8ODE-NC in LO (n=4)		a. 70 °C, 8 h	0.98 ± 0.05	24.6 ± 0.5	6.4 ± 0.4
		b. 70 °C, 16h	1.16 ± 0.09	26.7 ± 0.8	6.5 ± 0.6
		c. 70 °C, 16h, N_2	1.13 ± 0.33	22.9 ± 1.0	5.9 ± 0.9
		d. 70 °C, 32 h	1.03 ± 0.09	21.6 ± 1.6	6.7 ± 0.4
		e. 70 °C, 64 h	1.02 ± 0.12	22.5 ± 1.6	6.8 ± 0.5
		f. 100 °C, 16h	1.25 ± 0.11	21.6 ± 3.4	8.3 ± 1.7
		g. 120 °C, 16h	1.12 ± 0.20	27.4 ± 2.0	9.4 ± 1.1
5. 2.0 % 1.8ODE-MC/NC in LO (n=4)		h. 85 °C, 16 h	1.39 ± 0.08	31.0 ± 3.3	9.6 ± 1.3

4.4.9 Rinsing effect on coated CP by ethanol and acetone

The coated CP was rinsed with acetone and ethanol. This removed the 11.3 % unbound LO, leaving a net gain of 73.7 % which may include CP-bound transesterified FA, inter-cross-linked CP-bound FA, 1.8ODE-NC, some residual triglycerides cross-linked with CP-bound FA, and some unbound co-mingled triglycerides, glycerols, etc. The assumptions were made that 100 g CP is loaded with 73.7 g (73.7 %) of bound FAs (0.3 moles), while the estimated weight of 1.8ODE-NC in the CP coating is 0.06 g (**Eqn. 5**) based on 0.07 % of initial 85.0 % add-on weight on CP (**Tables 4-8, 9**). The hydroxyl contents in 1.8ODE-NC and CP were calculated to be 0.0004 (negligible) and 0.6 mols, respectively, following **Eqn. 6** and **7**, and related to esters in FAs (0.32 mols) in *ca.* 0.001 OH:1 FA and *ca.* 2 OH:1 FA molar ratios, respectively. This indicates that the estimated ~43.4 % of available CP-hydroxyls including 1.8ODE-hydroxyls may have transesterified with the esters of FA in LO (**Eqn. 8**) as a covalently bonded hydrophobic surface coating.

Table 4-8. Chemical components in 100 g linseed oil.

Fatty acid in 100g LO (0.114 moles) [# alkene]	Fatty acid (wt %)	Fatty acid (FA) MW (g/mol)	Esters in FA in 100 g LO (mol)	Alkene in 100 g LO (mol)
Saturated acid	10	n/a	0	0
Oleic acid [1]	21	282	0.07	0.07
Linoleic acid [2]	16	280	0.06	0.11
a-Linoleic acid [3]	53	278	0.19	0.57
Linseed Oil (100 g)	100	n/a	0.32	0.76

Table 4-9. Moles of functional groups in 0.07 % 1.8ODE-NC, LO and CP after rinsing.

1.8ODE-NC	*0.0595 g 1.8ODE-NC (mol)	LO	73.7 g FA (mol)	CP	100 g CP (mol)
†OH	0.0004	Ester	0.2	††OH	0.6
Alkene	0.0001	Alkene	0.6	Bound FA	0.3

Bulk DS=1.8 mmol ODE/g-cell
The average fatty acid $MW_{(avg.\ FA)}$ = 262 g/mol
73.7 g FAs bound to 100 g CP (due to 73.7 % avg. weight gain at 70 °C)

* Eqn. 5: Based on 85.0 g initial weight gain of CP with 0.07 % ODE/LO: 85.0 x 0.07/100 =0.06 g.

† Eqn. 6: OH on ODE-NC = $\frac{0.06\ g - (0.06\ g\ x\ 1.8\ mmol/g\ ODE\ x\ 109\ g\ ODE/mol)\ x\ \frac{1\ g}{1000\ mg}}{162\ AGU/mol}$ x 3OH x (1-0.6) (where 0.6 is the CrI of rice straw cellulose[31])

††Eqn. 7: OH on CP = (100 g AGU/162.14 g AGU/mol) x (1-0.65) x 3OH= 0.65 mole (where 0.65 is the CrI of pulp)

Eqn. 8: FA / (Free OH on CP) = (0.281 / 0.65 mole CP-OH) x 100 % = 43.4 %

The WCA over the surface of the coated CP (LO 70°C 8h, 1.8ODE-NC in LO at 70°C for 8h, and 1.8ODE-NC in LO at 70°C for 16h) ranged between 91, 99, and 117° at 3 min with the highest by 1.8ODE-NC in LO at 70°C for 16h (**Figure 4-15a)**. This is consistent with the lowest maximum % absorption capacity (10 %) of 1.8ODE-NC in LO at 70°C for 16h (**Table 4-10**). All coated CP were impenetrable by water for at least 3 h, while water passed through control 1 CP within 5 min **(Figure 4-15b**).

FTIR of the coated and rinsed CP after ethanol and acetone rinsing showed a strong C=O vibration at 1741 cm^{-1} indicating the bound FAs to CP via ester linkages (**Table 4-7, 4c**). All data

combined demonstrated reinforcing and hydrophobizing effects of LO/ODE-CNFs on CP. This chemical-free coating has a promise in food packaging and wrapping applications.

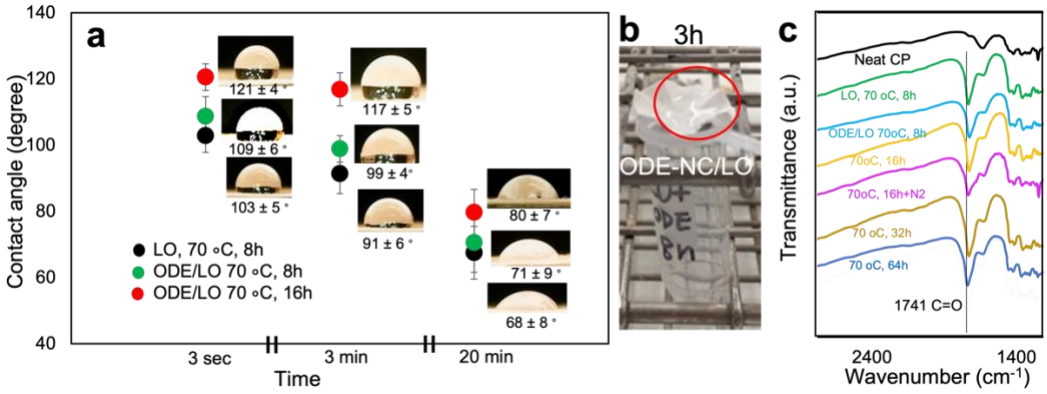

Figure 4-15. Characteristics of CP coated with 0.07 % 1.8ODE-NC in LO, heated at 70 °C for 8 h or 16 h, and rinsed with ethanol and acetone: (a) WCAs and photos of sessile drops; (b) a photo showing water repellency of the coated CP with 1.8ODE-NC in LO; (c) FTIR of coated CP with 1.8ODE-NC in LO heated in different conditions and after rinsing.

Table 4-10. Weight loss, density, % porosity and % absorption capacity of the coated CP with 0.07 % 1.8ODE-NC in LO.

Heating time (70 °C)	Weight Loss (%)	Density (g/cm^3)	Porosity (%)	Max absorbance Capacity (MAC, %)
CP (r.t.)	1.0 ± 0.2	0.8	46	51
LO (8 h)	16.6 ± 0.6	1.3	19	14
1.8ODE-NC in LO (8 h)	14.1 ± 0.9	1.3	16	12
1.8ODE-NC in LO (16 h)	10.5 ± 1.5	1.3	14	10

4.5 Conclusions

ODE-cellulose was defibrillated into nanocellulose with T: 3.3-5.1 nm and L: 0.5-1.7 μm (10/90-50/50 CNF/NPs) in $CHCl_3$ by sonication for 10 min (35 - 75 % *A*, 17-26 kJ) with ca. 15-18 % yield. Scale-up (0.5 g) telomerization under optimal conditions on a 0.1 g scale (6ODE110) generated ODE-cellulose with 0.67 mmol/g by mass gain, and produced 31 wt %, and 30 wt % ODE-NC in $CHCl_3$ and toluene, respectively, after 20 min sonication (50 % *A*), achieving the same yields as those from blending of aq. precipitate, but in less time. In addition, sonication enabled the use of a wide variety of organic solvents and linseed oil. Wetting of ODE-cellulose by TB

further increased the yield of ODE-NC in THF, $CHCl_3$, LO, and toluene by 55.6, 67.7, 40.4, and 23.3 wt %, respectively, compared with those without TB wetting. This confirmed the effect of H-bonding between TB hydroxyls and ODE-NC hydroxyls, increasing the compatibility between ODE-NC and aprotic organic solvents. By pre-sonicating (50 % *A*, 3 min) cellulose prior to telomerization (6ODE, 1h), DS of ODE-cellulose significantly improved to 1.2 mmol ODE/g-cell (113 % yield) and 1.8 mmol ODE/g-cell (119 % yield) as the average temperature increased in the range between 113-110 °C, in comparison with that obtained without pre-sonication (0.74 mmol ODE/g-cell) at 107 °C. Sonication (50 % *A*, 20 min) of ODE-cell directly in polymer solvents also improved efficiency of NC production by eliminating the aqueous blending and solvent exchange process, generating 45.5 % yield of 1.2ODE-cell in toluene and 73.3 % yield of 1.8ODE-cell in LO. Furthermore, they were directly mixed with polymers to create nanocomposites, or used as surface coatings on cellulose papers.

PBD film from a stirred solution of PBD combined with 2 % 1.2ODE-MC/NC (2.23 ± 0.34 MPa) without additional sonication demonstrated the highest yield strength (0.15 ± 0.04 MPa) without sacrificing the strain. In PSIS film with 2 % 1.2ODE-MC/NC, the highest modulus (7.8 ± 1.0 MPa), strength (17.3 ± 3.3 MPa) and strain (1780 ± 448 %), were achieved without any additional reagents, but only by 5 h thorough mixing of the two components in toluene. Coating of CP with 0.07 % ODE-NC/LO and heating at 70 ºC for 16 h has shown the optimal reinforcing effect of CP with strength of 26.7 ± 0.8 MP, which may reflect the highest extent of the grafting and cross-linking among CP, ODE-NC and LO. Hydrophobicity of the coated CP surface was evidenced by the WCA of 117º at 3 min for CP coated with LO/ODE at 70 ºC for 8h and LO/ODE at 70 ºC for 16h, and their water retention for at least 3 h.

By using sonication, facile process of disintegration and processing of ODE-cellulose in nonpolar polymer solvents and linseed oil was demonstrated. The excellent compatibility of 1.2 and 1.8ODE-NCs with toluene, PBD, PSIS, and bio-degradable LO suggests a broad array of potential applications in material fabrication with reinforced natural rubbers, elastomers, or chemical-free food packaging.

4.6 Acknowledgements

Financial support from the California Rice Research Board (Project RU-9) and the Henry A. Jastro Research Award, University of California, Davis is greatly appreciated.

4.7References

(1) Fukuda, J.; Hsieh, Y.-L. Hydrophobic 2,7-Octadienyl Ether-Cellulose Nanofibrils Using Butadiene Sulfone as the Dual Reagent and Medium. *ACS Sustainable Chem. Eng.* **2021**, *9* (18), 6489–6498. https://doi.org/10.1021/acssuschemeng.1c02092.

(2) Udoetok, I.; Wilson, L.; Headley, J. Ultra-Sonication Assisted Cross-Linking of Cellulose Polymers. *Ultrasonics Sonochemistry* **2017**, *42*, 567-576. https://doi.org/10.1016/j.ultsonch.2017.12.017.

(3) Suslick, K. S. Sonochemistry. *Science* **1990**, *247* (4949), 1439–1445. https://doi.org/10.1126/science.247.4949.1439.

(4) Johnson, R. K.; Zink-Sharp, A.; Renneckar, S. H.; Glasser, W. G. A New Bio-Based Nanocomposite: Fibrillated TEMPO-Oxidized Celluloses in Hydroxypropylcellulose Matrix. *Cellulose* **2009**, *16* (2), 227–238. https://doi.org/10.1007/s10570-008-9269-6.

(5) Li, W.; Wang, R.; Liu, S. Nanocrystalline Cellulose Prepared from Softwood Kraft Pulp via Ultrasonica-Assisted Acid Hydrolysis. *BioResources* **2011**, *6* (4), 4271–4281. https://ojs.cnr.ncsu.edu/index.php/BioRes/article/view/BioRes_06_4_4271_Li_WL_Nanocryst_Cellulose_SW_Kraft_Ultrason.

(6) Saito, T.; Kuramae, R.; Wohlert, J.; Berglund, L. A.; Isogai, A. An Ultrastrong Nanofibrillar Biomaterial: The Strength of Single Cellulose Nanofibrils Revealed via Sonication-Induced Fragmentation. *Biomacromolecules* **2013**, *14* (1), 248–253. https://doi.org/doi.org/10.1021/bm301674e.

(7) Jiang, F.; Hsieh, Y.-L. Assembling and Redispersibility of Rice Straw Nanocellulose: Effect of Tert-Butanol. *ACS Appl. Mater. Interfaces* **2014**, *6* (22), 20075–20084. https://doi.org/10.1021/am505626a.

(8) Lazzari, M.; Chiantore, O. Drying and Oxidative Degradation of Linseed Oil. *Polymer Degradation and Stability* **1999**, *65* (2), 303–313. https://doi.org/10.1016/S0141-3910(99)00020-8.

(9) Hess, P. S.; O'Hare, G. A. Oxidation of Linseed Oil. *Ind. Eng. Chem.* **1950**, *42* (7), 1424–1431. https://doi.org/10.1021/ie50487a044.

(10) Lu, P.; Hsieh, Y.-L. Preparation and Characterization of Cellulose Nanocrystals from Rice Straw. *Carbohydrate Polymers* **2012**, *87* (1), 564–573. https://doi.org/10.1016/j.carbpol.2011.08.022.

(11) Mesnager, J.; Quettier, C.; Lambin, A.; Rataboul, F.; Pinel, C. Telomerization of Butadiene with Starch under Mild Conditions. *ChemSusChem* **2009**, *2* (12), 1125–1129. https://doi.org/10.1002/cssc.200900167.

(12) Segal, L.; Creely, J. J.; Martin, A. E.; Conrad, C. M. An Empirical Method for Estimating the Degree of Crystallinity of Native Cellulose Using the X-Ray Diffractometer. *Textile Research Journal* **1959**, *29* (10), 786–794.

(13) Grönroos, A.; Pirkonen, P.; Ruppert, O. Ultrasonic Depolymerization of Aqueous Carboxymethylcellulose. *Ultrasonics Sonochemistry* **2004**, *11* (1), 9–12. https://doi.org/10.1016/S1350-4177(03)00129-9.

(14) Hausoul, P. J. C.; Bruijnincx, P. C. A.; Klein Gebbink, R. J. M.; Weckhuysen, B. M. Base-Free Pd/TOMPP-Catalyzed Telomerization of 1,3-Butadiene with Carbohydrates and Sugar Alcohols. *ChemSusChem* **2009**, *2* (9), 855–858. https://doi.org/10.1002/cssc.200900115.

(15) Boissou, F.; Mühlbauer, A.; Vigier, K. D. O.; Leclercq, L.; Kunz, W.; Marinkovic, S.; Estrine, B.; Nardello-Rataj, V.; Jérôme, F. Transition of Cellulose Crystalline Structure in Biodegradable Mixtures of Renewably-Sourced Levulinate Alkyl Ammonium Ionic Liquids, γ-Valerolactone and Water. *Green Chemistry* **2014**, *16* (5), 2463–2471. https://doi.org/10.1039/C3GC42396D.

(16) Jiang, F.; Hsieh, Y.-L. Chemically and Mechanically Isolated Nanocellulose and Their Self-Assembled Structures. *Carbohydrate Polymers* **2013**, *95* (1), 32–40. https://doi.org/10.1016/j.carbpol.2013.02.022.

(17) Wang, G.-Z.; Li, X.-L.; Dai, J.-J.; Xu, H.-J. AIBN-Catalyzed Oxidative Cleavage of *Gem* -Disubstituted Alkenes with O 2 as an Oxidant. *J. Org. Chem.* **2014**, *79* (15), 7220–7225. https://doi.org/10.1021/jo501203a.

CHAPTER 5: Facile Cellulose Isolation and Nanofibril Characterization for 1D To 3D Fiber, Film, and Aerogel Structures from Almond Shells

5.1 Abstract

Cellulose has been optimally isolated from almond shells (AS) in 35.2 % yield by a two-step $NaClO_2$/KOH process. Subsequent TEMPO (2,2,6,6-tetramethyl-piperidin-1-yl)oxyl mediated oxidization generated ribbon shaped cellulose nanofibrils (CNF) with 1.2 ± 0.44 nm height, 5.2 ± 1.2 nm width, and 1.6 ± 0.8 μm length in 90 % yield. Anisotropic 4.3 cross-sectional width-to-height aspect ratio with dominant hydrophilic planes and high length-to-height aspect ratio (1167) are distinctively unique to AS-CNFs. This study elucidated how this characteristic served in construction of material forms by analyzing different assembling and disassembling behaviors by three CNF material forms created under vaired solidification conditions. Fibers that were rapidly frozen (-196 °C) and freeze-dried were readily 100 % redispersible in water into CNFs with the original size indicating that they were assembled by predominantly polar-polar CNF associations. Aerogels fabricated from a slow freezing (-20 °C) and freeze-drying process, exhibited an amphiphilic characteristic by absorbing both water and chloroform. They redispersed only 10 wt % in water into CNFs with the original size indicating that nonpolar-nonpolar interfacial CNF associations are their dominant force for assembling along with some polar-polar CNF interactions. Films, from the slowest solidification via casting under the ambient condition, exhibited polar surfaces with water contact angles of 34-42° while they were partially redispersible in water (71.7 wt %), ethanol (11.4 wt %) and dimethylacetamide (7.4 wt %), indicating that they were formed by using dominant polar-polar and minor nonpolar-nonpolar interfacial associations. The higher char residues of the films in TGA may indicate that slow solidification process in air induced a calcitrant characteristic. All data combined suggest that solidification speed and environments largely influence strength and surface hydrophobicity/hydrophilicity/amphiphilicity of TOCNF materials, and their fundamental basis of material construction seems to be supported

by polar-polar TOCNF associations between wider hydrophilic-to-hydrophobic planes which are characteristic to AS-TOCNFs.

5.2 Introduction

Almonds are the largest tree nut crop in the world, with *ca.* 80% (kernel basis) being produced in California.[1] With a projected 1.5 million metric tons of kernels produced in 2020-21[2], an equal amount of shells (AS) and twice as much hulls (AH) are expected. In 2017, a total of 3.1 million metric tons of biomass was produced by the California almond industry, of which 53.5 % is categorized as woody biomass (19.7 % AS) and 46.5 % as fleshy biomass (46.1 % AH).[2,3] While AH is utilized as dietary supplement for cows, almond woody biomass has been used as a source for generation of bioenergy[4,5,6] and production of biochar and activated carbon[7–11]. AS exhibited a higher heating value (18.3 MJ/Kg) and moderately higher bulk density (373 kg/m^3)[4] than those of wood pellets or charcoal by combustion. The carbonization temperature of AS at 400 °C, lower than the generally-used 600 °C for carbonization of other agricultural residues, leads to cost-effective processes of energy production[7]. Almond shells have been studied for use as plastic fillers in polypropylene (PP)[12–15] or cation/anion absorbents[16–18]. As plastic fillers in polypropylene (PP), NaOH-treated AS modified with polypropylene-grafted-maleic anhydride improved the Young's modulus of the nanocomposite by 14 % to 1500 MPa compared with PP[15], and torrefied AS increased distortion temperatures by 8 °C to 24 °C[13]. AS with less than 180 μm granule size in PMMA composites improved flexural strength, modulus, and impact energy by up to 20 %, 5.6 %, and 56.7 %, respectively, for Duralight®PMMA[14]. Unmodified AS has also been widely investigated as a low-cost absorbent for removal of violet B cationic dye (96 mg dye/g AS at pH 11)[16], lead, and cadmium ions (9 mg/g NaOH-treated AS)[19], and pentachlorophenol (PCP)

pollutant (removal efficiency: 93 ±14% in 24 h)[17]. These are direct utilizations of bulk AS without isolating individual components.

AS is composed of mainly cellulose, hemicellulose, and lignin with an average composition of 28.9 ± 3.2, 32.1 ± 4.0, and 29.3 ± 2.2 %[20–27] (**Table 5-1**), respectively, by the standard ASTM[20,25–27], TAPPI[21,25], or Van Soest[22,23] analytical separation methods. AS is used directly for energy production[22,26], gasification[27], purification of xylo-oligosaccharides for the food and pharmaceutical industry[20], animal feed[23], particle board production, and is studied for chemical and composition characterization[23,24,25] to explore new applications. The Van Soest method led to a higher variation (32.6 ± 2.1%) of percent cellulose than ASTM or TAPPT methods (23.8 ~ 29.1 %), which may be attributed to a single 3~4 % H_2SO_4 treatment instead of two. While AS is named as a woody biomass, the cellulose content of AS (35 %) is about two thirds of that of hard and soft wood (45-50 %), but comparable to rice straw (36 %), providing a fair quantity of cellulose out of agricultural residue.

Table 5-1. Composition (wt %) of almond shells reported in the references.

AS variety	Organic extract	Lignin	Hemicellulose	Cellulose	Method
Abies alba & Pinus insignis[26]	3.7 ± 1.1[a]	27.2 ± 2.0	34.0 ± 4.9	29.3 ± 7.9	ASTM: D-1111[a]; D-1107[b]; D-1106[c], HPLC for carbohydrates
Prunus amygdalus L.[21]	N/A	32.7	35.2	29.1	TAPPI: T222-om[d] for lignin removal, Chloride method
Mallorca proprietor[22,23]	3.9	27.8 ± 0.1	33.6 ± 6.3	32.6 ± 2.1	Van Soest method[e]
Prunus dulcis[24]	5.7	28.8	32.4	23.8	Dichloromethane/Ethanol/Water/Acid hydrolysis (72 % and 3-4% H_2SO_4)
Tunisian[25]	11.8	30.1	25.1	29.9	ASTM: D-1107[b] TAPPI: T222-om[d]; T19m-54[f]

[a] Also 7.4 % hot water extractive prior to organic extraction.[26]
[b] Ethanol-toluene extraction to remove catechol, tannins, resin, fats, wax, and oil.[27]
[c, d] Lignin removal in 72% H_2SO_4 at 20 °C for 2h, then 3 % H_2SO_4 at boil for 4 h.[20]
[e] Hemicellulose content was the weight difference between Neutral Detergent Fiber (cellulose, hemicellulose, lignin are insoluble) and acid detergent fiber (cellulose, lignin are insoluble). Cellulose content was from removal of lignin by $KMNO_4$ oxidation, and lignin content was by solubilization of cellulose in 72 % H_2S0_4.[23]

[f] Holocellulose content was measured after removing lignin by sodium hypochlorite at 70 °C. Cellulose content was measured after removing hemicellulose from the holocellulose fraction by 10 w/v % NaOH extraction. Hemicellulose content was measured by subtracting cellulose content from holocellulose content.[28]

Nanocelluloses are one-dimensional cellulose nanocrystals (CNCs) or nanofibrils (CNFs) typically isolated from plant cellulose. CNCs and CNFs have been studied extensively because of their outstanding strength[29-31] and high aspect ratios (50-500)[32].

High surface area and high modulus are attractive qualities for sorbents and nanopapers. Efficient absorbents were created from TEMPO-oxidized cellulose nanocrystals (TOCNs) hydrolyzed from AS to remove Cu (II).[18] Between pH 4-5, freeze-dried TOCN demonstrated the highest Cu (II) absorption of 50-55 % at 30 °C, which is 16-33 % higher than those by bleached AS or lyophilized bleached AS. This is attributed to the higher surface area (1.82 m^2/g), the larger mesopores (0.201 cm^3/g), and the negatively charged surface carboxylate groups (0.424 mmol COO^-/g) of the TOCN that provided the increased binding sites for Cu (II) ions. CNC nanopapers, generated from acetylation and hydrolysis of AS cellulose, exhibited enhanced tensile strength (65.1 MPa) and Young's modulus (5.3 GPa)[33], seven- and three- fold higher than nanopaper made of microcellulose from canola straw[34]. While these are beneficial uses of AS nanocelluloses, the potential value of films, or membrane sorbents, derived from AS-TOCNFs has not been evaluated to date.

This study delves into three major subjects: 1) maximizing the efficiency of cellulose extraction, 2) identifying characteristics of TEMPO-oxidized CNFs unique to an AS source, and 3) identifying applications best suited for their characteristics. While direct utilization of AS has its own value, developing a facile and environmentally-benign extraction process will increase the value of AS-derived cellulose. Thus, the importance of organic extraction that removes fats, wax, oils and catechol[27] in AS, and the effectiveness of alkaline treatment in place of the

environmentally-concerning chlorinated reagent $NaClO_2$, were evaluated. This involved a comparative study of a 3-step process (toluene/ethanol, acidified $NaClO_2$, KOH)[32,35], a 2-step process (acidified $NaClO_2$, KOH), and the reversed-order process of toluene/ethanol, KOH or NaOH, acidified $NaClO_2$[36]. The study involved analyzing the yields, the surface structure by FTIR, and the thermal properties by TGA. The characteristics of CNFs unique to an AS source after TEMPO oxidation of cellulose were investigated for their assembling disposition through their morphology using AFM, TEM, conductometric titration for charge density, and surface chemical structure by ^1H NMR. Finally, the study investigated assembling and disassembling characteristics of solid structures fabricated from aqueous CNF dispersions in three different solidification environments: 1) rapid (-196 °C, 10 min), 2) slow (-20 °C, 10 h) freezing followed by freeze-drying at -56 °C, and 3) air-drying at room temperature, to understand the major interfacial interaction forces among CNFs and assess the most appropriate applications.

5.3 Experimental

5.3.1 Materials

Almond fruit (Carmel variety) was harvested and AS was collected in northern California. Toluene (certified), ethanol (EtOH, anhydrous, denatured, Millipore Sigma), sodium chlorite ($NaClO_2$, 80% Fluka), acetic acid glacial (CH_3COOH, 99.7% ACS GR, EMD), potassium hydroxide (KOH, 85%, EM Science), and sodium hydroxide (NaOH, pellets, 97 %, Millipore Sigma) for separation of lignin, hemicellulose and cellulose from AS, and acetone (certified), decane (certified), DMAc (certified), deuterium oxide (99.9 atom % D, Millipore Sigma) were all used as received without further purification. Water was purified by the Milli-Q Advantage A-10 water purification system (Millipore Corporate, Billerica, MA).

5.3.2 Isolation of AS cellulose

AS was milled (Thomas-Wiley Laboratory Mill model 4, Thomas Scientific, USA) to pass through a 60-mesh sieve (250 μm), then the cellulose was extracted by the different combinations of the following treatments**.** For the organic extraction, ground and sieved AS (30 g) was refluxed with 2:1(v/v) toluene-ethanol in a Soxhlet apparatus for 20 h and dried under a hood for two days, then in the oven at 55 °C for an additional two days. For de-lignification, sodium chlorite (1.4 % $NaClO_2$, 1000 mL) acidified with glacial acetic acid (pH 3.5) was added to AS and the mixture was stirred at 70 °C for 5 h, then rinsed with water until the pH of the filtrate reached neutral. For alkaline treatment, AS was immersed in 600 mL 5 % KOH or 4% NaOH and stirred at room temperature for 24 h then at 90 °C for 2 h, cooled and vacuum-filtered then rinsed with copious amounts of water until the filtrate became pH neutral. The wet solid from the alkaline extraction step was dispersed in water, then the aqueous suspension of cellulose was frozen in liquid nitrogen (-196 °C) and freeze-dried (FreeZone 1.0L Benchtop Freeze Dry System, Labconco, Kansas City, MO) and weighed to calculate the yield based on the original mass of AS. Cellulose from Route 1: the organic extraction/de-lignification/KOH treatment was designated as Cell 1. Cellulose from Route 2: the de-lignification/KOH extraction was designated as Cell 2. Cellulose from Route 3: the organic extraction/KOH and NaOH treatment/de-lignification was designated as Cell 3. Herein, all concentrations in wt % are listed simply as %, unless specified otherwise, and TOCNFs derived via Route 1, 2 or 3 are listed as TOCNF1, 2 or 3.

5.3.3 TEMPO-oxidized cellulose nanofibrils (TOCNFs)

AS-TOCNFs (1.0 g) were magnetically stirred in 100 mL water in an Erlenmeyer flask, then combined with 2 mL aqueous mixture of a catalytic amount of TEMPO (16.0 mg) and NaBr (100 mg) to which 5 mmol NaClO was added dropwise with the pH adjusted to 10~10.5 with 0.5

N NaOH. Once the pH ceased to decrease (i.e., stabilized at pH 10 at least for 15 min), the reaction time was recorded. The reaction mixture was neutralized to pH 7 by adding 0.5 N HCl, then centrifuged (5 k rpm, 15 min) to collect the white precipitate to be dialyzed against water to remove free ions over several days. The dialyzed suspension was diluted to 250 mL to be mechanically blended (Vitamix 5200) at 30 k rpm for 30 min (15 min x 2), then centrifuged (5 k rpm, 15 min) to collect the supernatant. The TOCNF yields were calculated gravimetrically, and triplicate results were averaged. All aqueous CNF suspensions were stored at 4 ˚C before characterization and use.

5.3.4 Characterization of TOCNFs

For conductometric titration, 50 μL of 1 N HCl was added to 50 mL of 0.1 % CNF suspension to protonate all the carboxyl groups, then carboxylic acid was titrated with 0.01 M NaOH solution. The conductivity values were recorded using an OAKTON pH/Con 510 series conductivity meter. The surface charge (σ, in mmol /g of cellulose) was determined,

$$\sigma = \frac{cv}{m} = \frac{c(v2-v1)}{m} \qquad \text{Eqn. 1}$$

where c is the NaOH concentration (in M), m is the CNF mass (g) in the suspension, and v1 and v2 are NaOH volumes (in mL) used in neutralizing the added HCl and carboxylic acid groups on the CNFs, respectively. The surface chemical structure of TEMPO-CNFs was examined by solution state ^{1}H NMR was analyzed in D_2O using a Bruker AVIII 800 MHz ^{1}H NMR spectrometer following a previously reported method for RS CNF[37]. The CNF dispersions (5 mL at 0.3 %) were precipitated by adding 10 mL acetone then centrifuged (5000 rpm, 15 min) to decant the supernatant. This was repeated three times. Then, 1 mL D_2O was added to a fraction of CNF acetone gel and homogenized by sonication (3 min, Branson 2510) followed by heating at 60 °C

under vacuum for 1 h to remove the acetone. This sonication and evaporation process was repeated several times to remove acetone residues and the additional D_2O was replenished to replace the evaporated acetone. The final nanocellulose concentration was ca. 0.2 %.

5.3.5 Drying of Aqueous TOCNFs

Aqueous TOCNFs were dried into fibers, aerogels, and films by three different processes. Aqueous TOCNFs (0.01, 0.05, 0.1, 0.3 w/v %) were frozen in liquid nitrogen (-196 °C, 15 min) and lyophilized (-50 °C, 0.05 mbar, 2days) in a freeze-drier (FreeZone 1.0L Benchtop Freeze Dry System, Labconco, Kansas City, MO) into fibers. Aerogels were fabricated by freezing aqueous TOCNFs (0.05, 0.1, 0.3, 0.6 w/v %) in PP tubes at -20 °C for 12 h (ThermoFisher, IsoTemp, Model HF-5017), followed by lyophilization for 2 days. Films were cast from aqueous TOCNFs (30 g, 0.3 %) after mechanically stirring for 1 h and drying at r.t. (24 h) in a hydrophobic polystyrene (PS) hexagonal weighing tray (51.4 cm^2).

5.3.6 Characterization of TOCNF2 fibers, aerogels and films

Surface functional groups of freeze-dried Cell 2 and fibers were analyzed using a Thermo Nicolet 6700 spectrometer (Thermo Fisher Scientific, USA) at ambient conditions in the form of KBr (1:50, w/w) disks. The spectra were collected in the transmittance mode from an accumulation of 128 scans at a 4 cm^{-1} resolution over a 4000–400 cm^{-1} range. XRD spectra of freeze-dried Cell 2 and TOCNF2 were collected to determine crystallinity on a Scintag XDS 2000 powder diffractometer using a Ni-filtered Cu Ka radiation (λ = 1.5406 Å) at an anode voltage of 45 kV and a current of 40 mA. The samples were compressed between two glass slides into flat sheets with around 1 mm thickness. Diffractograms were recorded from 5° to 40° at a scan rate of 2° per

minute. Crystallinity Index (CrI) was calculated by using the intensity of the 200 peak (I_{200}, 2θ = 22.6°) and the intensity minimum between the peaks at 200 and 110 (I_{am}, 2θ =18.7°) by using the empirical equation[38] as follows.

$$CrI = \frac{I_{200} - I_{am}}{I_{200}} \times 100 \qquad \text{Eqn. 2}$$

The crystallite dimensions of these samples were calculated using the Scherrer equation[44].

$$D_{hkl} = \frac{0.9\,\lambda}{\beta 1/2\,\cos\theta} \qquad \text{Eqn. 3}$$

Where D_{hkl} is the crystallite dimension in the direction normal to the *h k l* lattice planes, λ is the X-Ray radiation wavelength (1.5406 Å), $\beta_{1/2}$ is the full width at half-maximum of the diffraction peak, and θ is the corresponding Bragg angle.

The Bragg angle $\beta_{1/2}$ was determined by multiple peak fitting using Origin software. Fiber morphology was studied using a field emission scanning electron microscope (FE-SEM) (XL 30-SFEG, FEI/Philips, USA) at 5 kV accelerating voltage by sputter-coating fibers from different concentrations with gold under vacuum at 20 mA for 2 min (Bio-Rad SEM coating system) on aluminum stubs covered with conductive carbon tape. The widths were measured from more than 100 individual fibers by using ImageJ software. The effect of concentration on the aerogel construction was studied by SEM, while the physical properties were analyzed using the aerogel 0.3 w/v % TOCNF2. The density (ρ_a) of aerogels was calculated from the weighed mass and volume of 1 cm sections of cylindrical samples, and the porosity (ϕ) of the aerogel was calculated as:

$$\text{Porosity } (f) = \left(1 - \frac{r_a}{r_c}\right) \times 100\ \% \qquad \text{Eqn. 4}$$

where ρ_c is the specific gravity of cellulose (1.6 g/cm^3) (Polymer Data Handbook).

Liquid absorption (LRA, mL/g) was calculated as

$$\text{LRA} = \frac{\left(\frac{w_s - w_o}{w_o}\right)}{r_l} \qquad \text{Eqn. 5}$$

where w_s and w_0 are the weight of fully solvated and dry aerogel, respectively, and ρ_l is the density of the liquid (g/mL).

The ability to reabsorb water and $CHCl_3$ by 0.05, 0.1, 0.3, and 0.6 % CNF aerogel was measured by repeatedly absorbing then squeezing out the liquids (using a tweezers against the beaker wall) for five cycles. The densities (ρ) of films were calculated from the weighed mass and volume of dried films with a thickness of 14 μm. The film was examined using a Leica DM2500 optical microscope equipped with a cross-polarizer. Water contact angles were measured by depositing 5 mL of pure water on the top and bottom sides of film surfaces, and triplicate measurements were averaged. In AFM height images, the surface roughness (represented by RMS) was measured using Gwyddion software over an area of 100 μm^2, and values from 3 images were averaged. Water and decane absorption of aerogels and films were measured by immersing them in the liquid for three seconds and lifting out and squeezing (with a tweezer) to determine the amount of liquid absorbed. Absorption was repeated for five cycles after lightly blotting excess surface liquid.

5.3.7 Re-dispersibility and thermal degradation of TOCNF2- fibers, aerogels and films

TOCNF2 fibers in the amounts 10, 20, 60 and 120 mg (0.05, 0.1, 0.3 w/v % and 0.6 w/v %), were immersed in 20 mL water, and 30 mg cylindrical shaped aerogels (diameter = 1 cm) (0.3 w/v %) were immersed in 10 mL water. Separately, a 30 mg film (3 x 3 x 0.0014 cm square, 0.3 w/v %) was immersed in 10 mL water, ethanol, and DMAc and sonicated (40 kHz, 130 W max, Branson ultrasonic processor model 2510) for 1 min to study the extent of re-dispersibility, and thus disassembling behaviors. The disassembled CNFs were observed by AFM at 0.0005 w/v % for height measurement. To measure thermal properties of Cell 2, fibers, aerogels, and films, 5 mg samples were heated at 10 °C min^{-1} from 25 °C to 500 °C under purging N_2 (50 mL min^{-1}), then measured using a TGA-50 (Shimadzu, Japan). This process was repeated three times for each of the four materials, and the average of the three runs was reported.

5.4 Results and Discussion

5.4.1 Cellulose Isolation from AS

Cellulose isolation was performed by three different routes (**Figure 5-1**). In Route 1, chestnut brown ground AS lost 2 % organic extractives after 2:1 v/v toluene-ethanol extraction, 18 % lignin by acidified $NaClO_2$ oxidation, and 44.7 % lignin/hemicellulose by 5 % KOH treatment, yielding pure white 35.3 % Cell 1. In Route 2, 17.2 % and 47.6 % was lost after respective the $NaClO_2$ and KOH steps, yielding 35.2 w/v % of equally white Cell 2, with virtually the same yield as Cell 1, indicating that an organic extraction may not be a crucial step for AS cellulose isolation. The effectiveness of KOH and NaOH was compared in two consecutive alkaline treatments in Route 3. While potassium is a slightly less electronegative alkali metal than sodium, the solubility of NaOH on a molar basis is slightly higher than that of KOH. The results showed that they can be used interchangeably for hemicellulose extraction by exhibiting the

identical yields after two consecutive treatments. Also, both treatments produced brown-colored products signifying significant presence of lignin, requiring the subsequent $NaClO_2$ oxidation. This route resulted in the lowest yield (26.6 %), with pure white product (Cell 3).

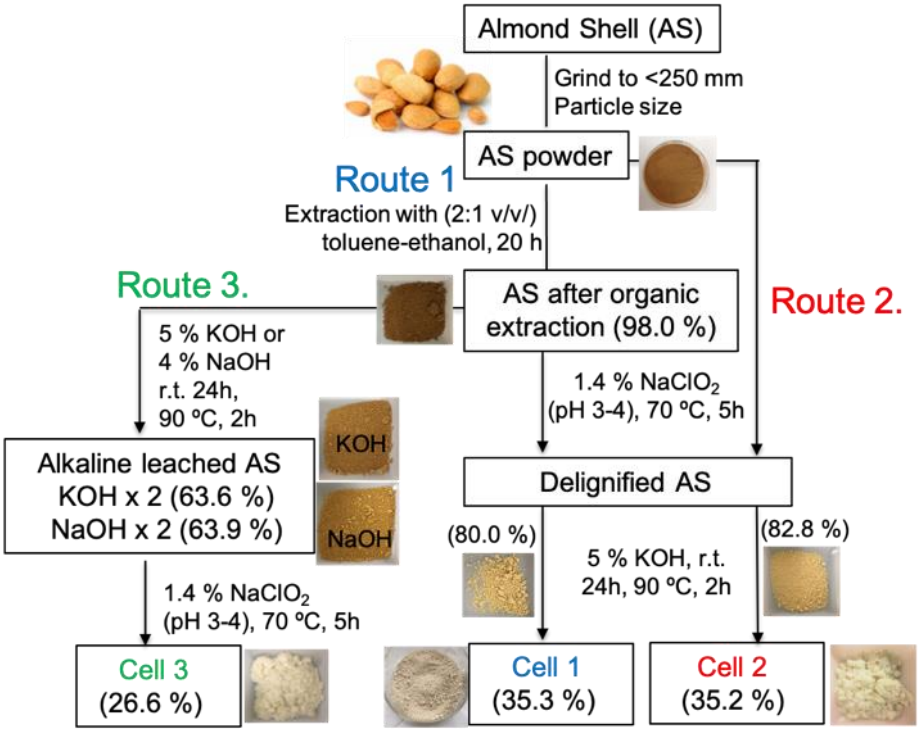

Figure 5-1. Extraction flow chart for almond shell cellulose: Routes 1, 2 and 3 for the three-step, the two-step, and the reversed-order methods.

FTIR analyses of Cell 1 and Cell 2 are virtually identical showing disappearance of lignin peaks at 1507 cm^{-1} for aromatic skeletal vibrations and 818 cm^{-1} for aromatic C=C-H bending after $NaClO_2$ treatment. Disappearance of a peak at 1729 cm^{-1} for carbonyl stretching after KOH treatment (**Figure 5-2a, b**) indicates removal of pectin, xylan, or some phenolic acids. On the other hand, the Route 3 (**Figure 5-2c**) showed persistent lignin peaks at 1507 cm^{-1} after two consecutive alkaline treatments, suggesting that the use of oxidant is essential for removal of lignin. A small shoulder peak for carbonyl stretching at 1740 cm^{-1} in Cell 3 may indicate possible oxidation of

glucopyranose rings, implying that the treatment with a series of two alkaline treatments followed by $NaClO_2$ oxidation was too harsh and caused a change in cellulose surface chemistry. Therefore, Cell 1 and Cell 2 not only had comparable yields but equivalent surface chemistry, indicating that an organic extraction is inessential to producing pure cellulose (**Figure 5-2d**).

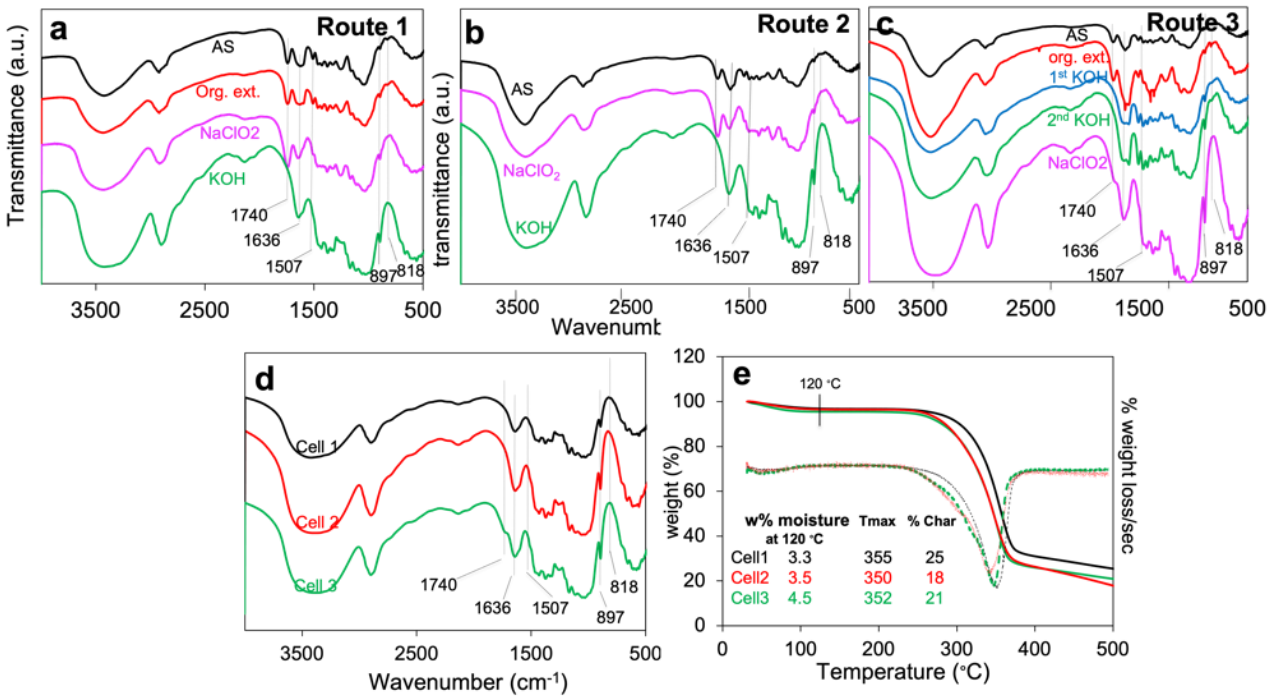

Figure 5-2. Characteristics of cellulose 1-3: FTIR of extraction products from (a) Route 1; (b) Route 2; (c) Route 3; (d) pure cellulose from Route 1, 2, and 3; (e) TGA of pure celluloses.

TGA curves (**Figure 5-2e**) showed the virtually identical moisture loss of Cell 1 and 2 (3.3, 3.5 %) while Cell 3 showed slightly higher moisture (4.5 %), which supports additional oxidation of glucopyranose rings by Route 3 leading Cell 3 to be more hygroscopic. Tmax was measured as 355 °C, 350 °C and 352 °C for Cell 1, 2 and 3, respectively, indicating that there is no significant difference in their purity based on their thermal behaviors. These results, combined with the overall composition of products generated from each step, are shown in **Table 5-2**. Therefore, the 2-step

extraction (Route 2) was the simplest and most effective in producing cellulose with negligible impurities.

Table 5-2. Overall composition of Route 1-3 products.

	Organic Extractables (wt %)	Lignin + Hemicellulose (wt %)	Cellulose (wt%)
Route 1	2.0	62.7	35.3
Route 2	n/a	64.8	35.2
Route 3	2.0	71.6	26.6
Standard[20-27]	3.7 - 11.8	55.2 - 67.7	28.9 - 32.6

5.4.2 TEMPO-mediated oxidation of cellulose and characteristics of TOCNF2

Cellulose isolated from AS, Cell 2, was oxidized by TEMPO/NaBr/NaClO with primary oxidant NaClO (5 mmol per g of cellulose) to transform the C6 primary hydroxyls to carboxyls regioselectively at pH 10. From a mechanistic viewpoint, at pH 10, the oxidation of hydroxyls with TEMPO occurs by means of a five-membered transition state which accelerates the oxidation rate leading to a greater selectivity for primary alcohols over secondary ones (**Figure 5-3a**).[39] Defibrillation of cellulose was aided by high-speed blending, producing an opaque aqueous slurry (ca. 0.4 w/v %) of cellulose nanofibrils (TOCNF2). The charges associated with the sodium carboxylates of TEMPO-oxidized TOCNF2s were determined by conductometric titration which exhibited a parabolic function with added NaOH (**Figure 5-3b**). Before starting titration, all carboxylate groups were protonated by adding 0.5 M HCl (200 μL), thus the initial steep decline in conductivity reflected the neutralization of excess HCl with NaOH, and the plateau region is a buffering zone where both carboxylic acids and carboxylates are present, followed by the final increasing trend that indicates accumulation of the excess NaOH. The yield and charge density of TOCNF2 increased exponentially as oxidation time increased, reaching a maximum of 90 % and 1.30 mmol COO^-/g-cell at 130 min, respectively (**Figure 5-3c**), with a lower yield than that of RS

cellulose but a comparable charge density to RS TOCNF (1.32 mmol COO^-/g-cell)[32]. The duration of oxidation time is similar to that of hardwood cellulose (130 min)[40] but longer than that of RS cellulose (65 min)[32]. The slower migration of TEMPO nitroxyl radicals to the reaction site of AS cellulose than RS is possibly due to the unique structural characteristics of AS cellulose. The light transmittance of the aqueous TOCNF2s increased to 90 % as concentration decreased to 0.025 % due to less entanglement or physical association among TOCNF2s **(Figure 5-3d, e**). Similar results were observed for TOCNF1 and TOCNF3.

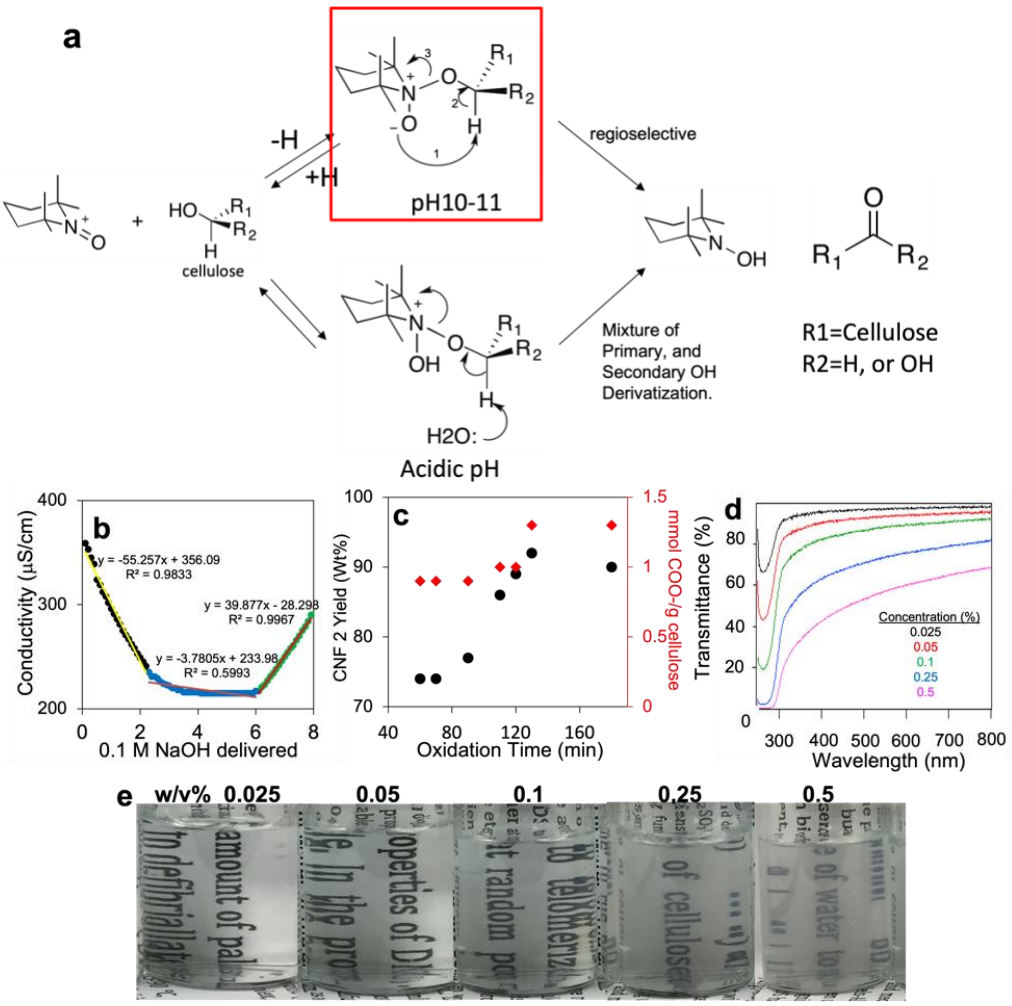

Figure 5-3. (a) Mechanism of TEMPO-mediated oxidation. (recreated referencing Tojo and Fernández[39]) Characteristics of TOCNF2: (b) conductometric titration with 0.1 M NaOH; (c) TOCNF2 yield and charge density as a function of oxidation time. (d) UV-vis transmittance (%). (e) the appearance of aqueous TOCNF2s at 0.025, 0.05, 0.1, 0.25, and 0.5 w/v %.

5.4.3 Morphology, crystal structure of TOCNFs

Height (H) / width (W) / length (L) of TOCNFs were revealed by AFM and TEM images, respectively, to be 1.2 ± 0.5 nm / 5.2 ± 1.2 nm / 1.4 ± 0.7 μm (**Figure 5-4, a-e**), showing a rectangular transverse cross-section with 4.3 W / H and 1,167 L / H aspect ratios, or a long, ribbon-like morphology. In consideration of the standard deviations, the dimension of TOCNF1 and TOCNF3 were also identical to that of TOCNF2, H / W / L: 1.5 ± 0.8 nm / 4.1 ± 1.2 nm / 1.4 ± 0.6 μm and H / W / L: 1.0 ± 0.4 nm / 4.4 ± 1.2 nm / 1.2 ± 0.6 μm, respectively, (**Figure 5-4f~o)** supporting the effectiveness of 2-step extraction. As a comparison, the TOCNFs from another agricultural residue, rice straw source (RSS) had the reported dimensions of 1.5 nm / 2.1 nm / 1 μm[32], two thirds of the length of AS-TOCNFs, with an aspect ratio of 1.4 (one third of that for AS-TOCNFs), implying their different fibrillar characteristics, and thus merits, in different applications.

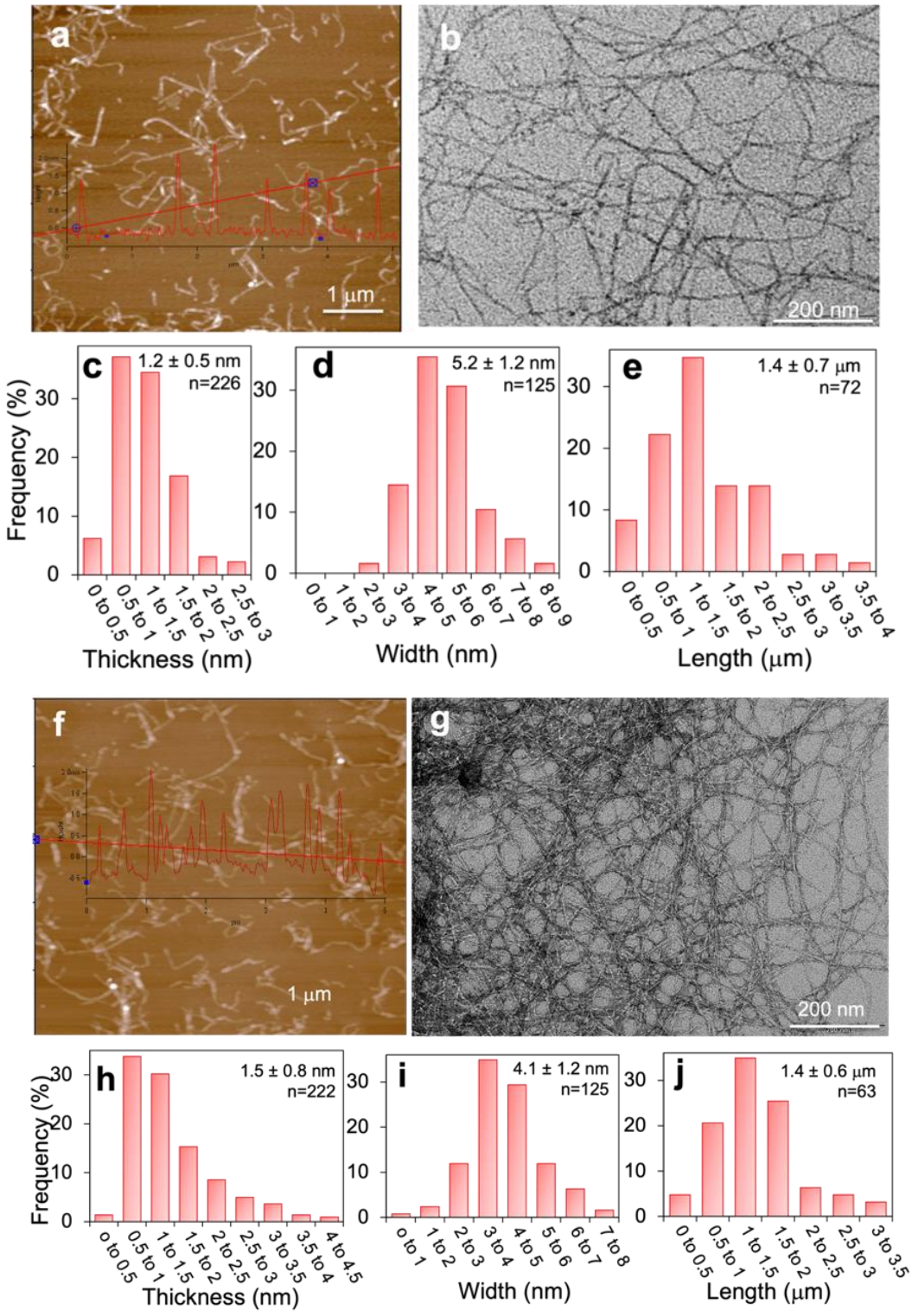
a
1 µm
b
200 nm
c
1.2 ± 0.5 nm
n=226
d
5.2 ± 1.2 nm
n=125
e
1.4 ± 0.7 µm
n=72
Frequency (%)
Thickness (nm)
Width (nm)
Length (µm)
f
1 µm
g
200 nm
h
1.5 ± 0.8 nm
n=222
i
4.1 ± 1.2 nm
n=125
j
1.4 ± 0.6 µm
n=63

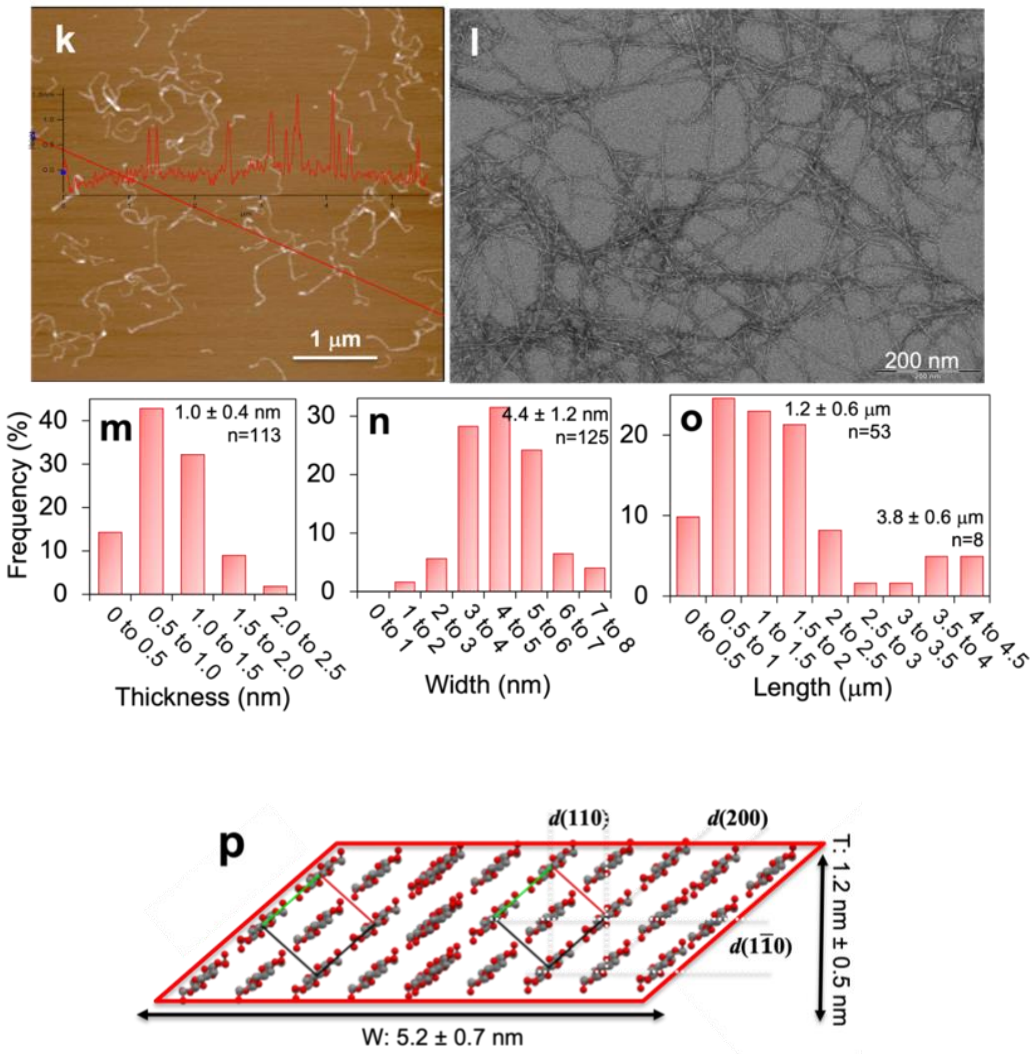

Figure 5-4. Characteristics of TOCNF1s: (a) AFM height image; (b) TEM image on discharged carbon; distribution of (c) thicknesses; (d) widths; (e) lengths. Characteristics of TOCNF2s and TOCNF3s: (f, k) AFM height images; (g, l) TEM images on discharged carbon; distribution of (h, m) thicknesses; (i, n) widths; (j, o) lengths. Characteristics of TOCNFs: (p) model representation of TOCNF with the end of the cellulose chain on the plane.

Functionalization of CNFs takes place on the accessible regions of crystalline surfaces and amorphous domains. To estimate the percent functionalization of the primary OHs on a fibril, a simplified nanofibril cross-sectional model was created using hydrophilic (110) and (1$\bar{1}$0) planes and hydrophobic (200) planes as the respective width (W) and the height (H) direction (Figure. 5-4p), based on AFM and TEM of CNFs on hydrophilic mica and discharged carbon. D-spacings

between d(110), d($1\bar{1}0$), d(200) lattice planes are 0.53 nm, 0.61 nm and 0.39 nm, respectively. In this model, the number of AGU chains in the width directions are presented by $\frac{W}{d(1\bar{1}0)} + 1$, which has to be multiplied by two since AGUs on the top and the bottom rows bear exposed OHs (Eqn. 7), and the total number of AGU chains in the cross section is given by Ns (Eqn. 8). The primary OHs are given by Ns divided by Nt multiplied by $\frac{1}{2}$ since there are 1 primary OHs per 2 AGUs (Eqn. 6). Finally, the percentage of surface primary hydroxyls oxidized is presented by dividing the charge (mmol/g) by the total AGU (mmol/g) multiplied by j as in Eqtn.9. The calculation led to 60.7 % conversion of the total surface primary OHs to carboxylate groups on CNF, suggesting that more than half of surface primary OHs has double-capacity of hydrogen bonding. The effect of surface hydrophilicity along (110) planes and hydrophobicity along d(200) of this model are consistent in the aerogels and the films which are described later in the section 5.4.8.

$$\text{Surface } 1^{\circ}\text{ OH} = \varphi = \frac{1}{2}\frac{N_s}{N_t} = \frac{\frac{W}{d(1\bar{1}0)} + 1}{(\frac{T}{d(100)} + 1)(\frac{W}{d(1\bar{1}0)} + 1)} \qquad \text{Eqn. 6}$$

$$\text{Where:} \quad N_s = 2 \cdot \{(\frac{W}{d(1\bar{1}0)} + 1)\} \qquad \text{Eqn. 7}$$

$$N_t = \{\frac{T}{d(110)} + 1\} \cdot \{\frac{W}{d(1\bar{1}0)} + 1\} \qquad \text{Eqn. 8}$$

$$\%\text{ exposed } 1^{\circ}\text{ OH oxidized} = \frac{COO-charge}{total\ AGU \cdot \varphi} \qquad \text{Eqn. 9}$$

5.4.4 ^{1}H NMR surface chemistry elucidation of TOCNF2

The surface protons on TOCNF2 were evaluated by solution state ^{1}H NMR (**Figure 5-5**) using never-dried aq. TOCNF2, solvent-exchanged with acetone, then with D_2O to prevent

agglomeration caused by drying. The furthest downfield peak at δ4.38 (H1) is assigned to the anomeric proton, which is consistent with the previously-reported chemical shift of H1 at δ4.41 in TOCNFs from rice straw[37]. H6 diastereotopic protons appeared apart from each other at δ4.00 and δ3.27, also agreeing with the previously-reported chemical shifts at δ4.18 and δ3.29 of similarly prepared TOCNF from rice straw[37]. H3, H5, and H4 protons at δ3.83, 3.83, and 3.45 appeared as undefined multiplets, while a triplet for H4 exhibited a merged doublet-doublet peak coupled with H3 and H5. These shifts were approximately consistent with the same protons at δ 3.75, 3.77, and 3.52 of rice straw TOCNF[37]. The slightly downfield peaks of H1', H4', and H5' (δ 4.42, 3.63, and 3.78) that belong to glucuronic acid rings relative to H1, H4, and H5 on the unoxidized AGU are attributed to induction of the electron-withdrawing carboxylate group, causing H1, H4, and H5 to be more deshielded. The clear observance of these protons that belong to glucuronic acid rings is evidence of abundant COO- groups (1.3 mmol COO^- /g-cell) on the wider hydrophilic-to-hydrophobic planes or high aspect ratio of 4.3. However, the average integration could not be calculated from the ratio of glucuronic acid rings/AGU due to the low signal-to-noise ratio and heavy overlapping of peaks including some impurities in the region of 3.4 - 3.8 ppm.

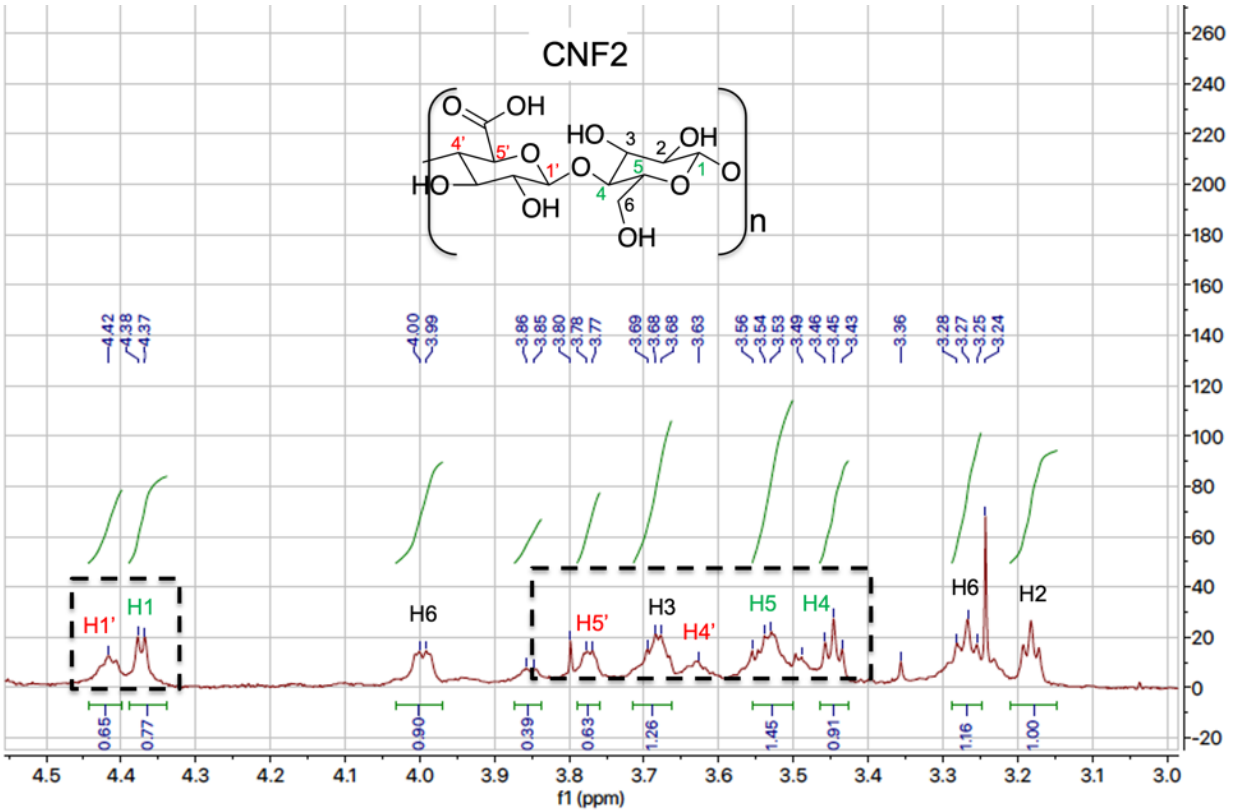

Figure 5-5. ^{1}H NMR of TOCNF2 at ca.0.02 w/v % in D_2O.

5.4.5 Fibers

Self-assembling of TOCNF2 was induced by rapid (-196 °C, 15 min) freezing and freeze-drying into a featherlight white fibrous mass (**Figure 5-6, a-d**). Those from lower concentrations (0.05 %-0.1 %) were particularly fragile and tended to deform or fall apart upon handling. The self-assembled fibrils from 0.01 % were 127 ± 72 nm wide, and those from 0.05 % were ribbon-like shaped and more heterogeneous in size at 278 ± 174 nm wide (**Figure 5e, f)**, transitioning into mostly thin films at 0.1 % then into lamellar structures at 0.3 %.

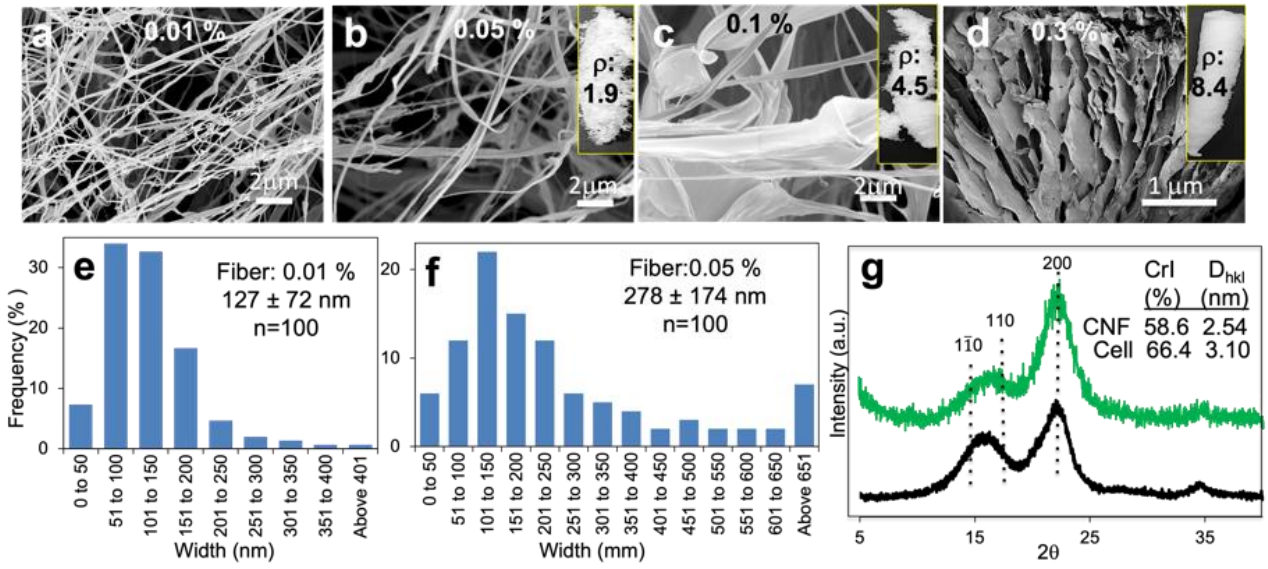

Figure 5-6. Fibers self-assembled from TOCNF2 by freezing at -196 ºC and freeze-drying: morphologies by SEM from initial concentration at (a) 0.01 %; (b) 0.05 %; (c) 0.1 %; (d) 0.3 %; width distributions of fibers from: (e) 0.01 % and (f) 0.05 %; (g) XRD.

The XRD pattern of freeze-dried Cell 2 and freeze-dried TOCNF2 showed peaks characteristic for cellulose at 2θ = 14.7°, 16.8° and 22.7° (**Figure 5-6g**). These represent the $1\bar{1}0$, 110, and 200 crystallographic planes of the monoclinic cellulose I lattice, respectively. The higher CrI of TOCNF2 (66.4 %) than that of cellulose (58.6 %) by 13.3 % indicated removal of amorphous regions. The crystallite size of TOCNF2 calculated from the XRD pattern was 2.54 nm, 18 % lower than AS cellulose (3.10 nm). Similarly, RS TOCNF had a 35 % smaller crystallite size compared to RS cellulose (2.27 nm and 3.51 nm, respectively). The significantly thinner AS-TOCNF2 (1.2 nm thickness) suggests that oxidation reagents may have penetrated into crystalline structures during the reaction[32].

5.4.6 Aerogels

Aerogels were produced by freezing at -20 °C and freeze drying of the aqueous TOCNF2 at 0.05, 0.1, 0.3 and 0.6 w/v % concentrations (**Figure 5-7a, b**). At 0.05 %, 2-D film structures

with highly irregular pores were interspersed with some thin fibers (red arrows). This transitioned to a predominantly film-like porous structure at 0.1 %. This further evoleved into a 3-D isotropic honeycomb structure with a cellular diameter of ca. 200-300 μm at 0.3 and 0.6 %. These are typical aerogels (**Figure 5-7d**). The super low density (2.2 to 10.6 mg/mL) and the super high porosity (99.3 % to 99.9 %) of AS aerogels are directly and inversely correlated to increasing concentrations (**Figure 5-7e**), demonstrating an outstanding capability to hold liquids at higher 6.5 and 10.6 mg/mL density, consistent with the more organized cell walls and smaller pore structures in higher density aerogels (**Figure 5-7c, d**).[41,42] The calculated water absorption values based on constant volume are significantly higher than those of lower density aerogels (**Figure 5-7f**) due to the under-developed pores and cell walls of lower density aerogels (**Figure 5-7a, b**). These aerogels are all amphiphilic, absorbing 74.8 to 121.0 mL/g and 47.6 to 127.3 mL/g liquids in organic ($CHCl_3$) and aqueous media, respectively (**Figure 5-7f**). **Figure 5-7g** shows how cycles of liquid absorption and desorption of $CHCl_3$ (89.0 - 127.3 mL/g) and water (83.9 - 121.0 mL/g) demonstrate the binary polar and non-polar nature and wet resiliency of the cell walls, characterized by both polar-polar and nonpolar-nonpolar TOCNF associations. Note that the highest absorption corresponded to the highest density (6.5 mg/cm^3) aerogel.

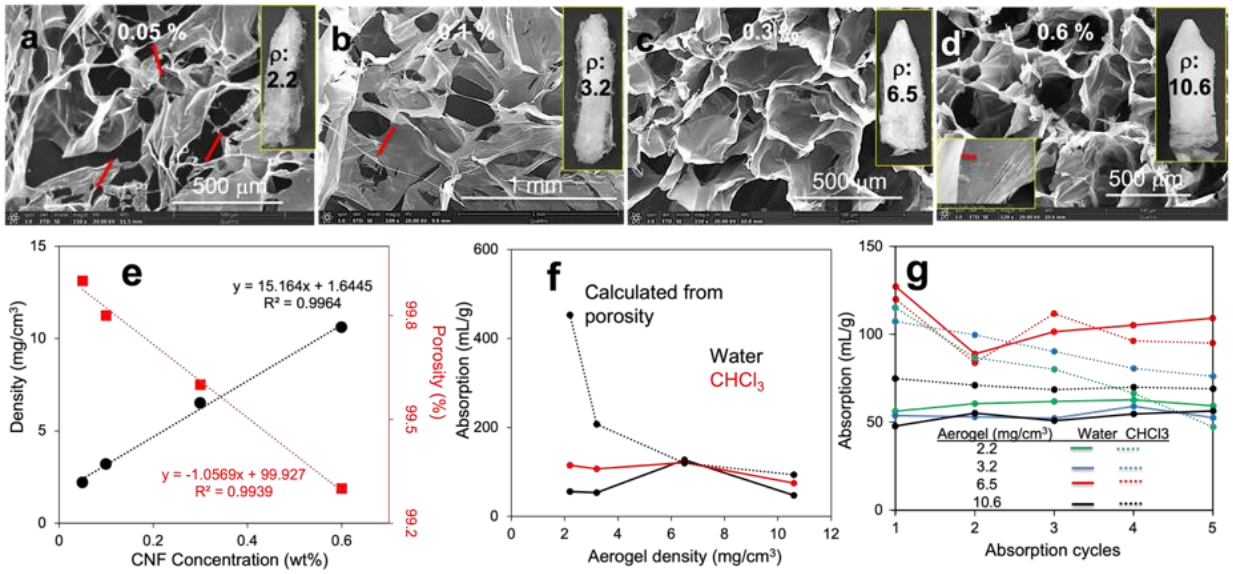

Figure 5-7. Characteristics of aerogel frozen at -20 °C: SEM image of radial cross-section of aerogel formed from dispersion at (a) 0.05 w/v %; (b) 0.1 w/v %; (c) 0.3 w/v %; (d) 0.6 w/v %. Inset photos are the appearance of the corresponding aerogel with their densities. The red arrows indicate directionality of fibers; (e) aerogel density and porosity as a function of TOCNF2 concentration; (f) water and $CHCl_3$ absorption capacity as a function of aerogel density; (g) cyclic water and $CHCl_3$ absorption of 0.05, 0.1, 0.3 and 0.6 w/v % aerogel with the density of 2.2, 3.2, 6.5 and 10.6 mg/cm^3.

5.4.7 Films

Cast films (CF) were created by air-drying 0.3 w/v % TOCNF2 dispersion in a polystyrene (PS) tray for 24 h. The respective dry weight, volume-density, thickness, and area-density of CF were 90.6 mg, 1.25 g/cm^3, 14 µm, and 1.75 mg/cm^2. The calculated CF density of 1.25 g/cm^3 as a fraction of cellulose density of 1.55 g/cm^3 (**Figure 5-8a**) is translated to 22.1 weight % of CF being pores (**Figure 5-8f**). CF appeared clear, transparent, and smooth with surface roughness (represented by RMS) of 30.2 ± 10.8 nm and 62.2 ± 25.0 nm for the top and bottom, respectively, over the large area of 100 mm^2, with the higher RMS of the bottom surface reflecting the rough surface of the PS tray (**Figure 5-8e**). Microscopic images of the top and the bottom surface showed aligned microfibers parallel to the fibril axis (**Figure 5-8b, c**), that exhibited faint birefringence, with the micropores (diameter = 94.1 ± 33.1 µm, n = 50) in the internal bulk structure (**Figure 5-**

8d). The horizontal alignment is attributed to a capillary flow during the drying process that transported hydrophilic CNFs along with water on the hydrophobic hexagonal PS tray. The calculated water absorption values based on constant volume are significantly higher than films of all densities for both water and decane, suggesting disordered or undeveloped pores, especially for films with lower densities (**Figure 5-8g**). The initial water absorption was 1.96, 3.25, 3.70 and 4.72 mL/g for films of the decreasing density of 1.36, 1.25, 1.14 and 0.99 g/cm^3, while irrespective of the film density, increasing water up-take was observed in each cycle (i.e., 3.25, 4.38, 4.54, 5.11, and 5.57 mL/g absorption for film ρ = 1.25 g/cm^3) (**Figure 5-8h**). On the other hand, non-polar decane exhibited far less absorption, only one third that of water (**Figure 5-8h**), indicative of a relatively hydrophilic film surface favoring the interaction with water molecules over hydrophobic decane. The water contact angle (WCA) of 34.0 ± 3.3° on the top film surface, which coincides with the literature value of 34° WCA on cast cellulose film[43], revealed a hydrophilic surface. This implies nonpolar-nonpolar TOCNF associations at the air-film interface, whereas WCAs on the bottom film surface were slightly higher, 42.6 ± 5.8° due to the hydrophobic interaction between TOCNFs and the PS tray (**Figure 5-8, b-c bottom**).

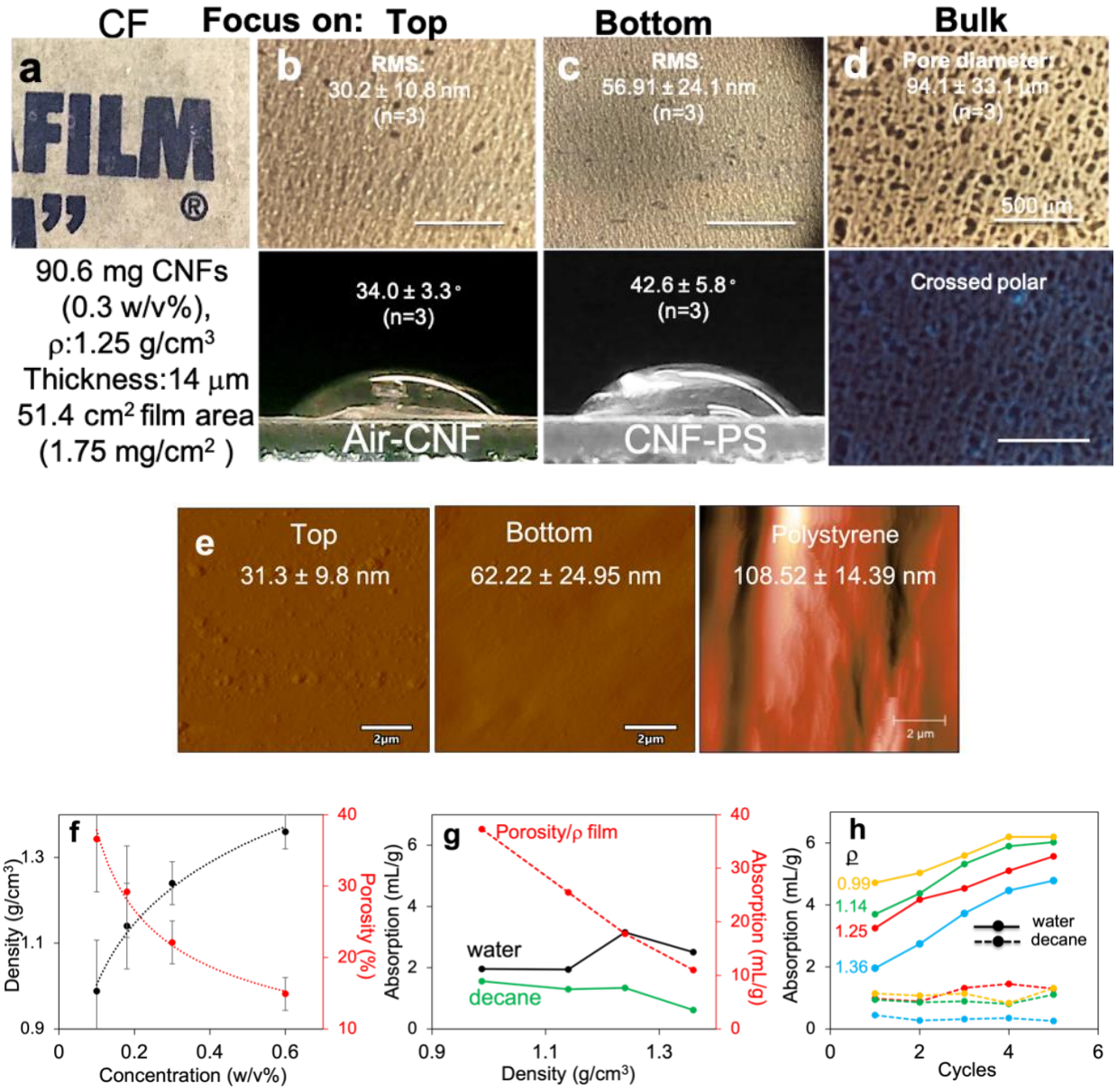

Figure 5-8. Characteristics and properties of cast film (CF) from the 0.3 w/v % aqueous TOCNF2 dispersion in a polystyrene (PS) tray: (a) appearance of film and its properties; optical microscopic images of CF focused on (b) the top; (c) the bottom; (d) inside the bulk, with respective surface roughness values (RMS) based on AFM measurement and the corresponding WCA (5mL). All scale bars are 500 μm. (e) RMS of top and bottom CF facing air (top) or PS (bottom), and the PS surface based on AFM height images. Images shown are amplitude images; (f) density and porosity as a function of concentration; (g) calculated water absorption and the actual absorption of water and decane by CF films as functions of density; (h) water and decane absorption by CF films with density of 0.988, 1.14, 1.24, 1.36 and 1.09 g/cm^3, respectively.

5.4.8 Disassembling behaviors

The disassembling behaviors of fibers, aerogels, and cast films (CF) in water and organic solvents were observed following 1 min sonication. All fibers frozen and freeze-dried from TOCNF2s at varying concentrations (0.05, 0.1, 0.3 and 0.6 w/v %) were 100 % re-dispersible in water back to their original concentrations with statistically the same thickness of 1.2 ± 0.6 nm, 1.2 ± 0.4 nm, 1.7 ± 0.7 nm, and 1.1 ± 0.4 nm, respectively (measured from AFM images) (**Figure 5-9a**). Lengths appeared shorter than the original length (1.4 μm) in all cases, indicating possible chain scissions caused by sonication. 100 % redispersion of TOCNF fibers was expected because freezing at −196 °C promotes instantaneous freezing of TOCNFs around ice crystals, not allowing enough time to arrange the strongest H-bonding. This implies that TOCNF associations are weak and breakable by water. The assembled TOCNF fibers from the 0.6 w/v % dispersion took a longer time (2-3 days) to fully redisperse in water, indicating that the increased local TOCNF concentration during freezing intensified the extent of TOCNF entanglements at higher concentration. Quick and full redispersibility of fibers from fast freezing is advantageous for transportation and re-processing while maintaining the characteristics of TOCNFs.

The aerogel (30 mg, 6.5 mg/cm^3) immersed in 10 mL water showed no change in appearance for three days, even after vortexing for 3 sec (3x) each day (**Figure 5-9b Day 0-3**). Then the aerogel gradually dissociated into smaller pieces, taking about 10 days to form relatively homogenously-dispersed TOCNF2s (**Figure 5-9b Day 10**). However, centrifugation at 5000 rpm for 15 min could not separate the gel and the supernatant completely (**Figure 5-9b Centrifuge**). **Figure 5-9b AFM** reveals that the top part of the centrifuged sample contains a mass of micro-gel structures interspersed with only a few TOCNF2s that are similar to the original TOCNF2 thickness (T: 1.0-1.5 nm) by AFM images, but slightly shorter due to repetitive sonication. The

majority of the aerogel (ca. 90%) did not disintegrate back to the original TOCNF2 size in water for at least 10 days, corroborating super strong polar-polar interface adhesions most likely between wider hydrophilic-to-hydrophobic TOCNF planes.

The CF from 0.3 % TOCNF dispersion in water disintegrated into smaller pieces in water in 2 days (**Figure 5-9c**). However, it took three months with periodic vortexing for 71.7 % of the film to be re-dispersible in water back to the original TOCNF size (T: 1.0 ± 0.3 nm, the original T: 1.2 ± 0.6 nm) (**Figure 5-9c**) while the rest (28.3 %) remained as a gel. In the less polar ethanol ($\varepsilon = 24.3$) and DMAc ($\varepsilon = 37.8$), only 11.4 % and 7.5 % of the CF were re-dispersed, and both supernatants exhibited only aggregated nanoparticles (**Figure 5-9d**) without individual fibrils by AFMs. Re-dispersibility of the CF by 72 %, 11.4 % and 7.5 % in water, ethanol, and DMAc (with decreasing H-bonding ability), relates to dominant hydrophilic TOCNF interfacial associations in CF over hydrophobic interactions.

Fibers formed by instantaneous freezing in liquid N_2, and freeze-drying showed 100 % re-dispersibility to the original concentration in water, while the aerogels and the CF that were more slowly assembled into 3-D structures never re-dispersed completely into 100 % original TOCNF morphology in water. These assembling-disassembling behaviors demonstrated that the drying environment to assemble fibrils into 3-D structures influenced the quality of inter-TOCNF associations and the subsequent ability to absorb water and nonpolar liquids. The thermal degradation pattern (by TGA) exhibited comparable % moisture and Tmax among the fiber, the aerogel, and the CF (9.2, 8.8, 8.9 % and 266, 270, 266 °C for the respective moisture and Tmax) (**Figure 5-9e**), two-fold higher moisture and significantly lower Tmax than those of cellulose (4.7 %, 347 °C, respectively). The higher moisture content of the fibers, the aerogels and the films are due to higher quantity of carboxylate groups on the surface of TOCNFs than those on cellulose,

which renders the CNF surface more hygroscopic. The lower Tg's of TOCNF materials are due to decarboxylation reactions of carboxylate groups followed by degradation of cellulose backbone at the elevated temperature. In TGA, the higher char residue of the CF (31 %) compared with those of the fiber (22 %) and the aerogel (24 %) may imply that solidification process under air caused the calcitrant characteristic of the CF.

All data combined suggest that the slower solidification process create stronger interfacial associations among TOCNFs and rearrange them into more amphiphilic surfaces. However, the foundation of bottom-up material construction seems to be dependent on the polar-polar interfacial associations between wider hydrophilic-to-hydrophobic planes of TOCNF, which is the characteristic of TOCNF from an AS source.

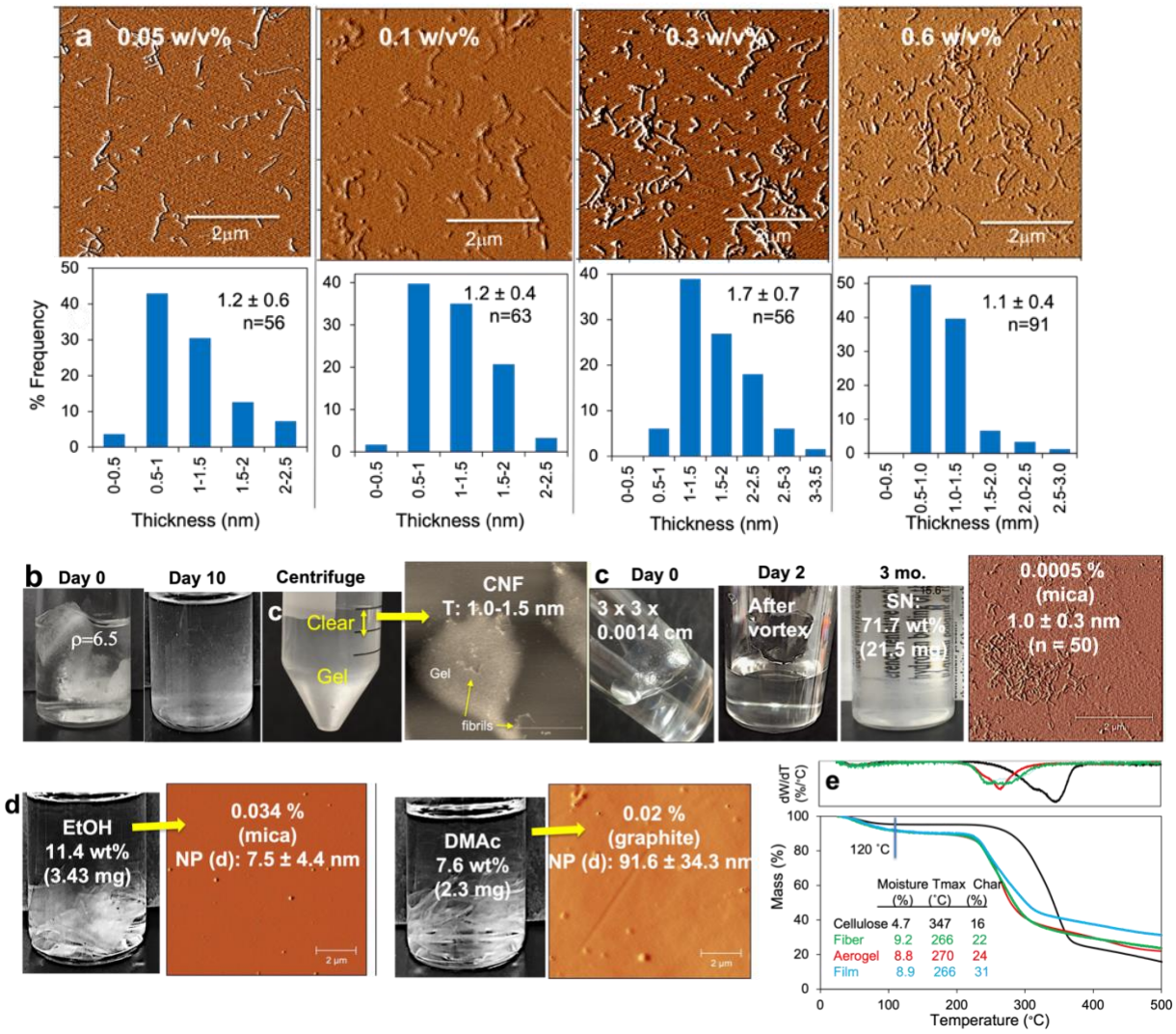

Figure 5-9. Disassembling characteristics of fibers, aerogels and cast films in water: (a) AFM of 100 % redispersed freeze-dried TOCNF2 fibers; 0.05, 0.1, 0.3, 0.6 %, and their respective thickness distribution, all at 0.0005 w/v % on mica; (b) re-dispersibility of 0.3 % aerogel (ρ = 6.5 mg/cm^3) at Day 0, Day 10, post centrifugation of Day 10 dispersion, and an AFM image of the top clear part at Day 10 at 0.0005 w/v % on mica. (c) re-dispersibility of CF at Day 0, Day 2, and 3 months immediately after vortexing for 3 sec and an AFM image of supernatant (3 mo.) on mica after centrifugation at 30 k rpm for 15 min with height measurement. (d) re-dispersibility of the CF of ethanol and DMAc, with corresponding AFM image of supernatant. (e) TGA of cellulose, the fiber, the aerogel and the CF.

5.5 Conclusions

AS-CNFs, generated from the efficient and facile two-step extraction of cellulose followed by TEMPO-mediated oxidation and mechanical blending revealed a unique ribbon-shaped

morphology of TOCNFs with high aspect ratios of 1167/4.3/1 (L/W/T) characterized by wider hydrophilic-to-hydrophobic CNF planes. The charge density of 1.3 mmol COO-/g cell combined with the fibrillar cross-sectional model suggested 68.8 % of surface primary OHs being converted into carboxylate groups, supporting the dominantly hydrophilic CNF surfaces. CNF fibers, frozen at -196 °C and freeze-dried into fibrous mass, were most readily and completely disassembled back to CNFs with the original thickness (1.1-1.7 nm) in water, compared with aerogels and films, indicating weak polar-polar CNF most likely associations using the wider hydrophilic-to-hydrophobic CNF planes represented in the cross-section of crystalline model. The aerogels frozen at -20 °C and freeze-dried, that developed 3D porous cellular structures at above 0.3 w/v %, were amphiphilic and resilient not only absorbing both water (127.3 mL/g) and chloroform (119.6 mL/g) but also holding the higher volume of chloroform than water at least five absorption-desorption cycles, and never fully disassembled into CNFs in water except 10 wt %. These indicated that 3D binary nonpolar-nonpolar and polar-polar CNF associations were developed during slow solidification process, which is supported by the parallelogram of the crystallite cross-sectional model. The 2D cast film (CF) formed by the slowest solidification process in air exhibited hydrophilic top and bottom surfaces with the respective WCA of 34.0 ± 3.3° and 42.6 ± 5.8°, and absorbed more water (3.4 mL/g) than hydrophobic decane (1.3 mL/g). A partial and decreasing redispersibility of the CF in the order of water, ethanol and dimethylacetamide in the respective 71.7, 11.4 and 7.4 w/v % suggested that CNF-CNF associations involved some binary but predominantly polar-polar interactions. In TGA, the CF showed the highest char residue of (31 %) compared with the fibers and the aerogels indicating the more calcitrant characteristic of the films. All the observations combined indicate that solidification speed and environments largely influence strength and surface hydrophobicity/hydrophilicity/amphiphilicity of TOCNF materials.

The most significant finding is that the wider hydrophilic-to-hydrophobic CNF planes, which is depicted in the cross-sectional crystalline model of CNFs, serve as a major interfacial association plane between CNFs as a foundation for a bottom-up material construction in fibers, aerogels and films derived from AS-CNFs. The data presented here demonstrated a huge application potential of AS-CNFs as amphiphilic absorbents and cast films.

5.6 Acknowledgements

The financial support of the USDA Western Sun Grant Program, and the Henry A. Jastro Research Award, University of California, Davis, are greatly appreciated.

5.7 References

(1) International Treenuts and Dried Fruits Council (INC), Statistical Yearbook 202/2021. https://www.nutfruit.org/industry/news/detail/statistical-yearbook (accessed 2021-07-25).

(2) Huang, G., K. Lapsley, Chapter 15 Almond in *Integrated Processing Technologies for Food and Agricultural By-Products, edited by* Pan, Z.; Zhang, R.; Zicari, S.; Academic Press, 2019.

(3) Almond Board of California, 2020 Almond Almanac. https://www.almonds.com/sites/default/files/2020-12/2020%20Almond%20Almanac.pdf

(4) García, R.; Pizarro, C.; Lavín, A. G.; Bueno, J. L. Biomass Sources for Thermal Conversion. Techno-Economical Overview. *Fuel* **2017**, *195*, 182–189. https://doi.org/10.1016/j.fuel.2017.01.063.

(5) Gong, D.; Holtman, K. M.; Franqui-Espiet, D.; Orts, W. J.; Zhao, R. Development of an Integrated Pretreatment Fractionation Process for Fermentable Sugars and Lignin: Application to Almond (Prunus Dulcis) Shell. *Biomass and Bioenergy* **2011**, *35* (10), 4435–4441. https://doi.org/10.1016/j.biombioe.2011.08.022.

(6) Kacem, I.; Koubaa, M.; Maktouf, S.; Chaari, F.; Najar, T.; Chaabouni, M.; Ettis, N.; Ellouz Chaabouni, S. Multistage Process for the Production of Bioethanol from Almond Shell. *Bioresource Technology* **2016**, *211*, 154–163. https://doi.org/10.1016/j.biortech.2016.03.057.

(7) Nabais, J. M. V.; Laginhas, C. E. C.; Carrott, P. J. M.; Ribeiro Carrott, M. M. L. Production of Activated Carbons from Almond Shell. *Fuel Processing Technology* **2011**, *92* (2), 234–240.

https://doi.org/10.1016/j.fuproc.2010.03.024.

(8) Izquierdo, M. T.; Martínez de Yuso, A.; Rubio, B.; Pino, M. R. Conversion of Almond Shell to Activated Carbons: Methodical Study of the Chemical Activation Based on an Experimental Design and Relationship with Their Characteristics. *Biomass and Bioenergy* **2011**, *35* (3), 1235–1244. https://doi.org/10.1016/j.biombioe.2010.12.016.

(9) Klasson, K. T.; Uchimiya, M.; Lima, I. M. Characterization of Narrow Micropores in Almond Shell Biochars by Nitrogen, Carbon Dioxide, and Hydrogen Adsorption. *Industrial Crops and Products* **2015**, *67*, 33–40. https://doi.org/10.1016/j.indcrop.2015.01.010.

(10) Thomas Klasson, K.; Ledbetter, Craig. A.; Wartelle, L. H.; Lingle, S. E. Feasibility of Dibromochloropropane (DBCP) and Trichloroethylene (TCE) Adsorption onto Activated Carbons Made from Nut Shells of Different Almond Varieties. *Industrial Crops and Products* **2010**, *31* (2), 261–265. https://doi.org/10.1016/j.indcrop.2009.11.002.

(11) Martínez de Yuso, A.; Rubio, B.; Izquierdo, M. T. Influence of Activation Atmosphere Used in the Chemical Activation of Almond Shell on the Characteristics and Adsorption Performance of Activated Carbons. *Fuel Processing Technology* **2014**, *119*, 74–80. https://doi.org/10.1016/j.fuproc.2013.10.024.

(12) Chiou, B.-S.; Valenzuela-Medina, D.; Bilbao-Sainz, C.; Klamczynski, A. P.; Avena-Bustillos, R. J.; Milczarek, R. R.; Du, W.-X.; Glenn, G. M.; Orts, W. J. Torrefaction of Almond Shells: Effects of Torrefaction Conditions on Properties of Solid and Condensate Products. *Industrial Crops and Products* **2016**, *86*, 40–48. https://doi.org/10.1016/j.indcrop.2016.03.030.

(13) Chiou, B.-S.; Valenzuela-Medina, D.; Wechsler, M.; Bilbao-Sainz, C.; Klamczynski, A. K.; Williams, T. G.; Wood, D. F.; Glenn, G. M.; Orts, W. J. Torrefied Biomass-Polypropylene Composites. *Journal of Applied Polymer Science* **2015**, *132* (10). https://doi.org/10.1002/app.41582.

(14) Sabbatini, A.; Lanari, S.; Santulli, C.; Pettinari, C. Use of Almond Shells and Rice Husk as Fillers of Poly (Methyl Methacrylate) (PMMA) Composites. *Materials* **2017**, *10* (8), 872. https://doi.org/10.3390/ma10080872.

(15) El Mechtali, F. Z.; Essabir, H.; Nekhlaoui, S.; Bensalah, M. O.; Jawaid, M.; Bouhfid, R.; Qaiss, A. Mechanical and Thermal Properties of Polypropylene Reinforced with Almond Shells Particles: Impact of Chemical Treatments. *Journal of Bionic Engineering* **2015**, *12* (3), 483–494. https://doi.org/10.1016/S1672-6529(14)60139-6.

(16) Hashemian, S. A Comparative Study of Cellulose Agricultural Wastes (Almond Shell, Pistachio Shell, Walnut Shell, Tea Waste and Orange Peel) for Adsorption of Violet B Dye from Aqueous Solutions. *Orient J Chem* **2014**, *30* (4), 2091–2098. https://doi.org/10.13005/ojc/300478.

(17) Estevinho, B. N.; Ratola, N.; Alves, A.; Santos, L. Pentachlorophenol Removal from Aqueous Matrices by Sorption with Almond Shell Residues. *Journal of Hazardous Materials* **2006**,

137 (2), 1175–1181. https://doi.org/10.1016/j.jhazmat.2006.04.001.

(18) Maaloul, N.; Oulego, P.; Rendueles, M.; Ghorbal, A.; Díaz, M. Novel Biosorbents from Almond Shells: Characterization and Adsorption Properties Modeling for Cu(II) Ions from Aqueous Solutions. *Journal of Environmental Chemical Engineering* **2017**, *5* (3), 2944–2954. https://doi.org/10.1016/j.jece.2017.05.037.

(19) Mehrasbi, M. R.; Farahmandkia, Z.; Taghibeigloo, B.; Taromi, A. Adsorption of Lead and Cadmium from Aqueous Solution by Using Almond Shells. *Water Air Soil Pollut* **2009**, *199* (1–4), 343–351. https://doi.org/10.1007/s11270-008-9883-9.

(20) Nabarlatz, D.; Torras, C.; Garcia-Valls, R.; Montané, D. Purification of Xylo-Oligosaccharides from Almond Shells by Ultrafiltration. *Separation and Purification Technology* **2007**, *53* (3), 235–243. https://doi.org/10.1016/j.seppur.2006.07.006.

(21) Pirayesh, H.; Khazaeian, A. Using Almond (Prunus Amygdalus L.) Shell as a Bio-Waste Resource in Wood Based Composite. *Composites Part B: Engineering* **2012**, *43* (3), 1475–1479. https://doi.org/10.1016/j.compositesb.2011.06.008.

(22) González, J. F.; Ramiro, A.; González-García, C. M.; Gañán, J.; Encinar, J. M.; Sabio, E.; Rubiales, J. Pyrolysis of Almond Shells. Energy Applications of Fractions. *Ind. Eng. Chem. Res.* **2005**, *44* (9), 3003–3012. https://doi.org/10.1021/ie0490942.

(23) Saura-Calixto, F.; Canellas, J.; Garcia-Raso, J. Contents of Detergent-Extracted Dietary Fibers and Composition of Hulls, Sheels, and Teguments of Almonds (Prunus Amygdalus). *J. Agric. Food Chem.* **1983**, *31* (6), 1255–1259. https://doi.org/10.1021/jf00120a027.

(24) Queirós, C. S. G. P.; Cardoso, S.; Lourenço, A.; Ferreira, J.; Miranda, I.; Lourenço, M. J. V.; Pereira, H. Characterization of Walnut, Almond, and Pine Nut Shells Regarding Chemical Composition and Extract Composition. *Biomass Conv. Bioref.* **2020**, *10* (1), 175–188. https://doi.org/10.1007/s13399-019-00424-2.

(25) Maaloul, N.; Arfi, R. B.; Rendueles, M.; Ghorbal, A.; Diaz, M. Dialysis-Free Extraction and Characterization of Cellulose Crystals from Almond (Prunus Dulcis) Shells. **2017**, 11. http://hdl.handle.net/10651/45376

(26) Martínez, J. M.; Reguant, J.; Montero, M. Á.; Montané, D.; Salvadó, J.; Farriol, X. Hydrolytic Pretreatment of Softwood and Almond Shells. Degree of Polymerization and Enzymatic Digestibility of the Cellulose Fraction. *Ind. Eng. Chem. Res.* **1997**, *36* (3), 688–696. https://doi.org/10.1021/ie960048e.

(27) De Bari, I.; Barisano, D.; Cardinale, M.; Matera, D.; Nanna, F.; Viggiano, D. Air Gasification of Biomass in a Downdraft Fixed Bed: A Comparative Study of the Inorganic and Organic Products Distribution. *Energy Fuels* **2000**, *14* (4), 889–898. https://doi.org/10.1021/ef990243g.

(28) Nepomuceno, N. C.; Santos, A. S. F.; Oliveira, J. E.; Glenn, G. M.; Medeiros, E. S. Extraction

and Characterization of Cellulose Nanowhiskers from Mandacaru (Cereus Jamacaru DC.) Spines. *Cellulose* **2017**, *24* (1), 119–129. https://doi.org/10.1007/s10570-016-1109-5.

(29) Wu, X.; Moon, R. J.; Martini, A. Tensile Strength of Iβ Crystalline Cellulose Predicted by Molecular Dynamics Simulation. *Cellulose* **2014**, *21* (4), 2233–2245. https://doi.org/10.1007/s10570-014-0325-0.

(30) Iwamoto, S.; Kai, W.; Isogai, A.; Iwata, T. Elastic Modulus of Single Cellulose Microfibrils from Tunicate Measured by Atomic Force Microscopy. *Biomacromolecules* **2009**, *10* (9), 2571–2576. https://doi.org/10.1021/bm900520n.

(31) Fukuzumi, H.; Saito, T.; Iwata, T.; Kumamoto, Y.; Isogai, A. Transparent and High Gas Barrier Films of Cellulose Nanofibers Prepared by TEMPO-Mediated Oxidation. *Biomacromolecules* **2009**, *10* (1), 162–165. https://doi.org/10.1021/bm801065u.

(32) Jiang, F.; Hsieh, Y.-L. Chemically and Mechanically Isolated Nanocellulose and Their Self-Assembled Structures. *Carbohydrate Polymers* **2013**, *95* (1), 32–40. https://doi.org/10.1016/j.carbpol.2013.02.022.

(33) Urruzola, I.; Robles, E.; Serrano, L.; Labidi, J. Nanopaper from Almond (Prunus Dulcis) Shell. *Cellulose* **2014**, *21* (3), 1619–1629. https://doi.org/10.1007/s10570-014-0238-y.

(34) Yousefi, H.; Faezipour, M.; Hedjazi, S.; Mousavi, M. M.; Azusa, Y.; Heidari, A. H. Comparative Study of Paper and Nanopaper Properties Prepared from Bacterial Cellulose Nanofibers and Fibers/Ground Cellulose Nanofibers of Canola Straw. *Industrial Crops and Products* **2013**, *43*, 732–737. https://doi.org/10.1016/j.indcrop.2012.08.030.

(35) Lu, P.; Hsieh, Y.-L. Cellulose Isolation and Core–Shell Nanostructures of Cellulose Nanocrystals from Chardonnay Grape Skins. *Carbohydrate Polymers* **2012**, *87* (4), 2546–2553. https://doi.org/10.1016/j.carbpol.2011.11.023

(36) Sun, J. X.; Sun, X. F.; Zhao, H.; Sun, R. C. Isolation and Characterization of Cellulose from Sugarcane Bagasse. *Polymer Degradation and Stability* **2004**, *84* (2), 331–339. https://doi.org/10.1016/j.polymdegradstab.2004.02.008.

(37) Jiang, F.; Dallas, Jerry. L.; Ahn, B. K.; Hsieh, Y.-L. 1D and 2D NMR of Nanocellulose in Aqueous Colloidal Suspensions. *Carbohydrate Polymers* **2014**, *110*, 360–366. https://doi.org/10.1016/j.carbpol.2014.03.043.

(38) Segal, L.; Creely, J. J.; Martin, A. E.; Conrad, C. M. An Empirical Method for Estimating the Degree of Crystallinity of Native Cellulose Using the X-Ray Diffractometer. *Textile Research Journal* **1959**, *29* (10), 786–794. https://doi.org/10.1177/004051755902901003.

(39) Tojo, G.; Fernández, M. TEMPO-Mediated Oxidations. In *Oxidation of Primary Alcohols to Carboxylic Acids: A Guide to Current Common Practice*; Tojo, G., Fernández, M., Eds.; Basic Reactions in Organic Synthesis; Springer: New York, NY, 2007; pp 79–103.

https://doi.org/10.1007/0-387-35432-8_6.

(40) Saito, T.; Kimura, S.; Nishiyama, Y.; Isogai, A. Cellulose Nanofibers Prepared by TEMPO-Mediated Oxidation of Native Cellulose. *Biomacromolecules* **2007**, *8* (8), 2485–2491. https://doi.org/10.1021/bm0703970.

(41) Jiang, F.; Hsieh, Y.-L. Amphiphilic Superabsorbent Cellulose Nanofibril Aerogels. *J. Mater. Chem. A* **2014**, *2* (18), 6337–6342.
https://doi.org/10.1039/C4TA00743C

(42) Patterson, G.; Hsieh, Y.-L. Tunable Dialdehyde/Dicarboxylate Nanocelluloses by Stoichiometrically Optimized Sequential Periodate–Chlorite Oxidation for Tough and Wet Shape Recoverable Aerogels. *Nanoscale Advances* **2020**, *2* (12), 5623–5634. https://doi.org/10.1039/D0NA00771D.

(43) Luner, P.; Sandell, M. The Wetting of Cellulose and Wood Hemicelluloses. *Journal of Polymer Science Part C: Polymer Symposia* **1969**, *28* (1), 115–142. https://doi.org/10.1002/polc.5070280112.

(44) Scherrer, P. (1918). Estimation of the size and internal structure of colloidal particles by means of Röntgen rays. Nachrichten von der Gesellschaft der Wissenschaften zu Göttingen, 96–100.

CHAPTER 6: Summary

This Ph.D. project has presented a new facile approach to generating hydrophobic nanocellulose directly from macro-size cellulose by utilizing the safer reagent BDS as a precursor of 1,3-BD for telomerization, combined with mechanical blending to generate ODE-nanocellulose. The project then explored ultra-sonication as a disintegration tool in organic solvents. The sonicated ODE-cellulose in organic solvents contains both micro and nanofibers that can be directly brought into processing without separation. Ultra-sonication not only enabled a continuous transition from cellulose disintegration to processing in a single organic solvent, but also expanded the choice of media, such as vegetable oils, beyond that possible for mechanical blending.

In Chapter 2, one pot telomerization of 1,3-BD with cellulose (0.1 g scale) under optimal conditions, the optimal condition, followed by mechanical blending, successfully produced hydrophobic 2,7-octadienyl-ether (ODE) functionalized nanocellulose (ODE-NC) with DS = 0.74 mmol ODE/g-cell. The reaction was carried out by using butadiene sulfone (BDS), which is a solid at room temperature, melts at 65 ºC, and generates gaseous 1,3-BD and sulfur dioxide above 90 ºC. It is thus a safer alternative to using gaseous 1,3-BD in a cylinder. ODE-NC (NPs and CNFs) were dispersible in DMSO, THF, and $CHCl_3$ at 27- 41 % of the aqueous precipitate (90 % of cellulose), and the dispersed CNFs' average thickness was 3.7 - 4.4 nm, with the thinnest CNFs found in less polar $CHCl_3$. The surface chemistry of ODE-CNFs was elucidated by FTIR and ATR-FTIR, showing methylene groups at 2800-2980 cm^{-1}, and C=C groups at 1640-1704 cm^{-1}. The solution phase ^{1}H NMR, and ^{13}CNMR in d_6-DMSO confirmed the cellulose structure and ODE-groups, and a 30 % conversion of surface OH to ODE was estimated based on the integration value of the average ODE proton normalized to that of an anomeric proton in AGU. The hydrophobicity of ODE-NC was evidenced by a WCA of 102 ± 1° on coated mica with 1 % ODE-NC in $CHCl_3$.

These organic solvent compatible, thermally stable, and high aspect ratio ODE-CNFs are the most hydrophobic reported to date.

In Chapter 3, 2D NMR of heteronuclear single quantum coherence spectroscopy (HSQC) elucidated the correlation between the chemical shift of protons in ODE-CNFs to the ^{13}C NMR chemical shift of their directly-attached carbons. Furthermore, homonuclear correlation spectroscopy (COSY) was used to identify spins of vicinal hydrogens in ODE-CNFs which are coupled to each other.

In Chapter 4, sonication was proven to be effective in disintegrating ODE-cellulose into ODE-NC with T: 3.3-5.1 nm and L: 0.5-1.7 μm (10 / 90 – 50 / 50 CNF / NPs) in $CHCl_3$ for 5-10 min (35 - 75 % *A*, 17-26 kJ) with ca. 15-18 % yield. More importantly, 20 min sonication (50 % *A)* produced the same quantity of ODE-NC in $CHCl_3$ and toluene as 30 min blending of the aq. precipitate did. Scale-up (0.5 g) telomerization under the optimal condition from the 0.1 g scale (6ODE110) generated ODE-cell with DS 0.67 relatively in good agreement with 0.74 from the 0.1 g scale within 10 % discrepancy, validating scale-up reaction. tert-Butanol (TB, 2 v/v%) treatment of ODE-cell prior to 20 min sonication improved the yield of ODE-NC by 23-68 % in THF, $CHCl_3$, LO and toluene with respect to those without TB treatment. The DS were further optimized by incorporating 3 min pre-sonication of cellulose in DMF prior to telomerization. The DS improved to 1.2 (113 % yield) and 1.8 mmol ODE/g-cell (119 % yield), compared with DS (0.74 mmol ODE/g-cell) of ODE-cell generated without pre-sonication at the similar temperature range.

Sonication (50 % *A*, 20 min) of 1.2ODE-cell in toluene produced 1.2ODE-NC (40 / 60 NP / CNF) with 45.5 % yield, while sonication of 1.8ODE-cell yielded 73.3 % 1.8ODE-NC in LO. Toward applications, 1.2ODE-MC/NC was evaluated as a reinforcing agent in polymer films while 1.8ODE-NC in LO was probed as hydrophobic paper coating. The film cast from a stirred solution

of PBD in toluene combined with the previously sonicated 1.2ODE-MC/NC (2 % of PBD) preserved the elastomeric character, with modulus (2.23 ± 0.34 MPa) significantly improved by six-fold with respect to that of pristine PBD (0.35 ± 0.11 MPa). On the other hand, the film cast from the co-sonicated (50 *A*, 20min) solution of PBD and 1.2ODE-MC/NC exhibited plastic characteristics with an improved modulus (0.79 ± 0.49 MPa) with respect to that of pristine PBD. The reinforcing effect of cross-linking 2 % 1.2ODE-NC/MC with PSIS with only a small quantity of AIBN (1:1 FR/*t*-ene) has shown a remarkable increase in modulus (8.0 ± 1.6 MPa) by 67.7 % with respect to the 4.8 ± 0.6 MPa of pristine PSIS depending on the processing condition. Further improvements in modulus (7.8 ± 1.0 MPa), strength (17.3 ± 3.3 MPa), and strain (1780 ± 448 %) were accomplished without any additional reagent but only by 5 h thorough mixing of two components in toluene. This indicated that longer mixing time has likely separated and re-oriented the polymer chains forming the homogenized mixture with ODE-MC/NC, which created stronger surface adhesions among polymer chains and 1.2ODE-NC/MC.

Coating of CP at the optimum condition of 0.07 % 1.8ODE-NC/LO, then heating at 70º for 16 h has shown the reinforcing effect on CP, with a strength of 26.7 ± 0.8 MP that may be attributed to the grafting and cross-linking among CP, 1.8ODE-NC and LO. After ethanol and acetone rinses, the hydrophobicity of the coated CP surface was evidenced in WCAs of 91, 99, and 117º at 3 min for CP coated with LO r.t, LO / ODE 70 ºC 8h, LO / ODE 70 ºC 16h, respectively. Water retention was at least 3 h.

In Chapter 5, cellulose has been successfully isolated from almond shells (AS) in 35.2 % yield by a two-step extraction process ($NaClO_2$/KOH) and subsequent TEMPO-mediated oxidation, generating ribbon-shaped cellulose nanofibrils (CNF, 90 % Y) with average thickness / width / length of 1.2 ± 0.5 nm / 5.2 ± 1.2 nm / 1.4 ± 0.7 μm. A high aspect ratio (W / T) of 4.3 and

the wide hydrophilic planes of fibrils are unique to AS-TOCNFs. Thus, the effect of this characteristics on 3-D material formation was studied by analyzing assembling and disassembling behaviors of fibers, aerogels and films formed under different solidification environments. The aerogels and the films solidified by the slower processes than the fiber never fully reverted back to TOCNFs of the original sizes in water. The aerogel particularly exhibited an amphiphilic characteristic by absorbing and holding both aqueous and organic media. The higher char residue of the films observed in TGA may indicate the calcitrant characteristic of the films developed during drying in air. All data indicated that slow solidification process may induce stronger CNF-CNF interfacial associations, and the rearrangement of fibrils to form amphiphilic surfaces. Concurrently, it was found that the wider hydrophilic-to-hydrophobic CNF planes, characteristic to AS-TOCNFs, serve as a major interfacial association plane between CNFs as a foundation for bottom-up material formation of TOCNFs.

Future investigations are needed to deepen the understanding of ODE-CNFs and broaden their applications. NMR analysis of ODE-CNFs obtained from 0.5 g scale telomerization should be evaluated and compared with the DS calculated from the mass gain. The recommended future research areas for ODE-CNFs are: 1) co-polymerization of ODE-CNFs with alkene-containing monomers; 2) epoxidation of ODE alkene groups to form adhesives, and Grubb's metathesis of ODE alkene groups with vegetable oils for solid film formation; and 3) formation of chemical-free emulsions by manual shaking of ODE-CNFs and vegetable oils for skin care products.